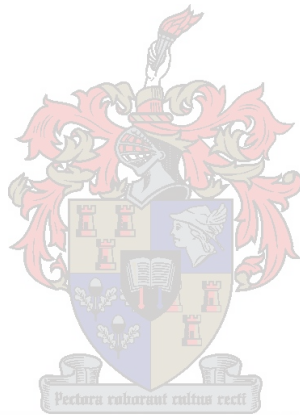# Power Line Corona Noise Prediction from Small Cage Measurement

Rodney Gordon Urban

Dissertation presented for the degree of Doctor of Philosophy in Engineering at the University of Stellebosch

Promoters: Prof. H.C. Reader and Dr. J.P. Holtzhausen
September 2004

Declaration

I, the undersigned, declare that the work contained in this dissertation is my own original work, unless otherwise stated, and has not previously, in its entirety or in part, been submitted at any university for a degree.

R.G. Urban   September 2004

Abstract

The radio noise (RN) performance of an AC high voltage transmission line is a determining factor when accessing the reliability of the design. The conducted RN level across the terminals of a PLC receiver, used in the teleprotection system of the line, is of particular concern. In this dissertation, existing empirical and semi-analytical RN prediction methods are evaluated by comparing the conducted RN levels of four South African lines to the predicted levels.

Existing RN measurement protocols are consolidated and a new RN measurement protocol is proposed for the comparison. A prediction methodology, based on the EdF, EPRI and IREQ semi-analytical methods, is formulated. The semi-analytical methods are not able to accurately predict the variation of the conducted RN with frequency in the PLC band, nor are they able to predict the RN performance of short lines. A wideband excitation function, which considers the statistical characteristics of the measured RN pulse train, is therefore proposed in this dissertation. Having investigated the extraction of this excitation function from ESKOM's Megawatt Park corona cage, it is concluded that a small corona cage is required. The design of a small cage is presented and the extraction of the excitation function is described. Attention is given to assessing the effect of changes in space charge distributions. The effect of space charge collision with an insulated cage on the extracted pulse parameters is linear, provided space charge diffusion is negligible. The onset streamer, positive streamer and negative streamer corona modes were identified as the only modes with measurable RN in the frequency regime 150 kHz to 30 MHz. Formulas are derived for the prediction of the inception gradients for these modes. The RN performance of an ACSR Hare conductor is extracted from the small cage. The RN performance of the Acacia-Koeberg line is also approximated in the PLC band.

The dissertation concludes that the proposed wideband excitation function method is capable of accurately predicting the variation of RN levels with frequency. It can also be used to predict the RN performance of short line sections, as well as the relationship between RMS, QP and average RN levels from a transmission line.

Opsomming

Die korona-werkverrigting van 'n WS hoogspanningstransmissielyn het belangrike gevolge vir die betroubaarheid van die ontwerp van die lyn. Die geleide radioruis (RR) vlak op die kraglyn-dragolf kommunikasie sisteem, wat vir tele-beveiliging gebruik word, is veral van belang. In hierdie werkstuk word bestaande metodes gebruik om die korona-werkverrigting te bepaal en dan met gemete waardes van vier Suid Afrikaanse lyne te vergelyk.

Bestaande RR meetmetodes word saamgevat en 'n nuwe metingsprotokol word voorgestel om resultate te vergelyk. Na aanleiding van hierdie vergelykings word 'n tegniek ontwikkel om die RR van 'n lyn te voorspel. Hierdie tegniek gebruik die EdF, EPRI en IREQ metodes. Die voorgestelde tegniek kan nie die verandering van die RR met frekwensie bepaal nie. Dit kan ook nie die RR van kort lyne bepaal nie. 'n Wyeband RR bron word dus voorgestel. Nadat ESKOM se Megawatt Park korona-kou ondersoek is, is die gevolgtrekking gemaak dat 'n klein korona-kou die nodige wyeband RR bron sal voorsien. Ruimtelading bots met die klein korona-kou. Die effek van hierdie botsings op die pulsparameters is lineêr indien ladingsdiffusie nie plaasvind nie. Die aanvangs, positiewe en negatiewe kanaalontladings ("streamers") is identifiseer as die enigste koronamodusse wat RR veroorsaak tussen 150 kHz en 30 MHz. Die spanning waarby hierdie modusse voorkom, is bepaal. Die korona-werkverrigting van 'n "ACSR Hare" geleier is bepaal. Die korona-werkverrigting van die Acacia-Koeberg transmissie lyn is ook gekwantifiseer by die kraglyn-dragolf kommunikasie frekwensies.

Die wyebandbron metode kan die verandering in RR met frekwensie goed voorspel. Die nuwe metode kan ook gebruik word om die RR van kort lyne te bepaal, asook die verband tussen RMS, QP en gemiddelde RR vlakke.

Acknowledgements

Many have helped make this work possible:

God, without whom nothing is possible.

Louise. Your love, support, and patience over the past few years has inspired and motivated me and has made this possible.

Mom, Dad, Graeme and Evelyn. Your love and support has always been a constant in my life and my studies.

Our families and friends. You have helped both me and Louise throughout.

The Tourell family. You've always been there for me.

Howard. It has been a privilege to study under your supervision. You have taught me so much, while always allowing me the freedom to explore my own paths. It is easy to listen to someone you respect.

Koos. Your guidance has made it easy to adapt to the high voltage environment. Your insight into this field has been invaluable in my work.

Wernich. Your work has been immensely helpful. I'm grateful that you have so kindly shared some of it with me.

Prof. Wedepohl who has generously made his unpublished notes on the theory of natural modes available through Prof. Cloete. This was an important starting point for the work.

Roy Hubbard. Your support for the program has facilitated much of this work.

Tony Britten and Dave Smith. Your insight into and support for my research has been encouraging and helpful. I appreciate you're support.

Petrus, Ulrich and Wilhelm. You've helped me immensely over the past few years. Your enthusiasm and willingness to go the extra distance has made this work possible.

The students with whom I have shared office space for so long. Nothing is more important than a great work environment. I wish you all the best in your studies.

Willem and Koos. Thank you for helping me with the *opsomming*.

Contents

v

4   Large Corona Cage Measurements

5   Extraction of a Wideband Excitation Function from a Small Corona Cage

6   Small Corona Cage Measurements

List of Figures

x

List of Tables

xiv

List of Abbreviations

RN	Radio Noise
RI	Radio Interference
TVI	Television Interference
PLC	Power Line Carrier
QP	Quasi Peak
RMS	Root Mean Square
RAD	Relative Air Density
RH	Relative Humidity
pdf	Probability Density Function
STP	Standard Temperature and Pressure
DFT	Discrete Fourier Transform
ACSR	Aluminium Conductor Steel Reinforced

Chapter 1

Introduction

1.1   Conductor Corona on High Voltage Transmission Lines

A large quantity of electrical energy is continuously transported throughout South Africa along a network of high voltage transmission lines. To meet increasing demands for this energy, the carrying capacity of the network has to be increased. New lines must therefore be built. The design of a high voltage transmission line is a multi-faceted undertaking in which economical cost and reliability are of primary concern. Both mechanical and electrical factors are considered when assessing a line's reliability. Mechanical factors include conductor vibration which can cause damage to either the conductors or their support structures and conductor heating which increases sag between attachment points. Insulation is one of the most important electrical considerations. The air gap clearances and insulator selection for a line must be sufficient so as to prevent complete breakdown, i.e. flash-over, which will interrupt energy transfer and damage line components. This requires knowledge of the electrical withstand and breakdown characteristics of the line under different weather and pollution conditions and under normal operating voltage as well as over-voltage conditions. Transmission lines should be designed as compact as possible without compromising their reliability.

An important electrical consideration, which is the focus of this dissertation, is the line's corona performance. Significant electric fields at the surfaces of the line's conductors cause ionization of the adjacent air. If these surface gradients are sufficiently high so as to facilitate self-sustaining ionization, corona discharges occur near the conductor surfaces. Conductor corona discharges are responsible for many macroscopic phenomena on the line. Three phenomena considered when characterizing the corona performance of a line are corona loss, radio noise (RN) and audible noise. Corona loss is the rate at which energy is expended by the high voltage source in the ionization and recombination collisions and charge movements associated with conductor corona. It reduces the efficiency of power transmission. Corona discharges also have acoustic emissions over a wide range of the audible spectrum. Audible noise from corona has a high

annoyance factor and the need for public acceptance of this noise source forces line designers to ensure that it is within specified limits.

Corona discharges also cause electron movement near the conductor surfaces which induce current pulses in the conductors. The resultant pulse trains propagate along the conductors and produce electromagnetic emissions over a wide frequency range both at the terminals of the line, i.e. conducted emissions, and in the vicinity of the line, i.e. radiated emissions. The radiated emissions cause interference to broadcast radio reception near the line and are referred to as radio interference (RI). Collectively, the conducted and radiated corona noise is referred to as radio noise in this dissertation. Conductor corona produces RN predominately below 5 MHz [1]. Transmission line RN above 15 MHz is from sparks and micro-sparks on faulty equipment such as insulators and not from conductor corona [1]. Precipitation and pollution on or near a line conductor will cause surface gradient distortions. This results in gap-type corona discharges which produce significant RN up to 1 GHz [1]. The RI of these propagating pulses interferes with television reception and is referred to as television interference (TVI).

RN is dependent on many variables besides the line's geometry. These include temperature, air pressure, relative humidity, weather, pollution, conductor surface irregularities and ground resistivity. An account of the RN must therefore include a description of ambient conditions.

1.2   Methods of Predicting RN Performance

An evaluation of the acceptability of a line design must consider the line's RN. A method of predicting the RN must therefore be available to the design team. The RN of a line varies randomly with respect to time due to changes in environmental conditions. It cannot therefore be characterized by a single value. It is more appropriate to consider RN as a random variable and characterize it with statistical methods. Such a statistical model describes the probability that the RN of a line is within a certain range of values.

A prediction of the RN based entirely on analytical methods is not practical due to the complex nature of the discharge processes and the large number of variables that affect them. Measurements made on existing lines have produced a large database of RN levels for various

line geometries and weather conditions. This data has been analyzed with statistical methods to produce empirical formulas which are used to predict the RN of a proposed line. These methods are only valid for the range of line geometries studied and may not be applicable to a new design.

Adams [2] proposed that RN generation be decomposed into a "generation density" quantity and a geometrical quantity. The generation density takes into account the random, pulsative nature of induced currents and is independent of geometry. Gary [3] refined this generation density concept and developed the concept of an excitation function that can be measured in a corona cage. The measured excitation function is used to calculate a line's RN by including it in an analytical propagation model. This semi-analytical method better predicts the RN of a line design for a wide range of geometries. A corona cage is a coaxial structure that facilitates the use of lower voltages and smaller dimensions to reproduce transmission line surface gradients on bundle conductors. The corona cage is less expensive to construct than a full-scale test line and can be used for many line designs.

1.3   Need for a New RN Prediction Method

In the event of a fault on a line, for example a phase conductor fails and a flash-over occurs to ground, damage to the line is limited by uncoupling the line's supply as quickly as possible. This is in part done by teleprotection in South Africa. Power line carrier (PLC) signals are transmitted along line conductors in the band 50 kHz to 500 kHz. If these signals are not distinguishable above the noise floor at either end of a line, the supply is disconnected from the line, i.e. the line is tripped. A good calculation of the signal-to-noise ratio for PLC communication is therefore essential when designing a line with teleprotection. Conductor corona is the dominant noise source in the PLC band and is calculated with empirical and semi-analytical prediction methods. Such a calculation on the 400 kV Hydra-Droërivier line was 20 dB below the measured level [4]. An investigation was therefore initiated to evaluate the accuracy of existing RN prediction methods, propose an accurate RN prediction methodology and implement the methodology in an executable code.

3

1.4 Claims Made by This Dissertation

Existing RN measurement protocols and prediction methods are consolidated. A comprehensive measurement protocol is proposed for both conducted and radiated RN. An accurate prediction methodology is formulated for local lines at 500 kHz. A new excitation function prediction method, which more accurately predicts the frequency variation of the RN in the band 150 kHz to 30 MHz, is proposed. A small laboratory corona cage is designed for the extraction of this wideband excitation function. The new method also facilitates the calculation of RN on any length of line. The significant effect of negative streamers on the RN performance of practical transmission line bundle conductors is identified.

1.5 Layout of Dissertation

Since RN is influenced by so many variables, RN prediction methods are numerous. In order to restrict the investigation to methods applicable to local conditions and also ensure a high level of confidence in the predicted RN, it is necessary to first identify the most important influencing factors and determine the accuracy of the RN measurements on actual lines. This is considered in chapter 2. This chapter consolidates existing RI measurement protocols and considers the use of conducted RN measurements in the evaluation of RN prediction methods.

Having determined the measurable RN characteristics and the accuracy to which they can be measured, suitable prediction methods are next identified in chapter 3. To understand the accuracy and limitations of each method for a specific line design, individual correction terms are isolated and their effect on each method's accuracy is investigated by comparison with the line measurements of chapter 2. The chapter is concluded with a discussion of the proposed prediction methodology. This was implemented in executable code [5] for the calculation of a line's RN performance.

Certain limitations of the existing prediction methods were identified in chapter 3 and studied in a large corona cage. The design and measurement protocol for such an experimental setup is presented and reasons for the limitations are suggested in chapter 4. Based on the measurements and findings presented in this chapter, it was decided to develop a new prediction method based on a wideband excitation function which is extracted from a small corona cage. The new

prediction method and the small cage design are presented in chapter 5.

The wideband excitation function is then extracted from small cage measurements and the RN performance of a line is approximated with the new method in chapter 6. Finally, the most important conclusions made in the dissertation are summarised in chapter 7 and recommendation are made for future research.

1.6   References

[1]   F.W. Warburton, T. Liao, N.A. Hoglund, "Power Line Radiations and Interference Above 15 MHz", IEEE Trans., Vol. PAS-88, 1969, pp. 1492-1498.

[2]   G.E. Adams, "The Calculation of Radio Interference Level of Transmission Lines Caused by Corona Discharges", AIEE Trans., Part III, 1956, pp. 411-419.

[3]   C.H. Gary, "The Theory of the Excitation Function: A Demonstration of its Physical Meaning", IEEE Trans., Vol. PAS-91, 1972, pp. 305-310.

[4]   Personal Discussion with D.C. Smith, 1999, University of Stellenbosch.

[5]   R.G. Urban, *Corona Generated Noise Modelling, V3.1: User Manual*, Unpublished internal document, 2004, University of Stellenbosch.

Chapter 2

Operational Transmission Line Measurements

2.1   Introduction

Good measured data must be available for a transmission line in order to evaluate the accuracy of a prescribed method in predicting its RN performance. Such performance data is presented in the literature (e.g. [1], [2] and [3]), accompanied by descriptions of the line geometry and various conditions that influence the RN levels. As most of these measurements are used to derive the empirical prediction methods evaluated, an objective evaluation cannot be made with the data. The validity of a method for a certain line requires that all input variables are within bounds specified for that method. These bounds may be unique to a geographical region. Some of the weather and pollution factors which influence the RN levels are also unique to geographical regions. It is therefore necessary to measure the RN performance of local lines in order to access the accuracy of international prediction methods in the South African context. The RN measurements of four South African lines are described in this chapter.

To determine the best prediction method, the RN performance must be comprehensively measured. All significant variables that affect a line's RN performance must be accounted for in the measurements. A measurement protocol must therefore be formulated by consolidating various measurement protocols proposed in the literature. A literature survey of operational line measurements is presented in section 2.2 and is used to formulate the proposed RI measurement protocol presented in appendix B. Four local lines were carefully selected. The selection criteria, line descriptions and measured RN performances of these lines are presented in section 2.4. Certain practical limitations may not permit for all of the requirements stated in the proposed measurement protocol to be met. These limitations are highlighted in section 2.4 and their affect on the accuracy and validity of the measured data is discussed. This discussion will assist in determining the level of confidence with which RN is predicted in chapter 3.

2.2 Literature Survey

The conditions under which RN measurements are made must be standardised in order to facilitate a comparison of the RN performance of various lines. The CISPR 18-2 document [4] outlines the standard proposed for the evaluation of RI generated by electric power transmission and distribution facilities. The scope of the document encompasses RI from overhead power lines and high voltage equipment in the regime 0.15 MHz to 300 MHz, that may cause interference to radio reception, excluding fields from PLC signals. The document describes RI characteristics, measurement methods and procedures for determining RI limits. An ANSI/IEEE standard [5] was compiled for the measurement of corona generated noise on high voltage transmission lines. Various IEEE and CIGRE committee reports ([1], [6], [7] and [8]) describe aspects of operational RI measurements not dealt with in the standards. The discussion presented in this section is a qualitative audit of the most important variables which must be accounted for, based primarily on the above mentioned standards and committee reports, and is used to formulate a RI measurement protocol. A conducted RN measurement protocol is proposed in [9]. A new conducted RN measurement protocol is proposed in section 2.4 based on [9] and the RN characteristics identified in this section as being necessary to evaluate a prediction method.

2.2.1 Characterizing the RN Performance of a Transmission Line

Three main characteristics of a radiated noise field are: the frequency spectrum of the field at a single measurement location and over a documented frequency band; the profile of the noise level at a single frequency and over a documented lateral displacement; the statistical variation of the noise level at a single frequency and position. The RI performance of a line is fully described by these characteristics [10].

Measured RI levels are subject to wide variations due to environmental changes [10]. The use of a statistical model to characterize these variations was mentioned in chapter 1. Such a model is best defined in terms of the probability density function [10]. It is however often necessary to describe the RI performance with a single value. Exceedance levels, referred to as L-levels [2], are therefore calculated from the density function. In L-level notation, L_{50} is a median level (i.e. the level exceeded 50% of the time). The L_5 or L_1 levels are often used to describe the maximum RI level [10].

Between 15 and 20 measurement sets are required for each ambient condition to make a good account of the statistical nature of the RI levels [4]. A measurement set in [4] is an average of three measurements made at three locations spaced uniformly along the length of the line. When the total RI performance is analysed, the number of measurement sets used for each condition must be proportional to the occurrence of that condition during the time interval considered.

2.2.2 Instrumentation

The instantaneous RI level varies randomly and is not measurable as a single value. The average or weighted-average power, measured over a sufficiently long period of time, yields a measurable stationary random value. Examples of such measurable quantities, which are used to describe the RI performance, are the peak, quasi-peak (QP), average and RMS levels. Each of these are used to describe different aspects of the RI field. The RMS level defines RI in terms of energy. The average level is a time average of the RI. The peak level is the peak indication of RI level over a specified time interval, while the QP level defines the nuisance effect of the noise. The QP level has traditionally been adopted as the standard [2] while the RMS level is more recently favoured as the standard [2]. The RI performance is measured on a RN meter. This device is a calibrated, tunable, radio receiver equipped with peak, average, QP and RMS detectors. The bandwidth and response characteristics of a RN meter must conform to CISPR 16 specifications [4]. A description of the RI performance must include a record of the bandwidth and the detector used.

The measured RI field consists of contributions from many discharge sources distributed along the length of the line. The separation time between consecutive pulses of the measured pulse train affects the RI level measured in a specified bandwidth. If pulses do not overlap within the bandwidth, the peak and QP levels increase linearly with increased bandwidth, while the average level is independent of bandwidth and the RMS level increases as the square root of the bandwidth increase [2]. The linear increase in the QP level is an approximation which is valid only for certain repetition rates [2]. If the pulses do overlap within the meter bandwidth, the increase in all detector levels is proportional to the square root of the bandwidth increase [2]. The accuracy and regularity of the RN meter calibration must be noted. It was found in [7] that RI level readings made with meters of the same type and model differed due to calibration and operator error. This error was less than 2 dB 95% of the time.

A measurement frequency must be carefully selected. The CISPR reference frequency is chosen as 500 kHz because it is between the low and medium broadcast bands and because the RI level at this frequency is representative of higher levels [4]. The reference frequency adopted by the old ANSI standard is 1 MHz [5]. The ambient noise floor must also be considered when selecting a measurement frequency. The set of ten frequencies, suggested in [4] for the RI spectrum measurement, are 0.15, 0.25, 0.5, 1, 1.5, 3, 6, 10, 15 and 30 MHz.

Vertical rod and vertical loop antennas are used for RI measurements. The antenna suggested for RI measurements in [2] and [4] is an electrically screened vertical loop antenna and is used because the calibration of the vertical rod antenna assumes a flat, perfectly conducting ground plane, free of metallic obstructions. An assumption which is not always valid. The dimensions of the loop antenna must be such that it is completely enclosed by a square having sides 60 cm long [4]. The balance of this antenna must be such that the ratio of minimum and maximum indications when rotated through 360° in a uniform field is not less than 20 dB [4]. Since the loop antenna is directional, both the maximum level and the orientation of the antenna at this maximum indication must be noted. For the prescribed loop antenna aperture, plane wave conditions (i.e. $E = 377H$) exist at a distance greater than 15% of the measurement wavelength from the line [2]. The standard proposed in [4] assumes plane wave conditions at all lateral distances.

2.2.3 Measurement Location

The weight and thermal characteristics of transmission line conductors cause them to sag between their attachment points at height H_a (i.e. along its span length). The conductors will therefore be closer to the ground plane at the centre of the span, causing an increase in surface gradient at this point. This results in non-uniform RI generation along the length of the span. The variation in RI generation along a line due to the conductor sag, S, is accounted for by defining an equivalent conductor height. This is the height for which a line with conductors parallel to the ground plane along its length would produce the same RI level as the actual line [2]:

$$H_{eq} = H_a - \frac{2}{3}S \tag{2.1}$$

9

Corona currents propagating along the conductors produce both a near field and a far field which is radiated in a lateral direction away from the line. The lateral profile is a measure of the total field, i.e. the near and far fields. It is made along a direction perpendicular to the line at the centre of a span of average length for the line. The CISPR reference position is 20 m from the outer phase conductor [4] along the ground. Both current propagation and field radiation are affected by ground conductivity. This variable is affected by ambient weather conditions and can be non-uniform along the line's length. The moisture content of the soil due to recent precipitation must be noted.

Spurious corona discharges occur on polluted insulators and corroded line fittings. These discharges induce currents in the conductors and radiate interference fields in the vicinity of the line. Their presence near the measurement site will therefore adversely affect the accuracy of the RI measurements. Spurious noise levels from sources other than the line must also be noted. This is best done with the line de-energised. The ambient noise levels at the test site must be at least 6 dB below the RI level at all measurement frequencies [6]. This ensures that the spurious noise level at any lateral displacement will be less than the measured level, even if the direct and reflected noise field components add in phase at the antenna location. The difference between the QP and average levels must not be less than 20 dB if only conductor corona noise is measured [2]. The difference between QP and peak levels must be approximately 5 dB if spark-gap noise is absent, and about 15 dB if it is present [2]. These tests must be performed at the test location to verify if the site is free of significant spurious noise sources. The effect of substation RN sources on the RI measurements at the test site is discussed in [11]. The paper concludes that the effect of substation RN is not significant in fair weather unless arcing occurs.

Discontinuities along the length of the line, such as transpositions and interconnections, cause reflections of the propagating RN currents and negate the aggregation of corona source contributions along the line's length. Sharp changes in line direction will cause reflections and radiation. The measurement location must be at least 10 km from the nearest line discontinuity, change in line direction, substation or faulty line equipment [4]. It may not always be possible to avoid line discontinuities. Standing wave patterns will then appear in the measured frequency spectrum. The geometric mean of consecutive minimum and maximum levels, measured in

μV/m, of a frequency spectrum exhibiting standing wave characteristics, is within 3 dB of the actual RN frequency spectrum [12]. This geometric mean transform was derived from measurements in the frequency range 0.23 MHz to 1.95 MHz. Measurements made more than 5 km from a significant discontinuity at 1 MHz are within 3 dB of the ideal RI level [12]. The position of discontinuities must therefore be noted and the frequency spectrum must be corrected with the geometric mean transform if the measurement site is near a line discontinuity.

2.2.4   Identification of Influencing Variables

The surface gradient is dependent on the line voltage and the phase and bundle geometries. The RI level is approximately a linear function of surface gradient [6] which must therefore be calculated to a precision of at least 1% [10]. The RI level is also dependent on the divergence of the radial electric field. A low electric field divergence can support longer streamers and will therefore affect the pulse amplitude and repetition rate.

Conductor stranding and surface irregularities cause local electric field enhancements at the conductor's surface. This decreases the voltage at which corona first occurs, i.e. the corona inception voltage, and affects the RI level. The surface gradient to which RI is related is a nominal value [10]. The nominal surface gradient of a stranded conductor is equal to the surface gradient of a smooth conductor with a diameter equal to the outer diameter of the stranded conductor. The presence of pollutants on or near the conductor's surface will also affect the surface gradient. Water drops, dust particles, insects, pollen particles and aerosols are examples of such pollutants. Since precipitation has such a large effect on the RI level and is so prevalent in most environments, it is dealt with separately. Stranded conductors are coated with grease during the manufacturing process. This makes them hydrophobic. Gravity causes rain drops to collect on the underside of hydrophobic conductors and distorts the surface gradient in the vicinity of the water drop. Both the type and size of the contaminant will affect the RI level and must be noted.

Changes in relative air density (RAD) and relative humidity (RH) affect the corona discharge processes. The RAD is dependent on temperature, atmospheric pressure and altitude. The relationship between the RI level and altitude is approximately linear [10]. This linear

11

relationship is disputed in [6] where it is noted that there is an absence of corona pulses with small amplitudes at high altitudes. The load current of a line causes an increase in temperature and therefore also RAD near the conductor surface. No relation between load current and RN has however been reported. The RAD, RH and load current must be monitored during the measurements.

A description of the ambient weather condition is an account of the presence and form of precipitation in the vicinity of the line's conductors along its length. Since precipitation occurs in many forms and intensities, it is necessary to classify it with a standard [13] comprising a finite number of categories. A summary of the weather categories referred to in this dissertation is presented in appendix A. Also included in appendix A is the classification of weather conditions in [3] considered sufficient to describe the variation of RI levels due to weather changes. Since the RI levels of conductor corona are due to an aggregation of the currents from all corona sources on the line, the uniformity of the weather condition along the length of the line must be noted. Rain measurements are only valid if the rain extends uniformly along the line for at least 10 km in both directions from the measurement point [4]. A set procedure must be implemented to categorize the prevailing weather conditions according to the limitations of the equipment available. For the continuous measurements in [14], the precipitation indicator used was not capable of detecting the presence of fog and mist, nor if the conductor was wet. Fair weather measurements were therefore made between the hours of 10:00 and 18:00 so as to exclude the effect of fog and mist. Measurements were also excluded if the precipitation indicator detected rain during a time period beginning 4 hours prior and ending 1 hour after the commencement of the measurement. The RI levels of wet conductors were therefore excluded.

Corona discharges produce charge in the air surrounding the conductor. This space charge distorts the electric field near the conductor surface and will affect corona activity. Wind removes space charge near the conductor and increases corona activity [3]. The effectiveness of the space charge removal depends on the amount of space charge produced, the wind speed and the wind direction. The RI level increases non-linearly with wind speed [3]. Wind also causes an increase in non-metallic pollutants near the conductor surface, as well as the deposit of such pollutants on the conductor. This will also increase corona activity. A particular form of pollution may be

12

prevalent during a season (e.g. the abundance of pollen and flying insects during spring). RI levels will then be higher than normal during that season. The washing effect of rain removes pollutants from the conductor surfaces and greatly reduces the RI level. The RI level will therefore be lower during seasons of increased rainfall. Seasonal changes are specific to a line and must be determined when assessing its RI performance. This could be done by continuously recording RN levels at a calibrated test site over a period of time greater than a year [4].

The continuous measurement of RI levels, at a calibrated site and frequency, produces statistical data which can be analysed to obtain temporal and seasonal RI changes. Temporal changes are caused by conductor aging [2]. When a conductor is installed, nicks and scratches due to handling cause local surface gradient perturbations which increase corona activity. AC corona activity produces space charge of both positive and negative polarity. Space charge of opposite polarity to the source will collide with the line's conductors. This ion bombardment at the conductor surface reduces the metallic irregularities over a certain period of time. Only about 15 minutes is required, at normal operating voltage, for this aging process to reduce the RI level to a stable value [2]. Severe conductor damage will however not be remedied by this aging process and the RI level will stabilize at a higher level. Non-metallic pollutants such as grease and dirt are removed by the washing effect of rain and other atmospheric effects. The effect of grease on the RI level has already been mentioned. Conductor weathering takes much longer to reduce the RI level to a stable value. Most references suggest a typical period of about a year (e.g. [2]). Once conductor weathering has removed the grease, the conductor will change from being hydrophobic to being hydrophilic and will absorb water into its strands. The increase in RI during rain is therefore reduced. The age of the line conductors must therefore be noted.

2.3   Operational Transmission Line Measurements

A consolidated RI measurement protocol, based on the standards and experiments described in the previous section, is proposed in appendix B. This protocol will be considered when making operational transmission line measurements. RN performance measurements could only be made on a few local lines due to the effort involved in doing so. The choice of which lines to measure was therefore carefully made. The most important selection criteria were the line geometry, accessibility to the line and the uniformity of conditions along the line. The RN performance of the Hydra-Droërivier line was not as predicted and initiated the research. This line was therefore studied. It is a long 400 kV compact-delta line with no transpositions along its length. The effect of various bundle geometries and transpositions must also be studied. A second 400 kV compact-delta line, the Aries-Kokerboom line was therefore studied. Both lines are longer than 100 km. A short line, the Acacia-Koeberg line, was therefore included. This 30 km long 400 kV untransposed flat-horizontal line is situated close to Stellenbosch allowing for easy access. Finally, a longer 400 kV transposed flat-horizontal line, the Kriel-Tutuka line, was included for comparison with the Acacia-Koeberg line. This line is unique in South Africa in that it consists of sections of different bundle geometry along its length. This facilitates the evaluation of non-uniformity along a line's length.

The measurement protocol presented in appendix B refers only to the radiated RN (i.e. RI measurements). This research is however also concerned with the RN voltage measured across the terminals of a PLC receiver. This can be calculated by evaluating the current flow on the conductors using RI measurements and a radiation model. The validity of a radiation model must first be evaluated however, another important component of the research. The PLC system is easier to model than a radiating transmission line. The conducted RN is therefore measured and used, along with the PLC system model, to calculate the RN currents on the line. RI measurements are made simultaneously with the conducted RN measurements so that the validity of the radiation model can also be evaluated. Continuous conducted RN measurements were made by W. de Villiers on the Acacia-Koeberg [9] and Kriel-Tutuka [15] lines. These continuous

14

RN measurements will be used, with the author's permission, in the dissertation where indicated. Conducted and radiated RN performance measurements for the Acacia-Koeberg and Hydra-Droërivier lines were made with the assistance of R. Hubbard from ESKOM TSI.
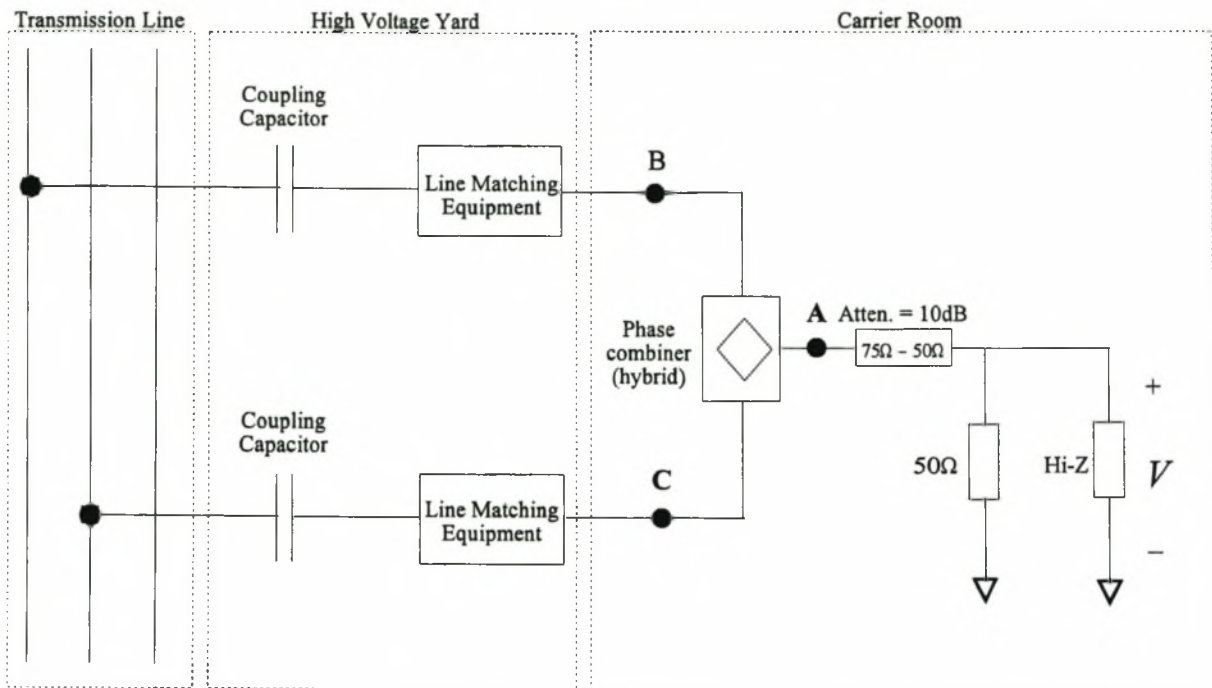
Figure 2.1: Schematic diagram of a conducted RN measurement setup (after [9]).

The measurement setup used for the conducted RN measurements in a substation carrier room is illustrated in figure 2.1. RN current, propagating along the line's conductors, is decoupled with a coupling capacitor. The line matching equipment matches the line's surge impedance to 75 Ω in the frequency band 50 kHz to 500 kHz. The standard coupling scheme used in the PLC systems of the studied lines is (1,-1,0) and sums the centre and outer phase RN with a phase combiner. The adopted conducted RN measurement protocol is summarized below:

▸ A "Risk of Trip" is organised well before the measurement is to be made. This permits the deactivation of the line's PLC teleprotection. The 20 W carrier signal can then be disconnected from the phase combiner at position A in figure 2.1. Permission to do this may be revoked on the day of the measurement. The "Risk of Trip" must be confirmed and the necessary people informed before the carrier signal is disconnected.

▸ A spectrum analyser is connected to the phase combiner with a 75 Ω-to-50 Ω pad. The resolution bandwidth of the analyser is set to 10 kHz and the spectrum between 50 kHz and

15

500 kHz is scanned. Carrier frequencies of neighbouring lines couple onto the measured line. Conducted RN measurements cannot be made at these frequencies. Other spurious noise signals in the observed spectrum must also be avoided.

▸ A set of 10 uniformly spaced frequencies are selected for the RN measurement between the carrier and spurious noise frequencies observed in the spectrum analyser measurement.

▸ The line voltage, load current, RAD, RH and ambient weather condition at the substation are recorded. The conducted RN measurements can now be made.

▸ The spectrum analyser is disconnected and replaced with an EMI receiver. The receiver used is equipped with a peak, QP and average detector. An RMS selective voltmeter, with a high input impedance, is connected across the terminals of the phase combiner. In this way, both the QP and RMS noise levels can be measured simultaneously.

▸ The outer phase coupling is disconnected from the phase combiner and connected to the measurement devices. The measurement procedure is repeated at position B in figure 2.1.

▸ The centre phase coupling is disconnected from the phase combiner and connected to the measurement devices. The measurement procedure is repeated at position C in figure 2.1.

▸ The line voltage, load current, RAD, RH and ambient weather condition at the substation are again recorded.

2.3.1 The Measured Acacia-Koeberg RN Performance

The Acacia-Koeberg line is approximately 40 km from Stellenbosch. Its close proximity facilitates the continuous measurement of RN [9]. The line is situated near the sea. A potential pollutant is therefore salt deposits on the conductors and insulators. Heavy rain during winter months will wash this pollution from the conductors. This may result in large seasonal RN variations. Mist and fog is prevalent and will affect the average foul weather RN level. The RN measurements were made at the end of September. This is usually at the end of the region's rain season and mist is prevalent in the mornings and evenings. The line has been in operation for many years and the conductors are well aged.
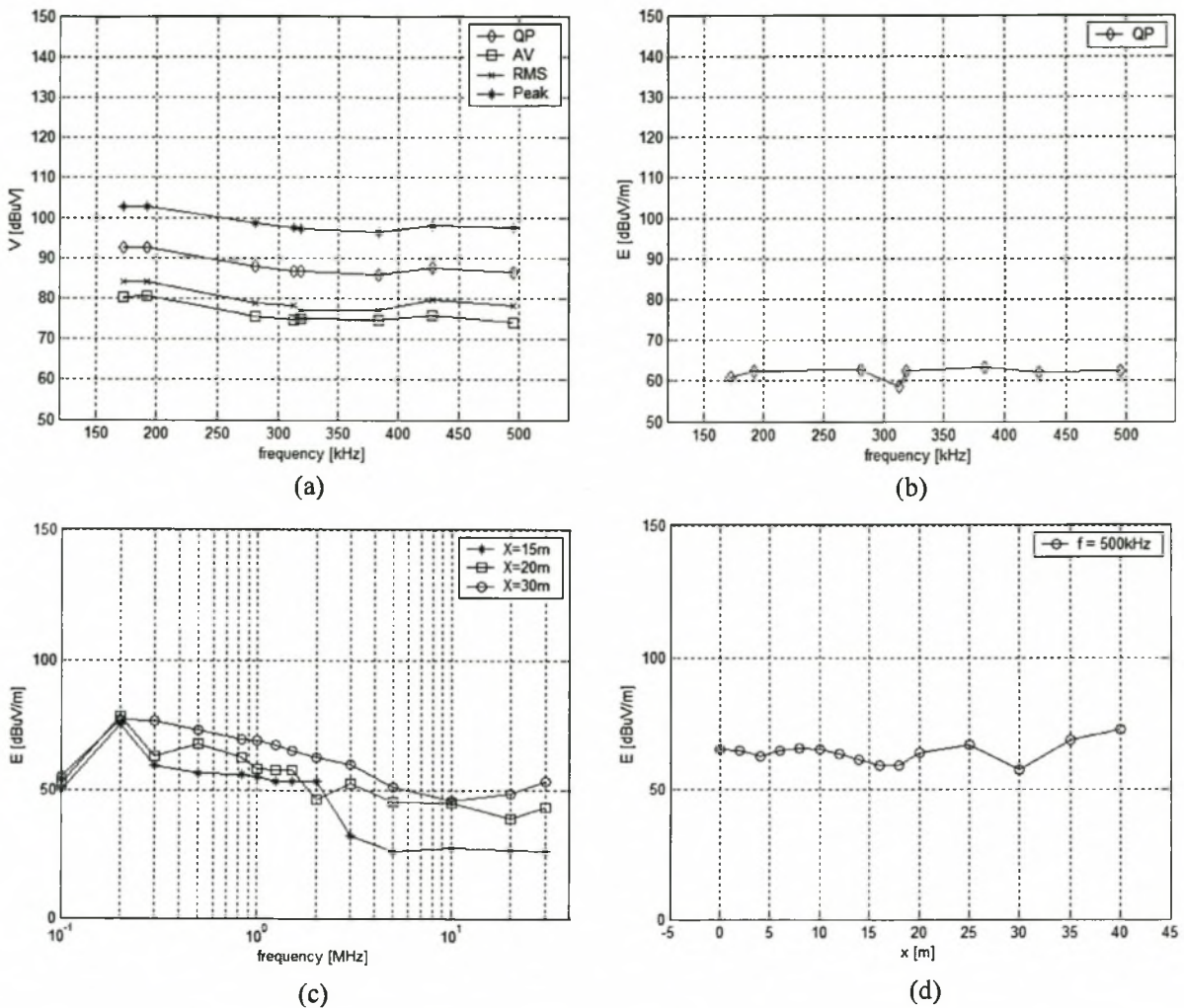
Figure 2.2: The measured RN performance of the Acacia-Koeberg line: (a) conducted RN levels in the PLC band; (b) the RI frequency spectrum in the PLC band [$x = 20$ m]; (c) RI frequency spectra at selected frequencies and various lateral distances; (d) a lateral profile at 500 kHz. [BW = 10 kHz]

The conducted and radiated RN levels measured in the PLC and CISPR bands on the Acacia-Koeberg line are plotted in figure 2.2. A description of the geometry, measurement devices and weather conditions for all measured lines discussed in this chapter is presented in appendix C. Peak, QP and average measurements were made on the EMI receiver in a 10 kHz bandwidth. RMS levels were measured on the selective voltmeter in a 3.1 kHz bandwidth. The relationship between the measured RN level and the meter's bandwidth was discussed in section 2.2. The repetition rate of the measured corona pulse train is not known. With regards to the various detectors used, only the relationship between the RMS detector output and the measurement bandwidth is not affected by the pulse repetition rate. Measurements are therefore converted to

a 10 kHz bandwidth. The conducted RN measurements were made at the Acacia substation. An active loop antenna was used to measure the RI levels. These measurements are converted to an equivalent electric field level using the plane wave approximation $E = 377H$. The selection of a suitable measurement location for the RI measurements was complicated by the close proximity of two adjacent lines in a shared servitude. The measured line is positioned between the other two lines. One of the lines separates from the measured line, which makes a 45^0 change in direction at this point, 5 km from the Koeberg substation. This is the only available measurement location and does not comply with the requirements of the proposed RI measurement protocol. The RI measurements in figure 2.2 are therefore only valid for a small lateral distance from the line.

The response of the various detectors used is dependent on the pulse amplitudes and repetition rates. The ratio of QP and RMS levels will decrease, while the ratio of average and RMS levels will increase, if the mean repetition rate increases [10]. The product of these two ratios is nearly constant for mean repetition rates between 200 Hz and 20 kHz [10]. This constant product is specific to the meter used and the pulse train measured [10]:

$$K = \frac{RI_{RMS}}{\sqrt{RI_{QP} \cdot RI_{AV}}} \qquad (2.2)$$

A comparison of the measured RMS and QP RN levels in figure 2.2 (a) reveals that the product defined in equation 2.2 is indeed nearly constant across the PLC band for the measured fair weather RN on the Acacia-Koeberg line ($K = 0.78$ at 500 kHz). Continuous conducted RN measurements were made, over a period of one week, at the Acacia substation at 500 kHz with a RMS detector by W. De Villiers [9]. The ambient weather conditions during this time period included periods of rain. The expected difference between QP levels under various weather conditions will be discussed in chapter 3. Similar relationships between the RN of different weather conditions are not given for RMS levels. RMS levels can also not be obtained directly from the QP and AV levels using equation 2.2 unless the value of K is known for the various weather conditions. Statistical variations in pulse amplitude and repetition rate are dependent on various factors including precipitation.
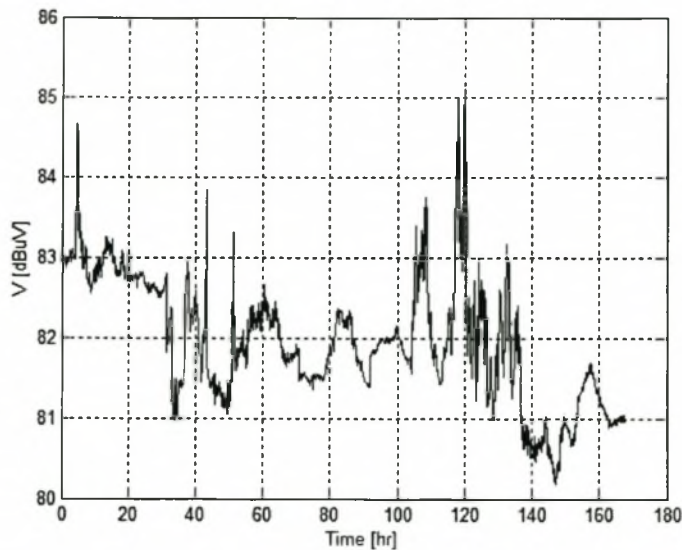
Figure 2.3: Continuous conducted RN measured at the Acacia substation, over a period of one week, at 500 kHz with a RMS detector (data provided by W. de Villiers [9]).

The continuous conducted RN, measured with a RMS detector, at the Acacia substation is plotted in figure 2.3. The value of K, derived from fair weather measurements in figure 2.2 (a), cannot be used to estimate the QP level in figure 2.3 since precipitation occurred. The maximum RMS level variation in figure 2.3 is less than 5 dB.

2.3.2   The Measured Aries-Kokerboom RN Performance

The Aries-Kokerboom line is situated in a low rainfall region and no obvious forms of pollution were identified. Seasonal RN variations should therefore not be large. The line has been in operation for many years and the conductors are considered well aged. The conducted and radiated RN measurements in the PLC and CISPR bands were initiated by R. Hubbard at the Aries substation and at a valid RI test site. The results are plotted in appendix C for a 10 kHz bandwidth. These measurements appear to saturate and are not used to evaluate RN prediction models in chapter 3. The conducted RN measurements did not saturate however and will be used.

2.3.3   The Measured Hydra-Droërivier RN Performance

The Hydra-Droërivier line is situated in a low rainfall region and no obvious forms of pollution could be identified. Seasonal variations in RN performance should therefore not be large. The line has been in operation for many years and the conductors are well aged. The conducted

19

RN measurements were made at the Droërivier substation. A valid measurement location was found for the radiated measurements. The RI measurements suffered from the same saturation effect as the Aries-Kokerboom measurements and had to be repeated at a lower load current.
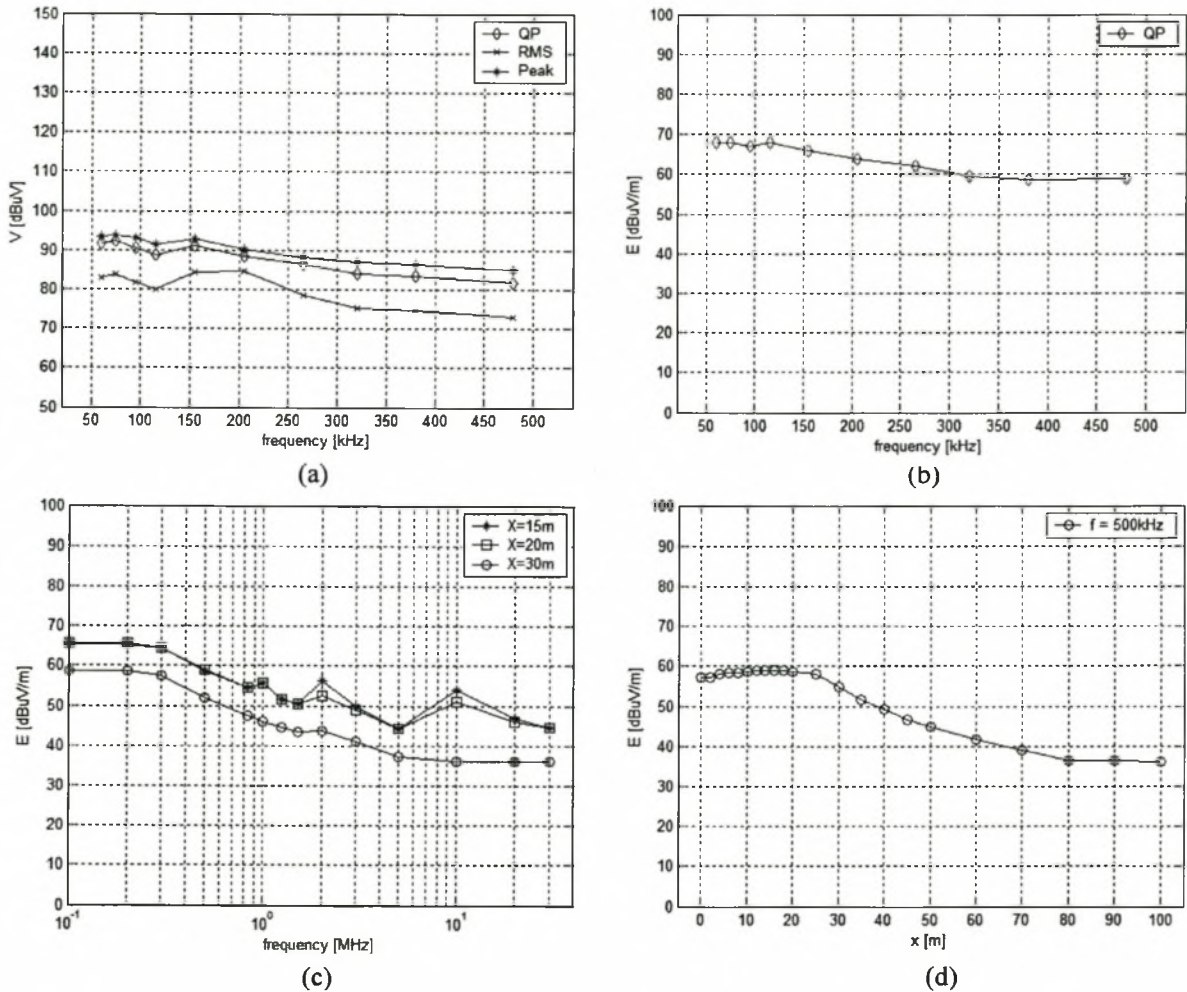
Figure 2.4: The measured RN performance of the Hydra-Droërivier line: (a) conducted RN levels in the PLC band; (b) the RI frequency spectrum in the PLC band [x = 20 m]; (c) RI frequency spectra at the CISPR frequencies and various lateral distances; (d) the lateral profile at 500 kHz. [BW = 10 kHz]

The valid conducted and radiated RN level measurements made in the PLC and CISPR bands on the Hydra-Droërivier line are plotted in figure 2.4 for a 10 kHz bandwidth. The RI measurements exhibit no saturation for lateral distances more than 25 m from the outer phase conductor along the ground. The active loop antenna used has a transistor amplifier which ensures that the antenna

20

factor is constant across the specified band. It is concluded from the measurements that the strong power frequency magnetic field component near the line overloads this amplifier. The measured RI levels are therefore not accurate. To protect the transistor amplifier and ensure the accuracy of the RI measurements, the lateral distance at which the active loop antenna saturates must be measured. The lateral displacement of all test sites must be greater than this distance.

2.3.4   The Measured Kriel-Tutuka RN Performance

The Kriel-Tutuka line conductors are well aged and the variation in bundle geometry along its length is described in [15]. The line description in appendix C is that of the 47 km section near the Tutuka substation. The bundle geometry at the Kriel substation changes from a triple Dinosaur to a quad Zebra configuration after only 5 km.
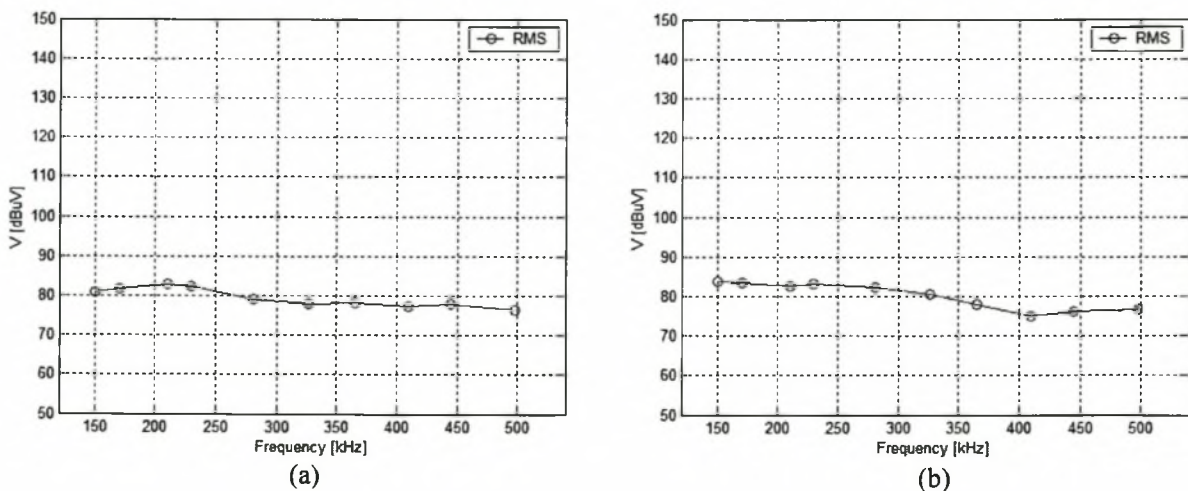
Figure 2.5: The measured conducted RN levels of the Kriel-Tutika line measured at (a) the Tutuka substation and (b) the Kriel substation (data supplied by W. de Villiers [15]).

The conducted RN levels in the PLC band for the Kriel-Tutuka line, at both substations, are plotted in figure 2.5. The measurements were supplied by W. de Villiers [15]. All RMS measurements are made in a 75 Hz bandwidth and are converted to a 10 kHz bandwidth. The two plots indicate that while the RN levels at 500 kHz are similar at the two substations, the variation of the conducted RN level within the PLC band is not the same. This is attributed to the variation in bundle geometry along the length of the line and is investigated further in subsequent chapters.

This measurement concludes the operational transmission line measurements and the chapter. Various parameters were found to influence the RN in this chapter. Not all of these could be adequately accommodated or accounted for in the measurements due to practical limitations. This made it difficult to fully implement the measurement protocol proposed in appendix B on the operational transmission lines. The accuracy and validity of these measurements must therefore be considered in the next chapter when comparing them to predicted data. In chapter 3, each line's RN performance is approximated with selected prediction methods which consider the factors identified in this chapter as having a significant effect on a line's RN performance. The measured RN levels presented in this chapter are then compared to these predictions in order to determine the most appropriate prediction method for each of the four lines. A RN prediction methodology for transmission line designs, which can be implemented in executable code, will then be extracted from the conclusions of chapter 3.

2.4   References

[1]   IEEE Committee Report, "CIGRÉ/IEEE Survey on Extra High Voltage Transmission Line Radio Noise", IEEE Trans., Vol. PAS- 92, 1973, pp. 1019-1028.

[2]   *Transmission Line Reference Book: 345kV and Above/Second Edition*, Electric Power Research Institute (EPRI), Palo Alto, CA,1982.

[3]   J.J. LaForest, M. Baretsky, Jr., D.D. MacCarthy, "Radio-Noise Levels of EHV Transmission Lines Based on Project EHV Research", IEEE Trans., Vol. PAS- 85, 1966, pp. 1213-1226.

[4]   CISPR Publication 18-2, *Radio Interference Characteristics of Overhead Power Lines and High Voltage Equipment. Part 2. Methods of Measurement and Procedure for Determining Limits.*

[5]   ANSI/IEEE Standard No. 430-1986, *IEEE Standard Procedures for the Measurement of Radio Noise from Overhead Power Lines and Substations.*

[6]   IEEE Committee Report, "Transmission System Radio Influence", IEEE Trans., Vol. PAS- 84, 1965, pp. 714-722.

[7]   IEEE Committee Report, "Correlation of Various RI Meters and Reading Comparison of RI Meter Operators on a 735-kV Line", IEEE Trans., Vol. PAS- 87, 1968, pp. 1249-1257.

[8]   IEEE Radio Noise Subcommittee Report, "Radio Noise Design Guide for High-Voltage

Transmission Lines", IEEE Trans., Vol. PAS- 90, 1971, pp. 833-840.

[9]   W. de Villiers, *Prediction and Measurement of Power Line Carrier Signal Attenuation and Fluctuation.*, MScEng Thesis, University of Stellenbosch, 2001.

[10]   P. Sarma Maruvada, *Corona Performance of High-Voltage Transmission Lines*, Research Studies Press Ltd, 2000.

[11]   J.J. LaForest, "The Effect of Station Radio Noise Sources on Transmission-Line Noise Levels", IEEE Trans., Vol. PAS- 84, 1965, pp. 833-837.

[12]   C.R. Bond, W.E. Pakala, R.E Graham, J.E. O'Neil, "Experimental Comparisons of Radio Influence Fields From Short and Long Transmission Lines", IEEE Trans., Vol. PAS- 82, 1963, pp. 175-182.

[13]   IEEE Standard No. 539-1990, *IEEE Standard Definitions of Terms Related to Corona and Field Effects of Overhead Power Lines*.

[14]   J.J. LaForest, C.B. Lindh, D.D MacCarthy, F. Olsen, M.W. Schultz, Jr., "Radio Noise and Corona Loss Results from Project EHV", IEEE Trans., Vol. PAS- 82, 1963, pp. 735-748.

[15]   W. de Villiers, "Frequency Scan of the Kriel-Tutuka 400 kV Transmission Line", Internal document, University of Stellenbosch, August 2003.

Chapter 3

Empirical and Semi-Analytical RN Prediction Methods

3.1 Introduction

Various factors were identified in chapter 2 as having an effect on the RN performance of a transmission line. This was done to develop a method of describing the ambient conditions adequately, so that sufficient information accompanied the RN measurements of a line for an accurate analysis. A RN prediction method will use this information to predict the RN performance of the line. A comparison between the measured data of chapter 2 and the predicted data, presented in this chapter, will help to determine the best method for local conditions.

A prediction method must calculate the frequency spectrum, lateral profile and statistical variation of a line's RN. The approach adopted in the methods described in this chapter is to predict a single RN level at a standard frequency, lateral distance and ambient environmental condition. The frequency spectrum, lateral profile and statistical variation are then extrapolated from this single value using known relationships between the RN level and the varied parameters. Two classes of prediction methods used are empirical and semi-analytical methods. Selected examples of both classes are introduced in sections 3.2 and 3.4 respectively. The semi-analytical methods are based on the theory of the excitation function and modal propagation which are discussed in sections 3.3 and 3.5 respectively. The individual correction terms included in the empirical and semi-analytical equations, as well as ancillary correction terms for various ambient conditions, are compared in section 3.6 and general correction terms are discussed. The predicted RN performance of the lines studied in section 2.3 are extracted with selected methods and compared to their measured performance in section 3.7.

3.2 Empirical Methods

Empirical methods are derived from a statistical regression analysis, performed on RN data measured on various lines as a function of several variables [1]. The accuracy of a method is

24

dependent on the accuracy of the data used and the variables included in the analysis. The validity of a method is restricted to the range of the included variables within which the measured data was obtained. The valid range of each variable must therefore be specified with the empirical method. A survey of empirical methods presented in [2] found that the predicted RN performance varied as much as 10 dB from the measured performance. The discrepancy increased when an empirical method, derived from line data of one country, was used to predict the RN performance of a line in another country. Attention must therefore be given to ensuring that the best method is chosen for the line studied and the range of the variables considered.

Empirical formulae are defined for a specific weather category and are written in terms of reference line parameters. The general form of the empirical formulae is [3]:

$$RI = RI_0 + \left(RI_g + RI_d + RI_n\right) + \left(RI_{rr} + RI_w + RI_{RAD} + RI_{RH} + RI_{ws}\right)$$

$$+ \left(RI_f + RI_m + RI_D\right) \tag{3.1}$$

The RI level of a line is determined in equation 3.1 by adding relevant correction factors to a reference line level RI_0. The correction terms have been grouped together in equation 3.1. The first grouping is for factors dependent on the line geometry and include correction factors for changes in surface gradient, RI_g, conductor diameter, RI_d, and the number of sub-conductors in a bundle, RI_n. The second grouping considers changes in environmental conditions and includes changes in rainfall rate, RI_{rr}, weather category, RI_w, RAD, RI_{RAD}, RH, RI_{RH}, and wind speed, RI_{ws}. The last group considers changes in measurement device variables and includes the measurement frequency, RI_f, detector type, RI_m, and the lateral distance between the outer phase and the measurement position, RI_D. Two of the most commonly used empirical prediction methods are the CIGRÉ (France) and BPA (USA) methods [1]. These two methods are presented in this section. Other empirical methods reported in the literature include the 400kV-FG (Germany), Shiobara (Japan), Ontario-Hydro (Canada), ENEL (Italy), EGU (Czech Republic) and Westinghouse (USA) methods. These methods are described in appendix D. The individual corrections expressed explicitly in equation 3.1 are often included implicitly in the equations.

The empirical formulae are used for each phase individually. The RI contributions of each phase are then added to find the total RI level. RI levels measured on an RMS detector are power additive. An empirical method is used to add QP levels [3]:

$$RI = \begin{cases} RI_{\Phi 1} & ; RI_{\Phi 1} > \max\left[RI_{\Phi 2}, RI_{\Phi 3}\right] + 3 \\ 0.5\left(RI_{\Phi 1} + \max\left[RI_{\Phi 2}, RI_{\Phi 3}\right] + 3\right) & ; RI_{\Phi 1} \leq \max\left[RI_{\Phi 2}, RI_{\Phi 3}\right] + 3 \end{cases} \qquad (3.2)$$

In equation 3.2, $RI_{\Phi 1}$ is the largest of the three calculated QP levels of a three phase line. The empirical methods mentioned thus far predict QP levels. Equation 3.2 will therefore be used to determine the RI performance of a line.

3. 2.1 The CIGRÉ Method (France):

The empirical equation proposed by CIGRÉ is [3]:

$$RI = -30 + 3.5g_m + 6d - 33\log_{10}(D'/20) \qquad (3.3)$$

Equation 3.3 is derived from average fair weather RI measurements on a CISPR meter with a QP detector in a 9 kHz bandwidth. The reference frequency is 500 kHz and the direct lateral distance between the phase conductor and the antenna is 20 m. The input variables are the average maximum gradient, g_m [kV/cm], conductor diameter, d [cm] and the direct lateral distance between the phase conductor and the antenna, D' [m]. The equation is valid for average maximum gradients between 12 and 20 kV/cm, and direct lateral distances smaller than 50 m.

3. 2.2 The BPA Method (USA):

The empirical equation proposed in the BPA method is [4]:

$$RI = 92.1 + 120\log_{10}\left(\frac{g_m}{15}\right) + 40\log_{10}\left(\frac{d}{4}\right) + 20\log_{10}\left(\frac{h}{h^2 + D^2}\right) \qquad (3.4)$$

Equation 3.4 is derived from average foul weather RI measurements on an ANSI meter with a

QP detector in a 5 kHz bandwidth. The reference frequency is 1 MHz and the direct lateral distance between the outer phase conductor and the antenna is 15 m. The variables included are the average maximum gradient, conductor diameter, conductor height above ground, h [m] and the lateral distance between the phase conductor and antenna along the ground, D [m]. The range of surface gradients for which the equation is valid is not specified. In the method, 2 dB is subtracted to convert to an equivalent CISPR value at 1 MHz.

In order to compare the various empirical and semi-analytical methods with each other and collectively to measured data, the empirical methods were converted to a common base and then optimized in [4]. This was done by converting the empirical equations to equivalent semi-analytical equations for maximum foul weather conditions, i.e. heavy rain conditions. The equations were optimized by comparing data collected in an international transmission line survey to predicted data and then minimizing the mean-square error by manipulating the reference RI level. An optimized equation for local lines, derived with this method and measured line data such as in chapter 2, should be considered.

3. 3   The Excitation Function

The various factors affecting the RI level of a line were grouped into geometry factors, environmental factors and measurement device factors in equation 3.1. Adams [5] recognized that a "Generation Density", which is dependent only on environmental factors and the charge and electric field distributions near the conductor surface, can be extracted from RN measurements. The propagation of the currents injected onto line conductors by this "Generation Density" is then calculated using analytical techniques. Gary [6] used this concept of a geometry independent term to define the "excitation function", Γ [dBμA/$\sqrt{m}$], which can be measured in a corona cage and applied directly to a line of arbitrary geometry.

A corona cage is a coaxial structure that is usually shorter than a typical transmission line span length. The conductor bundle investigated is strung in the centre of the cage and a surface gradient equivalent to that on the actual transmission line is applied to it. The corona cage is smaller and economically more feasible for RN performance investigations than a test line. Ambient weather conditions are also more uniform along the shorter cage length. The design and

27

use of corona cages is discussed in chapter 4. The excitation function of a conductor bundle, of length l, energized in a corona cage, with C the capacitance between the conductor bundle and the corona cage, is calculated from the induced current, i $[dB\mu A]$, measured on the cage [6]:

$$\Gamma = \left(\frac{C}{2\pi\varepsilon_0}\right)^{-1}\left(\frac{i}{\sqrt{l}}\right) \qquad\qquad (3.5)$$

The theory of the excitation function and the derivation of equation 3.5 is discussed in [7].

The number of individual sources per unit length in a corona cage is only sufficiently high so as to represent a statistically satisfactory sample that would be found on a long transmission line under stable foul weather conditions [8]. The excitation function is therefore most often extracted from heavy artificial rain measurements. Heavy artificial rain constitutes rain rates of between 8 and 20 mm/hr [9]. The RI level of a line is a maximum and there is less dispersion of measured data under heavy rain conditions. The more constant RI level is due to the reduced effect of RAD, RH and other environmental factors on RN generation under heavy rain conditions. Fewer experiments are therefore required to derive an empirical formula.

An analytical propagation analysis is then used to determine the heavy rain RI level near the line along its length. The fair weather RI level is determined from the heavy rain RI level using empirical relations. Since the excitation function is derived empirically while the propagation is determined analytically, the method is referred to as semi-analytical. RI levels calculated with a semi-analytical method for a wide range of line geometries should be on average more accurate than those calculated with an empirical method. This is because semi-analytical methods better consider the specific geometry of a line.

3. 4   Semi-Analytical Methods

Various heavy artificial rain excitation functions have been derived empirically from corona cage data by research organizations. Three recognized methods appear often in the literature and are found to, between them, predict the RN performance for a wide range of line geometries. These methods are presented in this section.

3. 4.1 The EdF Method (France):

The empirical equation proposed by the EdF method for the RI excitation function of a conductor bundle with n sub-conductors, each of radius r [cm], subjected to an average maximum bundle gradient g_m [kV/cm] under heavy rain conditions is [9]:

$$\Gamma = \Gamma'(g_m, r) + \left(11.5 + \log_{10} n^2\right)r - B(n) \qquad (3.6)$$

n	1	2	3	4	6	8
$B(n)[dB]$	0	5	7	8	9	9.5

Table 3.1: The value of B(n) for typical values of n for the EdF Method [9].
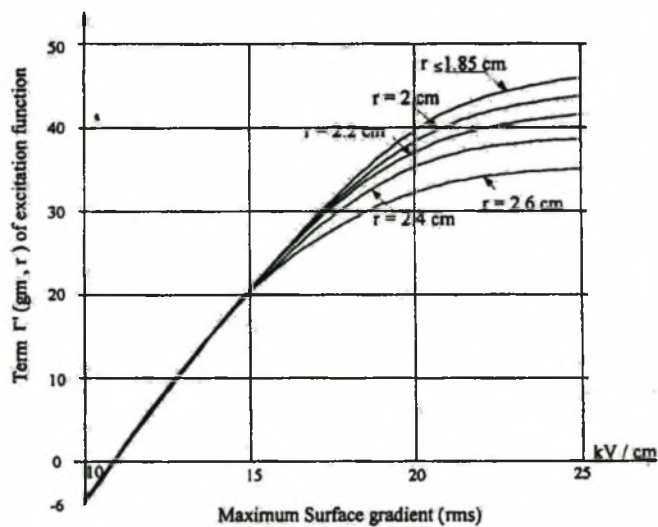
Figure 3.1: The variation of $\Gamma'(g_m, r)$ vs. g_m for various values of r [1].

The values of $B(n)$ and $\Gamma'(g_m, r)$ in equation 3.6 are obtained from table 3.1 and figure 3.1 respectively. The excitation function defined in equation 3.6 is for a CISPR meter with a QP detector at 500 kHz.

3. 4.2 The IREQ Method (Canada):

The empirical equation proposed by the IREQ method for the excitation function of a conductor bundle with n sub-conductors, each of diameter d [cm], under heavy rain conditions is [4]:

$$\Gamma = -90.25 + 92.42\log_{10}(g_m) + 43.03\log_{10}(d) - B(n) \tag{3.7}$$

n	1	2	≥ 3
$B(n)$	0	3.7	6

Table 3.2: The value of B(n) for typical values of n for the IREQ method [4].

The excitation function defined in equation 3.7 is for a CISPR QP meter at 500 kHz. The value of $B(n)$ in equation 3.7 is extracted from table 3.2.

3. 4.3 The EPRI Method (USA):

The empirical equation proposed in the EPRI method for the RI excitation function of a conductor bundle under heavy rain conditions is [8]:

$$\Gamma = 81.1 - \left(\frac{580}{g_m}\right) + 38\log_{10}\left(\frac{d}{3.8}\right) + K_n \tag{3.8}$$

where [8]:

$$K_n = \begin{cases} 0 & ;n \leq 8 \\ 5 & ;n > 8 \end{cases} \tag{3.9}$$

This formula is only valid if the ratio of the bundle and sub-conductor radii is between 10 and 20. For ratios smaller than 10, the excitation function is influenced by the variation of the surface gradient distribution around the circumference of the sub-conductors. The excitation function defined in equation 3.8 is for a CISPR QP meter at 500 kHz.

3. 5   Propagation Analysis

The empirically derived excitation functions in section 3.4 are introduced into a transmission line model in this section. The conducted and radiated RN levels of the line are then calculated.

3. 5.1 The Theory of Natural Modes

The variations in current and voltage along the length of an n conductor transmission line are described by a set of n coupled second-order differential equation pairs [8]:

$$\frac{d^2}{dz^2}[V] = \{[Z][Y]\}[V] = \left[P_v\right]^2[V] \tag{3.10}$$

$$\frac{d^2}{dz^2}[I] = \{[Y][Z]\}[I] = \left[P_i\right]^2[I] \tag{3.11}$$

In the equations, Z and Y are the series impedance and shunt admittance matrices of the transmission line, while P_v and P_i are the voltage and current propagation matrices. The solution of these coupled equations is simplified by recognizing that they can be resolved into a set of n uncoupled propagation modes. These propagation modes are approximately independent for low-loss lines. Energy propagating in one mode therefore does not interact with energy propagating in any of the other modes. Each mode will have its own surge impedance, attenuation and phase constants and propagation velocity. The non-singular modal voltage transformation matrix, E_v, and modal current transformation matrix, E_i, which decouple equations 3.10 and 3.11, are chosen such that [8]:

$$[\lambda] = \left[E_v\right]^{-1}\left[P_v\right]^2\left[E_v\right] \tag{3.12}$$

$$[\lambda] = \left[E_i\right]^{-1}\left[P_i\right]^2\left[E_i\right] \tag{3.13}$$

31

In equations 3.12 and 3.13, λ is a diagonal matrix. The non-zero diagonal elements of this matrix are the eigenvalues of the voltage and current propagation matrices squared. The columns of the modal transformation matrices are then the eigenvectors of the propagation matrices. The eigenvalues and eigenvectors are calculated using the idempotent method [10]. The solutions of equations 3.10 and 3.11, derived using the theory of natural modes, are [8]:

$$[V_z] = [E_v]\{[E_v]^{-1}[V_0]e^{-[\gamma]z}\}$$

(3.14)

$$[I_z] = [E_i]\{[E_i]^{-1}[I_0]e^{-[\gamma]z}\}$$

(3.15)

In equations 3.14 and 3.15, γ is the propagation constant matrix which is equal to the square root of the diagonal eigenvalue matrix. The propagation constant of mode m is therefore [8]:

$$\gamma_m = \alpha_m + \beta_m = \sqrt{\lambda_m}$$

(3.16)

The voltage and current at any point along the transmission line can be calculated from a known current or voltage distribution at $z = 0$ with equations 3.14 and 3.15. The corona generation model must next be included into the transmission line model described in this section.

3.5.2 Corona Generation on Single Conductor Lines

Each independent propagation mode of a line can be described by a single conductor above an ideal ground. Corona generation for this simple geometry will therefore be considered first.
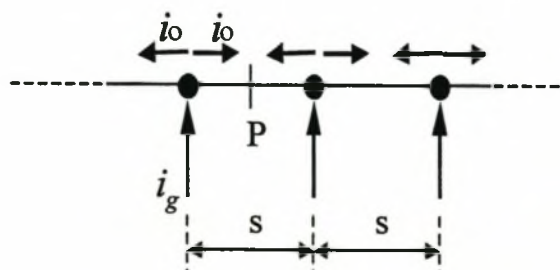
Figure 3.2: Multiple corona sources on a single conductor line (after [8]).

The semi-analytical methods described in this chapter predict the vertical electric field component above the ground plane at a specified lateral distance from the outer phase. Corona generation is introduced as a discrete number of current injections, uniformly spaced with separation interval s, along an infinitely long single conductor line. This is illustrated in figure 3.2. Two approaches used to calculate this electric field are described in [1] and [8]. The EPRI method [8] calculates the voltage on each phase due to corona current injection by recognizing that the voltage and current along the line are related by the line's surge impedance [8]:

$$V_P = Z_0 I_P = \left(\sqrt{\frac{Z}{Y}} \right) I_P \qquad (3.17)$$

The voltage at point P on the line, as depicted in figure 3.2, is then calculated using equation 3.14 for each current injection. The electric field near the ground plane is radially directed for an ideal transmission line with parallel conductors. It is first calculated vertically below point P for a single corona source and assuming a perfectly conducting ground. The total field, due to all corona sources along the line, is then calculated by RMS summation.

The method described in [1] calculates the current at point P due to all corona sources along the line's length. The magnetic field near the ground plane is then calculated from this current and the line geometry, assuming a perfectly conducting ground. The electric field is finally calculated from the magnetic field by assuming that the radiated field is a quasi-TEM plane wave. Since this method calculates the line currents, it can be used directly to calculate the conducted RN at the PLC receiver. The measurement protocol presented in appendix B requires that the orientation of the directional loop antenna, at which the maximum indication is observed, be recorded. If the quasi-TEM plane wave assumption is valid, the recorded orientation should be perpendicular to the line. Since this was the case for the measurements presented in section 2.4, the method proposed in [1] is also used to calculate the radiated and conducted RN.

The current injection along the line is calculated from the conductor bundle's excitation function using equation 3.5. This injected current divides into two equal currents, i_0 (see figure 3.2), which propagate in opposite directions along the line. The total current at point P on the line,

due to all the corona injections, as the corona source separation distance approaches zero, is [8]:

$$\lim_{s \to 0}\left[I_P\right] = \frac{i_g}{2\sqrt{\alpha}} \qquad (3.18)$$

The current variation along the length of the single conductor line is calculated from the excitation function and the line's attenuation constant with equation 3.18.
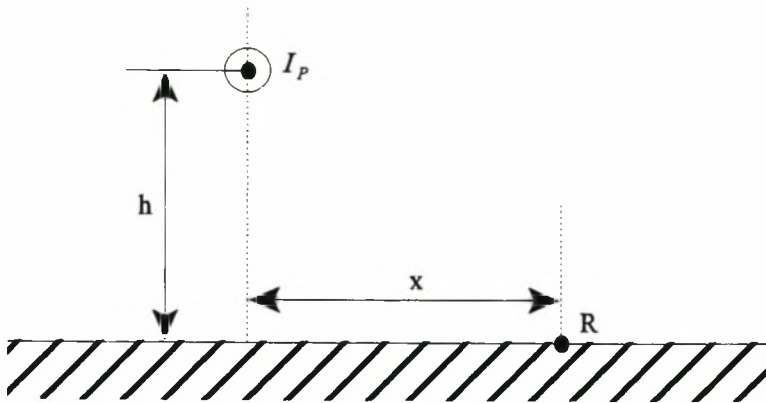
Figure 3.3: Schematic diagram of the single conductor line (after [1]).

The current at point P on the line is used to calculate the magnetic field at point R, illustrated in figure 3.3, which is in line with point P and laterally displaced away from the conductor [1]:

$$H_R = \frac{1}{2\pi}\left(\frac{2h}{h^2 + x^2}\right)I_P \qquad (3.19)$$

The electric field is calculated from the magnetic field by assuming plane wave conditions [1]:

$$E_R = (120\pi)H_R \qquad (3.20)$$

The conducted and radiated RN of a single conductor line can be calculated from the excitation function and equations 3.18 to 3.20.

3.5.3 Corona Generation on Multiconductor Lines: Simplified Analysis

The simplified analysis considers a lossless transmission line model with corona generation.
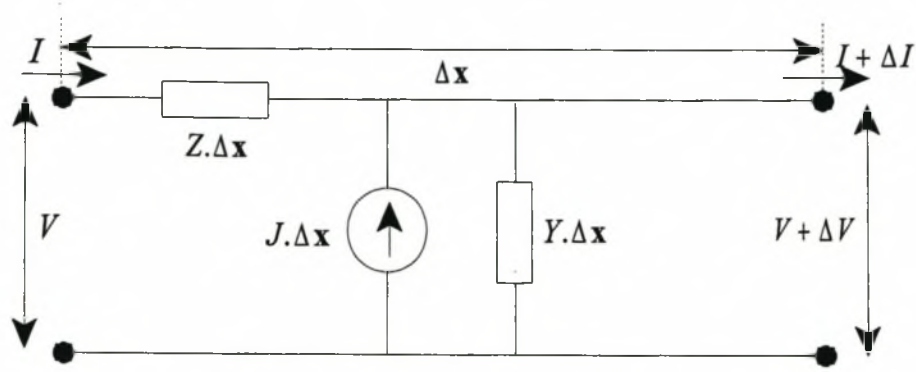
Figure 3.4: A transmission line model including corona generation (after [1]).

The lossless transmission line model with corona generation is presented in figure 3.4. This model is described by a set of coupled first order differential equations [1]:

$$\frac{d}{dz}[V] = -[Z][I]$$ (3.21)

$$\frac{d}{dz}[I] = -[Y][V] + [J]$$ (3.22)

The modal transformations are calculated for the lossless line. Equation 3.22, which describes the variation of current along the length of the line, is then decomposed into its natural modes for the case of a lossless line with corona generation [1]:

$$\frac{d}{dz}\left\{[E_i]^{-1}[I]\right\} = -2\pi\varepsilon_0\omega[\lambda]^{-1}\left\{[E_i]^{-1}[V]\right\} + [\lambda]^{-1}\left\{[E_i]^{-1}[\Gamma]\right\}$$ (3.23)

In equations 3.23, the non-singular modal current transformation matrix is defined such that [1]:

$$[E_i]^{-1}\left(2\pi\varepsilon_0[C]^{-1}\right)[E_i] = [\lambda]$$ (3.24)

The modal current transformation matrix can therefore be calculated from the capacitance matrix of the transmission line by extracting the eigenvectors as described in section 3.5.1. The propagation of the corona currents on the transmission line can now be determined by

35

considering the current propagation of each mode, described by a single conductor line above an ideal ground, individually. The current at point P due to corona generation on the line is obtained by first calculating the corona current distribution at each injection point [1]:

$$[i_g] = [E_i]^{-1}\left(\frac{1}{2\pi\varepsilon_0}[C][\Gamma]\right)$$

(3.25)

The current at $z = P$ is next calculated for each current mode using equation 3.18. These modal currents are finally combined using the modal transformation matrix, thereby producing the actual current distribution on the multiconductor line at point P. The electric field near the ground plane is calculated for the current on each phase individually using equations 3.19 and 3.20. These electric field components are combined by RMS summation to find the total electric field as measured on a RN meter with an RMS detector.

The RI level measured with a QP detector must be considered separately. This QP level is dependent on the time sequence of the corona pulses. The corona generation of the separate phases of a three phase transmission line are 120^0 out of phase. This will not affect the RMS level but will affect the QP level. The calculation method described in this section is therefore performed for corona generation on each phase separately. Summation of each phase contribution is then performed using equation 3.2 to predict the measured QP level.

The implications of the lossless transmission line assumption on the calculated RN levels of a lossy line must be considered. The modal propagation velocities are most often not equal for a lossy transmission line. Since the QP level is dependent on the time sequence of the corona pulse train, the assumption of a lossless transmission line, which implies equal modal propagation velocities, introduces an error into the calculation of the QP level. Equation 3.18 was derived for a transmission line with a non-zero attenuation constant (i.e. a lossy line). The method described above therefore requires the calculation of the attenuation constants for the lossy line. The lossless line assumption is only made in order to find the modal distribution of the corona current at the injection point (i.e. equation 3.25). The calculation of the modal attenuation constants for the lossy multiconductor transmission line must next be considered.

3. 5.4 Modal Attenuation Constants of a Lossy Transmission Line

Corona generation does not affect the modal attenuation constants of a line, defined in equation 3.16, in RN studies. The attenuation constants sought in the previous section are calculated from equations 3.13 and 3.16 for a lossy high voltage transmission line above a non-ideal earth:

$$[\gamma] = \sqrt{[E_i]^{-1}\{[Y_0]([Z_i]+[Z_g]+[Z_0])\}[E_i]} \qquad (3.26)$$

In equation 3.26, Z_i is a diagonal impedance matrix reflecting internal conductor losses, Z_g is the impedance matrix reflecting conductive earth losses while Z_0 and Y_0 are the impedance and admittance matrices of the lossless transmission line.

3. 5.4.1 Internal Conductor Losses

Current flow in a cylindrical conductor varies from a bulk current distribution to a current distributed in a thin annulus at the conductor's surface as the frequency is increased from DC. The thickness of this annular region at the surface of a typical cylindrical line conductor with radius r and at a frequency f is called the skin depth [10]:

$$d_e = \sqrt{\frac{\rho}{\pi f \mu}} \qquad (3.27)$$

The skin depth is dependent on the conductor's resistivity, ρ, and permeability, μ. The close proximity of sub-conductors in a conductor bundle also influences the current distribution at high frequencies. This current distribution can be approximated by defining an equivalent radius for the bundle. This equivalent radius is defined as the radius of a single conductor that has the same total charge as the conductor bundle at the same applied voltage [1]. The definition assumes that conductors in the bundle are connected at a discrete number of points, the separation of which is much smaller than the wavelength at the frequency investigated. The equivalent radius of a

bundle with n sub-conductors of radius r, uniformly spaced around a circle of radius R is [1]:

$$r_{eq} = \left[nrR^{n-1} \right]^{1/n}$$

(3.28)

Typical high voltage conductors consist of N_s aluminium strands of radius r_s. Of these strands, n_s will be on the outer surface of the conductor. The diagonal impedance terms reflecting internal conductor losses in a stranded conductor bundle is approximated in the PLC frequency band by the function [10]:

$$Z_i = \frac{K\rho}{r_s(n_s + 2)\pi d_e} \left[\coth\left(\frac{0.777r_{eq}}{d_e} \right) - \left(\frac{d_e}{0.777r_{eq}} \right) \right] + \frac{\rho}{N_s \pi r_s^2}$$

(3.29)

The proportionality constant K in equation 3.29 is determined by the conductor stranding.

3. 5.4.2   Conductive Earth Losses

The impedance matrix reflecting conductive earth losses due to finite ground resistivity is calculated in [1] from Carson's correction factors [11]. The Gary-Dubanton formula [12] is used in [10] as a simple, accurate approximation of Carson's integral for a single homogeneous earth layer. The error of this approximation is greater at higher frequencies but is within the bounds of uncertainty of the ground resistivity in the PLC frequency band. The approximation considers imaging the conductors in a symmetry plane located below the ground surface at a depth [10]:

$$d_e' = \sqrt{\frac{\rho_g}{\pi f \mu_g}}$$

(3.30)

The complex penetration depth of the ground is defined in equation 3.30 for a single ground layer of resistivity, ρ_g, and permeability, μ_g. The effect of conductive earth losses are included in equation 3.26 by calculating the lossless impedance matrix for the new plane of symmetry. The calculation of the magnetic field in equation 3.19 assumed a perfectly conductive ground. For a

non-ideal conductive ground, guided wave propagation over the lossy ground plane must be accounted for. The total magnetic field above the ground plane can also be approximated by again shifting the plane of symmetry by the complex penetration depth, defined in equation 3.30, into the actual ground plane.

3.5.4.3 Shield Wires

The effect of current propagation in the shield wires of a high voltage line has not yet been considered. Shield wires are placed symmetrically above the phase conductors and are electrically bonded to the tower structure to protect the line against direct lightning strikes. Their bonding to the grounded tower structure complicates the propagation analysis. The addition of p shield conductors will create as many new propagation modes. The attenuation due to current flow in the shield wires is however included in the impedance matrix without increasing the number of propagation modes by solving for [1]:

$$\begin{bmatrix} Z_{cc} & Z_{cg} \\ Z_{gc} & Z_{gg} \end{bmatrix} \begin{bmatrix} I_c \\ I_g \end{bmatrix} = \begin{bmatrix} V_c \\ 0 \end{bmatrix} \tag{3.31}$$

In equation 3.31, Z_{cc} and Z_{gg} are the impedance sub-matrices of the phase conductors and the shield wires respectively. Z_{cg} and Z_{gc} are the mutual impedance sub-matrices of the phase and shield wires. The assumption that $V_g = 0$ in this equation is valid only at frequencies whose wavelength is much longer than the span length. Solving the two equations simultaneously produces an equivalent impedance matrix [1]:

$$\begin{bmatrix} Z_{eq} \end{bmatrix} = \left\{ \begin{bmatrix} Z_{cc} \end{bmatrix} - \begin{bmatrix} Z_{cg} \end{bmatrix} \begin{bmatrix} Z_{gg} \end{bmatrix}^{-1} \begin{bmatrix} Z_{gc} \end{bmatrix} \right\} \tag{3.32}$$

The grounding of the shield wires at each tower will also result in resonance [13]. The frequency of this resonance is approximately the half wavelength frequency of the average span length. It was found in [14] that shield wire impedances and resonance only has a significant effect on the

attenuation of the most attenuated mode in the PLC band for the Acacia-Koeberg line. It was further noted in [15] that the removal of shield wires did not affect the measured RI level in the frequency regime 1 MHz to 30 MHz. The effects of shield wires on the RN performance of the measured lines are therefore ignored in this dissertation.

3.5.5 Corona Generation on Multiconductor Lines: Improved Analysis

The simplified method described in section 3.5.3 uses an approximate modal injected current distribution for the propagation analysis. The only significant discrepancies occur in the predicted lateral profile data, particularly at large distances from the line [1]. The actual modal corona current distribution is calculated by differentiating equations 3.21 and 3.22 with respect to z, the displacement along the line's length. Since the corona current injection is constant over the length of the line, it is removed from equation 3.22 by the differentiation, producing the results in equations 3.10 and 3.11. The modal transformation matrices of these equations, for the impedance and admittance matrices of a lossy line defined in section 3.5.4, are defined in section 3.5.1. The same modal current transformation matrix applies to both the conductor current and the injected corona current [16]. The modal injected current distribution is therefore:

$$[J^m] = 2\pi\varepsilon_0 [E_i]^{-1} \{[C]^{-1}[\Gamma]\}$$

(3.33)

Equation 3.18 is then used to find the total corona current distribution at any point along the line. This improved analysis is suggested in the EPRI method [8] for lines where the attenuation has not been measured.

The prediction of the conducted RN measured in the PLC system requires that the frequency characteristics of the coupling capacitor and line matching equipment described in chapter 2 are known. These are obtained from the manufacturer's specifications, for the conducted RN predictions calculated in this dissertation.

3.6 Isolating Individual Correction Terms

The RN prediction methods proposed in the literature were derived from measurements on lines designed by the power utility or research organization to which the method is attributed.

40

Variations in design philosophies between such organizations should therefore produce prediction methods which collectively span a wide range of possible line geometries and environmental conditions. A comparison of individual correction terms and models should therefore reveal how certain changes in geometry affect the RN performance. It was therefore decided to extract the individual correction terms, defined for the various parameters in equation 3.1, from each prediction method and then compare these individual terms. In this way general relationships are identified for a wide range of parameter values. The comparisons and general relationships are presented in this section.

Besides the correction factors included in equation 3.1, aging and seasonal effects must also be considered. These effects are difficult to quantify for the general case. A decrease of 6 dB in the average fair weather RI level was observed on a newly installed line over a 2.5 year period in [17]. This reduction was attributed to conductor weathering. A decrease of between 3 dB and 7 dB was attributed to conductor weathering over a period of 3 months in [18]. To exclude these effects from the calculations, it will be assumed that the line has been in operation for more than a year and that pollution levels are not excessive.

3. 6.1 Surface Gradient $\left(RI_g \right)$:

The relationship between the RI level and the applied surface gradient is included in all prediction formulas. There are three general relationships derived in the literature:

$$RI_g = A_1 \left(g - g_0 \right) + A_2 \qquad (3.34)$$

$$RI_g = A_3 \log_{10} \left(\frac{g}{g_0} \right) + A_4 \qquad (3.35)$$

$$RI_g = - \left(\frac{A_5}{g} \right) + A_6 \qquad (3.36)$$

The relationships defined in equations 3.34 to 3.36 are referred to in the dissertation as gradient models A, B and C respectively. A comparison of the relationship between the RI level and the surface gradient included in the empirical and semi-analytical formulas in sections 3.2, 3.4 and

appendix D is presented in appendix E. The comparison reveals that gradient model A is used to predict the relationship under fair weather conditions. Foul weather and heavy rain RN levels are then predicted by adding an empirical correction factor to the average fair weather level. It was found in [9] and [19] that the value of A_1 is dependent on the range of gradients and conductor diameters used to obtain the data from which the constant was extracted. This explains the variation in this proportionality constant between 2.5 and 4.5 in appendix E. The validity of each method must therefore be considered for the gradients and conductor diameters studied.

Empirical formulas derived from average foul weather and heavy rain data use gradient models B and C. Results presented graphically in [9] suggest that the RI level, in dB, under heavy rain conditions, increases as:

$$\frac{d}{dg}\left(RI_g\right) \propto \frac{1}{g^n} \tag{3.37}$$

In equation 3.37, $n = 1$ for $g \leq 17\,\text{kV/cm}$. Gradient model B describes this rate of increase. For $g > 17\,\text{kV/cm}$, $n \geq 2$ and this rate of increase is described by gradient model C. The change in rate of increase at a gradient of 17 kV/cm is also noted in the Shiobara method [20]. The rate of increase is however also dependent on the conductor radius. The selection of gradient model and proportionality constants is therefore dependent on the ambient weather conditions, as well as the range of gradients and conductor diameters investigated.

Most empirical equations use the average maximum surface gradient for bundle conductors. The exceptions are the ENEL method which uses the average gradient and the Shiobara method which uses the average maximum gradient on the lower phase for double circuit, vertical lines.

3. 6.2 Conductor Diameter $\left(RI_d\right)$:

The conductor diameter affects the RI level in two ways. Firstly, it will affect the divergence of the electric field near the conductor surface. Secondly, it will affect the total surface area on which corona activity can occur. It was evident in the previous section that the conductor

42

diameter and surface gradient are closely related. In fact, the selection of the gradient model is dependent, in part, on the conductor diameter studied. A dependence on conductor diameter is therefore implicit to the gradient model, but such a model does not sufficiently describe the dependence of the RI level on the conductor diameter. An explicit conductor diameter term is therefore added to most empirical formulas:

$$RI_d = A_1 \log_{10}\left(\frac{d}{d_0}\right)$$
(3.38)

In equation 3.38, $A_1 = 40$ for most of the empirical formulas discussed so far. The exceptions are the Westinghouse, CIGRÉ and EdF methods. The Westinghouse method uses $A_1 = 30$. This value was derived from laboratory measurements of various conductor diameters under heavy artificial rain at the Apple Grove test facility [5]. It is suggested in [9] that equation 3.38 is only accurate for conductors of "medium" diameter under heavy rain conditions. A more accurate model for conductors with a diameter greater than 4 cm is used in the EdF method [9]:

$$RI_d = A_2 d$$
(3.39)

The accuracy of this model should be checked for conductor diameters less than 4 cm.

3. 6.3 Sub-conductor Number $\left(RI_n\right)$:

The bundle geometry, i.e. the sub-conductor separation and number, affects the surface gradient distribution on the individual sub-conductors. Most prediction formulas presented in this chapter define a relationship between the RI level and the average maximum sub-conductor gradient. The deviation of the exact gradient distribution at the sub-conductor surface from the average maximum value is assumed to have no significant affect on the accuracy of the prediction model. This assumption is only valid if the ratio of bundle radius to sub-conductor radius is between 10 and 20 [8]. For ratios smaller than 10, the RI level becomes dependent on the actual surface gradient distribution. It was concluded in [9] that the bundle radius has no effect on the RI level, provided that the ratio of bundle radius to sub-conductor radius is between 10 and 15. There is

43

however a strong correlation between the number of sub-conductors and the RI level. The general correction for sub-conductor number used in fair weather prediction methods is:

$$RI_n = 10\log_{10}\left(\frac{n}{n_0}\right) \tag{3.40}$$

Heavy rain and foul weather prediction methods use correction terms which are read off a table and are dependent on the gradient model used. Foul weather prediction models were optimized, in part, by removing the dependence on sub-conductor number in [4].

3.6.4 Weather Conditions (RI_w):

Method	average fair (L_{50d})	average foul (L_{50w})	stable foul/rain (L_{5w})	maximum foul / heavy rain(L_{1w})
CIGRÉ	(equation 3.3)	$L_{50d} + 17$	$L_{50d} + 20$	$L_{50d} + 24$
BPA	$L_{5w} - 25$	(equation 3.4)	$L_{50w} + 8$	-
EdF	$L_{5w} - 17$	$L_{5w} - 5$	(equation 3.6)	$L_{5w} + 5$
IREQ	-	-	-	(equation 3.7)
EPRI	$L_{50w} - 17$	(equation 3.44)	-	(equation 3.8)
400kV-FG	(equation C.1)	$L_{50d} + (17 \pm 3)$	-	-
Ontario-Hyrdo	(equation C.7)	$L_{50d} + 20$	$L_{1w} - 6$	(equation C.7)
ENEL	(equation C.12)	$L_{50d} + 14$	$L_{50d} + 20$	-
Westinghouse	(equation C.15)	$L_{50d} + 17$	-	$L_{50d} + 24$
EGU	(equation C.14)	$L_{50d} + 10$	$L_{50d} + 16$	$L_{50d} + 20$

Table 3.3: Comparison of weather correction factors used in the empirical and semi-empirical equations of sections 3.2, 3.4 and appendix D.

The stability and reproducibility of RN is best under heavy continuous rain conditions [8]. Heavy artificial rain conditions are often used in corona cage studies (e.g. EPRI and IREQ). This is

because the rainfall rate is controllable and can be increased to levels comparable to those exceeded no more than 1% of the time on actual lines. The EPRI method [8] proposes that the RI level saturates at a maximum level for the line and gradient when the rainfall rate exceeds between 8 and 12 mm/hr. This maximum level is independent of the conductors surface state and corresponds to the L_1 wet level. The EdF method uses a rainfall rate exceeded 50% of the time. The RI measured for this rate corresponds to the L_5 wet level and is a good indication of the RI level under average rain conditions, but requires that the rain rate is known.

Two weather relationships are consistent in most of the prediction methods compared in table 3.3:

$$L_{50wet} = L_{50dry} + (17 \pm 3) \tag{3.41}$$

$$L_{1wet} = L_{50dry} + (24 \pm 1) \tag{3.42}$$

The variation between heavy artificial rain and average fair weather RI levels is smaller than that of average fair and average foul weather RI. The difference between heavy artificial rain and wet conductor RI levels is a function of the gradient and conductor diameter [8]. This is possibly the reason for the higher deviation in equation 3.41. The average foul weather RI level can therefore only be accurately extracted from the heavy artificial rain level if this relationship is known for the line geometry. This relationship is approximated for $2 < d < 8$ cm by [8]:

$$L_{50wet} = L_{1wet} + \left[8.2 - 14.2 \left(\frac{g_{6dB}}{g} \right) \right] \tag{3.43}$$

where [8]:

$$g_{6dB} = \begin{cases} \dfrac{24.4}{d^{0.24}} & ;n \le 4 \\ \dfrac{24.4}{d^{0.24}} - \dfrac{1}{2}(n-4) & ;n > 4 \end{cases} \qquad (3.44)$$

The increase in RI level with increasing rainfall rate, P [mm/hr], from wet-conductor to heavy rain conditions is described in the general case by [18]:

$$RI_{rr} = \beta(d,n)\left[1 - e^{K(d,n)P}\right] \qquad (3.45)$$

In equation 3.45, β and K are empirical constants which describe the saturation level and rate of increase of the RI correction and are dependent on the sub-conductor number and diameter.

A continuous conducted RN measurement, made at the Acacia substation with a RMS detector, was presented in figure 2.3. The maximum variation in the RMS level was only 5 dB for a variation in weather from fair weather to rain conditions. From the empirical QP relations defined in equation 3.41 and 3.42 and the discussion in this chapter, it is concluded that the continuous conducted RN measurement cannot be compared to predictions made with the methods presented in this chapter. It is suggested that the reason for this is the variation of the statistical amplitude and repetition rate distributions of the measured RN pulse train due to the change in weather condition. The RN performance analysis presented in this chapter is therefore limited to QP measurements or RMS measurements under fair weather conditions for which the relationship between the various detectors outputs is known (i.e. the value of K, defined in equation 2.2, has been calculated). The relationship between QP and RMS RN measurements under various environmental conditions should be further investigated.

3. 6.5 Relative Air Density and Relative Humidity $\left(RI_{RAD} + RI_{RH}\right)$:

The relative air density is a function of the temperature t [$^\circ$C] and pressure p [mmHg] of the air surrounding the conductor surface [1]:

$$\delta = \frac{273 + 25}{273 + t} \cdot \frac{p}{760}$$ (3.46)

An empirical correction term for a change in RAD was derived by LaForest et al. [18]:

$$RI_{RAD} = -K(\delta - 1)$$ (3.47)

In equation 3.47, $K = 42.7$ for fair weather conditions and 54 for foul weather conditions [18]. A change in altitude will also affect the RAD. The decrease in pressure with an increase in altitude, A [km], is approximated by the empirical relation [1]:

$$p = p_0 \left(1 - \frac{A - A_0}{k} \right)$$ (3.48)

The constant is extracted empirically as $k \approx 10.7$. The correction term for a change in altitude, ΔA [km], used in the CIGRÉ, BPA and ENEL methods is [1]:

$$RI_A = \frac{\Delta A}{0.3}$$ (3.49)

This is essentially the same as the correction term derived empirically from measurements made at the Leadville high altitude test site and used in the Westinghouse method [4]:

$$RI_A = 40 \left(1 - \frac{\delta}{\delta_0} \right)$$ (3.50)

The influence of RH on RN is not well understood. An empirical correction term for a change in RH was derived by LaForest et al. [18]:

47

$$RI_{RH} = 0.05(RH - 50) \tag{3.51}$$

3.6.6 Wind Speed $\left(RI_{ws}\right)$:

An empirical correction term for wind speed, W_S [km/hr], was derived by LaForest et al. [18]:

$$RI_{WS} = 1.33W_s^{0.3} \tag{3.52}$$

Equation 3.52 describes a non-linear relation between wind speed and the measured RI level.

3.6.7 Measurement Frequency $\left(RI_f\right)$:

The correction term for a change in measurement frequency from the reference frequency, f_0 [MHz], used in the BPA and CIGRÉ methods is [1]:

$$RI_f = 10\left(f_0 - \log_{10} 10f\right)^2 \tag{3.53}$$

This correction factor accounts for the shape of the frequency spectrum of the corona source as well as the frequency dependent attenuation and radiation characteristics of the transmission line.

3.6.8 Meter Characteristics $\left(RI_m\right)$:

A 2 dB correction term is subtracted from the predicted RI level in the BPA method to convert from ANSI to CISPR meter bandwidths for a QP detector [1].

3.6.9 Lateral Distance $\left(RI_D\right)$:

The general form of the lateral distance correction factor used in the various empirical and semi-analytical methods presented in this chapter is [3]:

$$RI_d = -20k \log_{10}\left(\frac{D'}{D'_0}\right) \tag{3.54}$$

This correction factor accounts for both the radiated and near fields associated with a multi-conductor transmission line. The value of k is therefore dependent on the cross-sectional geometry of the line and the position of the antenna. This is evident in the Ontario-Hydro method where $k = 2$ for horizontal lines and $k = 1.1$ for vertical lines. Values for k are suggested in the CISPR 18-2 document for various line geometries. Further from the line, the value of k decreases to 1. A more rigorous correction term for a variation in lateral distance is suggested in the BPA method. It considers the effects of the direct wave (DW), surface wave (ESU) and the induced field (EIND) components on the antenna measurement [1]:

$$RI_D = C(D,\delta) - C(21,4) \tag{3.55}$$

where [1]:

$$C(D,\delta) = 10\log_{10}(DW^2 + ESU^2 + EIND^2) \tag{3.56}$$

$$DW = \begin{cases} \dfrac{\lambda h_c}{2\pi D} & ,D \le \dfrac{12h_c h_a}{\lambda} \\ \dfrac{\lambda h_c}{2\pi D}\cdot\dfrac{12h_c h_a}{\lambda D} & ,D > \dfrac{12h_c h_a}{\lambda} \end{cases} \tag{3.57}$$

$$ESU = \frac{2 + 0.3(52.5D/\delta\lambda^2)}{2 + (52.5D/\delta\lambda^2) + 0.6(52.5D/\delta\lambda^2)}\cdot\frac{\lambda h_c}{2\pi D} \tag{3.58}$$

$$EIND = \frac{\lambda^2 h_c}{(2\pi D)^2} \tag{3.59}$$

49

This more rigorous method should produce more accurate RI predictions, especially at large distances from the outer phase.

3. 7   Comparison of the Measured and Predicted RN for the Lines Studied

The RN measurements in section 2.3 are compared in this section to levels predicted with the methods discussed in this chapter to determine the best prediction methods for the studied lines. The Acacia-Koeberg RN measurements were described in section 2.3.1. They were made under fair weather conditions at sea level. No altitude correction is therefore required and any significant pollution should have been washed off the conductors during the rain season. The measurements were made after 10:00 am, so the conductors are considered to be dry. Only RH and wind correction factors, defined in equations 3.51 and 3.52, were added to both the empirical and semi-analytical predictions to account for 40% RH and a light 2 km/hr wind. It was noted in chapter 2 that the only possible RI measurement site was not ideal. The validity of the RI measurements must therefore be determined from the comparison made for this line.

Figure 3.5: The measured and predicted RN performance of the Acacia-Koeberg line: (a) conducted RN levels in the PLC band; (b) RI frequency spectrum in the PLC band [$x = 20$ m]; (c) RI frequency spectra at selected frequencies and various lateral distances; (d) the lateral profile at 500 kHz. [BW = 10 kHz]

The measured and predicted RN levels for the Acacia-Koeberg line are plotted in figure 3.5. The BPA method prediction, which is derived from average foul weather data, is more accurate than the CIGRÉ method, which was derived from fair weather data. Both empirical methods are however significantly less accurate than the semi-analytical methods. All excitation functions are calculated at 500 kHz and then assumed to be constant across the PLC band. The shape of the predicted curves is therefore due to the variation of the modal attenuation constants with frequency. The comparison in figure 3.5 (a) suggests that this variation does not adequately account for the measured frequency variation and therefore that the excitation function varies with frequency in the PLC band. The accuracy of the excitation function is evaluated at 500 kHz.

The most accurate excitation function for the Acacia-Koeberg line is that of the EdF method.

The comparison of the predicted and measured RI performance suggest that the change in line direction at the test location causes standing waves. More frequency points should therefore be measured in the frequency scan. The geometric mean transform can then be used to find the actual RI spectrum. The lateral profiles in figure 3.5 (d) are plotted against the lateral displacement from directly under the centre phase. Having identified the EdF method as the most accurate method for this line, the comparison in this plot indicates that the measured lateral profile is inaccurate at lateral distances less than 11 m from the outer phase. This is attributed to the saturation of the active loop antenna. The measured RI levels appear invalid at lateral displacements of more than 21 m from the outer phase. This is attributed to the RN from the other lines in the shared servitude at the test location, as well as the excessive radiation due to the change in direction of the measured line. The saturation of the active loop antenna therefore limits the validity of the lateral profile measurement to a small range of lateral distances from the outer phase conductor. The validity of the plane wave assumption for lateral displacements close to the line can therefore not be evaluated.

The radiation models can only be the verified at a lateral distance of 11 to 21 m from the outer phase. The shape of the various predicted lateral profiles in this range suggest that the EPRI radiation model, which calculates the electric field directly from the voltage on the line conductors, is not a significant improvement on the simpler model described in section 3.4, which calculates the electric field from the magnetic field assuming plane wave conditions. This comparison also indicates that the more rigorous lateral displacement correction term defined in equation 3.57 for the BPA method does better predict the shape of the lateral profile.

The Hydra-Droërivier line measurements were described in section 2.3.2. The measurements were made under similar conditions to the Acacia-Koeberg line measurements. The same wind and RH corrections were therefore again made for this line. The line is at a much higher altitude. The altitude correction, defined in equation 3.49, is therefore also added to the empirical and semi-analytical predictions for the compact-delta transmission line.
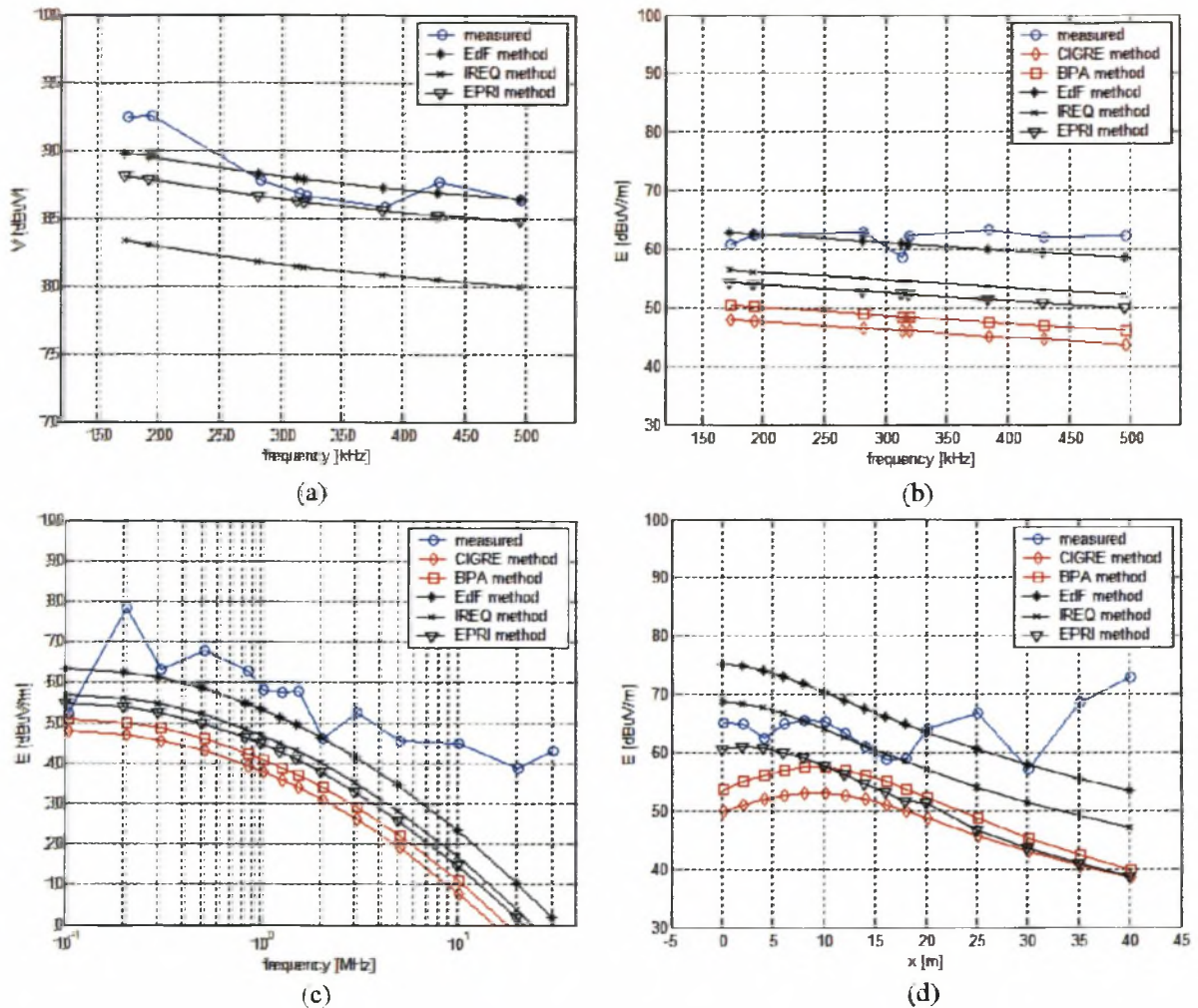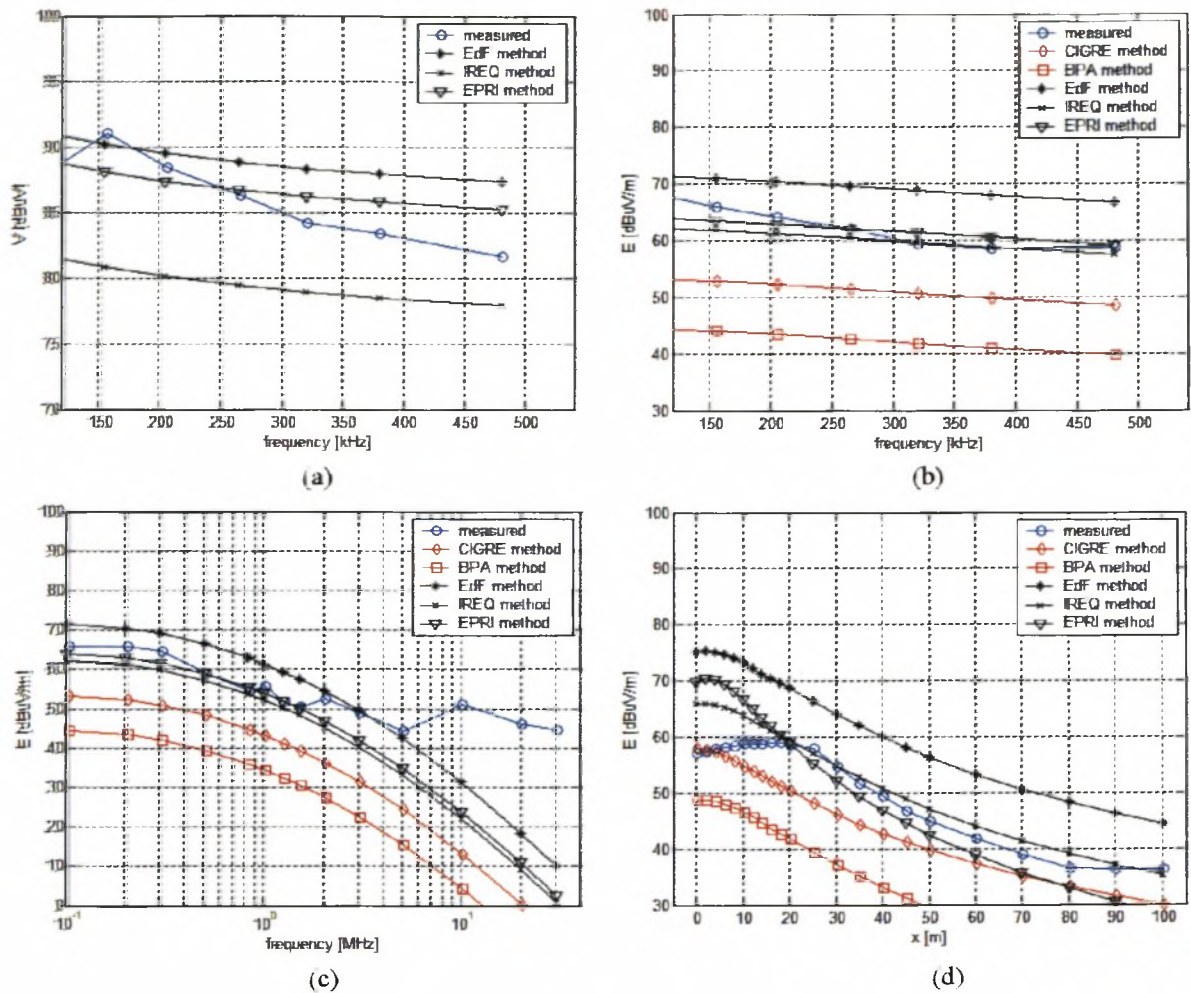
Figure 3.6: The measured and predicted RN performance of the Hydra-Droërivier line: (a) conducted RN levels in the PLC band; (b) RN frequency spectrum in the PLC band [$x = 20$ m]; (c) RI frequency spectra at selected frequencies and various lateral distances; (d) the lateral profile at 500 kHz. [BW = 10 kHz]

The measured and predicted RN levels for the Hydra-Droërivier line are plotted in figure 3.6. The comparison of the predicted and measured conducted RN indicates that the EPRI and IREQ excitation functions are more accurate than the EdF excitation function for this line. The valid range of conductor diameters for which the EdF method was defined is 3.7 to 5.2 cm. This method is therefore not applicable to the Hydra-Droërivier line which has Tern sub-conductors with diameters smaller than 3.7 cm. This explains the lack of accuracy for this semi-analytical method. The IREQ method is more accurate for the triple Tern bundle than it was for the twin Dinosaur bundle of the previous measurement. The variation of the measured RN with frequency in the PLC band is again not adequately accounted for by the semi-analytical methods.

53

A comparison of the RI performance for the compact delta geometry indicates that the semi-analytical methods are again more accurate than the empirical methods. The comparison also suggests that the more rigorous radiation models used by the BPA and EPRI methods are more accurate for the line's phase conductor geometry. The simple radiation model described in section 3.5.2 is therefore not adequate for the more compact line design. Saturation of the active loop antenna occurs at a lateral distance of 20 m from the outer phase.

It is noticeable in the CISPR frequency spectra of both the Acacia-Koeberg and Hydra-Droërivier lines that the spectra deviate significantly from the predicted data at frequencies above 2 MHz. QP, RMS and average detector levels were measured at 50 m from the outer phase to check for the presence of spurious noise at these frequencies (this methods was described in section 2.2.2). The results confirmed that the noise was indeed generated by conductor corona. A frequency scan at the CISPR lateral distance revealed that the saturation of the active loop antenna created spurious levels at frequencies above 2 MHz. The saturation of the antenna at the reference distance restricts the valid frequency band to below 2 MHz.

The same wind, RH and altitude correction factors used for the previous line predictions were used for the Aries-Kokerboom and Kriel-Tutuka lines. The RI measurements of the Aries-Kokerboom line suffer from antenna saturation. These measurements are therefore not used to evaluate the prediction methods. The conducted RN levels of the two lines were measured with an RMS detector only. Equivalent QP levels were estimated for the Aries and Tutuka measurements using the value of K defined in equation 2.2 and measured at the Droërivier and Acacia substations respectively. These approximations should be accurate since the geometries of these lines and the ambient weather conditions are similar. The approximation was necessary since the prediction methods only calculate QP levels.
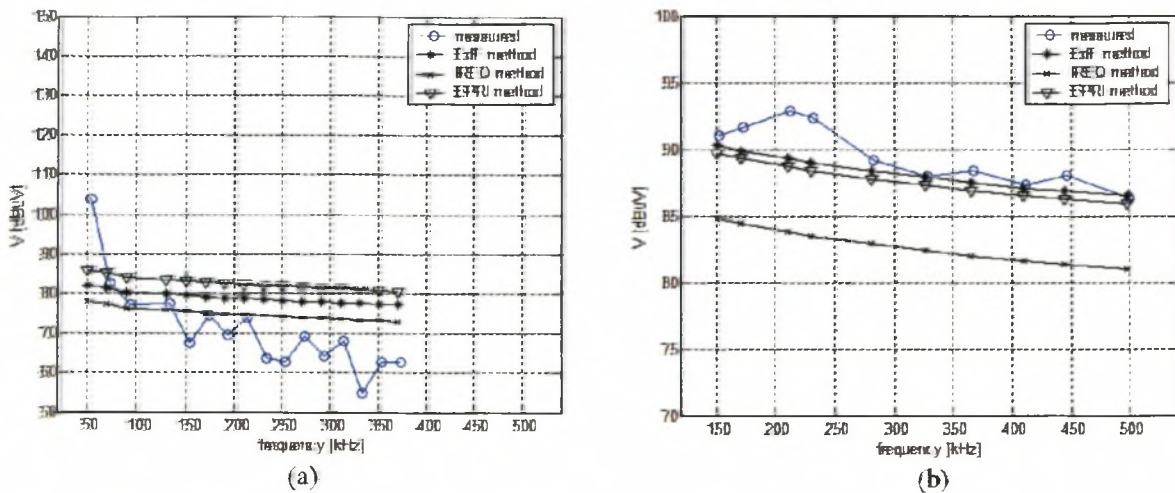
Figure 3.7: The measured and predicted conducted RN levels of (a) the Aries-Kokerboom line (measured data supplied by R. Hubbard) and (b) the Kriel-Tutuka line measured at the Tutuka substation (measured data supplied by W. de Villiers).

The measured and predicted RN levels for the Aries-Kokerboom and Kriel-Tutuka lines are plotted in figure 3.7. The comparison between the predicted and measured conducted RN at the Aries substation in figure 3.7 (a) again indicates an improvement in the accuracy of the IREQ method. This method is in fact the most accurate of the three semi-analytical methods, as determined at 500 kHz. The EdF method is again not applicable to this line because of the small diameter Tern sub-conductors. The method does however predict the RN level more accurately than the EPRI method. The improved accuracy of the IREQ method and the inaccuracy of the EPRI method in predicting the RN performance of the Aries- Kokerboom line, which has a quad Tern bundle geometry, is attributed to the different sub-conductor number correction models used. These models are discussed in section 3.6.3. The basis for this conclusion is found in the comparisons made in sections 3.6.1 to 3.6.3. Both the EdF and IREQ methods use the same surface gradient correction models. This model therefore does not explain the improvement of the IREQ prediction. The IREQ and EPRI methods share the same sub-conductor diameter correction models. The EdF method which uses a sub-conductor diameter correction model that is not valid for the Tern conductors produces a more accurate prediction than the EPRI method. The EPRI method does however not have a rigorous sub-conductor number correction term while the IREQ and EdF methods do. The sub-conductor number correction must therefore be carefully chosen for bundles with four or more sub-conductors.

55
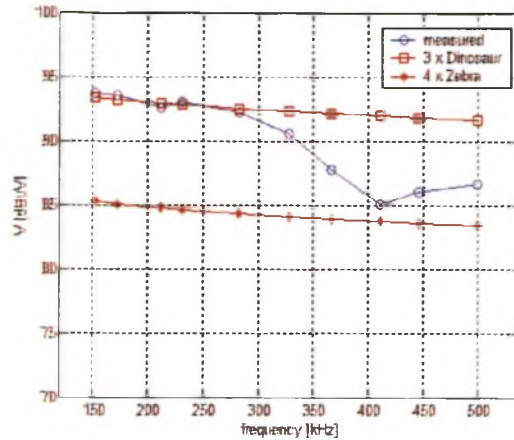
Figure 3.8: The measured and predicted conducted RN levels of the Kriel-Tutuka line measured at the Kriel substation (measured data supplied by W. de Villiers).

As was the case for the Acacia-Koeberg line, the EdF method best predicts the conducted RN levels of the Kriel-Tutuka line measured at the Tutuka substation since it has large diameter sub-conductors (c.f. figure 3.7 (b)). The frequency variation of the RN level in the PLC band is not accurately predicted by any of the semi-analytical methods. These methods can also not be used to isolate the individual contribution of the various conductor bundle sections at the Kriel substation. The predicted levels of the triple Dinosaur section closest to the substation and the subsequent quad Zebra section are calculated with the EdF and IREQ methods respectively. These predictions are compared to the measured RN level at the PLC receiver in figure 3.8. The predicted level of the 30 km quad Zebra section is almost 8 dB lower than that of the 5 km triple Dinosaur section across the PLC band. The measured RN at 500 kHz lies between the saturated levels of the two sections. To predict this measured level, the accuracy of equation 3.18 for short line sections must be evaluated.

The comparison of measured and predicted RN performance for the measured lines revealed that the semi-empirical methods were significantly more accurate than the empirical methods. The use of empirical methods to predict the RN performance of a line will therefore not be further considered and the idea of deriving an optimized empirical equation for local lines, as was done in [4], will not be pursued. Instead, a RN prediction methodology that uses only semi-analytical methods is implemented in executable code for the prediction of the RN performance of an arbitrary transmission line design. This methodology was derived from the results presented in

this section and is summarized in appendix F.

The prediction methods discussed in this chapter are derived from corona cage measurements at 500 kHz. These methods were not able to predict the frequency dependence of the conducted RN at other frequencies. They were also not able to predict the RN of short line sections. The variation of the excitation function with frequency and the validity of equation 3.18 for short line sections must be further studied. It was decided to do this in a large corona cage. The excitation function extracted from a corona cage should also be more accurate than the empirically derived excitation functions used in the semi-analytical methods since the actual conductor bundle is studied in the corona cage. This is discussed in the next chapter.

3. 7.1 References

[1]   P. Sarma Maruvada, *Corona Performance of High-Voltage Transmission Lines*, Research Studies Press Ltd, 2000.

[2]   IEEE Committee Report, "CIGRÉ/IEEE Survey on Extra High Voltage Transmission Line Radio Noise", IEEE Trans., Vol. PAS- 92, 1973, pp. 1019-1028.

[3]   CISPR Publication 18-2, *Radio Interference Characteristics of Overhead Power Lines and High Voltage Equipment. Part 2. Methods of Measurement and Procedure for Determining Limits.*

[4]   R.G. Olsen, S.D. Schennum, V.L. Chartier, "Comparison of Several Methods for Calculating Power Line Electromagnetic Interference Levels and Calibration with Long Term Data", IEEE Trans., Vol. PWRD-7, 1992, pp. 903-913.

[5]   G.E. Adams, "The Calculation of Radio Interference Level of Transmission Lines Caused by Corona Discharges", AIEE Trans., Part III, 1956, pp. 411-419.

[6]   C.H. Gary, "The Theory of the Excitation Function: A Demonstration of its Physical Meaning", IEEE Trans., Vol. PAS- 91, 1972, pp. 305-310.

[7]   R.G. Urban, *Modelling Corona Noise on High Voltage Transmission Lines*, MScEng Thesis, University of Stellenbosch, 2001.

[8]   *Transmission Line Reference Book: 345kV and Above/Second Edition*, Electric Power Research Institute (EPRI), Palo Alto, CA,1982.

[9]   M.R.Moreau, C.H. Gary, "Predetermination of the Radio-Interference Level of High

Voltage Transmission Lines: I - Predetermination of the Excitation Function", IEEE Trans., Vol. PAS- 91, 1972, pp. 284-291.

[10]   L.M. Wedepohl, *The Theory of Natural Modes in Multi-Conductor Transmission Systems*, Unpublished lecture notes, Westband, Brittish Columbia, Canada, 1999.

[11]   R.H. Galloway, W.B. Sharrocks, L.M. Wedepohl, "Calculation of Electrical Parameters for Short and Long Polyphase Transmission Lines", Proc. IEE, Vol. 111, 1964, pp. 2051-2059.

[12]   C.H. Gary, M.R. Moreau, *L'effet Couronne en Tension Alternative*, Eyrolles, Paris, 1976.

[13]   L.M. Wedepohl, "Wave Propagation in Polyphase Transmission Systems - Resonance Effect Due to Discretely Bonded Earth Wires", IEE Proc., Vol. 112, No. 11, 1965, pp. 2113-2119.

[14]   W. de Villiers, *Prediction and Measurement of Power Line Carrier Signal Attenuation and Fluctuation.*, MScEng Thesis, University of Stellenbosch, 2001.

[15]   C.R. Bond, W.E. Pakala, R.E. Graham, J.E. O'Neil, "Experimental Comparisons of Radio Influence Fields From Short and Long Transmission Lines", IEEE Trans., Vol. PAS- 82, 1963, pp. 175-185.

[16]   L.M. Wedepohl, J.N. Saha, "Radio Interference Fields in Multi Conductor Overhead Transmission Lines", Proc. IEE, Vol. 116, 1969, pp. 1875-1884.

[17]   M.C. Perz, "Method of Evaluating Corona Noise Generation from Measurements on Short Test Lines", IEEE Trans., Vol. PAS- 82, 1963, pp. 833-839.

[18]   J.J. LaForest, M Baretsky, Jr., D.D. MacCarthy, "Radio-Noise Levels of EHV Transmission Lines Based on Project EHV Research", IEEE Trans., Vol. PAS- 85, 1966, pp. 1213-1226.

[19]   IEEE Radio Noise Subcommittee Report, "Radio Noise Design Guide for High-Voltage Transmission Lines", IEEE Trans., Vol. PAS- 90, 1971, pp. 833-840.

[20]   Y. Sawada, "Calculating Method of Radio Noise Level and Its Application to Design of AC Power Transmission Line", IEEE Trans., Vol. PAS- 89, 1970, pp. 844-851.

Chapter 4

Large Corona Cage Measurements

4. 1   Introduction

The empirical excitation functions presented in section 3.4 are derived from corona cage measurements. Such a facility is used by ESKOM to extract the excitation function of a conductor bundle either currently in use, or to be used on one of its lines. It will be referred to as the Megawatt Park corona cage in this dissertation. Excitation function data for the conductor bundles of the studied lines was made available by R. Hubbard. In order to determine the usefulness of this data, the design and measurement protocol used at the Megawatt Park facility is investigated. A one week visit was made to the facility and a twin IEC-800 conductor bundle, similar to the twin Dinosaur bundle used on the Acacia-Koeberg line, was measured under fair weather conditions.

Two limitations of the semi-analytical methods were identified in chapter 3 as the inability to predict the RN of a short line section and also the variation of the RN with frequency in the PLC band. The latter is attributed to the narrowband definition of the excitation function. The extraction of a wideband excitation function in the Megawatt Park corona cage is therefore investigated in this chapter. The design of a large corona cage is introduced in section 4.2. In section 4.3, the visit to the Megawatt park corona cage is described along with the measurements made. The available excitation function data is then used to predict the RN performance of the measured lines and a comparison with the measured RN performance is presented in section 4.4.

4. 2   Literature Survey

A corona cage is described in [1] as a rectangular, grounded-mesh cage structure surrounding a centred conductor bundle, between 15 and 60 m long and energized by a single phase high voltage source. Cylindrical cages are more expensive to construct, but provide a uniform radial

58

electric field along the length of the conductor bundle. If the radius of the corona cage, R_c [cm], is much larger than the radius of the conductor bundle, R_b [cm], the average surface gradient for each of the n sub-conductors of radius r_s [cm] is approximated by [2]:

$$E_a = \frac{1}{n} \cdot \frac{V}{r_s \ln(R_c / r_{eq})}$$

(4.1)

In equation 4.1, r_{eq} is the equivalent radius of the conductor bundle defined in equation 3.28. The average maximum surface gradient on the centre phase bundle of the Acacia-Koeberg line was calculated using the method of successive images in chapter 3 in order to predict the RN performance of the line. This gradient was 15.64 kV/cm (RMS) for a line-to-line voltage of 405kV (RMS). The average maximum bundle gradient of a n conductor bundle in a corona cage is approximated from the average surface gradient defined in equation 4.1 [2]:

$$E_{AM} = E_a \left[1 + (n-1)\frac{r_s}{R_b} \right]$$

(4.2)

The voltage required to create a surface gradient on the corona cage bundle equivalent to that of the Acacia-Koeberg line's centre phase bundle is calculated from equations 4.1 and 4.2 as:

$$V = 2.963.E_{AM}\left[\ln(R_c) - 2.107 \right]$$

(4.3)

The voltage required if the corona cage radius is $R_c = 350$ cm is therefore 171.7 kV. This is much lower than the line voltage. The cage radius is determined by the range of gradients required, the bundle geometry studied and the maximum voltage rating of the high voltage source. The range of surface gradients should be sufficient so as to ensure that corona inception occurs and that this inception gradient is lower than the flash-over gradient. The corona inception

gradient is defined in [2] as that surface gradient at which self-sustaining partial discharges occur near the conductor surface and was derived empirically by Peek [3] for a concentric cylindrical geometry and a 50 Hz AC source voltage [2]:

$$E_c = 21.9 m \delta \left(1 + \frac{0.308}{\sqrt{\delta r_c}} \right) \qquad (4.4)$$

In equation 4.4, δ is the RAD factor defined in equation 3.47, r_c is the conductor radius in centimetres and m is the surface irregularity factor. This factor equals 1 for an ideally smooth and clean conductor. It is reduced towards zero by surface irregularities and pollution. The margin between the inception gradient and the breakdown gradient should be at least 50% [2].

The average maximum surface gradient of a line conductor can be replicated in a coaxial corona cage geometry without replicating the exact surface gradient distribution around the perimeter of the conductor. A technique of replicating the exact surface gradient distribution by offsetting the conductor bundle inside the corona cage is described in [4]. The total corona current on a single conductor line, such as the corona cage setup, saturates at the level defined in equation 3.18 if the separation distance between individual corona sources is sufficiently small, i.e. there is a sufficient number of corona sources on the line. The corona cage is much shorter than a transmission line and the number of corona sources on the centre conductor of a corona cage may therefore not be sufficient to ensure a saturated RN level. Corona activity increases under heavy rain conditions and the cage length required to ensure a saturated corona current level is reduced. A minimum cage length has not been derived in the literature, although it is suggested in [4] that the cage should be longer than 30 m for heavy rain tests. An advantage of corona cages is the ability to apply uniform rainfall of a controllable intensity along the entire length of the conductor tested. The design and calibration of rain apparatus for corona cages is described in [5].

The radial electric field inside the corona cage must be uniform along the length of the centre conductor. The average maximum surface gradient defined in equation 4.2 is for an infinitely long coaxial cage geometry. Charge will accumulate at the ends of a finite length, open circuit coaxial transmission line. This results in a much higher surface gradient at both ends of the centre

conductor. Since corona activity is a function of the surface gradient, increased corona activity from the regions of higher surface gradient will impede the extraction of the relationship between the measured corona noise and the surface gradient calculated for an infinitely long corona cage.
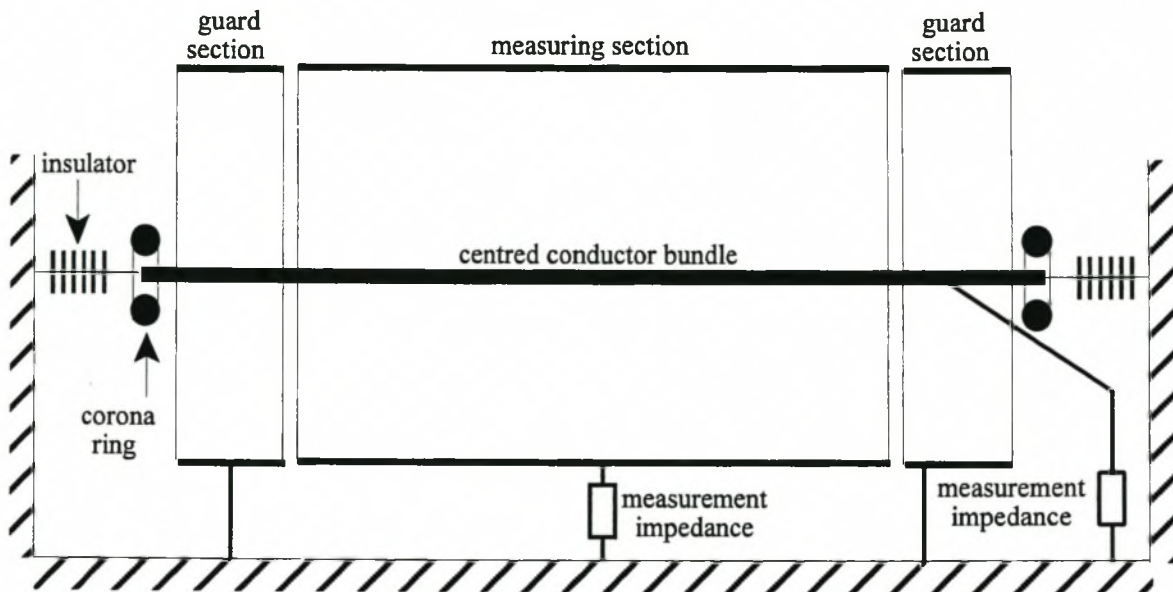
Figure 4.1: Schematic cut-away view of a typical corona cage.

A cut-away view of a typical cylindrical corona cage is illustrated in figure 4.1. The surface gradient near the unterminated ends of the centre conductor is reduced with corona rings. The corona cage is also divided into three isolated sections. The outer guard sections are grounded, thereby removing spurious corona current near the conductor ends from the measurement. The central measuring section is terminated with a measurement impedance. The generated corona current may also be measured directly off the centre conductor. The length of the guard ring section should be chosen so that the radial electric field between the measuring section and the conductor bundle is uniform along the length of the measuring section. This is discussed in [6]. The centre conductor is tensioned between two appropriately chosen insulators. This eliminates conductor sag, thereby ensuring a uniform field along the length of the conductor.

The excitation functions described in section 3.4 were obtained from narrowband measurements at 500 kHz. This is in accordance with the CISPR 18 specifications. The free space wavelength

at 500 kHz is 600 m. A cage less than 60 m long will therefore not exhibit significant wavelength effects, such as reflections from the open-circuited ends. For longer cages, e.g. [4], the centre conductor is matched to the surge impedance of the coaxial setup at the measurement frequency.

Wind increases corona activity. This is attributed, in section 2.3, to the removal of space charge produced by corona activity near the conductor surface. Under windless AC conditions, the space charge attains a steady state position due to the sinusoidally varying electric field. The maximum radius, d_m [cm], from the conductor surface at radius a [cm], of this space charge distribution is derived for a coaxial geometry under AC conditions [2]:

$$d_m^2 = a^2 + \frac{4a\mu E_c}{2\pi f} \tag{4.5}$$

In equation 4.5, μ is the space charge mobility. If the corona cage radius is less than the maximum radius defined in equation 4.5, the space charge will collide and recombine with the metallic cage. This removal of space charge will increase the corona activity just as was the case with wind. The cage radius must therefore be chosen so that space charge will not recombine with the cage under windless conditions.

4. 3   Megawatt Park Corona Cage Measurements

The excitation functions of numerous conductor bundles, under various weather conditions, were made available for the RN performance predictions of the studied lines. These excitation functions were extracted from the Megawatt Park corona cage and are similar to the measurements used to calculate the empirical excitation functions in chapter 3, since they were made in accordance with CISPR specifications. The empirical functions are however general functions defined for a wide range of conductor bundle geometries. By using the excitation function for the actual conductor bundles used on the studied lines, a more accurate prediction of the line's RN performance should be obtained, provided all significant variables are accounted for. The Megawatt Park corona cage design and the measurement protocol used in the cage are described in this section.

The Megawatt Park corona cage is a screened cylindrical cage design located in Johannesburg at an altitude of 1750 m. The visit to the facility was organised by R. Hubbard and the measurements were performed with the assistance of R. Hubbard, R. Roets and P. Tlhathletji.
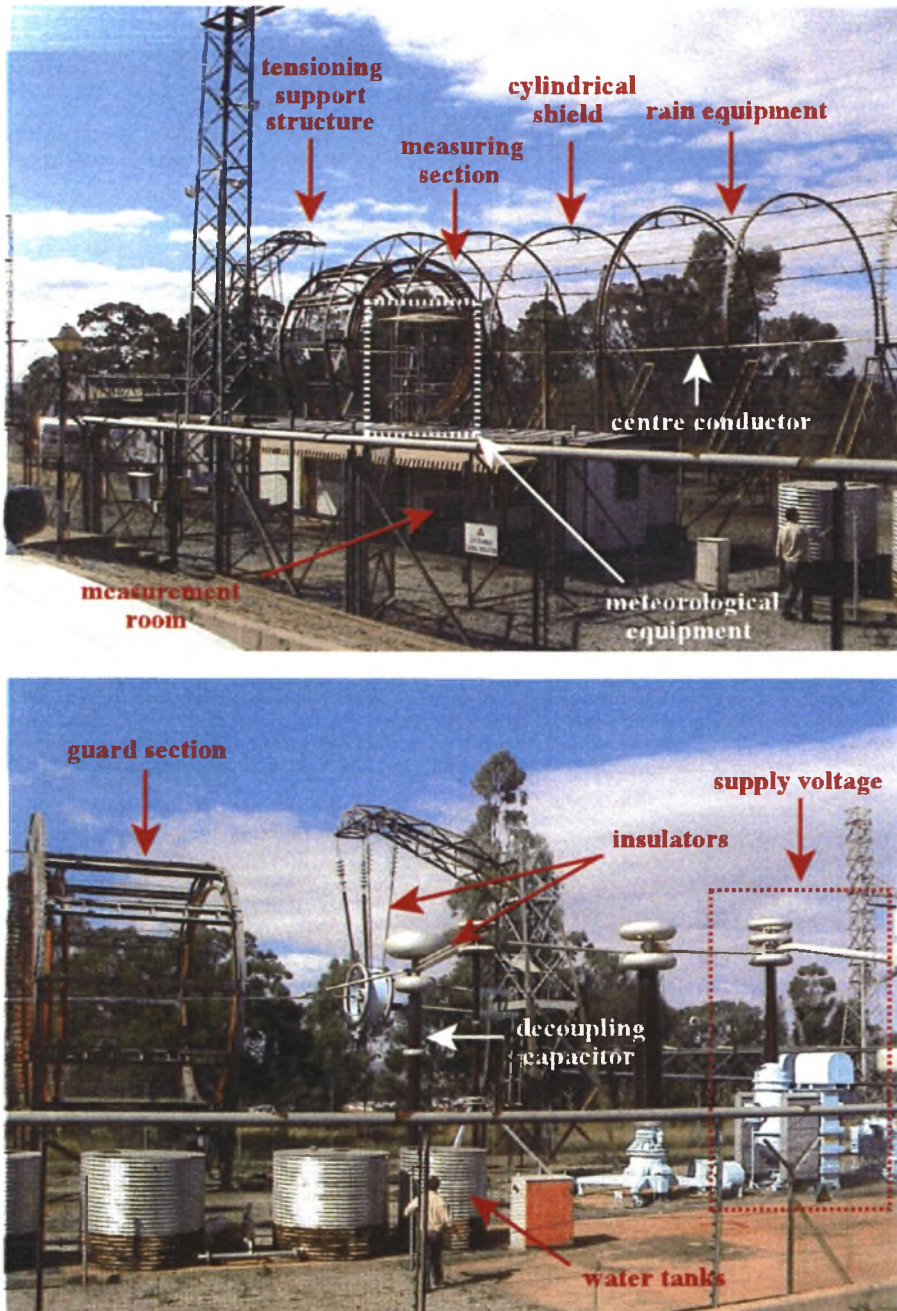
Figure 4.2: Photographs of the Megawatt Park corona cage facility.

Two photographs of the Megawatt Park corona cage are presented in figure 4.2. The various cage

components and measurement positions are indicated in the figure. The central measuring section of the cage is 30 m long. Each guard section is 5 m long and the cage radius is 3.5 m. The facility is equipped with meteorological equipment which is used to log ambient weather conditions during each measurement sequence. The conductor bundle measured is a twin IEC-800 conductor bundle. The sub-conductors are similar to the Dinosaur sub-conductors of the Acacia-Koeberg and Kriel-Tutuka transmission lines. Numerous reactive elements are used at the facility to ensure a low harmonic content in the source voltage.
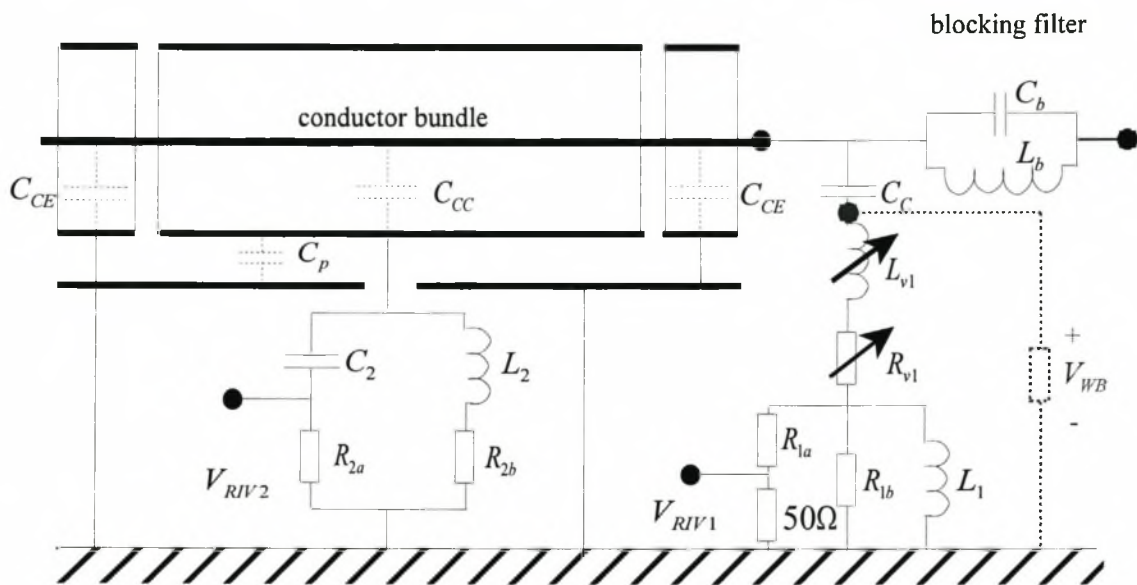
Figure 4.3: The equivalent RN measurement circuit of the Megawatt Park cage.

An equivalent circuit for the RN measurements is suggested in figure 4.3. The high voltage supply is connected to the tested conductor bundle via a blocking filter. This filter is tuned to the measurement frequency and prevents this frequency component passing through the low impedance of the supply to ground. RN measurements are made at either RIV_1 or RIV_2. V_{RIV1} is measured off the decoupling capacitor indicated in figure 4.2. The variable inductor, L_{v1}, and the variable resistor, R_{v1}, are used to match the decoupling network to the surge impedance of the conductor bundle studied. A drain coil, L_1, removes the large power frequency components from the measurement. The values of R_{1a} and R_{1b} are chosen such that the passband of the

decoupling network is centred at 500 kHz. V_{RIV2} is measured directly off the corona cage. The surge impedance of the corona cage is not affected by the bundle conductor geometry. Fixed component values are therefore used for matching. Again the component values are chosen for a centre frequency of 500 kHz. In order to investigate the feasability of making wideband measurements in the large cage setup, a wideband measurement location was sought in the narrowband measurement system in figure 4.3. The only location that was physically realizable with the equipment available is indicated in figure 4.3. In the figure, the wideband measurement, V_{WB}, is made across a wideband 50 Ω resistor placed in shunt with the RIV_1 matching network.

The measurement resistor effectively shorted out the filter characteristics of the decoupling network. The drain coil protects the wideband measurement equipment from power frequency components.
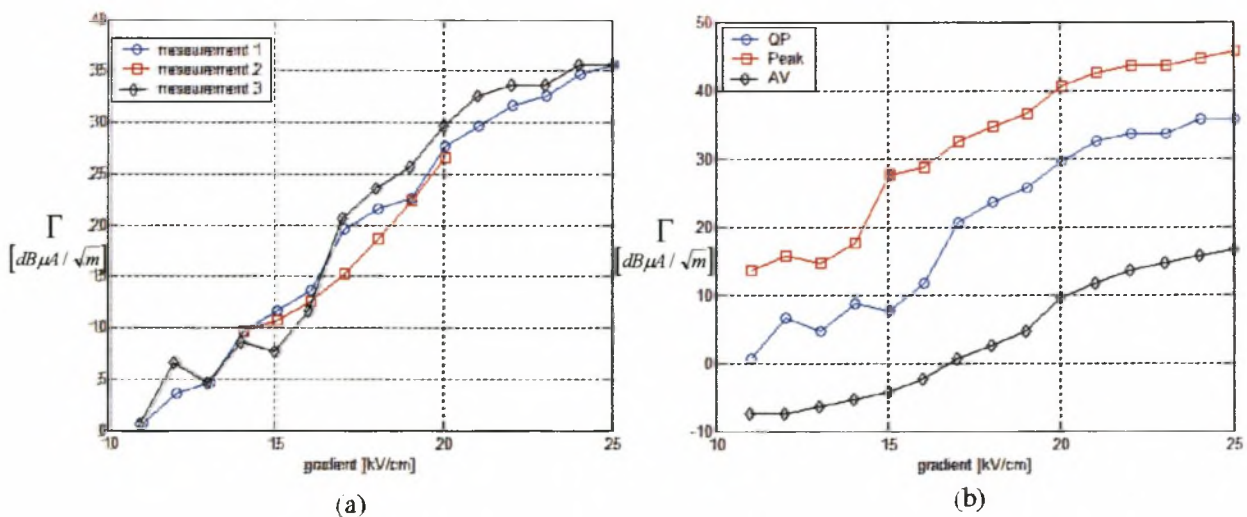
Figure 4.4: (a) Fair weather QP RN excitation function measurements and (b) measured QP, peak and average excitation functions extracted from the Megawatt Park cage.

Three fair weather RN excitation function measurement sequences were made on separate days with a QP detector at 500 kHz in a 10 kHz bandwidth. The measurements were made at RIV_1 since this was the measurement preferred by ESKOM. The excitation function is calculated from

65

the measured voltage, V_{RIV1} $[dB\mu V]$, using equation 3.5 and the transfer function of the measurement system:

$$\Gamma = V_{RIV1} - 26.4$$ (4.6)

The measurement results are plotted in figure 4.4 (a). The ambient temperatures for measurements 1 to 3 were $28\,^{o}C$, $25\,^{o}C$ and $15\,^{o}C$. The RH for each measurement was 50%, 57% and 65%. A 4 km/hr wind was measured on the third day. Foul weather excitation functions can also be measured in the cage although such measurements were not made for the conductor bundle studied over the three days. The L_{5wet} excitation function is extracted by applying uniform rain at a rate of about 2 mm/hr. The L_{50wet} level is next extracted by switching the artificial rain off and waiting 1 minute. After the minute has passed, the RN level is measured. This procedure is repeated, producing a measurement sequence of RN levels measured at one minute intervals until the RN level reaches the fair weather level. The average and peak detector RN levels were also measured on the third day. They are compared to the QP level in figure 4.4 (b).
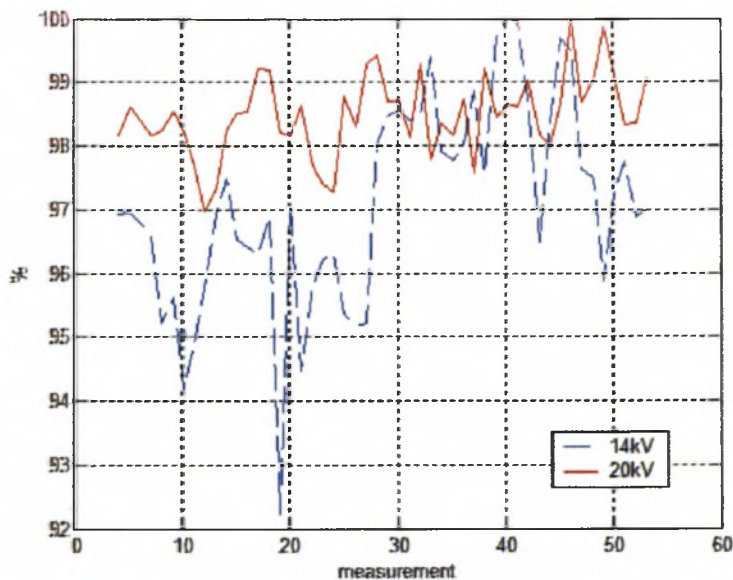
Figure 4.5: Percentage variation of the extracted excitation function from its maximum measured value at a low and a high surface gradient.

The plots in figure 4.4 indicate that the relationship between the RN level and the surface gradient is a smooth curve above about 18 kV/cm. The variation of the RN level at a single surface

66

gradient was next investigated by making 50 consecutive measurements at regularly spaced time intervals. The measured variation at 14 kV/cm and 20 kV/cm over a 5 minute period is plotted in figure 4.5. The result indicates that the variation of the measured RN is reduced from 8 % to 3 % with an increase in surface gradient from 14 kV/cm to 20 kV/cm.
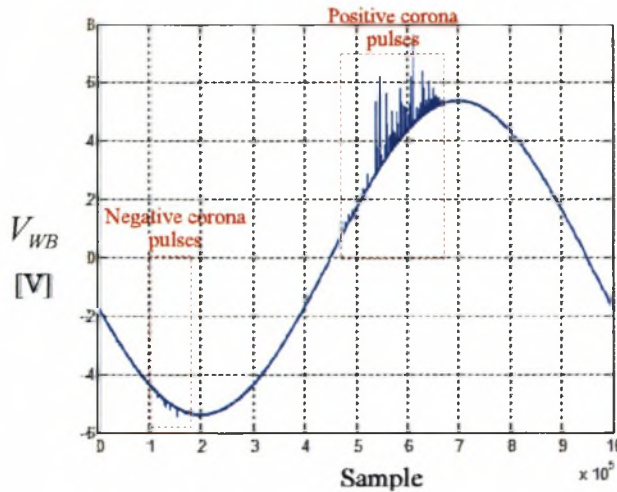
Figure 4.6: The wideband RN waveform measured on a fast sampling card at V_{WB}. The positions of the positive and negative corona pulses are indicated on the 50 Hz source voltage waveform (E_{AM} = 20 kV/cm).

The time domain waveform plotted in figure 4.6 was measured at V_{WB} in figure 4.3 at an average maximum gradient of 20 kV/cm on the twin IEC-800 bundle. The positions of the positive and negative corona pulses are indicated. Similar time domain measurements of the RN pulse train will be made in a small corona cage in the next two chapters. A method of extracting the pulse parameters from such a measurement is also described in these chapters. The number of positive and negative corona pulses observed in figure 4.6 are 78 and 15 respectively.

4. 4   The Predicted RN Performance of Lines Studied

The measured conducted RN levels presented in section 2.3 are compared to conducted RN levels predicted with the most accurate semi-analytical method for that line, as determined in section 3.7, and the conducted RN predicted with the excitation functions measured in the Megawatt Park corona cage. The results are presented in this section.
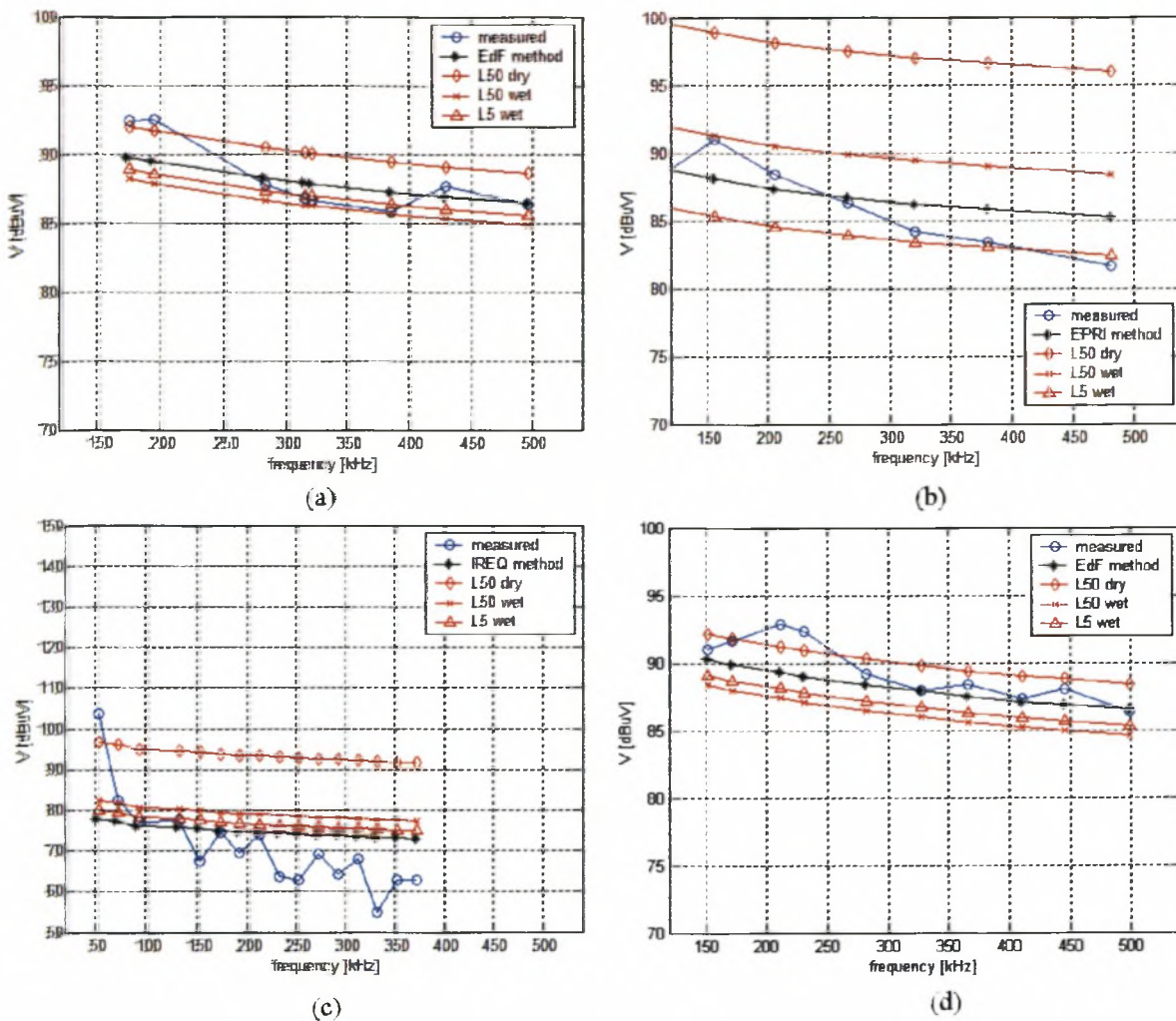
Figure 4.7: The measured and predicted conducted RN performance of (a) the Acacia-Koeberg, (b) Hydra-Droërivier, (c) Aries-Kokerboom and (d) Kriel-Tutuka lines.

The measured and predicted conducted RN levels at the Acacia, Droërivier, Aries and Tutuka substations are plotted in figure 4.7. As was the case with the semi-analytical RN predictions, only altitude, wind and RH correction factors are added to the measured excitation function predictions. It is evident in all four comparisons that the conducted RN performance is best predicted by the measured L_{5wet} excitation function. The empirical weather relations defined in section 3.6.4 are used to calculate the fair weather RN from the average and stable foul weather data. This confirms that the RN excitation function is best extracted from a corona cage under heavy rain conditions. Two possible reasons for this were identified in this chapter. They are the reduced sensitivity of the cage RN measurements to changes in environmental conditions under heavy rain and secondly, the decrease in the separation distance between pulses along the

68

line, which causes the RMS summation of current pulses to saturate to a long line current level. Since the separation distance is not known in either measurement, the accuracy of equation 3.18 in predicting short line RN levels cannot be evaluated. This calculation is important, equation 3.18 will therefore be re-derived in chapter 5 and a new method of predicting the separation distance will be proposed. This will facilitate the calculation of short line RN levels. The fair weather excitation function produced higher predictions than the heavy rain function in all four line measurements in figure 4.7. The inaccuracy of the fair weather function is attributed to increased dispersion of data under fair weather conditions and not the RN saturation effect of a short line.

The comparison between the RN performance predictions in figure 4.7 revealed that an appropriately chosen semi-analytical method produced a more accurate result for all measured lines except the Hydra-Droërivier line. This is attributed to the number of measurements used to derive both the measured cage and empirical excitations functions. Since more measurements are used for the empirical excitation function, the statistical average will have a narrower confidence interval. In chapters 2, all significant variables which influence the RN level were identified. Empirical relationships were derived in the literature for all these variables and were included in the RN prediction as correction factors. Each correction factor had a certain level of uncertainty. The overall confidence with which the RN prediction is made is therefore dependent on the variables included, the accuracy to which these variables are measured and the number of correction factors used. All the measurements included in chapter 2 were made under favourable conditions and only a few correction factors needed to be included. The RN predictions for these lines could therefore be made in chapter 3 with a high level of confidence and were within 3 dB for lines measured (c.f. figure 4.7 at 500 kHz). To obtain a high level of confidence under less favourable conditions, the RN measurement protocol proposed in chapter 2 must be strictly adhered to and the best semi-analytical method must be chosen according to the methodology proposed in appendix F.

The narrowband corona cage measurements are made at 500 kHz, as were the measurements used to derive the empirical excitation functions. The feasibility of a wideband measurement in the large corona cage was investigated in this chapter. Only one possible measurement position was

identified. This required that the filter effect of the existing measurement be removed by placing a wideband resistor in shunt with the measurement network and greatly reduced the dynamic range of the measurement. Good wideband measurements cannot therefore be made in the large corona cage. The large corona cage measurements presented in this chapter can therefore not be used to predict the frequency variation of the excitation function in the PLC band. A new experimental setup must therefore be designed for the extraction of a wideband excitation function.

It is suggested in [6] that a wideband corona model should be derived from small corona cage measurements. Small cage measurements are easier to shield and interpret. Corona cage scaling will however influence the space charge distribution and its effect on the measured RN must be investigated. It is further suggested in [6] that small cage measurements can only be used to derive excitation functions if the statistical properties of the generated pulse trains are known. These properties should be extracted from time domain measurements. The derivation and extraction of a wideband corona generation model, which can be used to calculate the frequency variation of the RN on a line, from a small corona cage is described in the next two chapters.

4. 5   References

[1]   *Transmission Line Reference Book: 345kV and Above/Second Edition*, Electric Power Research Institute (EPRI), Palo Alto, CA,1982.

[2]   P. Sarma Maruvada, *Corona Performance of High-Voltage Transmission Lines*, Research Studies Press Ltd, 2000.

[3]   F.W. Peek, *Dielectric Phenomena in High-Voltage Engineering*, McGraw-Hill, 1929.

[4]   M.G. Comber, L.E. Zaffenella, "The Use of Single Phase Test Lines and Test Cages to Evaluate the Corona Effects of EHV and UHV Transmission Lines", IEEE Trans., Vol. PAS-93, 1974, pp. 81-89.

[5]   R. Cortina, P. Nicolini, G. Frate, "A UHV Cage for the Study of Corona Phenomena", 2nd International Conference on Progress in Cables and Overhead Lines for 220 kV and Above, IEE Conference Publication No. 176, 1979, pp. 67-70.

[6]   R.G. Urban, *Modelling Corona Noise on High Voltage Transmission Lines*, MScEng Thesis, University of Stellenbosch, 2001.

Chapter 5

Extraction of a Wideband Excitation Function from a Small Corona Cage

5. 1 Introduction

The current injected on a line's conductors by corona discharges is modelled using the excitation function concept in chapter 3. A narrowband excitation function was extracted in a large cage setup in chapter 4. This excitation function was then assumed to be constant over the frequency band in which the RN performance was calculated. This assumption produced RN predictions which did not adequately describe the frequency variation of the measured RN. The frequency characteristics of the propagation and radiation models, used in conjunction with the excitation function to predict the RN, are well understood. A wideband excitation function is therefore necessary to better predict the RN performance across the required frequency band.

The bandwidth of an excitation function is limited to the frequency range over which the corona noise, generated in an electrically large corona cage, can be measured and interpreted. Such measurements are made using frequency selective devices and are susceptible to spurious noise sources. The background noise floor must therefore be considered when determining the bandwidth of the extracted excitation function. The use of a small corona cage negates many of the wavelength effects which limit this bandwidth and is easier to shield electrically, thereby reducing the ambient noise floor. Closer control over the presence and range of weather conditions is also possible in a small laboratory corona cage.

It is difficult to define an excitation function at frequencies above 30 MHz [1]. In fact, no wideband excitation function has been defined in the literature above a few MHz. A new wideband excitation function, which can be extracted from a small corona cage, is described in section 5.2. The design of a small corona cage is discussed in section 5.3. In section 5.4, the extraction of the excitation function parameters from time domain measurements is described.

71

5. 2 The Proposed Wideband Excitation Function

The basis for the derivation of an excitation function is the Ramo-Shockley theorem [2]. This theorem defines the current flow on all conductors in the vicinity of a corona discharge. Both the time and frequency domain characteristics of the current flow are described. Various parameters, deemed necessary and sufficient to described the corona current over the specified frequency band, are identified and their extraction from a measured pulse train is described. The inclusion of a narrowband corona source, derived from the wideband excitation function, into a frequency domain propagation code is then discussed.

5. 2.1 The Ramo-Shockley Theorem

Charged particles generated during a corona discharge move under the influence of the applied electric field. This movement of charge induces current flow in neighbouring conductors.

(a)   (b)
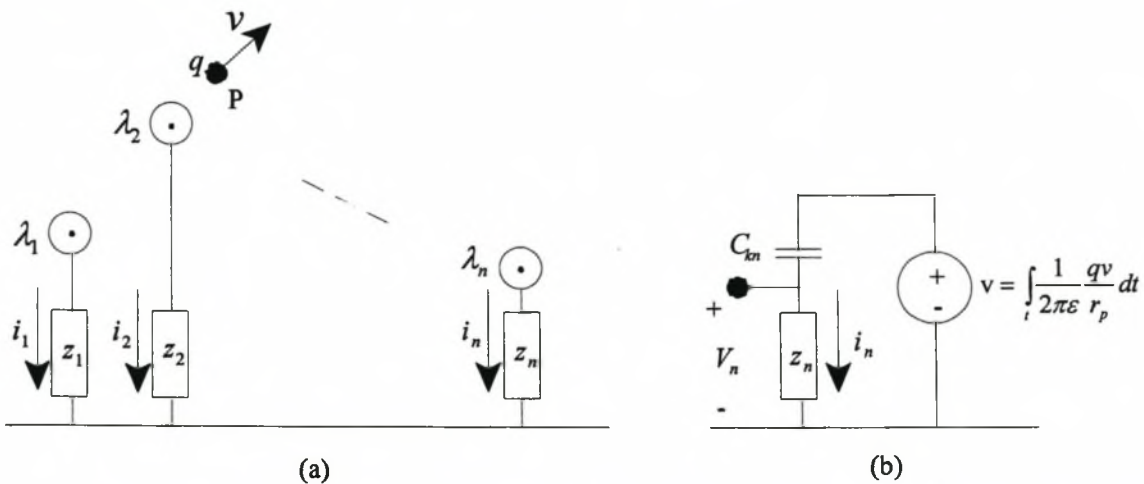
Figure 5.1: Schematic diagram of (a) a generalized n-conductor configuration and (b) the proposed corona generation model.

Considering the generalised case of a charged particle with position $P(x,y)$ and charge q travelling with velocity v in the vicinity of an arbitrary n-conductor configuration, as illustrated in figure 5.1 (a), the current induced in the n'th conductor is [2]:

$$i_n = qvE_{vn} \tag{5.1}$$

The assumptions are made in equation 5.1 that induced currents due to B-field effects are

72

negligible and that the electrostatic field propagates instantaneously. It is further assumed that $z_n = 0$ in figure 5.1. E_{vn} is the component of the electric field in the direction of v that would exist at position $P(x, y)$ if the charge was removed, a unit potential was applied to conductor n and zero potential was applied to all other conductors. The charge distribution, described by the charge on each conductor, λ_n, in this system, is [1]:

$$
\begin{bmatrix} \lambda_1 \\ \lambda_2 \\ \vdots \\ \lambda_n \end{bmatrix} = \begin{bmatrix} C_{11} & C_{12} & \cdots & C_{1n} \\ C_{21} & C_{22} & \cdots & C_{2n} \\ \vdots & \vdots & \ddots & \vdots \\ C_{n1} & C_{n2} & \cdots & C_{nn} \end{bmatrix} \begin{bmatrix} 0 \\ 0 \\ \vdots \\ 1 \end{bmatrix} = \begin{bmatrix} C_{1n} \\ C_{2n} \\ \vdots \\ C_{nn} \end{bmatrix} \tag{5.2}
$$

The value for E_{vn} is then [1]:

$$
E_{vn} = \frac{1}{2\pi\varepsilon} \sum_{k=1}^{n} \frac{\lambda_k}{r_{pk}} = \frac{1}{2\pi\varepsilon} \left[\frac{C_{1n}}{r_{p1}} + \frac{C_{2n}}{r_{p2}} + \ldots + \frac{C_{nn}}{r_{pn}} \right] \tag{5.3}
$$

In equation 5.3, r_{pn} is the distance between the n'th conductor's centre and P. The contribution of each charge in the discharge is calculated using equations 5.1 to 5.3 and then summed together to determine the total current. It should be noted however that the most significant source of RN on transmission line conductors is due to the movement of high velocity electrons concentrated in a point-element size discharge head near the conductor surface. Only the contributions from these point-element electron concentrations need therefore be considered for RN studies. For a corona discharge near the surface of conductor k, it can be assumed for practical transmission line geometries that:

$$
r_{pk} << r_{pn} \quad , n \neq k \tag{5.4}
$$

The current flow on conductor n due to a corona discharge near conductor k, under this assumption , simplifies to:

$$i_n = C_{nk} \frac{d}{dt}(v_c)$$

(5.5)

where:

$$v_c = \frac{1}{2\pi\varepsilon} \int \frac{q_k \cdot v}{r_{pk}} dt$$

(5.6)

Corona generation is therefore modelled as a voltage source, v_c, capacitively coupled to the conductors. It is evident in equation 5.6 that the value of v_c is dependent on the position, velocity and charge of the point charge element and not the line geometry. The circuit element can therefore be extracted from a corona cage and applied to a transmission line.

5. 2.2   Time and Frequency Domain Corona Pulse Descriptions

The pulse shape of the various corona modes is described by a double exponential function [3]:

$$v_c(t) = Kv_p\left(e^{-\alpha t} - e^{-\beta t}\right)$$

(5.7)

The pulse parameters, v_p, α and β are influenced by discharge conditions and vary randomly. The peak pulse amplitude occurs at $t = t_p$ such that $d/dt\left[v_c(t)\right]_{t=t_p} = 0$:

$$t_p = \left(\ln\beta - \ln\alpha\right)/\left(\beta - \alpha\right)$$

(5.8)

The parameter, K, is introduced in equation 5.7 so that the peak value at $t = t_p$ is v_p, the

measured peak pulse amplitude. The value of K is therefore:

$$K = \left(e^{-\alpha t_p} - e^{-\beta t_p}\right)^{-1} \tag{5.9}$$

The time between two successive pulse peaks in a corona pulse train is another important parameter which varies randomly and is termed the repetition rate. AC conditions affect the discharge conditions and therefore also the pulse parameters. The random variation of the pulse parameters during a single period of the 50 Hz source voltage has been investigated in [4]. Here it was found that the pulse amplitude, v_p, varies randomly with a normal distribution while the repetition rate varies randomly with an exponential distribution. The normal distribution is described by a mean, μ, and a standard deviation, σ, while the exponential distribution is described by a minimum value, a, and an average value, b. It will be assumed for now that the values of α and β also vary with a normal distribution. This will be verified in section 5.4. Under AC conditions and these assumptions, the time domain description of a corona pulse is:

$$v_c(t) = Kv_p(\mu_i,\sigma_i)\left\{e^{-[\alpha(\mu_\alpha,\sigma_\alpha)]\cdot[t-t_0(a,b)]} - e^{-[\beta(\mu_\beta,\sigma_\beta)]\cdot[t-t_0(a,b)]}\right\} \tag{5.10}$$

The frequency domain representation of the corona pulse is obtained by calculating the Fourier transform of equation 5.10:

$$v_c(\omega) = Kv_p(\mu_p,\sigma_p)\left\{\frac{\beta(\mu_\beta,\sigma_\beta) - \alpha(\mu_\alpha,\sigma_\alpha)}{[\alpha(\mu_\alpha,\sigma_\alpha) + j\omega][\beta(\mu_\beta,\sigma_\beta) + j\omega]}\right\}e^{-j\omega t_0(a,b)} \tag{5.11}$$

The various random distributions in equations 5.10 and 5.11 must next be extracted from small corona cage measurements.

5. 2.3 Corona Pulse Parameter Extraction

Corona pulses do not occur in isolation in a corona cage, but rather they occur as a pulse train.

The extraction of individual pulse parameters from such a pulse train using both time domain and frequency domain techniques is described in this section.

5. 2.3.1 Time Domain Extraction

Known pulse parameters are first extracted from a theoretical pulse train of three identical pulses in order to verify the validity of the extraction method. The pulse parameters used for the pulse train are typical of the mean pulse parameters measured in a small corona cage.
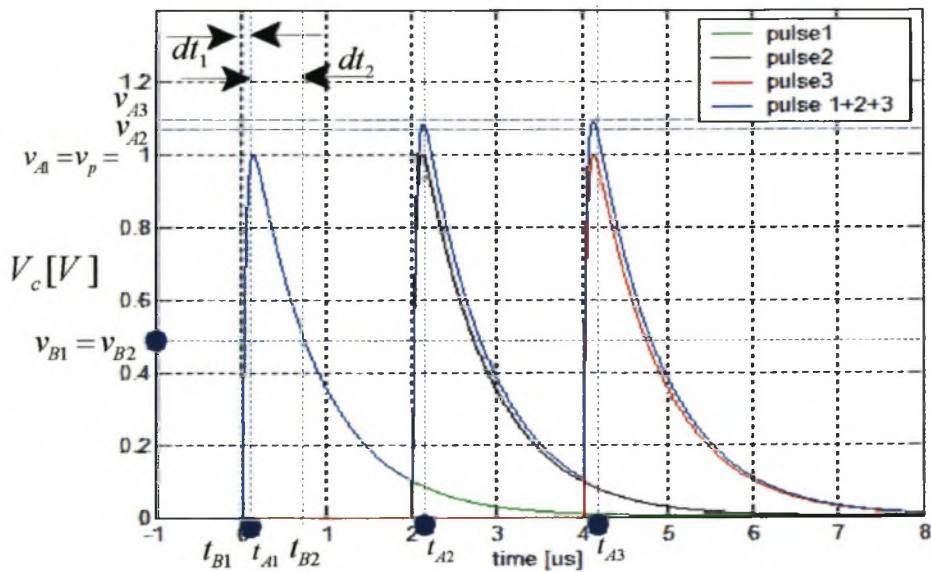
Figure 5.2: A theoretical corona pulse train ($v_p = 1$, $f_\alpha = 200$ kHz, $f_\beta = 4$ MHz).

A time domain corona pulse train, $v_c(t)$, is plotted in figure 5.2. The pulse shape and repetition rate is typical of positive corona. It is evident that the characteristics of an individual pulse cannot be extracted directly from the pulse train since the total current is the summation of all current pulses. All pulses must be considered. The peak of the first pulse is $v_{p1} = v_{A1}$. A second level, $v_{B1} = v_{B2} = 0.5v_{p1}$, is next chosen and lead and lag times, $t_{B1} = t_{p1} - dt_1$ and $t_{B2} = t_{p1} + dt_2$, are extracted. The values of α_1 and β_1 are then calculated by iteratively solving for:

$$\frac{e^{-\alpha_1.dt_2} - e^{\alpha_1.dt_1}}{\alpha_1} = \frac{e^{-\beta_1.dt_2} - e^{\beta_1.dt_1}}{\beta_1} \tag{5.12}$$

76

and for t_{p1}, defined in equation 5.8. The parameters of the n'th pulse are similarly obtained.

The individual pulse amplitudes are calculated from the observed pulse train peaks:

$$v_{pn} = v_{An} - \sum_{k=1}^{n-1} K_k . v_{Ak}\left[e^{-\alpha_k\left(t_{An} - t_{Ak} + t_{pk}\right)} - e^{-\beta_k\left(t_{An} - t_{Ak} + t_{pk}\right)} \right] \qquad (5.13)$$

Next, $t_{B1} = t_{An} - dt_1$ is chosen and v_{B1} is calculated:

$$v_{B1} = v_c(t_{B1}) - \sum_{k=1}^{n-1} K_k . v_{Ak}\left[e^{-\alpha_k\left(t_{B1} - t_{Ak} + t_{pk}\right)} - e^{-\beta_k\left(t_{B1} - t_{Ak} + t_{pk}\right)} \right] \qquad (5.14)$$

The value of $t_{B2} = t_{An} + dt_2$ is then found iteratively such that:

$$v_{B2} = v_{B1} = v_c(t_{B2}) - \sum_{k=1}^{n-1} K_k . v_{Ak}\left[e^{-\alpha_k\left(t_{B2} - t_{Ak} + t_{pk}\right)} - e^{-\beta_k\left(t_{B2} - t_{Ak} + t_{pk}\right)} \right] \qquad (5.15)$$

Finally, the values of α_n and β_n are calculated by iteratively solving for:

$$v_{Bx} = v_{pn}\left[e^{-\alpha_n t_{Bx}} - e^{-\beta_n t_{Bx}} \right]\left[e^{-\alpha_n t_{pn}} - e^{-\beta_n t_{pn}} \right]^{-1}; x = 1,2 \qquad (5.16)$$

and equation 5.12. Implicit to equation 5.14 and therefore the extraction method is the approximation, $t_{An} \approx t_{pn}$. This is valid for the measured repetition rate range.

5. 2.3.2 Frequency Domain Extraction

The Fourier transform of a single isolated pulse was defined in equation 5.11. This will be considered first. The magnitude of the Fourier transform, in dB, is:

$$|v(\omega)| = 20\log_{10}\left[K.v_p \frac{\beta - \alpha}{\sqrt{(\beta^2 + \omega^2)(\alpha^2 + \omega^2)}} \right] \qquad (5.17)$$

Equation 5.17 can be simplified for various frequency regimes [1]:

$$
|v(\omega)| = \begin{cases} 20\log_{10}\left[K.v_p\dfrac{\beta-\alpha}{\beta\alpha}\right] & ,\omega << \alpha, \omega << \beta \\[4em] 20\log_{10}\left[K.v_p\dfrac{\beta-\alpha}{\beta\alpha}\right] - 20\log_{10}\left[\dfrac{\omega}{\alpha}\right] - 3 & ,\omega \approx \alpha, \omega << \beta \\[4em] 20\log_{10}\left[K.v_p\dfrac{\beta-\alpha}{\beta\alpha}\right] - 20\log_{10}\left[\dfrac{\omega^2}{\alpha\beta}\right] - 3 & ,\omega \approx \beta, \omega >> \alpha \end{cases}
\tag{5.18}
$$

The values for α and β are therefore obtained by finding the radian frequency at which the magnitude spectrum is 3 dB and $[3 + 20\log_{10}(\beta/\alpha)]$ dB below the DC spectrum respectively. At these frequencies, the frequency spectrum decreases by 20 dB/decade and 40 dB/decade.
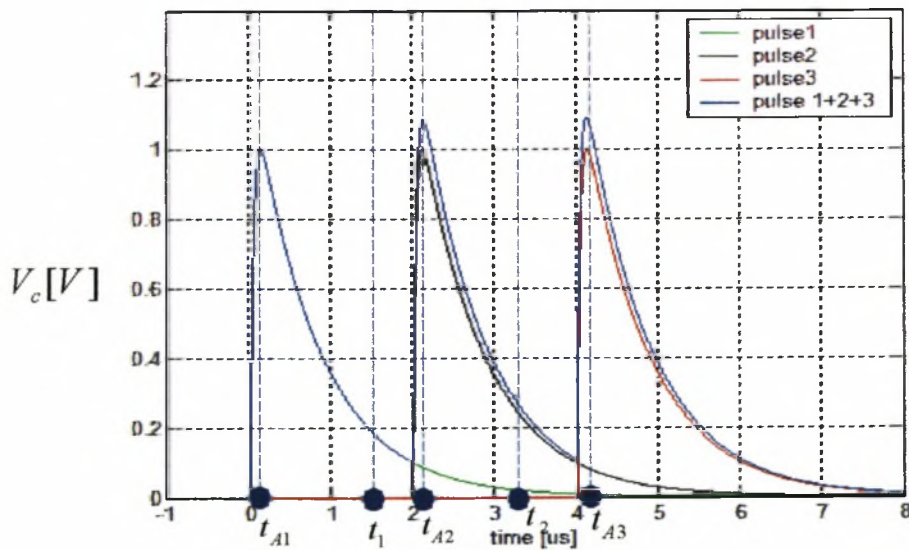
Figure 5.3: A theoretical corona pulse train ($v_p = 1, f_\alpha = 200$ kHz, $f_\beta = 4$ MHz).

A theoretical pulse train is again used to establish a valid extraction method. The magnitude of

the Fourier transform of the pulse train waveform, $v_c(t)$, comprising n pulses is:

$$\left| v_c(\omega) \right| = \sum_{k=1}^{n} K_k . v_{pk} \left[\frac{\beta_k - \alpha_k}{\sqrt{\left(\alpha_k^2 + \omega^2\right)\left(\beta_k^2 + \omega^2\right)}} \right] \tag{5.19}$$

It is evident in equation 5.19 that the parameters of individual pulses cannot be isolated from the frequency spectrum of the entire pulse train. The parameters of the n'th corona pulse are isolated by calculating the Fourier transform over a selected time period which includes the peak of only the n'th pulse. The magnitude of the frequency spectrum then becomes:

$$\left| v(\omega) \right| = \sum_{k=1}^{n} K_k . v_{pk} \left[\frac{F_k}{\sqrt{\left(\beta_k^2 + \omega^2\right)\left(\alpha_k^2 + \omega^2\right)}} \right] \tag{5.20}$$

$$F_k = \left| \left(\beta_k + j\omega\right)e^{-\alpha_k(t - t_{Ak} + t_{pk})} - \left(\alpha_k + j\omega\right)e^{-\beta_k(t - t_{Ak} + t_{pk})} \right|_{t_2}^{t_1} \tag{5.21}$$
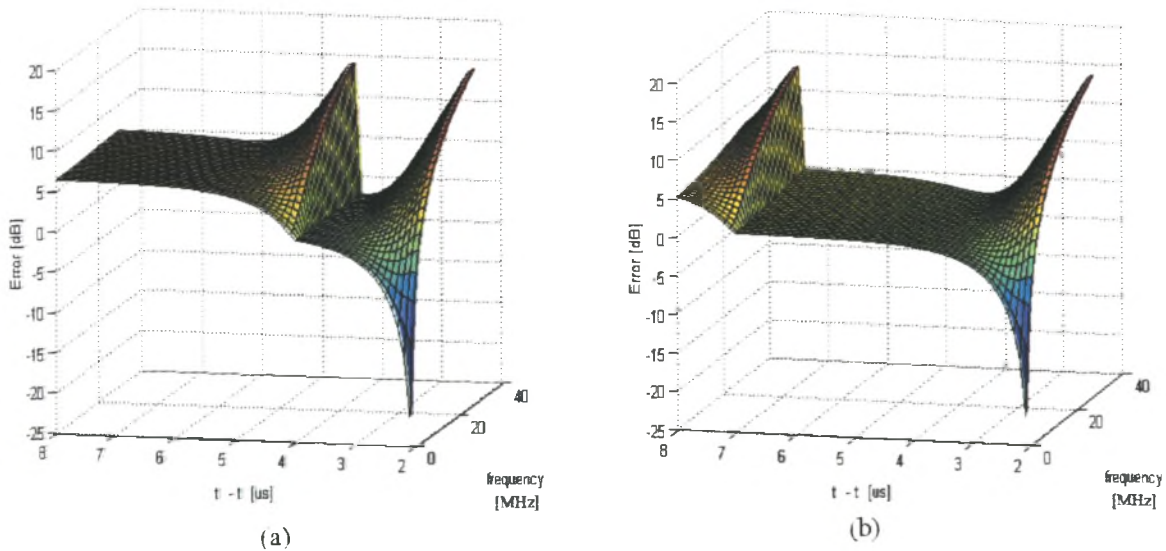
Figure 5.4: A surface plot of the dB difference between the magnitude spectrum of pulse 2 in figure 5.3 and the approximate spectrum calculated between points t_1 and t_2 for repetition times of (a) 2 µs (i.e. as in figure 5.3) and (b) 5 µs.

79
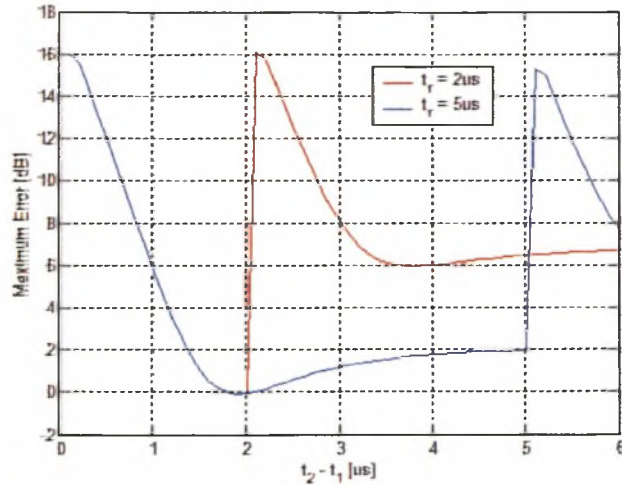
Figure 5.5: A 2-D plot of the maximum dB difference across the band 0 to 30 MHz, between the magnitude spectrum of pulse 2 in figure 5.3 and the approximate magnitude spectrum calculated between points t_1 and t_2 for various repetitions times.

The magnitude spectrum of the pulse train is calculated using equations 5.20 and 5.21 and is compared to the magnitude spectrum of an isolated pulse, pulse 2 in figure 5.3. The error made by calculating the Fourier transform over a finite specified time interval is plotted in figures 5.4 and 5.5 for two repetition times, $t_r = 2\mu s$ (as in figure 5.3) and $t_r = 5\mu s$. In these plots, $t_1 = t_{An} - t_{pn}$ and t_2 is varied. The plots indicate that in order to extract the parameters of an individual pulse using this method the values of t_1 and t_2 must be chosen such that:

$$t_1 = t_{An} - t_{pn} \tag{5.22}$$

$$t_1 + 20.t_{pn} < t_2 < t_1 + \left(t_{A(n+1)} - t_{p(n+1)}\right) \tag{5.23}$$

This will result in a maximum difference between the actual and approximate pulse magnitude spectra of less than 2 dB across the frequency band 0 to 30 MHz.

80

5. 2.4 Narrowband Radio Noise Measurements

RN Measurements are made on a line with a narrowband RN meter and either a QP, RMS or average detector. An equivalent voltage source element must therefore be derived from the model defined in equation 5.11 for the specified meter bandwidth and detector type.
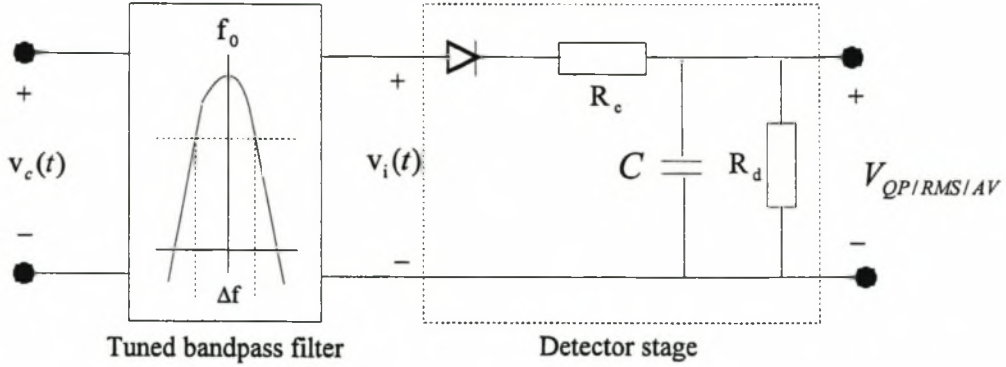
Figure 5.6: Schematic diagram of a typical RN meter (after [5]).

The QP, RMS and average levels of an ideal RN meter, such as illustrated in figure 5.6, were derived for a corona pulse train, $v_c(t)$, in [5]:

$$V_{QP} = \frac{R_d}{R_c} \int_{V_i=V_{QP}}^{\infty} (V_i - V_{QP}) p(V_i) dV_i \tag{5.24}$$

$$V_{RMS} = \sqrt{\int_0^{\infty} V_i^2 p(V_i) dV_i} \tag{5.25}$$

$$V_{AV} = \int_0^{\infty} V_i p(V_i) dV_i \tag{5.26}$$

In equations 5.24 to 5.26, $V_i(t)$ is the positive waveform envelope at the output of the tuned bandpass filter, which is implemented using an ideal bandpass algorithm. In the equations, $p(V_i)$ is its amplitude probability density function (pdf). The analytical determination of $p(V_i)$

81

for a waveform with normal amplitude and exponential repetition time distributions is very complex. A digital simulation method was therefore used in [5]. This method samples the filter output waveform once in each repetition time. The n 'th sample time is [5]:

$$t_{sn} = y_{in}.dt_n \qquad (5.27)$$

In equation 5.27, y_{in} is the n 'th element of the uniformly distributed random variable Y_i and dt_n is the repetition time between the n 'th and $n + 1$ 'th pulses.

5. 2.5   Corona Source Injection on a Transmission Line

The calculated narrowband voltage source element must next be applied to a transmission line.
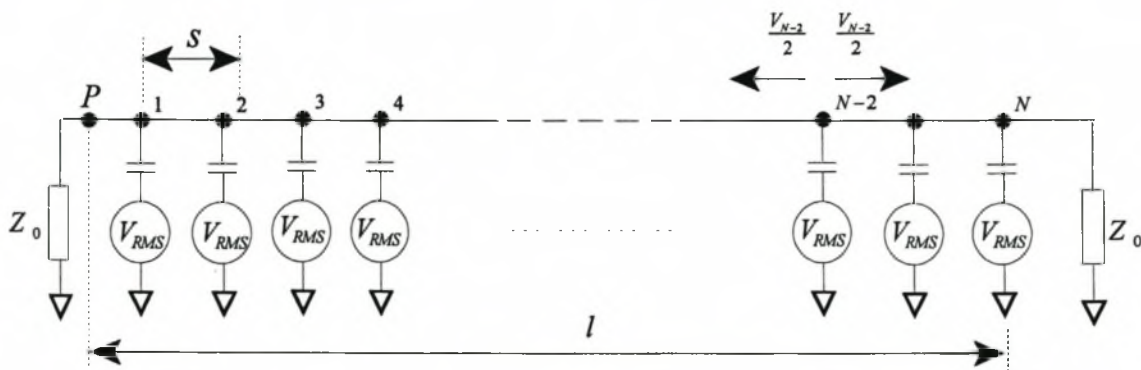
Figure 5.7: Schematic diagram of a two conductor transmission line with N corona sources separated by distance s.

In the case of a uniform two wire transmission line, such as the one illustrated in figure 5.7, individual corona sources occur at uniformly distributed positions along the length of the line and are statistically independent. The separation distance between the sources is:

$$s = l/(N-1) \qquad (5.28)$$

The RN model presented in figure 5.1 (b), including the narrowband RMS voltage defined in equation 5.25 (i.e. $v = V_{RMS}$), and with $C_{kn} = C$ and $z_n = Z_0$, is inserted at each injection point. Since the line is assumed to be terminated in its surge impedance at both ends, corona

injection at any point along the line will result in equal energy propagation in both directions as illustrated in figure 5.7. Since the sources are random and statistically independent, the voltage measured across the two conductors at point P is:

$$V_P = \sqrt{\sum_{k=1}^{N} \left[V_n e^{-\alpha_l (2k-1)s/2} \right]^2} \tag{5.29}$$

In equation 5.29, α_l is the attenuation constant for the two wire transmission line. It was noted in the previous section that V_n has a normal distribution. The linear summation of N such sources will therefore also be normally distributed with the mean and pooled variance of the summation equal to the mean and variance of the individual sources, if they are identical [6]:

$$\sum_{k=1}^{N} V_n (\mu, \sigma) = n.V (\mu, \sigma) \tag{5.30}$$

where:

$$V = \frac{1}{2} \left[\frac{j\omega C Z_0}{1 + j\omega C Z_0} \right] V_{RMS} \tag{5.31}$$

In equation 5.29, $N \gg 1$ for a realistic transmission line. Noting this, the voltage at P can be derived from equations 5.29 and 5.30 as:

$$V_p \approx V_{RMS} \sqrt{\left(1 - e^{-\alpha_l l}\right) / \sinh(\alpha_i s)} \tag{5.32}$$

The derivation of equation 5.32 is presented in appendix G. The noise voltage can therefore be calculated at any point along the length of the line with equation 5.32 if the line length, number of corona sources and the line attenuation are known. In this way the conducted and radiated RN of a transmission line can be calculated from a wideband excitation function extracted from small corona cage measurements.

5. 3   Small Corona Cage Design

Large corona cages are designed for the extraction of an excitation function under specified weather conditions, as discussed in chapter 4. The measured RMS level is a function of the frequency dependent line attenuation. The cage is therefore calibrated at the measurement frequency. The RMS level is also dependent on the cage length and the number of corona sources. This usually limits the validity of large cage excitation function to heavy rain conditions. Under these conditions, $\alpha_i s << 1$ and $\sinh(\alpha_i s) \approx \alpha_i s$. The excitation function is then a saturated value which is proportional to the inverse of the square root of the line attenuation. In a small corona cage, $\alpha_i l << 1$ and equation 5.32 simplifies to:

$$V_{cage} = \lim_{\alpha_i l \to 0} \left(V_P\right) = V.\sqrt{N} \qquad (5.33)$$

The measured voltage is therefore not dependent on the frequency dependent line attenuation. The measured frequency spectrum is then an accurate account of the frequency spectrum of an individual corona pulse. Small corona cage measurements can therefore be used to extract the wideband excitation function described in section 5.2. The design and calibration of a suitable small corona cage is discussed in this section.

5. 3.1   Defining the Design Specifications

The corona noise model presented in figure 5.1 (b) is only valid if the discharge conditions near the surface of the transmission line conductors are exactly replicated in the corona cage. The parameters influencing the discharge processes must therefore be reproduced in the cage. Spurious non-corona noise will reduce the dynamic range of the measurement system and impede the extraction of the model parameters from the cage measurements. Noise from corona discharges on conductors other than the cage's centre conductor will lead to the extraction of inaccurate and misleading data. These spurious corona sources must therefore be eliminated. The corona cage construction must be light-weight and versatile so that it can easily be set up in an arbitrary location. The centre conductor must be changed with ease so that either smooth or stranded single conductor and bundled conductor configurations can be fitted in the cage.

5. 3.2   Identifying the Influencing Parameters

The electric field and space charge distributions in the inter-electrode region must be calculated since these parameters influence the discharge processes. The source of corona discharges in a corona cage is the instantaneous electric field at the surface of the energized centre conductor. The RN excitation function described by equation 5.6 is dependent on the position, velocity and charge of the corona discharge. If it is assumed that the momentum of an electron in the presence of a strong electric field is not significant then the position and velocity of the discharge is determined entirely by the instantaneous electric field in the discharge region (i.e. near the conductor surface). Heavier, slower-moving space charge is produced during corona discharge by both the attachment and removal of electrons from neutral air molecules. These molecules do not directly affect the RN current induced in the conductors, but they do affect the electric field distribution in the discharge region and therefore indirectly affect the RN current. Environmental factors which also affect the discharge processes were identified in chapter 2. Weather conditions such as precipitation, wind and the presence of air-borne pollutants are easily removed from the laboratory. Only the RAD and RH are not controllable and must be monitored.

The electric field at radius r [cm] from the centre of a corona cage of radius R [cm] is defined for a centred conductor of radius a [cm] and source voltage V [kV] as [1]:

$$E_r = \frac{V}{r \ln(R/a)} \quad \text{[kV/cm]} \tag{5.34}$$

The radial electric field described by equation 5.34 is highly divergent near the conductor surface. The field divergence will affect the distance which a corona discharge can propagate into the gap before it is extinguished. The divergence of the electric field described by equation 5.34 is:

$$\nabla . \mathbf{E} = \frac{V}{\ln(R/a)} \left[\frac{1}{r^2} \right] \tag{5.35}$$

To calculate the electric field distribution for the more general case of an n-conductor bundle placed at an arbitrary position inside the cage, the method of successive images [7] is used. Each

conductor and its image are represented by a set of line charges, λ_i, which maintain the equipotential at the conductor's surface, in this method. To calculate the electric field distribution inside the cage, the coaxial geometry is first transformed to an equivalent conductor-plane geometry using a geometric inversion [7]. The conductor images are then calculated and the geometry is converted back to the coaxial geometry.
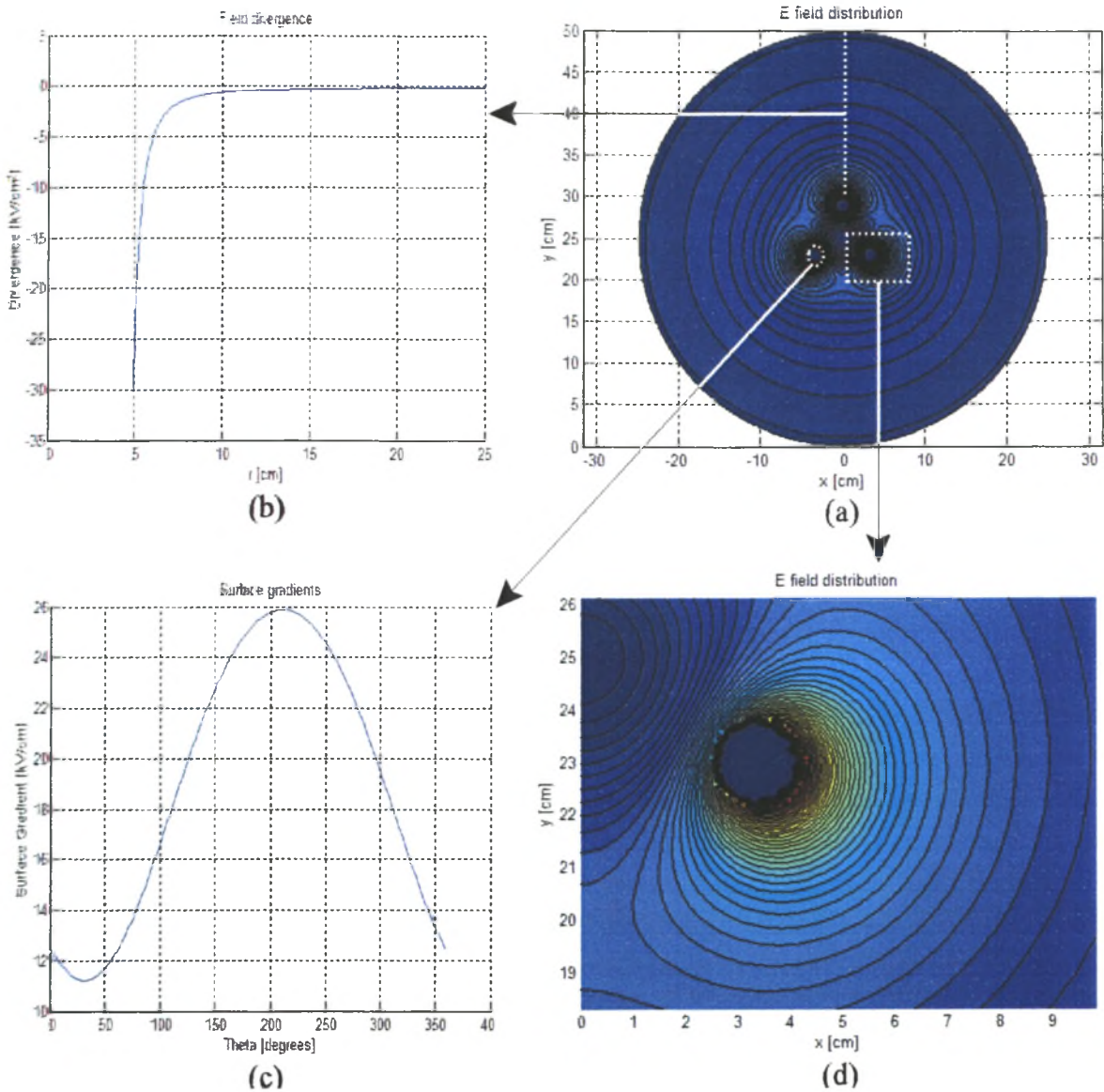
Figure 5.8: The method of successive images is used to extract (a) the electric field distribution, (b) the electric field divergence and (c) the surface gradient for a centred three conductor bundle ($R_{cage} = 25$ cm, $R_{bundle} = 3.9$ cm, $r = 0.78$ cm).

The number of line charges used to represent each conductor determines the accuracy of the solution. The calculated electric field converges to the exact solution for an infinite number of

line charges. This convergence is rapid and in most cases a low order approximation produces an acceptable accuracy. The field at any point, p, in the inter-electrode gap is calculated from the line charge distribution determined for the cage setup [7]:

$$\mathbf{E}_p = \frac{1}{2\pi\varepsilon_0} \sum_{k=1}^{n} \frac{\lambda_k}{\left|\mathbf{r}_{kp}\right|^2} \cdot \mathbf{r}_{kp} \qquad (5.36)$$

In equation 5.36, $\mathbf{r}_{kp}$ is the displacement between the k'th line charge and the field point. A correlation between the RN level and both the average maximum surface gradient and the electric field divergence near the surface of a conductor bundle was identified in the prediction methods described in chapter 3. These parameters are therefore extracted from the successive images simulation as illustrated in figure 5.8. Since the line charges are calculated for each conductor at a specified source voltage in the simulation, the partial capacitances of the multi-conductor system are also extracted. It should be noted that the parameters extracted from the simulation are obtained in the absence of space charge in the inter-electrode gap. The space charge distribution and its influence on the electric field distribution must also be determined.

A steady-state space charge distribution exists inside the corona cage under AC conditions in the absence of an irregular wind. The corona activity during one 50Hz cycle can therefore be considered statistically independent of the corona activity in previous cycles. This is an important assumption for the extraction of the wideband excitation function. The maximum distance travelled by space charge in an AC system was defined in equation 4.5. The mobility of the positive and negative space charge has been measured at STP as $\mu_+ = 1500$ [cm^2/kV.s] and

$\mu_- = -1800$ [cm^2/kV.s] [8]. Space charge may recombine and will therefore be lost to the system if it reaches the corona cage. This will disrupt the steady-state and the assumption of statistical independence will no longer be valid. By coating the corona cage with an insulating paint, recombination is prevented and a steady state is again restored. The new steady-state space charge position will however have changed and will affect the discharge processes.

A simplified model is presented in [8] to predict the quantity and position of the space charge in the inter-electrode gap for a smooth conductor positioned at the centre of the cylindrical corona cage. The implementation and use of this model is discussed in [9]. This model is extended to the general case of a smooth conductor bundle placed at an arbitrary position inside the corona cage in the remainder of this section.

The space charge distribution is approximated by discretizing the inter-electrode gap into a uniformly spaced grid. The movement of space charge between the grid points is calculated using the displacement law described in [8]:

$$d\mathbf{r} = \mu(\mathbf{E}_s + \mathbf{E}_q)dt \tag{5.37}$$

The applied electric field, $\mathbf{E}_s$, is calculated at each point using the method of successive images described previously. The electric field due to the space charge distribution, $\mathbf{E}_q$, is also calculated at each point by considering the contribution of each individual space charge and then, using the principle of superposition, summing these contributions together.

The charge and position of the emitted charge layer is described by an emission law. The emission law used in [8] states that the total charge on a conductor cannot exceed a critical inception value. The inception charge value of the n'th conductor, which has a radius a [cm], is [8]:

$$Q_{cn} = C_n . E_{cn} . \left[a \ln(R/a)\right] \tag{5.38}$$

In equation 5.38, E_{cn} is the conductor's inception gradient defined in equation 4.4. The total charge on each conductor is the sum of the charge provided by the voltage source, the space charge which recombines onto the conductor and the charge induced on the conductor by the space charge. Each conductor is discretized with a set of N points uniformly spaced around its circumference. The distribution of surface charge, σ_q, induced by the space charge at each of

these points, is calculated with Gauss' continuity condition by noting that the radial and azimuthal electric fields in a conductor are zero, thereby creating an electric field discontinuity at the conductor surface [10]:

$$Q_{induced} = \int_0^{2\pi} \sigma_q(r,\theta)d\theta \approx \sum_{n=1}^{N} \left[-\varepsilon_0 E_r - \varepsilon_0 E_\theta \right] \qquad (5.39)$$

If space charges are emitted at the discretized conductor surface, the positions of the emitted charges are calculated with a modified displacement law [8]:

$$d\mathbf{r} = a\sqrt{1 + \left[\mu(\mathbf{E}_s + \mathbf{E}_q)dt \right]/a} \qquad (5.40)$$

This modified displacement law describes the movement of the space charge formed in the discharge region where the electric field is distorted by the space charge field. The Maxwell potential functions of the emitted charges, P_e, the line charges describing the applied voltage, P_s, and the space charges at the surface grid points, P_q, are calculated using the principle of superposition. The contribution of each charge is calculated by generating an image charge in each conductor using the method of successive images and a geometric inversion. The Maxwell potential function of the n'th space charge and its images in the $N - 1$ conductors at the k'th grid point is [7]:

$$P_{kn} = \frac{1}{2\pi\varepsilon_0} \sum_{i=1}^{N} \frac{r_{ngi}}{\left| \mathbf{r}_{nki} \right|} \qquad (5.41)$$

In equation 5.41, r_{ng} is the distance between the charge and the reference potential plane and $\mathbf{r}_{nk}$ is the displacement between the charge and the grid point. The charge content of the emitted

space charge, Q_{ek}, is calculated from the emission law and the calculated potential:

$$[Q_e] = [P_e]^{-1}([\Phi_c] - [P_s][\lambda_s] - [P_q][Q_q])$$
(5.42)

Finally, a recombination law is required so that the charge can be calculated at a grid point should charges of opposite polarity be displaced to it. The recombination law in [8] states that the amount of charge that recombines during such a collision is proportional to the relative velocity of the charges. From the displacement law in equation 5.37, and recognising that the electric field is the same for both charges at a grid point, the amount of recombined charge during a collision is proportional to the ratio of the charge mobilities already defined.
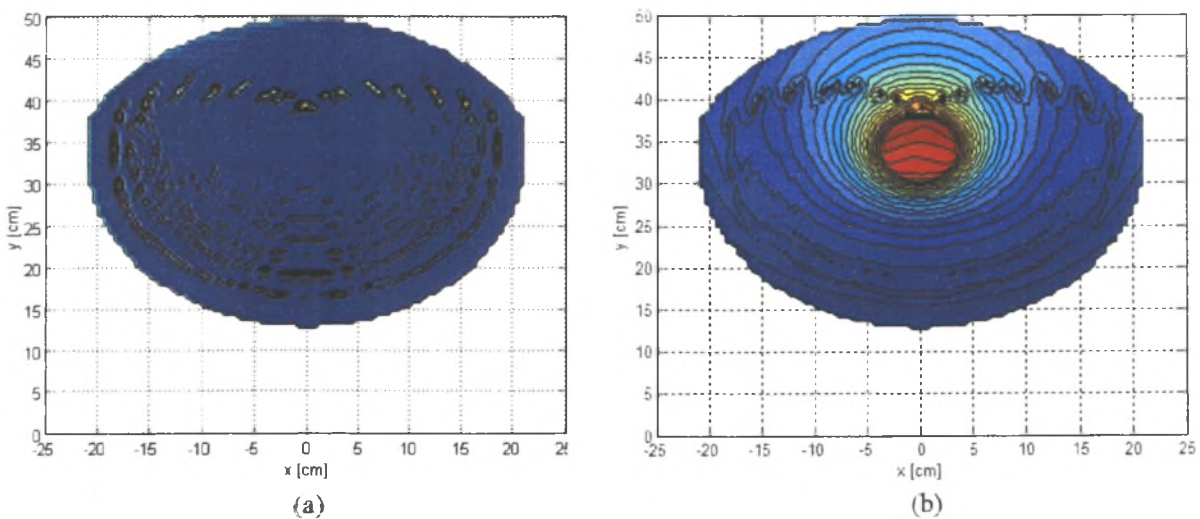
Figure 5.9: The calculated (a) space charge distribution and (b) actual electric field distribution in a corona cage including space charge effects ($R_{cage} = 25$ cm, $r = 0.78$ cm).

The accuracy of the space charge simulation method described above and used to obtain the results presented in figure 5.9 is verified by comparing the calculations to measured Q-V curves. A Q-V measurement protocol is described in [9].

The divergent radial electric field must be uniform along the length of the cage. This ensures uniform corona generation along the entire length of the cage and was discussed in chapter 4. Beyond the cage, the field must be below the corona inception level, thus excluding spurious

corona pulses from the measurements. Guard rings are used to obtain a uniform field along the length of the cage. The required length of these guard rings is discussed in [9]. The electric field along the length of the centre conductor and on all other conductors is calculated using Coulomb [11], a three dimensional electric field solver.

Changes in the RAD and RH are accounted for by recording the ambient pressure, temperature and RH, which are measured on calibrated devices at the beginning and end of each measurement.

5. 3.3 Developing a Measurement Protocol

The extraction of the proposed wideband excitation function from small corona cage measurements was discussed in section 5.2.2. Both the time and frequency domain extraction methods required a time domain pulse train waveform. A sampling card is therefore required. The sampling card must sample fast enough to accurately capture the pulse shape. Typical transmission line corona pulses have an average rise time of about 50 ns [1]. The sampling card must also record a sufficient number of samples so as to observe all corona events on a 50 Hz waveform. The sampling card selected is the National Instruments NI5112. The minimum sample time of this device is 10 ns and it can store up to 16 million samples. In order to evaluate the accuracy of equations 5.24 and 5.26, an EMI receiver equipped with both a QP and an average detector was used to simultaneously measure these levels in the bandwidth 150 kHz to 30 MHz. The device conforms to CISPR specifications.
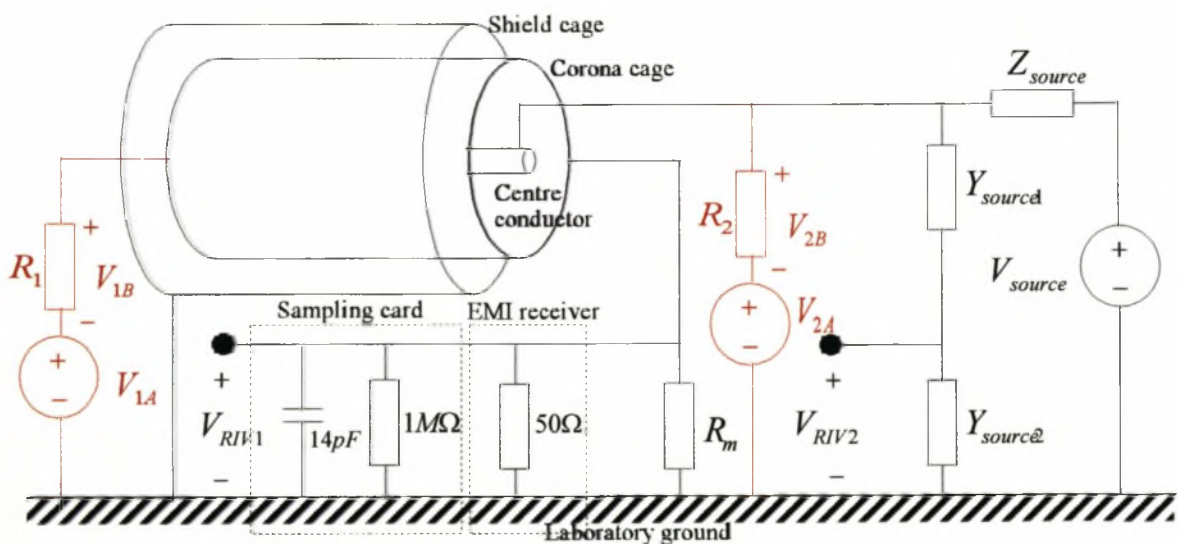

Figure 5.10: Schematic diagram of the small corona cage experimental setup.

91

The small corona cage experimental setup is illustrated in figure 5.10. The source voltage, V_s, is measured with an oscilloscope across a capacitive voltage divider. The corona pulse waveform, V_c, is measured off the cage across a wideband measurement resistor $R_m = 50\ \Omega$ with the EMI receiver and the sampling card. The EMI receiver's input impedance is $50\ \Omega$ while the sampling card channel's input impedance is set to $1\ M\Omega$. The stray capacitance at the sampling card channel's input is rated at 14 pF.
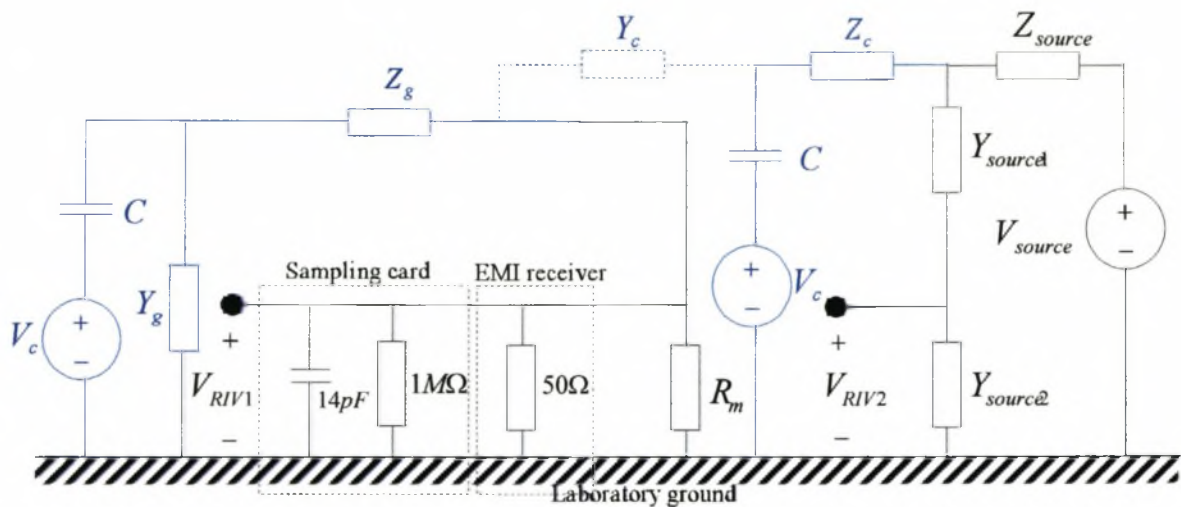
Figure 5.11: Schematic diagram of the equivalent high frequency model for the experimental setup including corona generation.

An equivalent circuit model of the experimental setup, including the corona generation model, is proposed in figure 5.11. The corona cage and centre conductor are both modelled as a series impedance and a shunt admittance. These four elements are frequency dependent. In figure 5.11, the shunt admittance between the corona cage and centre conductor is assumed sufficiently small enough so that the two circuits can be considered isolated. If this assumption is not valid, the two voltage measurements must be considered separately. The two measured voltages are:

$$\mathbf{V}_{RIVn} = \mathbf{H}_{RIVn}(\omega).\left(\frac{1}{1+j\omega C \mathbf{Z}_n(\omega)}\right)\mathbf{V}_c = \mathbf{H}_c.V_c \qquad ,n = 1,2 \qquad (5.43)$$

The frequency dependent variables $\mathbf{H}_{RIVn}(\omega)$ and $\mathbf{Z}_n(\omega)$, in equation 5.43, are measured for a specific experimental setup by injecting a sinusoidal signal of known magnitude, phase and frequency, as illustrated in red in figure 5.10, and then observing voltages $\mathbf{V}_{nB}$ and $\mathbf{V}_{RIVn}$:

$$\mathbf{Z}_n(\omega) = R_m\left(\frac{\mathbf{V}_{nA} - \mathbf{V}_{nB}}{\mathbf{V}_{nB}}\right) \qquad, n = 1,2 \tag{5.44}$$

$$\mathbf{H}_{RIVn} = \frac{\mathbf{V}_{RIVn}}{\left(\mathbf{V}_{nA} + \mathbf{V}_{nB}\right)} \qquad, n = 1,2 \tag{5.45}$$

These variables are extracted for the various cages used in this chapter across the frequency band 150 kHz to 30 MHz. The corona source element $\mathbf{V}_c$ can therefore be extracted from either $\mathbf{V}_{RIV1}$ or $\mathbf{V}_{RIV2}$ using equations 5.43 to 5.45. The high voltage capacitors available for the maximum source voltage used did not have favourable frequency responses above a few MHz. The coupling capacitor used for the RIV_2 measurement, a measurement that was preferred by ESKOM in chapter 4, will reduce the dynamic range and introduce resonance into the measurement system. Since the corona pulses are measured on an 8-bit sampling card, the maximum dynamic range of the measurement system is required. System resonances will make the extraction of pulse parameters more difficult. Only RIV_1 measurements are therefore made in the small corona cage for the extraction of a wideband excitation function.

Each experimental setup is first checked for spurious corona sources at the maximum applied voltage using a Corocam [12]. The use of the Corocam in this regard and the design of a corona-free feeder network and support structure are described in [9]. Spurious corona is not the only form of interference in the experimental setup illustrated in figure 5.10. While the corona cage is electrically small at 30 MHz, the high voltage feeder network, support structures and grounding structures in the laboratory are not. Large ground loops are formed by the various connections. Such ground loops may facilitate the flow of common mode current that will appear as spurious

noise across the terminals of the measurement resistor. The susceptibility of the experimental setup presented in figure 5.10 to spurious noise was investigated in [9] and a shielding protocol was developed for the small cage setup. This protocol is adopted for the small cage measurements presented in this dissertation to reduce spurious noise.

5.3.4   The Corona Cage Construction

The design requirements for the various small cage experiments could not be met by a single corona cage design. The various small corona cages used are described in this section.
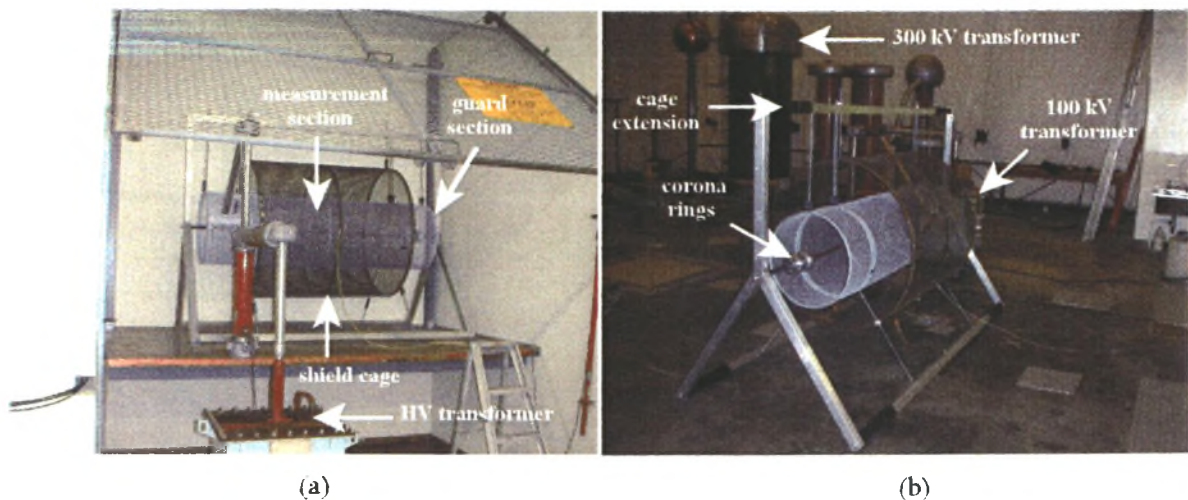

Figure 5.12: Photographs of the small size US corona cage in (a) the small laboratory with the 100 kV transformer and (b) the large laboratory with both the 100 kV and the 300 kV high voltage transformers.

Photographs of the small size US cage, $R = 25$ cm, are presented in figure 5.12. The cage has an outer screen cage and a light-weight aluminium frame. It was designed to be small enough to fit into the small high voltage laboratory as well as a small passenger vehicle once disassembled. The high voltage feed was placed through the guard section (cf. figure 5.12 (a)). This caused flash-over at this point at 90 kV (RMS). Cage extensions were made (cf. Figure 5.12 (b)) so that the feed network could be placed away from the guard section when the cage was setup in the large laboratory. This increased the flash-over voltage above 100 kV. The cage is primarily used with the 100 kV transformer and both smooth and stranded conductors of small outer diameter. This is discussed in chapter 6.
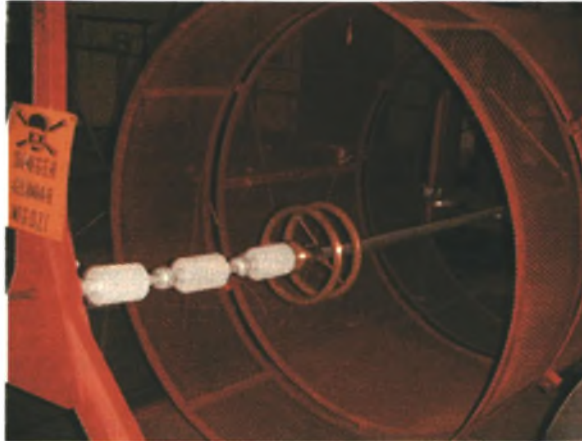
94

Figure 5.13: A photograph of the medium size UCT corona cage in the large laboratory with the 300 kV high voltage transformer.

Large diameter stranded conductors were placed in the medium size UCT cage, $R = 75$ cm, depicted in figure 5.13. This cage does not have an outer screen cage and the flash-over voltage is 160 kV. It is used in the large laboratory with the 300 kV transformer. The small size US cage was also converted to a medium size cage, $R = 50$ cm, similar to the UCT cage by removing the inner corona cage and using the outer screen cage as a corona cage. Guard sections were made with the same diameter as the screen cage for this purpose. This cage offers a higher dynamic range than the UCT cage for the corona measurements and is preferred to the UCT cage.

5. 4   Model Parameter Extraction

Having defined the extracted model and the experimental setup, it only remains to determine a method of extracting the model elements from the cage measurements. The time and frequency domain extraction methods described in section 5.2.2 are evaluated and applied in this section.

5. 4.1   Isolating an Individual Pulse in the Measured Pulse Train

The sampling card, set to the maximum record length of 16 million samples and the maximum sample rate of 100 million samples per second, captures all the corona pulses on 8 periods of the 50 Hz source waveform. The measurement is randomly triggered. There are therefore 7 complete 50 Hz periods starting at zero phase in the measured pulse train.

95
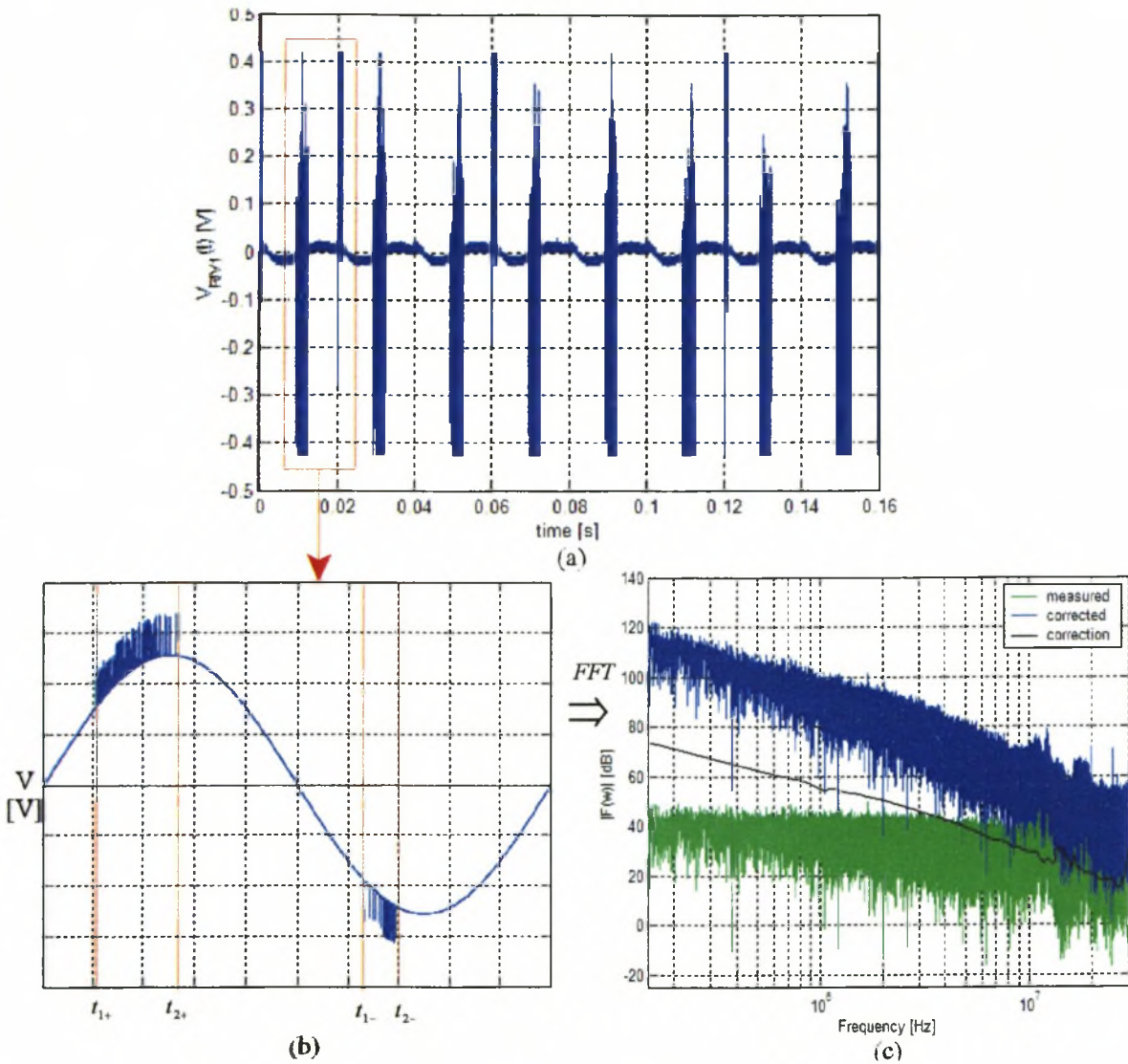
Figure 5.14: (a) The pulse train waveform captured on the sampling card; (b) one 50 Hz period with the frequency dependent phase and magnitude correction applied; (c) the amplitude spectrum of the measured and corrected pulse train waveforms.

A typical V_{RIV1} waveform is plotted in figure 5.14 (a). The frequency response of the measurement system emphasises the higher frequency components. The correction, $\mathbf{H}_c$, defined in equation 5.43, is applied to the measured waveform. The applied source voltage is calculated from the measured 50 Hz component with $R_m = 50\ \Omega$ in figure 5.10:

$$\mathbf{V}_{source} \approx \left(\frac{1}{1250\pi C} \angle -90^0 \right) . \mathbf{V}_{RIV1} \big|_{f=50Hz} \tag{5.46}$$

96

The first complete 50 Hz cycle in figure 5.14 (a) is isolated and the corrections defined in equations 5.43 and 5.46 are applied. The result is plotted in figure 5.14 (b). The times of the first and last pulses in both the positive and negative half cycles are recorded. The first parameters extracted from the measured waveform are therefore the phase of the source voltage at which corona activity begins, called the corona start phase, and the duration of the corona activity.

Each pulse in the pulse train $V_c(t)$ must next be isolated so that its parameters can be extracted. The peak detection algorithm developed to isolate the position of the pulse peaks is:

$$\left[V_{peak}, t_{peak}\right]_n = \max\left[\sqrt[N]{V_c(t) * \left\{2B\text{sinc}\left[B(t - t_0)\right]\cos\left[2\pi f_0(t - t_0)\right]\right\}}\,\Bigg|_{n-t_1/2}^{|n+t_1/2}\right] \quad (5.47)$$

The fundamental and significant harmonic frequency components of the sources voltage are filtered out with an ideal bandpass filter. The bandwidth, B, and centre frequency, f_0, of this filter were chosen as 28 MHz and 15 MHz respectively. The value of N in equation 5.47 is chosen so as to provide a signal to noise ratio which is adequate for the detection of the smallest valid corona pulse above the spurious noise signals. Finally, the value t_1 must be smaller than the minimum time between two successive detectable pulses and must satisfy the requirements defined in equations 5.22 and 5.23.

The NI5112 is an 8-bit sampling card. The dynamic range of the measurement is therefore only -48 dB. During a positive half cycle, various positive corona discharge modes occur. These discharge modes are discussed in [9]. The onset and positive streamer mode pulses are much larger than the burst pulses. It is therefore not possible, with the restricted dynamic range of the measurement system, to accurately account for all these modes in a single pulse train measurement. The RN contribution of burst pulses is insignificant in comparison to that of the other positive discharge modes [1]. Burst pulses are therefore not studied in this research. Similarly, Trichel pulses in the negative half cycle are also excluded from the analysis.
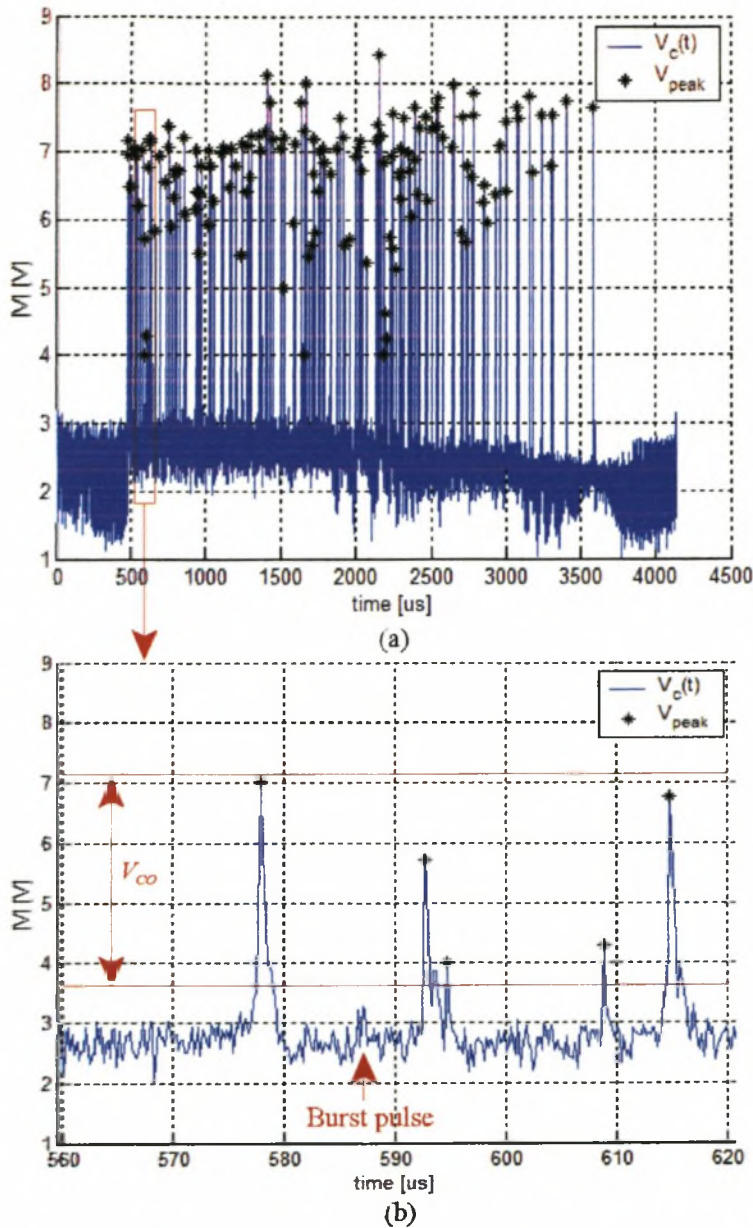
Figure 5.15: The pulse train and pulse peak waveforms of the positive half cycle in figure 5.14 (b) [$B = 28$ MHz, $f_0 = 15$ MHz, $N = 4$, $t_1 = 100$ ns, $V_{CO} = 50$ %].

The extracted corona pulse train and the calculated pulse peak waveforms are plotted in figure 5.13 for the positive half cycle of the waveform in figure 5.14 (b). In figure 5.15 (b), the parameter V_{CO} is introduced to specify the minimum detected pulse peak amplitude. It is expressed as a percentage of the largest pulse peak in the pulse train. The Burst and Trichel corona mode pulses are excluded from the analysis by selecting an appropriate value for V_{CO}.

5. 4.2   Time Domain vs Frequency Domain Analysis

Two extraction methods, a time domain method and a frequency domain method, were proposed in section 5.2. These methods must be compared in light of the measurement protocol. The calibrated measurement bandwidth of the NI5112 sampling card is 100 MHz. The frequency domain extraction technique can therefore be used to extract the pulse parameters, provided f_β is smaller than 100 MHz.
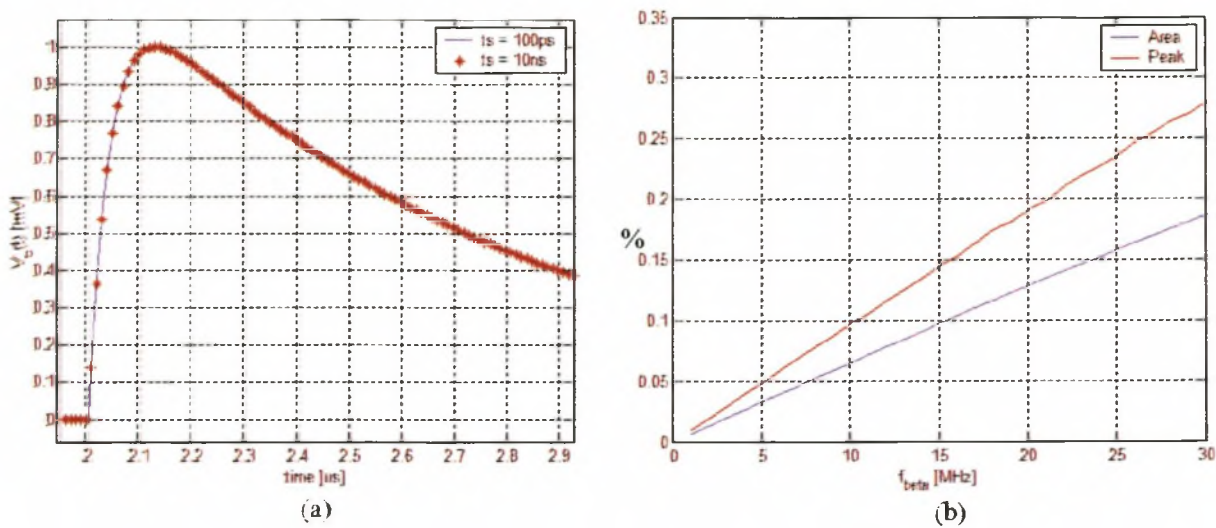

(a)
(b)

Figure 5.16: (a) Pulse 2 of figure 5.1, sampled with two different sample rates; (b) the maximum difference between the peaks and the areas of the two sampled curves for values of f_β between 1 MHz and 30 MHz.

The minimum sample interval of the NI5112 is 10 ns. Pulse 2 in figure 5.1 is sampled at intervals of 100 ps and 10 ns. The sampled points are interpolated using a cubic spline algorithm and plotted in figure 5.16 (a). The difference between the peak amplitudes and the areas of the two curves are plotted in 5.16 (b) for f_β varied between 1 MHz and 30 MHz. The result suggests that

the sampling rate of the measurement device is sufficient for the accurate extraction of the pulse parameters using either of the extraction methods suggested in section 5.2. The time domain extraction technique does however require that both the magnitude and phase of the cage's transfer function are known across the measured band for each experimental setup with a vector network analyser. Only the magnitude is required in the frequency domain technique and can be measured with the EMI receiver already included in the measurement setup. Frequency domain extraction is therefore used in the remainder of this dissertation for $f_\beta < 30$ MHz.

5. 4.3 Pulse Parameter Extraction

A curve fitting algorithm is developed in this section for the frequency domain analysis to extract the values of K, α and β from the measured pulse train.
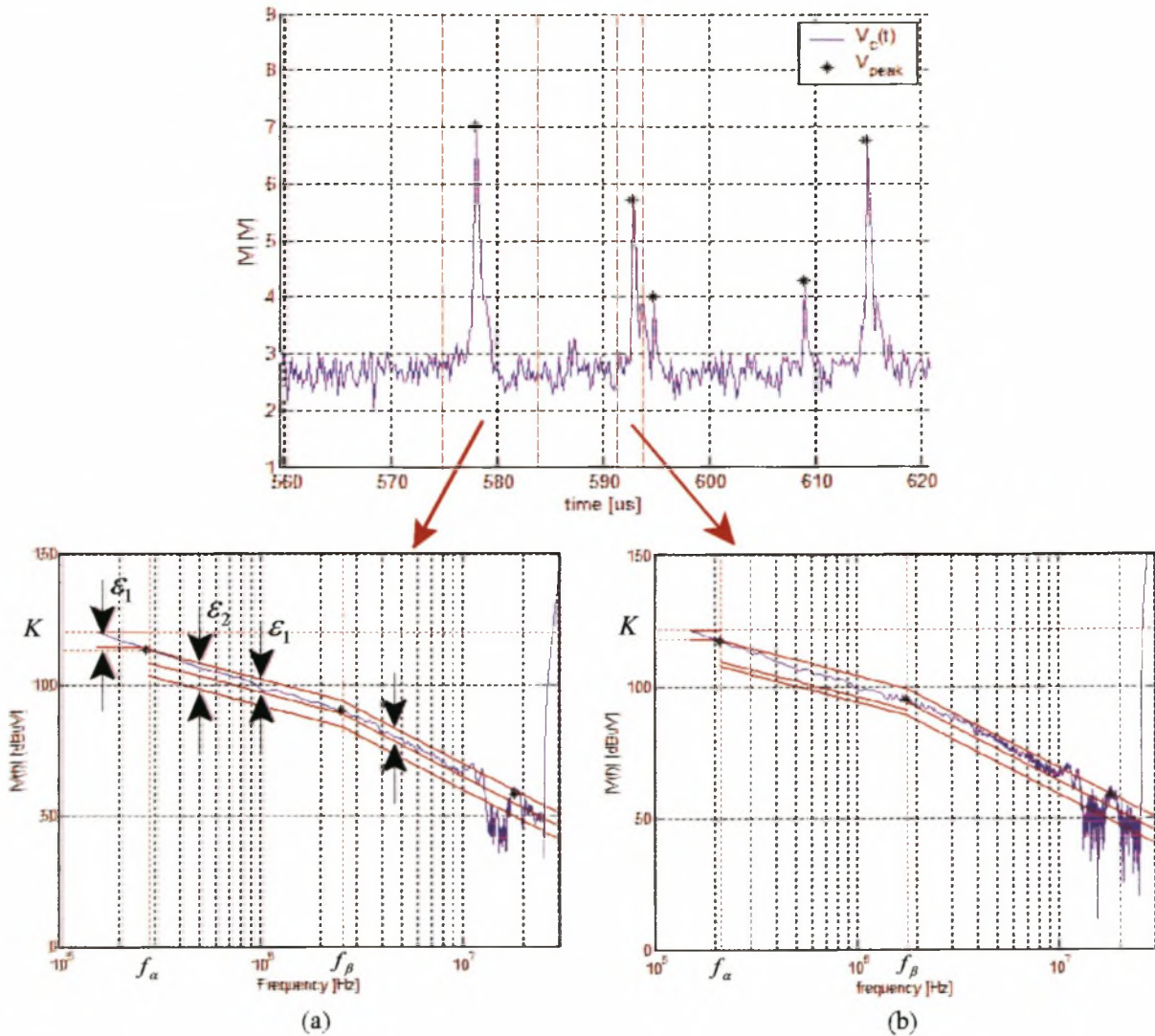
Figure 5.17: The curve fitting algorithm applied to two pulses in the measured pulse train [$\varepsilon_1 = 5$ dB, $\varepsilon_2 = 8$ dB].

The points between which the discrete Fourier transform (DFT) are calculated are first chosen. If consecutive pulses are adequately spaced, the time interval can be chosen according to the limits defined in equations 5.22 and 5.23. Such a pulse is analysed in figure 5.17(a). The limit $\varepsilon_1 = 5$ dB is used to determine if the DFT is that of a valid streamer discharge and to find f_α and f_β. It is

100

chosen according to equation 5.18 ($\omega = \alpha$, $\omega \ll \beta$) and a maximum DFT calculation error of 2 dB (cf. figure 5.5). If the separation time between consecutive pulses does not allow for the correct choice of t_2, as defined in equation 5.23, an error greater than 2 dB is made. By relaxing the limit ε_1 in the frequency regime $\omega \approx \alpha, \omega \ll \beta$, the parameters of the streamer pulse can still be accurately determined, provided the limit does not exceed ε_2. This is done for the pulse analysed in figure 5.15 (b). The value of ε_2 is chosen for a specific pulse train so that the number of valid pulses is sufficient for the extraction of good statistical information, while limiting the error of the extracted parameters to a maximum specified value. The optimization parameter ε_2 also makes the algorithm less sensitive to spurious noise, thus increasing the dynamic range of the measurement. The change in frequency between two consecutive points of a DFT, calculated from an N-point sampled time domain waveform, with sample time dt is:

$$df = 1/(N.dt) \tag{5.48}$$

If the pulse repetition rate is very high, the number of sample points which are used to calculate the DFT may not be sufficient to ensure that $df < f_\alpha$. The pulse is discarded if this occurs.
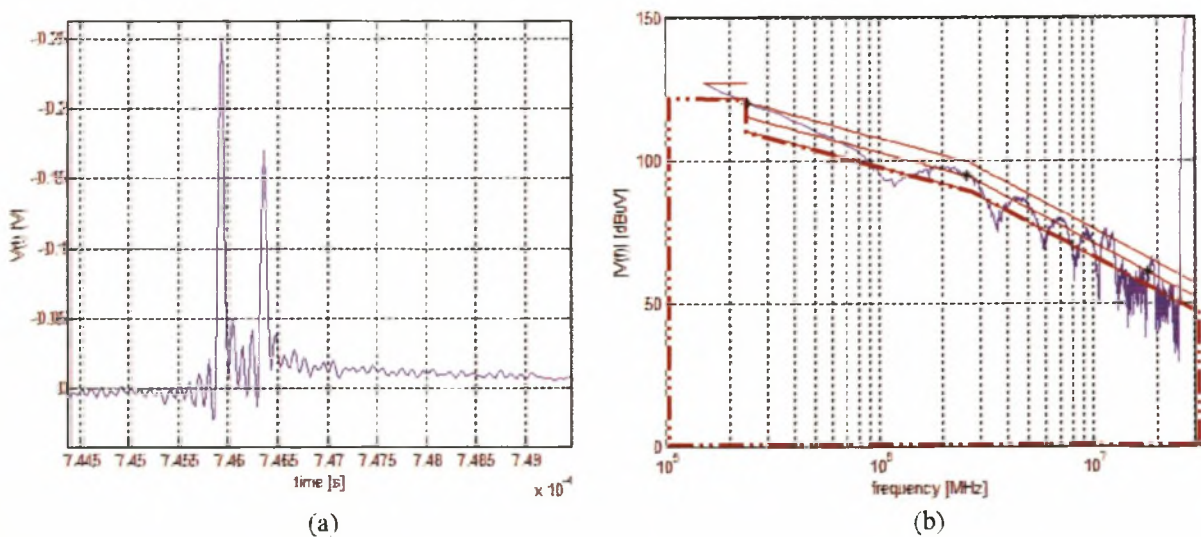

(a)   (b)

Figure 5.18: (a) A time domain pulse train of two pulses separated by a short repetition time and (b) the DFT of the pulse train.

If the parameter t_1, in equation 5.47 is not correctly chosen, the DFT of two pulses may be calculated. The parameters extracted from such a waveform are invalid and must be excluded from the analysis. The DFT of two pulses with a repetition time less than t_1 is plotted in figure 5.18(b). An exclusion area is defined in this figure with the parameter ε_2. The extracted parameters are excluded from the analysis if the calculated DFT enters this exclusion region.
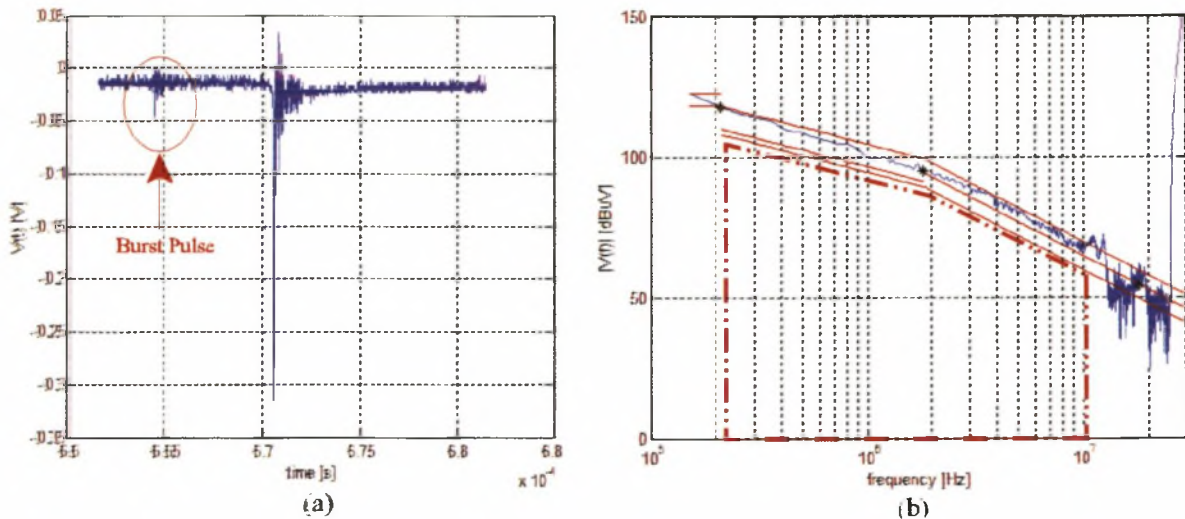

Figure 5.19: (a) A time domain corona pulse train of a positive streamer pulse and a burst pulse and (b) the DFT of the pulse train.

Burst pulses are excluded from the analysis since their RN contribution in the measured frequency band 150 kHz to 30 MHz is considered insignificant. The peak detector will therefore ignore these pulses and they may appear together with a valid pulse in the analysis. This is the case in figure 5.19 (a). The DFT of such a pulse train, plotted in figure 5.19 (b), does not enter the exclusion area defined in figure 5.18 (b) in the frequency regime $f_\alpha < f < 10\text{MHz}$. The exclusion area is therefore limited to this frequency regime and the effect of burst pulses is accommodated. The extraction algorithm can now be considered adequately capable of producing accurate data for the measurement protocol used. This data must next be analysed.

5. 4.4 Statistical Analysis of Extracted Parameters

The extraction algorithm discussed above outputs the pulse parameters of all the pulses in each 50 Hz half cycle. It was assumed in equations 5.10 and 5.11 that the repetition rate has an

exponential distribution, while the other parameters have normal distributions. The mean and standard deviations of the parameters must therefore be calculated.
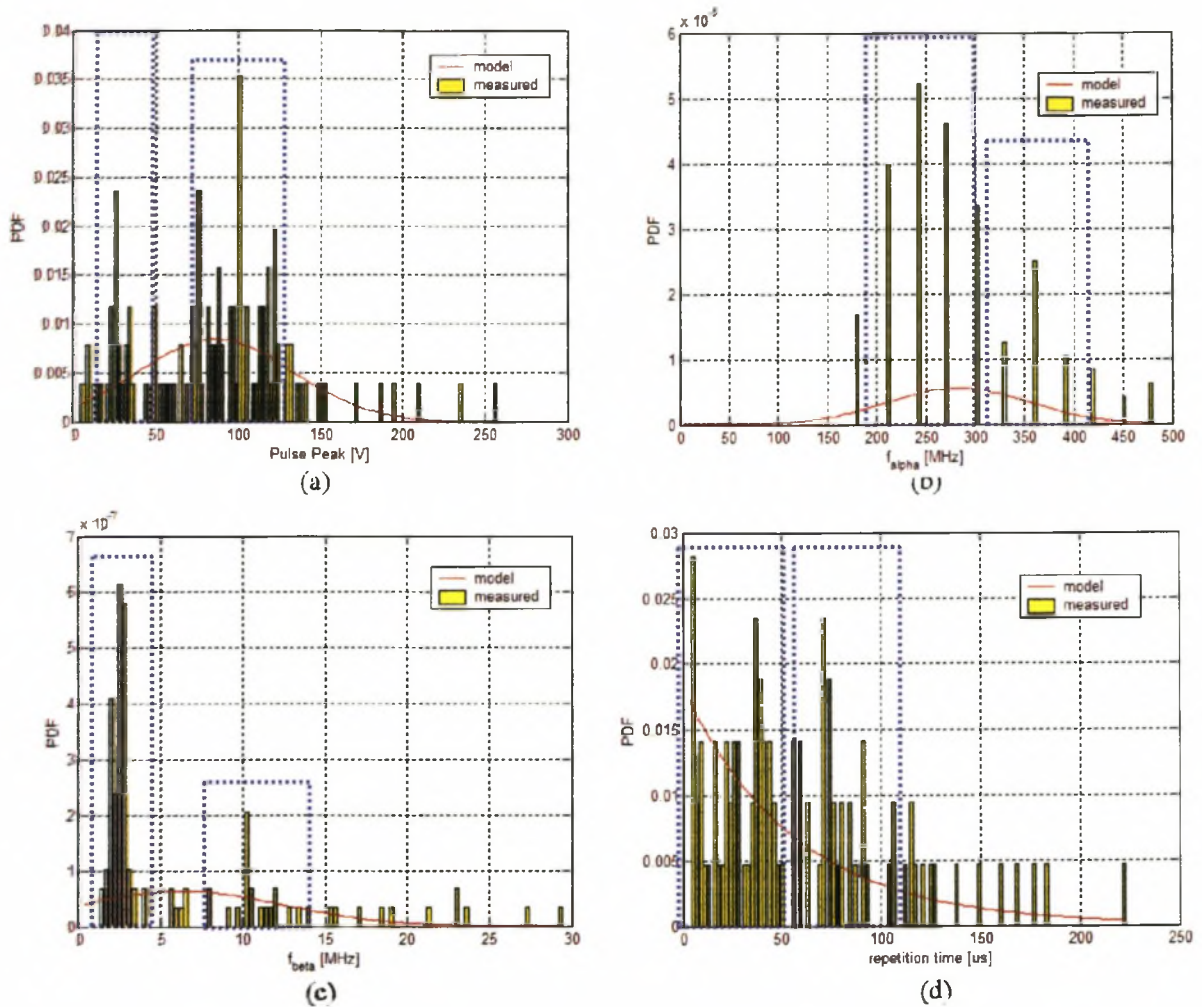

Figure 5.20: The measured and modelled probability density distributions of (a) the peak pulse amplitude, (b) f_α, (c) f_β and (d) the repetition time.

The probability density function plots in figure in 5.20 suggest the presence of two distinct populations in the positive half cycle. Two separate excitation functions must therefore be extracted for different pulse types. The two pulse types in the positive half cycle must be identified and the extraction algorithm must be adapted to differentiate between these pulses. A review of the corona physics discussion in [9] suggests that the two measurable pulse types in the positive half cycle are positive streamer pulses and onset streamer pulses. The peak amplitude of the onset streamer pulses are one or two orders smaller than the positive streamers and have shorter rise times.

103

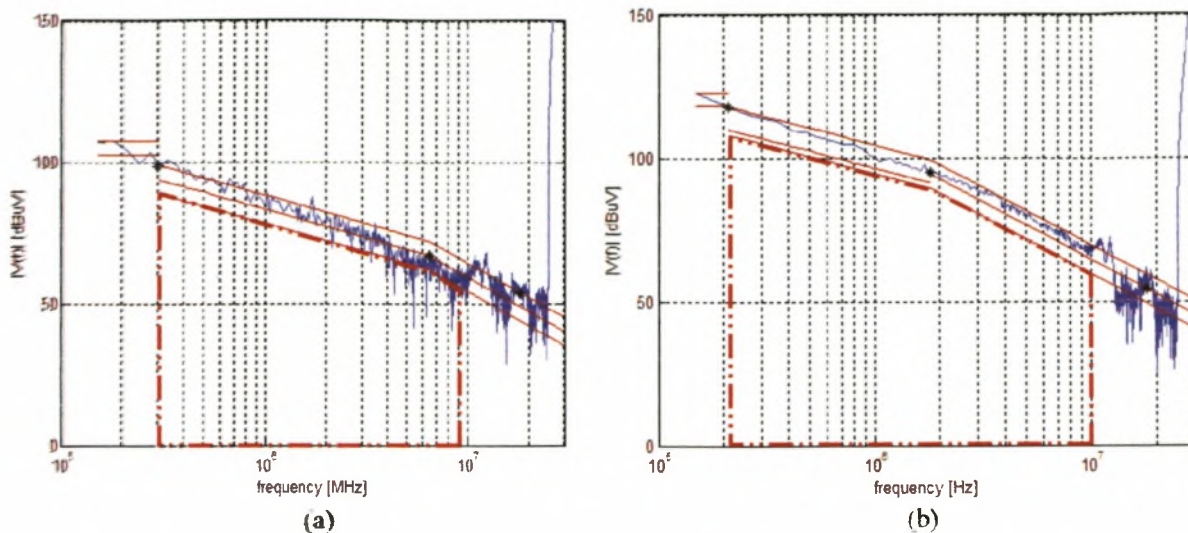(a)   (b)

Figure 5.21: The DFT of (a) an onset streamer pulse and (b) a positive streamer pulse.

The quantization noise of the 8-bit sampling card at frequencies above a few hundred kilohertz is significant for the small onset streamer pulses and is clearly visible in figure 5.21 (a). This noise causes the DFT to enter the exclusion region previously defined. The pulse would therefore normally be excluded. The extraction algorithm must be modified to further classify pulses, for which the DFT enters the exclusion region, as either invalid pulses or onset streamer pulses. This is achieved by recognising that $K < K_0$ and $f_\beta > f_{\beta 0}$ for onset pulses.

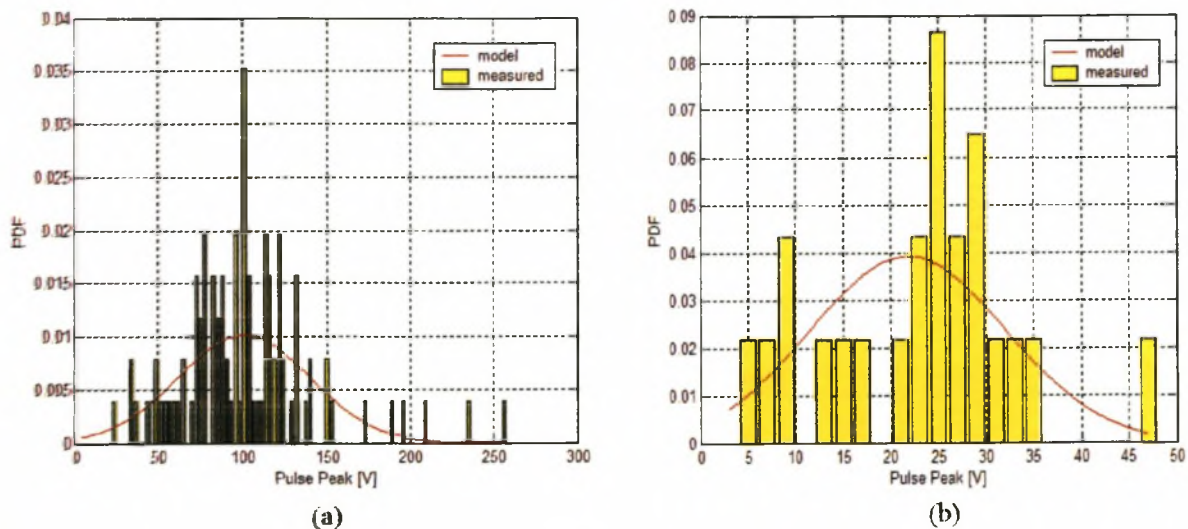(a)   (b)

Figure 5.22: The measured and modelled peak pulse amplitude probability density functions of (a) positive streamer and (b) onset streamer pulses. [$K_0 = 110$, $f_{\beta 0} = 2\,\text{MHz}$]

104

The pulse amplitude distributions of the two positive corona modes in figure 5.22 verify that the modified extraction algorithm is able to distinguish between these positive corona modes. The strict conditions used to distinguish between the various corona modes cause many pulses to be excluded. This is necessary to ensure the accuracy of the extracted parameters but will affect the sample statistics of the parameters. The number of pulses from which statistics are calculated will affect the confidence level for each parameter.

The mean and variance of the pulse parameters are extracted from a single 50 Hz cycle. These values are therefore sample statistics of the population mean and variance. The population consists of all the corona pulses of the specified mode on all 50 Hz cycles and is therefore an infinite population. The sample consists of all the corona pulses of the specified mode on a single 50 Hz cycle and is therefore a finite population. Since the statistical distributions of the parameters are known to be normal [4], the total population mean and variance will also be normally distributed amongst the samples [6]. It was mentioned in section 5.3 that the corona activity on consecutive 50 Hz cycles can be considered statistically independent if the space charge distribution maintains a steady state. A confidence level for each parameter's mean and variance can therefore be calculated from the mean and variance extracted for each of the seven consecutive 50 Hz cycles measured with the sampling card. The 95 % confidence interval for a normally distributed population mean is [6]:

$$\mu_{95\%} = \overline{Y} \pm t[0.975, n-1]\sqrt{s^2 / n} \tag{5.49}$$

In equation 5.49, the confidence interval is calculated from the Student's t distribution for $n = 7$ statistically independent samples, which have a sample mean $\overline{Y}$ and a sample variance s^2. The 95 % confidence interval for the population variance is also calculated [6]:

$$\frac{(n-1)s^2}{\chi^2[0.975; n-1]} < (\sigma_{95\%})^2 < \frac{(n-1)s^2}{\chi^2[0.025; n-1]} \tag{5.50}$$

In equation 5.50, the confidence interval is calculated from the χ^2 distribution.

The wideband excitation function proposed in this chapter should be capable of predicting the frequency variation of the RN performance of a line in the band 150 kHz to 30 MHz as well as the RN performance of short lines. A set of small cage experiments is formulated in the next chapter to evaluate the effect of environmental and cage scaling factors on the excitation function.

5. 5   References

[1]   P. Sarma Maruvada, *Corona Performance of High-Voltage Transmission Lines*, Research Studies Press Ltd, 2000.

[2]   S.Ramo, "Currents Induced by Electron Motion", Proc. IRE, Vol. 24, 1934, pp584 - 485.

[3]   B. Rakoshdas, "Pulses and Radio Influence Voltage of Direct Voltage Corona", IEEE Trans. Vol. PAS-83, 1964, pp. 483 - 491.

[4]   M.M. Khalifa, A.A. Kamal, A.G. Zeitoun, R.M. Radwan, S.El-Bedwaihy, "Correlation of Radio Noise and Quasi-Peak Measurements to Corona Pulse Randomness", IEEE Trans. Vol. PAS-88, 1969, pp. 1512 - 1518.

[5]   P.S. Maruvada, N. Hyltén-Cavallius, N.T. Chinh, "Radio Noise Meter Response to Random Pulses by Computer Simulation", IEEE Trans. Vol. PAS-93,1974, pp. 905-915.

[6]   O.J. Dunn, V.A. Clark, *Applied Statistics: Analysis of Variance and Regression*, John Wiley & Sons, 1974.

[7]   P.S. Maruvada, W. Janischewskyj, "Electrostatic Field of a System of Parallel Cylindrical Conductors", IEEE Trans., Vol. PAS-88, 1969, pp. 1069-1079.

[8]   J.J. Cladé, C.H. Gary, C.A. LeFevré, "Calculation of Corona Losses Beyond the Critical Gradient in Alternating Voltage", IEEE Trans., Vol. PAS-88, 1969, pp. .

[9]   R.G. Urban, *Modelling Corona Noise on High Voltage Transmission Lines*, MScEng Thesis, University of Stellenbosch, 2001.

[10]   H.A. Haus, J.R. Melcher, *Electromagnetic Fields and Energy*, Prentice Hall, 1989.

[11]   *Three Dimensional Electric Field Solver*, Users and Technical Manual, Integrated Engineering Software, Version 3.0, 1997.

[12]   W.L. Vosloo, G.R. Stolper, P. Baker, "Daylight Corona Discharge Observation and Recording System", Proceedings, International Symposium on High Voltage Engineering, Montreal, 1997, pp. 161 - 164.

Chapter 6

Small Corona Cage Measurements

6. 1   Introduction

The extraction of the wideband excitation function proposed in chapter 5 from small corona cage measurements is discussed in this chapter. In order to predict the fair weather excitation function of a conductor bundle comprising aluminium conductor steel reinforced (ACSR) conductors, a set of nine experiments was formulated. These experiments are described in section 6.2. The results of the experiments are presented in appendix H and are analysed in sections 6.3 to 6.5. The effect of various corona modes on the measured RN and the inception gradients of these modes is discussed in section 6.3. In section 6.4 the effect of the cage design on the space charge is discussed. Finally, the predicted wideband excitation functions for an ACSR conductor is calculated and the conducted RN at the Acacia substation is approximated in section 6.5.

6. 2   A Description of the Small Cage Experiments

ACSR conductors are used on the transmission lines studied in chapter 2. These conductors consist of steel strands which provide strength, surrounded by aluminium strands which conduct most of the energy. The surface gradient around the perimeter of a stranded conductor does not vary smoothly. The surface gradient and the electric field distribution near the conductor surface were identified in previous chapters as two important influencing variables in RN analysis. The relationship between these variables and corona generation will first be studied on smooth conductors which have more uniform surface gradient and electric field distributions. RN generation on stranded conductors is subsequently studied.

6. 2.1   Quality of Supply

Corona generation increases suddenly to a measurable level at the inception gradient defined in equation 4.4. The relationship between RN generation and surface gradient therefore has a non-linearity at the inception gradient. The surface gradient is linearly related to the source voltage.

The relationship between RN generation and the source voltage amplitude will therefore also have a non-linearity at corona inception. The number of discharges and the appearance of various corona modes, which have different RN characteristics, is dependent not only on the source voltage amplitude but also on the amount of space charge generated by previous corona activity. RN generation is therefore also dependent on the time variation of the source voltage.
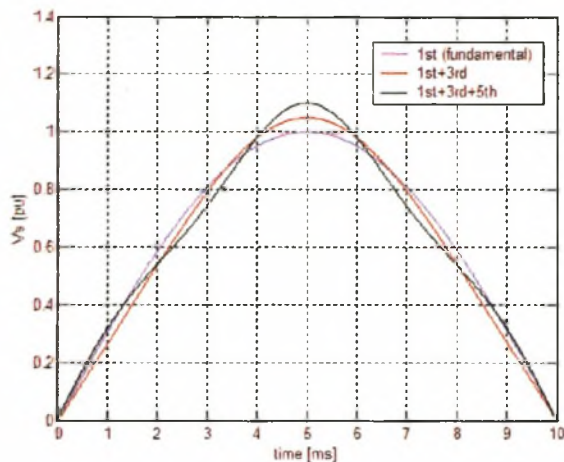

Figure 6.1: The positive half cycle of a theoretical source voltage waveform showing the effect of odd harmonic components on the waveform's amplitude and shape.

The effect of odd harmonics on the amplitude and shape of a theoretical voltage waveform is demonstrated in figure 6.1. Both the time variation and peak amplitude of the waveform are affected by the magnitude, phase and frequency of the harmonic components. The source voltage's harmonic content must therefore be considered before analysing RN measurements.
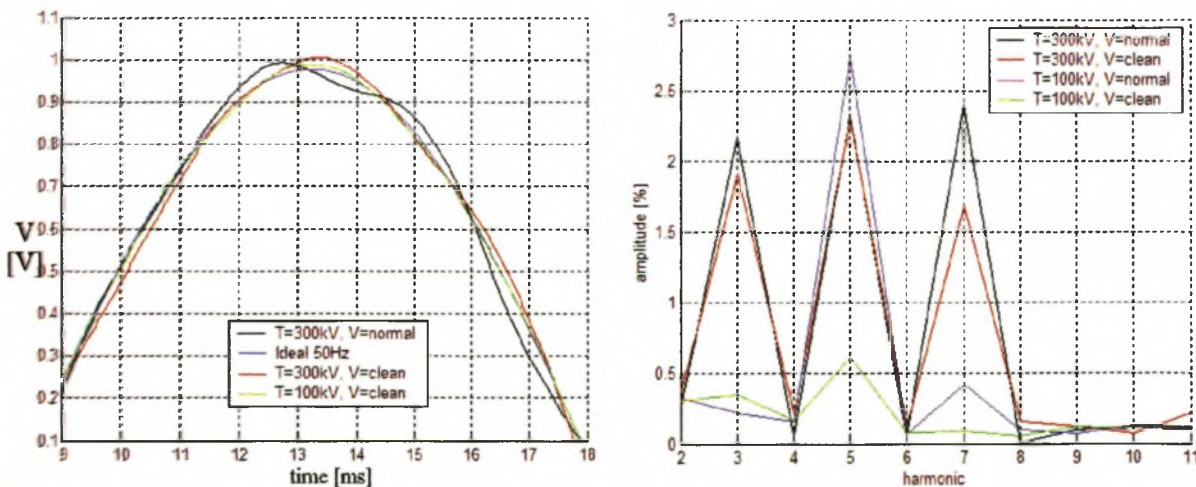

Figure 6.2: (a) The positive half cycle of the source voltages used and (b) the magnitudes of the first 10 harmonics of these source voltages.

108

The supply used in [1] is a 300 kV transformer and an unfiltered single phase primary voltage. The positive half cycle of this source voltage is plotted against an ideal 50 Hz waveform in figure 6.2(a). The quality of supply can be characterized by the distortion of the source voltage as compared to an ideal 50 Hz waveform for the purposes of RN analysis. This distortion will be quantified by the variation in peak amplitude, ΔV_p, and the difference between the two curves averaged over a 50 Hz period, V_{diff}. The quality of supply of the source voltage used in [1] is $\Delta V_p = 1.68\%$ and $V_{diff} = 2.39\%$. Both parameters are expressed as a percentage of the fundamental component. While only the magnitude plot of the harmonics is presented in figure 6.2, the phase of the harmonics is also important and will affect both the peak voltage and the waveform shape. In an effort to reduce the harmonic content of the source voltage, a motor generator set was used to filter the primary voltage. A 100 kV transformer was also available. The magnitudes of the first ten harmonics for various combinations of primary voltage and transformer type, measured at the inception voltage, are plotted in figure 6.2 (b). The comparison suggests that the filtering reduced the 3rd and 7th harmonic components. The combination of the 100 kV transformer and the filtered primary voltage produced the only acceptable quality of supply. For this combination, $\Delta V_p = 0.3\%$ and $V_{diff} = 0.58\%$.

The effect of quality of supply on RN is studied in the first experiment in the small US cage, which is coated with an insulating paint, and a centred smooth copper conductor, $r = 7.5$ mm. This cage was described in section 5.3.4. The combinations of transformers and primary voltages described above are used. The variation in RH and RAD factor during the experiment is 3% and 0.001 respectively. The only significant variable varied is therefore the quality of supply. The values of the influencing variables and the variation in the measured RN parameters for all experiments presented in this chapter are presented in appendix H. The combination of the filtered primary voltage and the 100 kV transformer is considered as an ideal supply in the experiment. The effect of the quality of supply on RN is therefore determined by a comparison of the parameters extracted from the measurements made in this experiment. The inception gradient is first determined in the experiment. The gradient is then increased in 1 kV/cm intervals up to the flash-over gradient. Measurements are made at each interval. This measurement protocol is used for all the experiments described in this chapter.

The experimental results reveal a significant variation in the pulse parameters due to the quality of supply. No correlation was found between the proposed quality of supply parameters, ΔV_P and V_{diff}, and the measured pulse parameters. It is therefore concluded from this experiment that the wideband excitation function must be extracted with a supply voltage which meets the specifications, with regards to the harmonic content, used by ESKOM.

6. 2.2 Conductor Material

Corona generation takes place near an aluminium surface on the ACSR conductors. Both smooth copper and aluminium pipes are available for use in the corona cage. This experiment investigates the effect of the choice of conductor material on the generation parameters.

The setup used for the experiment is the small US cage with insulation coating. The closely matched standard copper and aluminium pipe outer diameters used are 0.75 cm and 0.78 cm respectively. The small difference in conductor diameter results in a 4% increase in the field divergence at the surface of the copper conductor. The clean primary supply and the 100 kV transformer are used for the experiment. The variation in RH and δ during the experiment is 5% and 0.008.

6. 2.3 RAD and RH

Relationships between RN and both the RAD and RH were included in the empirical and semi-analytical prediction methods presented in chapter 3. The effect of changes in RAD and RH on the pulse parameters is investigated in this experiment.

The experiments presented in this chapter were made over a three month period. The maximum variation in RH and δ during this period, for all experimental setups, was 15% and 0.02 respectively. The effect of these two variables on the pulse parameters is investigated by comparing the extracted parameters of the same experimental setup under different ambient conditions. The small US cage with the insulation coating and a centred copper conductor of radius $r = 7.5$ mm is used. The source voltage used is the 100 kV transformer with the clean primary supply. The maximum variation in RH for this experimental setup is 10%.

In order to compare measurements under significantly different RAD values, measurements were made in an identical experimental setup at different altitudes. The small corona cage was moved to the Megawatt Park facility described in chapter 4. A clean high voltage supply was provided for the measurement. The RAD factor for the high altitude measurement was 0.825.

6. 2.4 Space Charge Distribution

RN in a cage will replicate that of a transmission line provided the electric field distribution near the bundle conductor surface is replicated in the corona cage. This was discussed in chapter 4. It was also mentioned in chapter 5 that space charge will affect the electric field distribution. The space charge distribution must therefore also be replicated in a corona cage. The affect of any disturbance in the space charge distribution, caused by the corona cage dimensions, on the pulse parameters is investigated in this experiment.

The maximum distance travelled by space charge in a corona cage was approximated by the empirical relation defined in equation 4.5. The space charge will collide with the cage's conductive surface if the cage radius is smaller than this maximum charge displacement. To investigate the effect of such collisions on the pulse parameters, three cages were made with the same length and diameter. The cage diameter is selected so that the space charge just reaches the cage for a centred copper conductor, $r = 0.75$ cm, at a surface gradient 1 kV/cm above inception. All cages were made with a meshed metal grid. One of the cages was coated with an insulating paint. The paint is used to prevent the space charge from recombining on the metal surface when it collides with the cage. The grid used for this cage consisted of diamonds with 2.5 cm sides. The same grid dimensions were used for the second cage which was left unpainted. Space charge will recombine on this cage if it collides with the metal surface. The third cage is made with grid dimensions twice those of the other two cages. It is also left unpainted. The large grid size is used to test how much charge will recombine if there is less surface area with which to collide. A simulation program, described in chapter 5, was developed to estimate the space charge distribution. In this program, the unpainted cage was simulated by removing space charge which collided with it. For the painted cage, the space charge which reached the cage remained stationary at its surface until the AC source reversed polarity and moved the space charge back towards the centre conductor.

The setup used for the experiment is the small US cage with the three centre cages just described. It was found that the effect of the space charge collision on the cage was best demonstrated with the centred aluminium conductor of radius 0.78 cm. The combination of the 100 kV transformer and the clean primary supply are used and no significant variation in RH and δ was observed during the experiment.

6. 2.5 Conductor Surface Area and Electric Field Divergence

The relationship between RN and the equivalent radius of a conductor bundle was included in the prediction methods in chapter 3. The equivalent radius affects both the surface area on which corona can occur and the divergence of the electric field near the conductor surface. The effect of these two variables on the pulse parameters is investigated in this experiment.

As many standard copper and aluminium pipe diameters as possible were used in this experiment. The largest pipe diameter that could be used in the cage with the 100 kV transformer was 2.5 cm. The inception gradient of smooth conductors with larger diameters would require an applied voltage greater than 100 kV. The setup used is the small US cage with the insulation coating. The centre conductor diameters used were 1, 1.56, 2.2 and 2.5 cm. The 100 kV transformer and the clean primary supply are used.

6. 2.6 Surface Gradient Distribution

The most important relationship when considering the RN of a conductor bundle was identified in chapter 3 as that between the average maximum sub-conductor surface gradient and the RN. The close proximity of other sub-conductors in a bundle causes the surface gradient to vary around the perimeter of each sub-conductor. As a result, some methods used bundle gradients other than the average maximum value.

Conductor bundling significantly increases the voltage required for corona inception. Since the source voltage used is limited by the quality of supply requirement to 100 kV, the effect of a variation in surface gradient is investigated in the small cage by displacing the centred 0.75 mm copper pipe towards the cage. In this way, a lower applied voltage will produce a variation in surface gradient on the copper pipe similar to that on the sub-conductors of a bundle.
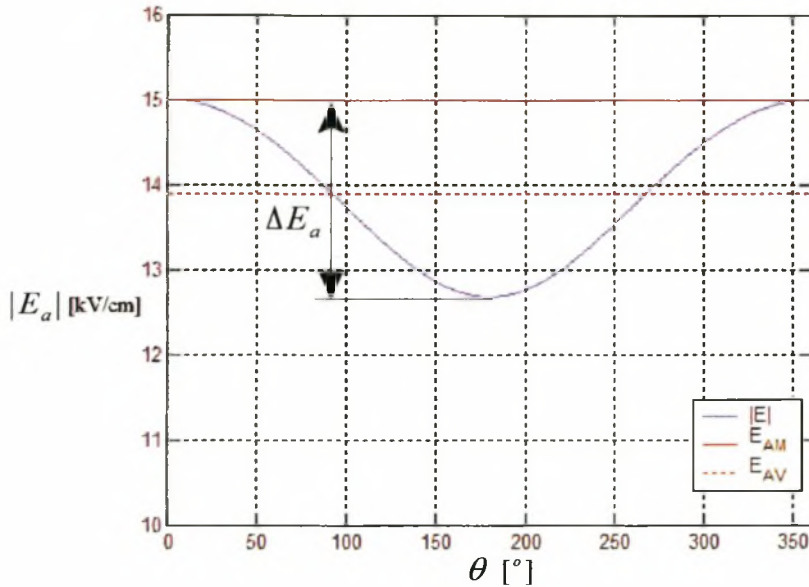
Figure 6.3: The surface gradient distribution on one of the two IEC-800 conductors, which comprise the conductor bundle whose excitation function was extracted in chapter 4. (R_{cage} = 350 cm, R_{bundle} = 22.5 cm, r_s = 1.88 cm and V = 190 kV).

The average maximum, average and actual surface gradients on one of the IEC-800 sub-conductors, which comprise the conductor bundle whose excitation function was extracted in chapter 4, is plotted in figure 6.3. The plot indicates that the actual surface gradient varies by more than 2 kV/cm. If the corona inception level for this conductor bundle was 14 kV/cm, less than 50% of the conductor surface would be subject to corona activity. The use of the average maximum surface gradient to define the relationship between RN generation and the surface gradient is investigated in this experiment by displacing the centre conductor.

In the case of a displaced centre conductor, the space charge produced by the corona activity will first reach the corona cage in the direction of the displacement. This is because the gap is smaller and the surface gradient is a maximum in this direction. The maximum allowable displacement is limited to that displacement for which the space charge distribution, and therefore the pulse parameters, are not significantly affected by the collisions with the cage. As in the previous experiment, it was found that the effect of space charge collisions was best observed with the aluminium conductor. The setup used for the experiment is the small US cage with the insulation coating. A smooth aluminium centre conductor with radius 0.78 cm was displaced by 3, 6 and 9 cm in this cage. The 100 kV transformer and the clean primary supply are used for the

113

experiment. The measurements were made on the same day and no significant variation in RH or δ was observed during the experiment.
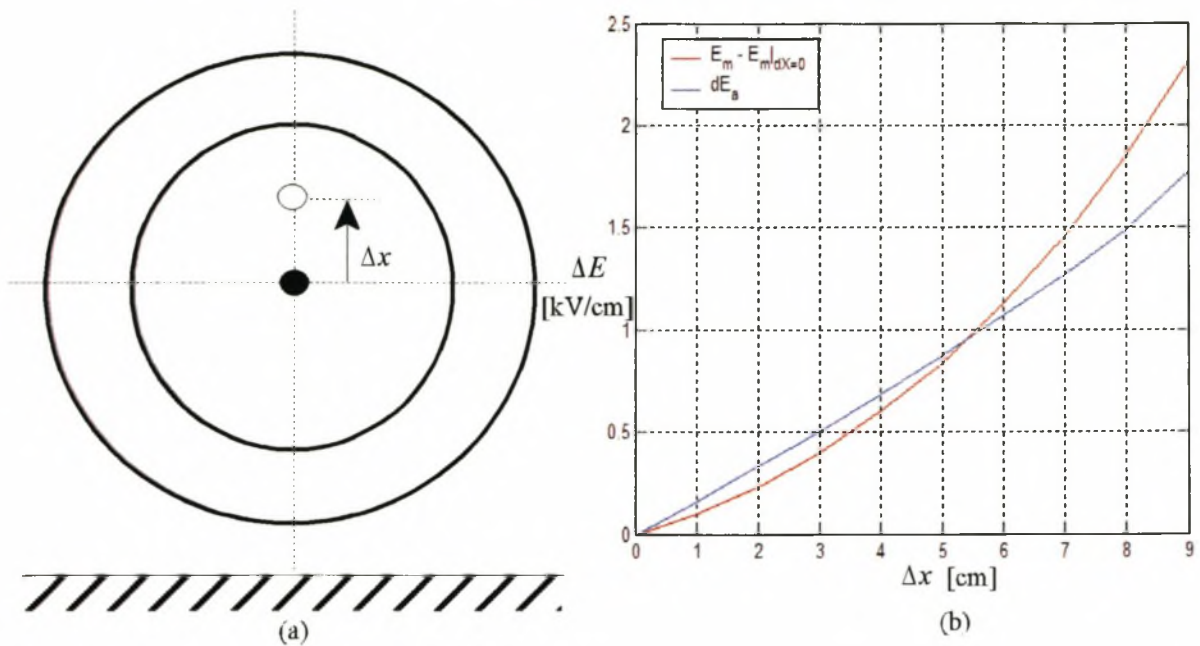

Figure 6.4: (a) A schematic diagram of the small corona cage indicating the displacement of the copper pipe inside the cage and (b) the variation of the maximum surface gradient and ΔE_a with Δx (R_{cage} = 25 cm, r_s = 0.75 cm and V = 90 kV).

The variation of maximum surface gradient and ΔE_a, defined in figure 6.3, in the small corona cage as the smooth aluminium conductor is displaced from the cage centre, is plotted in figure 6.4. The plot indicates that a variation in surface gradient, similar to that on one of the sub-conductors in a twin IEC-800 conductor bundle, can be created on a single conductor placed inside the small US cage by displacing the conductor 9 cm from the cage centre.

6. 2.7 Conductor Bundling

The displacement of the single conductor in the corona cage in the previous experiment caused a change in surface gradient distribution similar to that on a sub-conductor of a bundle. The electric field divergence near the sub-conductor surface in a bundle is however lower than the divergence near the surface of the single displaced conductor. The excitation function of a conductor bundle can therefore not be directly calculated from the excitation function of a single displaced conductor. This is investigated in this experiment.

114

A two conductor bundle is centred in the cage in this experiment. Two 0.75 cm copper conductors are used and the bundle radius is chosen as $R_b = 6$ cm, so that the inception level can be reached with a source voltage below 100 kV. The setup used for the experiment is the small US cage with the insulation coating. The 100 kV transformer and the clean supply are used.

6. 2.8 Conductor Stranding - Small and Medium Size Cages

The previous experiments have investigated the most important relationships, upon which the pulse parameters are dependent, using smooth conductors. Stranded ACSR conductors can now be studied in the small cage.
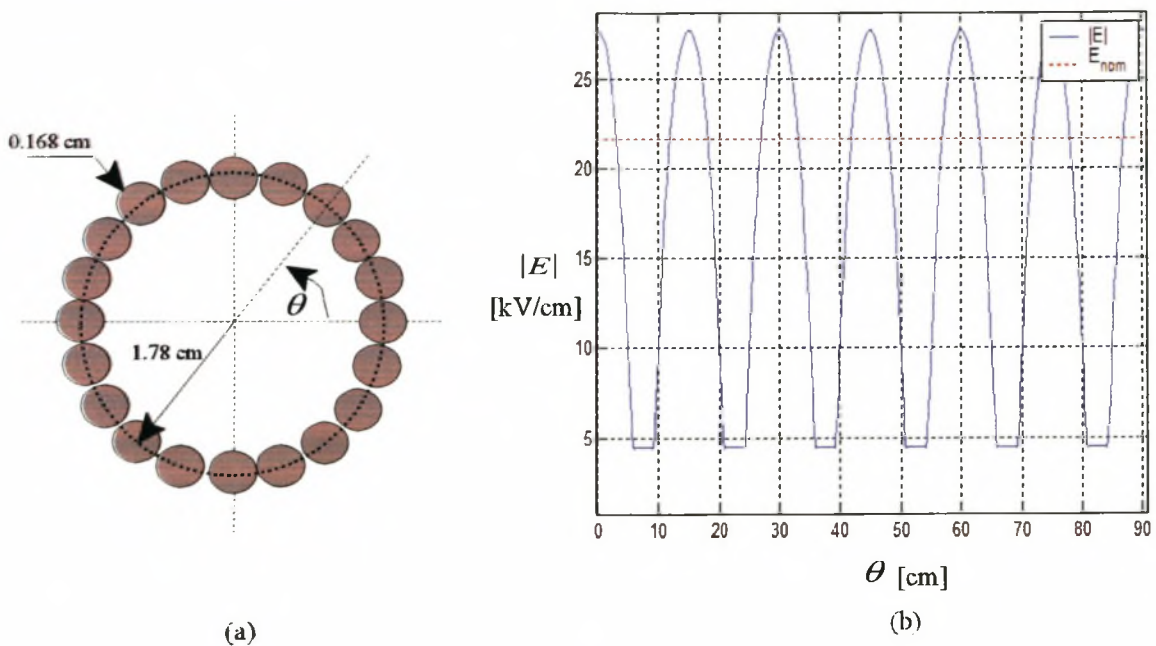

(a)

(b)

Figure 6.5: (a) A schematic diagram of the stranded Dinosaur conductor geometry used in the simulation and (b) the surface gradient calculated for this conductor in the small corona cage using the method of successive images ($R_{cage} = 25$ cm, $V = 90$ kV).

The nominal surface gradient of stranded ACSR conductors is used in the prediction methods of chapter 3. The actual surface gradient is plotted with the nominal surface gradient for a Dinosaur conductor centred in the small US cage in figure 6.5. The variation in surface gradient is larger than the variation due to conductor displacement in a corona cage. The effect of this variation and the use of nominal surface gradients is investigated in this experiment.

115

Dinosaur, Tern and Hare ACSR conductors were prepared for the experiment. The source voltage required for corona inception on all but the Hare conductor was above 90 kV. The experiment was therefore divided into two separate experiments. In the first, the Hare conductor was centred in the small US cage and the 100 kV transformer with clean primary supply was used. In the second experiment, all three ACSR conductors were centred in the medium size UCT cage described in chapter 5. The 300 kV transformer and normal supply voltage were used. This combination of transformer and primary supply was chosen based on the results of the quality of supply experiment. These two experiments concluded the small cage experiments. The data obtained from these experiments must next be analysed.

6. 3   Corona Mode Inception Gradients

Various measurable corona modes were identified in chapter 5. They are the onset and positive streamer pulses in the positive half cycle and the negative streamer pulses in the negative half cycle. These pulse modes were distinguished by their pulse characteristics. It was suggested that separate excitation functions be extracted for each of the three pulse types so that the relationship between each excitation function and the surface gradient is linear. The surface gradient at which the inception of a mode occurs differs for each corona mode and is dependent on factors such as line geometry and environmental conditions. To determine which of the three excitation functions must be included in a transmission line model for a specific line voltage, geometry and weather condition requires that the inception gradient of each mode is known for the line. The small cage experiments described in the previous section are used to determine the relationship between the corona mode inception gradients and various geometrical and environmental factors in this section.

6. 3.1   The Effect of Corona Modes on the RN Performance

The RN performance of a single, centred conductor in the small corona cage is first considered to determine the effect of the various corona modes on the total RN.
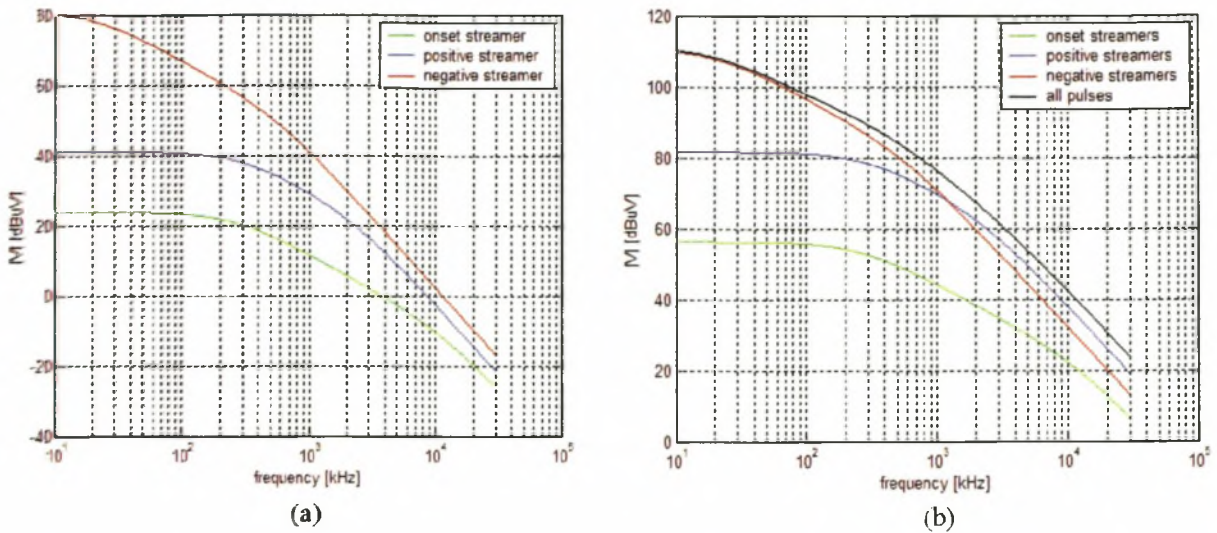
(a)

(b)

Figure 6.6: (a) The frequency spectra of individual pulses of each of the three corona modes and (b) the contributions of each corona mode to the total frequency spectrum.

The pulse train used for the analysis in figure 6.6 was measured from a 0.78 cm aluminium conductor centred in the small US cage at a source voltage of 95 kV. It consisted of 42 onset streamers, 106 positive streamers and 31 negative streamers. The mean pulse parameters are used to calculate the frequency spectra of each mode in figure 6.6 (a). The frequency spectrum of the pulse train is the weighted sum of each mode's contribution and is plotted in figure 6.6 (b). The contribution of the onset pulses is not significant across the band while the contributions of the positive and negative streamers to the total RN spectrum depends on their relative number.
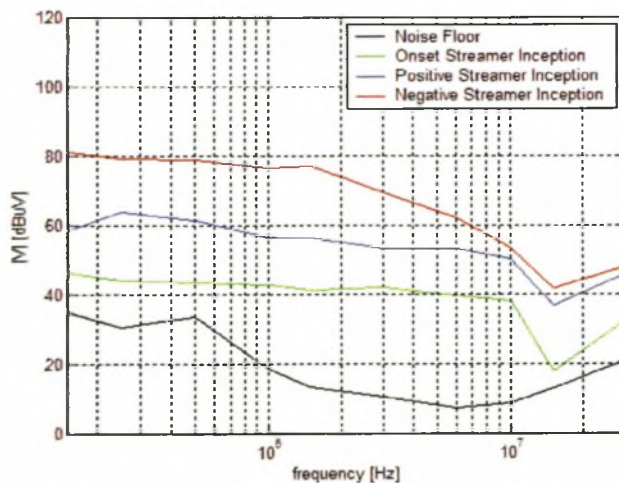

Figure 6.7: The measured QP frequency spectra at the various corona mode inception gradients of the experimental setup used for the data plotted in figure 6.6.

117

The measured QP spectra at the various corona mode inception gradients, for the experimental setup used for the data plotted in figure 6.6, are plotted in figure 6.7. It is evident in both figures, that the inception of either positive or negative streamers will have a large affect on the total spectrum if only onset pulses are present. In figure 6.6, the inception of negative streamers only had a large effect on the total spectrum below 700 kHz. This is because of the relative number of positive and negative streamer pulses at the negative streamer inception gradient and the time constants of the negative streamer pulses. The QP weighting function emphasises the contribution of pulses with larger amplitude. The increase in measured spectra in figure 6.7 therefore resembles figure 6.6 (a) more than figure 6.6 (b). It is concluded from this result that the appearance of only a few positive or negative streamer pulses will significantly affect the measured QP spectrum. The extraction of a wideband excitation function, especially a QP function, therefore requires that the inception gradients of the various corona modes are known.

6. 3.2   A Description of the Discharge Processes

To better understand the relationships between the corona mode inception gradients and the various geometrical and environmental variables, a brief description of the discharge processes involved is necessary. These processes are discussed in detail in [2] and [3] and a summary of these and other references is presented in [1].

When the surface gradient just exceeds the inception level, corona discharges occur in a region with no significant space charge. These are the positive Burst pulses and the negative Trichel pulses. The RN of these two modes is not measurable in the small cage setup used. They do however generate significant space charge and cause measurable corona loss. Negative space charges have higher mobilities than positive space charges and move faster away from the conductor. The secondary ionization mechanism, necessary for corona formation, is photo-ionization for positive corona and ionization by ion impact for negative corona. Photo-ionization is a faster mechanism and is responsible for the shorter rise times of the positive corona modes. The electrons released during the ion impact of negative corona neutralise the positive space charges formed. Negative corona modes therefore have a more efficient space charge clearing mechanism which results in higher repetition rates and higher corona loss. Corona loss is therefore first measured in the negative half cycle and is due to Trichel pulses.

An increase in the surface gradient above the inception level will increase corona generation and therefore also the space charge concentration. If the positive space charge concentration near the anode surface is high enough, the local electric field enhancement will cause the positive discharge to progress further into the gap thereby inducing a larger RN current. These positive discharges are called onset streamer discharges and are the first measurable mode as regards RN. A further increase in surface gradient facilitates more effective secondary ionization which promotes the propagation of positive discharges even further into the gap. These discharges are called positive streamers and are the final corona mode in the positive half-cycle. In the negative half cycle, the accumulation of negative space charge near the cathode surface also causes a local electric field enhancement which allows the ionizing electrons emitted from the conductor by ion impact to travel much further into the gap. These negative discharges have much larger amplitudes than Trichel pulses and are called negative streamers. The development of negative streamers in short gaps usually causes flash-over [3]. Since negative space charge has a higher mobility, it will form further from the conductor surface, thereby reducing its effect on the electric field. The negative streamer inception gradient should therefore be higher than that of positive streamers.

The displacement of the space charge from the conductor surface, Δx, has a significant effect on a inception gradients of the measurable corona modes. The velocity of positive space charge is proportional to the space charge mobility which is in turn proportional to the local electric field and inversely proportional to the RAD [2]. The space charge mobility in air can however be considered constant under normal environmental conditions [2]. The position of the space charge is therefore approximately proportional to the electric field strength [2]:

$$\Delta x \propto E \tag{6.1}$$

The inception gradients of both onset and positive streamer modes are therefore related primarily to the electric field. Negative corona discharges produce electrons near the conductor surface which are repelled by the cathode. Since air contains electronegative gasses such as oxygen, these electrons recombine to form negative space charge as they move away from the cathode. The mobility of electrons is much greater than that of space charge. The distance travelled by the

electrons before they recombine will therefore contribute significantly to the position of the negative space charge from the conductor surface. The number of electrons which recombine in air is related to the distance from the conductor surface by the attachment coefficient η [2]:

$$\frac{\eta}{\delta} \propto K_1 + K_2\left(\frac{E}{\delta}\right) + K_3\left(\frac{E}{\delta}\right)^2 \qquad (6.2)$$

The negative space charge will form further from the conductor surface than the positive space charge did. Once the negative space charge has formed, it will also be displaced away from the cathode as was described by equation 6.1 for positive space charge. The mobility of negative space charge formed in air is however greater. The inception gradient of the negative streamer mode is therefore related to both the electric field and the RAD.

Remnant space charge from the previous half-cycle of opposite polarity will also affect the corona modes. Remnant positive space charge accelerates the ionizing electrons of a negative discharge. These electrons then recombine with the positive space charge once they reach it, reducing the distance travelled by the discharge. In this way, Trichel pulses have increasing rise times and decreasing amplitudes as the remnant space charge increases. Remnant negative space charge in the positive half cycle will cause the positive space charge to form closer to the conductor surface. This will lower the onset streamer and positive streamer inception gradients.

6. 3.3 Inception Gradient Prediction Methods

Peek's empirical formula was given in equation 4.4 for calculating the corona inception gradient of a conductor bundle. It was not mentioned which corona mode this inception gradient was defined for. It was noted in [2] that the empirical constants derived by Peek for AC corona are the same as those derived by Whitehead [4] for negative DC corona. This suggests that equation 4.4 was derived from corona loss measurements. From the discussion in the previous section it is concluded that this equation is used to calculate the inception gradient of the Trichel pulse mode since this is the first significant corona loss mode. This corona mode does not produce significant RN. New equations must be derived to predict the inception gradients of the measurable corona modes. These equations will be derived from the small cage experiments described in section 6.2.

6. 3.4   Measuring the Inception Gradients

Equation 4.4 is used as the basis for deriving the inception gradients for the various corona modes. The roughness factor, m, must therefore be extracted for each conductor used. A method of deriving the Trichel mode inception gradient by calculating the Q-V relationship from the current induced on the corona cage is described in [1] and is used in this chapter. The burst pulse mode is typically the first corona mode in a small AC corona cage setup [2]. The inception gradient of this corona mode is therefore defined in this research as the gradient at which either visual or acoustic emissions are first observed. The Corocam, described previously, is used to make visual observations of burst pulse inception. The acoustic emission from burst pulses is significant and easily detected.

The effect of the corona modes on the measured RN was described in figure 6.6 and 6.7. The best method to determine the inception gradients of these modes is with the sampling card. It takes a long time however to record and process a sampled pulse train.

(a)   (b)
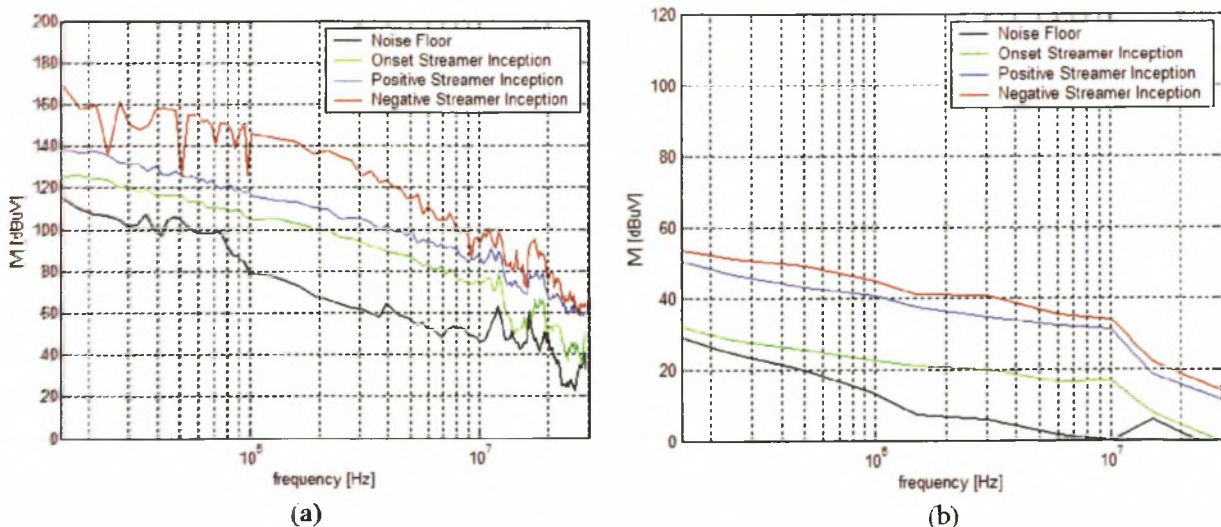
Figure 6.8: The (a) peak and (b) average RN frequency spectra at the various corona mode inception gradients for the experimental setup used for figure 6.6.

The measured peak and average frequency spectra at the various corona mode inception gradients, in the experimental setup used for the data plotted in figure 6.6, are plotted in figure 6.8. Comparing figures 6.7 and 6.8, it is concluded that the best method of measuring the inception gradients of the corona modes, which produce significant RN, is with a QP detector.

121

6. 3.5 Analysis of the Measured Inception Gradients

The various corona mode inception gradients are extracted from the experiments described in section 6.2. They are analysed in this section in order to derive empirical equations needed to calculate the corona inception gradients for a transmission line conductor bundle.

measurement (as in appendix H)	Inception Gradient [kV/cm]				Variables		
	Trichel + Burst	onset streamers	positive streamers	negative streamers	a	δ	RH [%]
1	26	28	30	34	0.75	1.026	67
2	26	28	29	33	0.75	1.026	67
3	26	28	31	32	0.75	1.025	70

Table 6.1: Measured corona mode inception gradients (quality of supply experiment).

A comparison of the various corona mode inception gradients for the quality of supply experiment is presented in table 6.1. The comparison indicates that the change in quality of supply used in the experiment only affects the positive and negative streamer inception gradients. This is because the quality of supply affects the quantity and position of the space charge produced during the half-cycle as well as the quantity and position of the remnant space charge produced during the previous half-cycle. The roughness factor of the smooth copper pipe used is extracted from the experiment as $m = 0.856$. A corona mode factor is added to equation 4.3 to include the corona inception gradients of the various measurable corona modes:

$$E_{cm} = k_m \cdot \left[21.9m\delta \left(1 + \frac{0.308}{\sqrt{\delta.a}} \right) \right] = k_m \cdot E_c \tag{6.3}$$

	Trichel + Burst	onset streamer	positive streamer	negative streamer
k_m	1	1.078	1.194	1.232

Table 6.2: Calculated corona mode factors.

The value of this factor for each mode is extracted from the measured inception gradients of measurement 3 in table 6.1 (i.e. the ideal supply measurement) and is presented in table 6.2.

measurement	Inception Gradient [kV/cm]				Variables		
	Trichel + Burst	onset streamers	positive streamers	negative streamers	a	δ	RH [%]
1	26	29	30	34	0.75	1.021	60
2	25	25	26	27	0.75	0.825	72
3	26	28	31	32	0.75	1.025	70

Table 6.3: Inception gradients measured in the RAD and RH experiment.

A comparison of the various corona mode inception gradients for changes in RAD and RH is presented in table 6.3. A 10% change in RH did not significantly affect the Trichel and Burst pulse onset gradients. It did however affect the quantity and position of the space charge produced and thereby affected the measurable corona mode inception gradients. A RH factor is therefore added to equation 6.3:

$$E_{cm} = k_m.E_c\left[1 - k_{RH}(70 - RH)\right] \tag{6.4}$$

	Trichel + Burst	onset streamer	positive streamer	negative streamer
k_{RH}	0	-0.0039	0.0029	0.0028

Table 6.4: Calculated RH factors.

The value of this factor for each mode is extracted from measurement 1 in table 6.3. The result is presented in table 6.4.

The relationship between the Trichel mode inception gradient and RAD factor is included in equation 4.4. A relationship between the space charge position and the RAD was discussed in section 6.3.2 and was found to differ for the positive and negative corona modes. A RAD factor term is therefore added to equation 6.4 for the measurable corona modes:

$$E_{cm} = k_m.E_c.\left[1 - k_{RH}(70 - RH)\right].\left[1 + k_{RAD}(1 - \delta)\right] \tag{6.5}$$

	Trichel + Burst	onset streamer	positive streamer	negative streamer
k_{RAD}	0	0.204	0.241	0.270

Table 6.5: Calculated RAD factor terms.

The value of the RAD factor term for each mode is extracted from measurement 2 in table 6.3. The result is presented in table 6.5. Considering equation 6.2 and the discussion in section 6.3.2, a decrease in RAD should increase the position of the negative space charge from the conductor surface but should not significantly affect the position of the positive space charge. The RAD factor defined in equation 6.5 is therefore expected to be larger for negative streamers than for positive streamers. The results in table 6.5 confirm this.

	Inception Gradient [kV/cm]				Variables		
measurement	Trichel + Burst	onset streamers	positive streamers	negative streamers	a	δ	RH [%]
1	26	28	31	32	0.75	1.025	70
2	30	32	32	36	0.78	1.033	65

Table 6.6: Inception gradients measured in the conductor material experiment.

A comparison of the inception gradients for smooth copper and aluminium conductors of similar dimensions is presented in table 6.6. Both conductors are cleaned so that their surfaces are in a similar state. The roughness factor of the aluminium conductor is therefore assumed to equal that of the copper conductor. The secondary ionization mechanism of the Trichel pulse discharges is positive ion impact. The amount of energy a positive ion must impart on the cathode surface in order to release an electron is called the work function of the conductor. The conductor's work function is unique to the specific metal used. In light of the comparison in table 6.6, the work function of aluminium must be higher than that of copper. The inception gradient of the Trichel pulse mode is therefore higher for aluminium conductors. The inception gradients of the measurable corona mode are dependent on space charge distributions and will be affected by the work function. An aluminium work function factor is therefore added to equation 6.5 for all the

124

corona modes:

$$E_{cm} = k_{Al} \cdot k_m \cdot E_c \cdot \left[1 - k_{RH}(70 - RH)\right] \cdot \left[1 + k_{RAD}(1 - \delta)\right] \qquad (6.6)$$

	Trichel + Burst	onset streamer	positive streamer	negative streamer
k_{Al}	1.153	1.141	1.031	1.123

Table 6.7: Calculated aluminium work function factors.

The value of this factor for each corona mode is extracted from measurement 2 in table 6.6 and is presented in table 6.7. It is noticeable that the positive streamer inception gradient is not significantly affected by the conductor work function. The secondary ionization mechanism of positive corona is photo-ionization. The work function therefore does not affect the quantity and position of the positive space charge formed. The result therefore suggests that the inception of positive streamers is more dependent on the applied electric field than on the exact position of remnant space charge.

measurement	Inception Gradient [kV/cm]				Variables		
	Trichel + Burst	onset streamers	positive streamers	negative streamers	a	δ	RH [%]
1	31	32	32	-	0.50	1.031	62
2	28	28	-	-	1.25	1.031	62
3	24	26	-	26	1.10	1.031	62
4	30	32	32	36	0.78	1.033	65

Table 6.8: Inception gradients measured in the electric field divergence experiment.

A comparison of the various corona mode inception gradients for changes in conductor diameter is presented in table 6.8. The measured Trichel pulse mode inception gradient corresponds to the value calculated with equation 6.6. The comparison in table 6.6 suggests that the inception gradients of the corona modes with measurable RN are related to the electric field divergence.

According to equation 4.4, the surface gradient is much lower for the 1.25 cm smooth aluminium conductor at Trichel pulse inception. The positive and negative space charges are therefore formed closer to the conductor surface at this lower surface gradient. As a result, onset streamer inception occurs at the same gradient as burst pulse inception in measurement 2. The maximum applied surface gradient is below the positive and negative streamer inception gradients in measurement 2 due to the 100 kV source voltage limitation for the clean supply. Measurement 3 uses a copper conductor of similar radius to measurement 2. Trichel pulse inception occurs at 24 kV/cm due to the lower work function of copper. Since the negative space charge forms closer to the surface than in measurement 4, the negative streamer inception level is reduced. In fact, negative streamer inception occurs before onset streamer pulse inception in measurement 3.

It has already been mentioned that the onset and positive streamer inception gradients are dependent more on the surface gradient than the exact position of the remnant space charge. A comparison of measurements 1 and 4 and previous results discussed in this section leads to the conclusion that there is a maximum onset and positive streamer inception gradient for smooth conductors. It is noted in [2] however that positive streamer inception does not occur on very thin conductors. This is not the case for conductor radii used on high voltage transmission lines. The inception of negative streamers in the small US cage leads to flash-over. This was observed in all the measurements used in this section. This phenomenon was also noted in [3] and is a significant limitation of the small cage design since it is not possible to measure corona at gradients above the negative streamer inception gradient. The inception of negative streamers did not cause flash-over in either the medium US or UCT cages. The choice of cage radius must therefore consider the maximum required surface gradient and the minimum negative streamer inception gradient. The clean supply voltage limitation and cage radius used does not allow for the extraction of the relationship between the inception gradients and the conductor radius.

measurement	Inception Gradient [kV/cm]				Variables		
	Trichel + Burst	onset streamers	positive streamers	negative streamers	a	δ	RH [%]
1	12	-	-	13	0.75	1.025	62

Table 6.9: Inception gradients measured in the conductor bundling experiment.

126

The electric field divergence near the surface of sub-conductors comprising a bundle is much reduced from that of an isolated single conductor of the same radius. The Trichel pulse inception gradient of the twin smooth copper bundle described in section 6.2.7 is correctly predicted by equation 4.4 and the equivalent radius of the bundle. The negative streamer inception gradient was measured below the onset and positive streamer inception gradients. This confirms the effect of field divergence on the negative streamer inception gradient discussed previously.

	Inception Gradient [kV/cm]				Variables		
measurement	Trichel + Burst	onset streamers	positive streamers	negative streamers	a	δ	RH [%]
1	20 (27)	21 (29)	23 (32)	-	0.71	1.02	50

Table 6.10: Nominal inception gradients measured in the conductor stranding experiment (the maximum surface gradients are given in brackets).
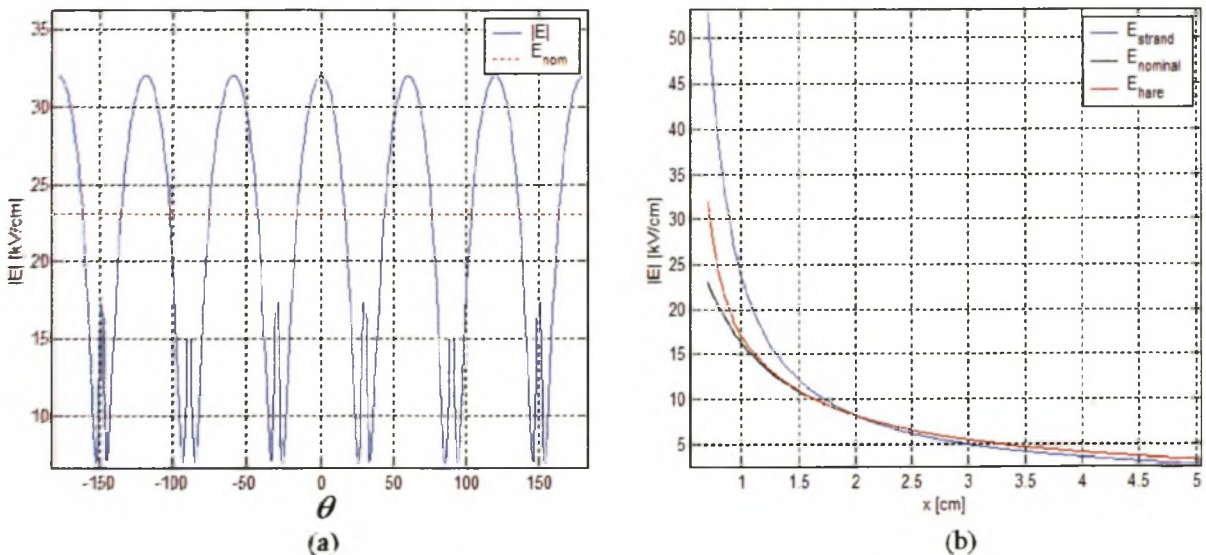
Figure 6.9: (a) The surface gradient calculated for the small corona cage conductor stranding experiment and (b) the radial electric field distribution between the ACSR Hare conductor and the corona cage ($R_{cage} = 25$ cm, $V = 58$ kV).

The nominal surface gradient of the stranded ACSR conductors is used in the prediction methods. The actual surface gradient and radial field distribution of a Hare conductor is plotted in figure 6.9. The plot indicates that the maximum surface gradient is significantly higher than the nominal value. The electric field divergence near the conductor surface lies between the

nominal value and the divergence of an isolated Hare conductor strand. The radial field reconciles with the nominal field at a distance of about 1 cm from the conductor surface.

The stranded conductor was cleaned of any pollutants and found to have more nicks and scratches than the smooth conductor. Its roughness factor should therefore be lower. The burst and Trichel pulse inception gradients were found to be nearly equal for the smooth conductors measured in the small US corona cage. For a stranded conductor however, the burst and Trichel pulse inception gradients were observed at maximum gradients of 27 kV/cm and 31 kV/cm respectively. The roughness factor was derived from the Trichel pulse inception gradient and the conductor's outer radius as $m = 0.78$. Comparing the results in table 6.8 to the result in table 6.10, two conclusions are made for the ACSR Hare conductor. Firstly, the positive corona mode inception gradients of the stranded conductor correspond to those of a smooth conductor with the same nominal radius if the maximum surface gradient on the stranded conductor is considered. This was previously attributed to the fact that the positive corona modes are more dependent on the surface gradient than on the exact position of the space charge. The negative corona inception gradients correspond to those of a smooth conductor with the same radius as the individual strand radius. This is because the secondary ionization mechanism of negative corona is ion impact. The increased field divergence due to conductor stranding forces the negative space charge to form further from the conductor surface. Conductor stranding therefore increases the gradient at which corona loss and negative streamers occur. The onset streamer inception gradient is reduced from its 32 kV/cm maximum value by remnant negative corona. Since the main sources of RN are the positive and negative modes, it is concluded that conductor stranding improves the RN performance of a conductor.

measurement	Inception Gradient [kV/cm]				Variables		
	Trichel + Burst	onset streamers	positive streamers	negative streamers	r_s / r_{nom}	δ	RH [%]
Dinosaur	15 (21)	16 (22)	19(26)	21 (29)	0.111	1.025	48
Tern	17 (22)	18 (23)	22(30)	26 (34)	0.125	1.025	48

Table 6.11: Inception gradients of two ACSR conductors measured in the medium UCT corona cage with the 300 kV transformer and normal supply.

128

In order to observe the corona modes on conductors used on the transmission lines described in chapter 2, a Dinosaur and a Tern conductor are placed in the medium size UCT cage and energized with the 300 kV transformer and the normal supply. It has already been shown how this non-ideal 50 Hz source voltage affects the positive and negative streamer inception gradients. Conclusions drawn from this experiment are therefore only valid for a similar supply. They do however illustrate an important point discussed below and are therefore included.
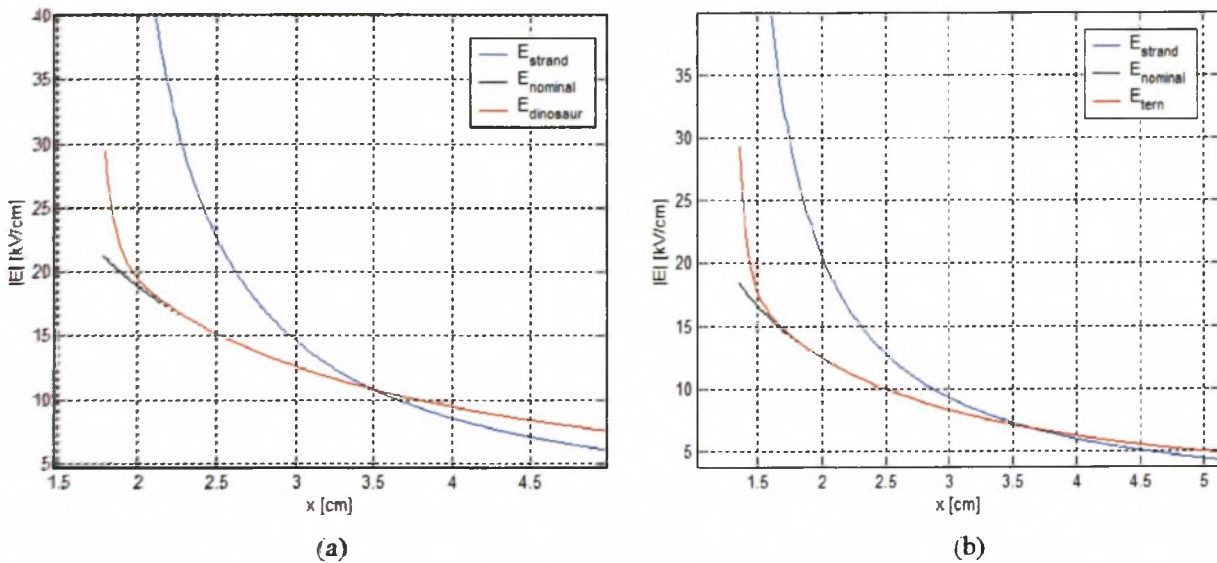
Figure 6.10: The radial electric field distribution between the corona cage and (a) a Dinosaur and (b) a Tern ACSR conductor (R_{cage} = 75 cm, V = 100 kV).

The radial electric field between the corona cage and both a Dinosaur and a Tern conductor is plotted in figure 6.10. An important parameter, the conductor stranding ratio, is calculated in table 6.10. This parameter is the ratio between the strand radius and the nominal conductor radius. The stranding ratio of a Hare conductor is 0.3324. A comparison of figures 6.9 and 6.10 suggests that a decrease in this parameter causes a decrease in both the maximum surface gradient and the field divergence near the conductor surface. The electric field near the conductor surface therefore more closely resembles that of a smooth conductor rather than that of an isolated strand. A reduction in the stranding ratio therefore reduces the inception gradients of the measurable corona modes. This is confirmed by the measurements presented in table 6.10. The effect of stranding ratio on the various corona mode inception gradients should be further investigated with a clean supply. It is concluded from the discussion in this section that the RN performance of a stranded ACSR conductor is improved by increasing its stranding ratio.

6. 3.6 Negative Streamers

It is stated in [2] that negative streamers cannot be observed under an AC excitation and normal environmental conditions because the breakdown gradient is lower than the negative inception gradient. Flash-over will therefore occur in the positive half cycle before negative streamers are formed. The large diameter electrode used in [2] did not permit the formation of negative streamers over the measured gradient range. The results presented in the previous section suggest that negative streamers do occur on stranded conductors at practical surface gradients. Since negative streamers produce high RN levels, they must be accounted for if they appear on transmission line conductors. The nominal negative streamer inception gradient of a single Dinosaur conductor is 21 kV/cm in table 6.11. This conductor has similar dimensions to the IEC-800 conductor used in the bundle which was tested in chapter 4. The maximum nominal gradient applied to this bundle was 25 kV/cm which is higher than the negative streamer inception gradient of a single Dinosaur conductor. It was also shown in the previous section that conductor bundling reduced the negative streamer inception gradient. Negative streamers were observed on the bundle conductor at an applied gradient of 17 kV/cm (c.f. figure 4.5). The effect of the ratio of bundle radius to sub-conductor radius on the negative corona inception gradient could not be tested in the small cage due to the restricted source voltage available. The RN measurements presented in figure 4.3 can however be used to determine the inception gradient of negative streamers. This is discussed in this section.
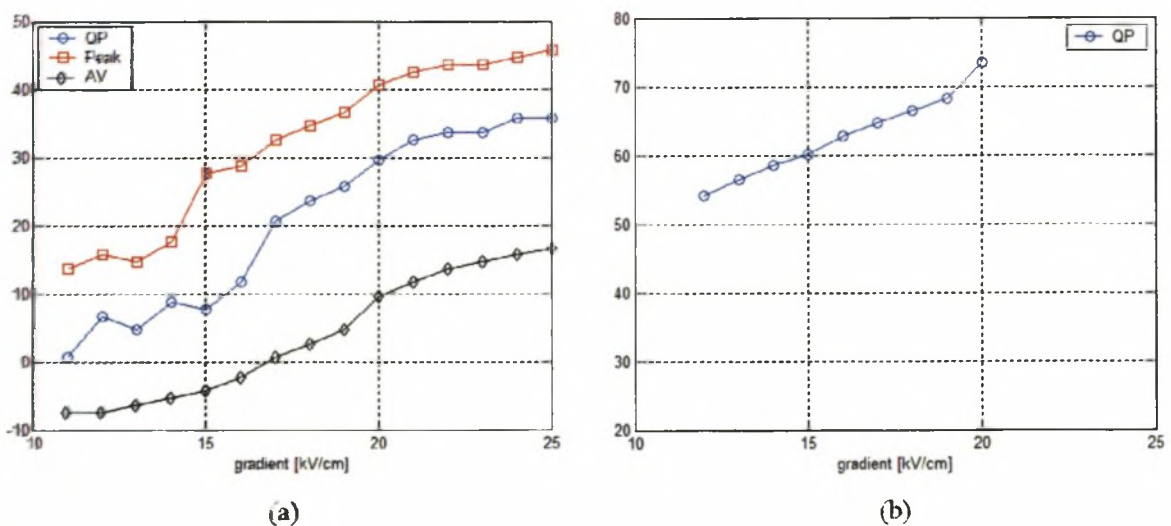
Figure 6.11: The QP, peak and average RN levels measured at the Megawatt Park facility on a twin IEC-800 conductor bundle at (a) 500 kHz and (b) 2 MHz.

Along with the time domain measurements, the QP and peak RN levels were measured at the wideband measurement point of the Megawatt Park corona cage from 500 kHz to 30 MHz. The measured narrowband RN levels at 500 kHz and the measured wideband RN levels at 2 MHz are plotted against the applied average maximum surface gradient in figure 6.11.

The nominal burst pulse and onset streamer inception gradients were found to be more dependent on the outer conductor radius and less sensitive to a change in field divergence. These levels should therefore be similar to those of the single Dinosaur conductor presented in table 6.11. Accounting for the reduction in the RAD factor due to the increase in altitude, the estimated onset inception level is 12 kV/cm. The conductor bundling will significantly decrease both the positive and negative streamer inception gradients. In figure 6.11 (a), the peak, QP and average RN levels increased steadily between 12 kV/cm and 15 kV/cm. The time domain measurements confirmed that both onset and positive streamers were present at these surface gradients. Conductor bundling therefore reduced the positive streamer inception level to 12 kV/cm which is the same as the onset streamer inception level. The peak RN level increased at 15 kV/cm by more than 10 dB. Time domain measurements confirmed the inception of a few isolated negative streamers at this point. There were however not enough negative streamers relative to the number of positive streamers to affect either the QP or average RN levels significantly. The ratio of negative to positive streamers increased steadily as the average maximum bundle gradient was increased above 15 kV/cm. The QP and average levels were first significantly affected by this increasing ratio at 17 kV/cm and 20 kV/cm respectively. Figure 6.11 (b) indicates that the effect of negative streamers on the measured QP and average RN levels is more significant at lower frequencies. This is due to the longer rise and decay time constants of this discharge mode. Conductor bundling therefore reduced the positive and negative inception gradients and made the RN performance of the phase conductor worse. The effect of conductor bundling on the RN performance is more significant at lower frequencies.

6. 4   Space Charge Distribution and Small Corona Cage Design

The space charge distribution experiment was not analysed in section 6.3. In this experiment the use of an insulating paint to prevent the recombination of space charge on the corona cage was investigated. It was proposed in section 6.2 that if the space charge reached the cage surface

which was coated with the insulating paint, the charge would linger near the surface until the source voltage reverses polarity and the space charge was attracted back towards the centre conductor. This theory and the effect of the disturbed space charge distribution on the pulse parameters is investigated in this section.

6. 4.1 Identification of Influencing Variables

The inception gradient investigation of section 6.3 revealed an important relationship between the space charge distribution and the corona discharge processes. The space charge distribution under fair weather laboratory conditions is influenced by the surface gradient, electric field divergence, RAD and RH. Diffusion is another important process which affects the movement of space charge but has not yet been mentioned. The existence of a space charge density gradient in or near the cage will give rise to diffusion. This process is described in [2].

6. 4.2 Space Charge Prediction Methods

The maximum radius of the space charge distribution from the centre conductor surface at corona inception was defined empirically for a coaxial geometry in equation 4.5. For a 50 Hz supply and a practical transmission line or corona cage geometry, this maximum space charge displacement is proportional to the square root of the charge mobility.

A space charge simulation model was described in chapter 5. This model does not however include the effect of space charge diffusion. The space charge displacement vector due to diffusion is related to the space charge density, n, by a diffusion coefficient D [2]:

$$\Gamma = D\left[\nabla.n(r,\theta)\right] \tag{6.7}$$

The diffusion coefficient of space charge is related to its mobility by the Einstein relation [2]:

$$\frac{D}{\mu} = 0.864 \times 10^{-4}.T \tag{6.8}$$

where T is the temperature of the gas in degrees Kelvin.

6. 4.3   The Affected Pulse Parameters

The definition and extraction of corona pulse parameters from the small cage measurements were described in chapter 5. The effect of a distortion in the space charge distribution, due to the cage radius, on the pulse parameters is analysed in this section.
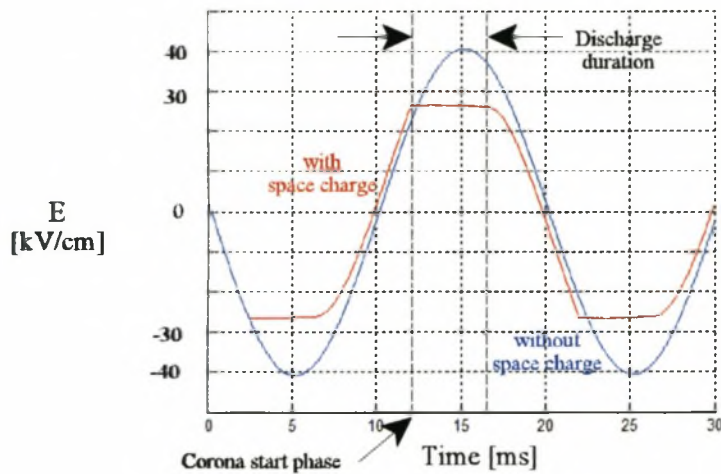
Figure 6.12: The surface gradient during the positive half cycle with and without space charge considered showing the expected duration of corona activity.

The space charge distribution experiment utilized the small US cage. Since negative streamers will cause flash-over in this cage, the effect of changes in space charge distribution is studied in the positive half cycle below the negative streamer inception gradient. The surface gradient variation on the centre conductor during the positive half cycle is plotted in figure 6.12 for the case of no space charge and also for a simulated space charge distribution. Remnant negative space charge from the previous half cycle is attracted towards the anode and induces positive charge on the conductor. This increases the anode's surface gradient so that the corona inception gradient is reached earlier than if space charge was not present. The amount of remnant negative space charge increases as the source voltage is increased, thus decreasing the source voltage phase at which inception occurs and increasing the duration of the corona activity. Positive space charge has a lower mobility than negative space charge in air. The effect of a change in the remnant positive space charge on the Trichel pulse activity in the negative half cycle is therefore not as significant as the effect of a change in the remnant negative space charge on the positive corona.

133

Onset and positive streamer discharges occur only if there is an accumulation of positive space charge near the anode surface. The positive space charge produced by Burst pulse activity must therefore first neutralise the remnant negative space charge before measurable discharge modes appear. An increase in remnant negative space charge therefore increases the duration of the Burst pulse mode but decreases the duration of the onset and positive streamer modes.
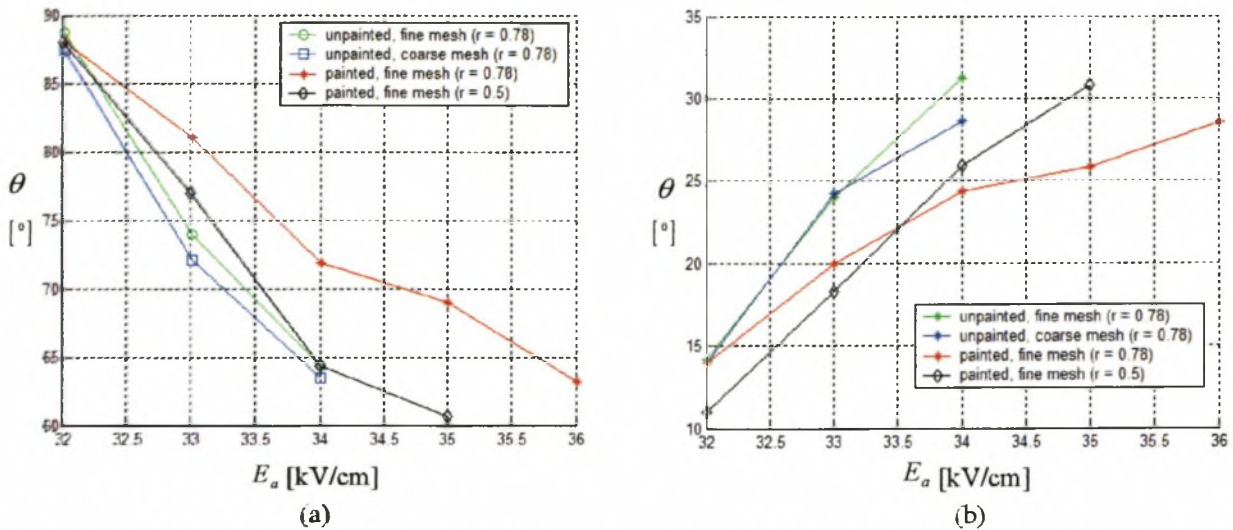
Figure 6.13: (a) The onset streamer start phase and (b) corona discharge duration for the space charge distribution and field divergence experiments.

The onset streamer start phase and corona discharge duration for the space charge distribution experiment is plotted in figure 6.13. Also included in the plot is the smaller diameter aluminium conductor measurement of the field divergence experiment. It is included because the space charge in this setup should not collide with the corona cage for the full range of applied gradients, according to equation 4.5. The Trichel pulse inception gradient is the same for all the measurements in the space charge distribution experiment. The comparison indicates that the start phase and discharge duration is also the same for all the measurements at the inception of onset streamers. This suggests that the space charge has not reached the corona cage and its distribution is therefore not affected by the cage. The rate of change in start phase and discharge duration differs however between the painted and unpainted cages above the onset streamer inception gradient. Onset and positive streamers produce space charge further into the gap than Burst or Trichel pulses. Space charge collision with the cage therefore first occurs in the positive half cycle and is not predicted by equation 4.5 which is only valid for Burst and Trichel pulses.

134

If the positive space charge recombines with the unpainted cages, there will be no remnant positive space charge in the negative half-cycle. In the case of the painted cage, positive space charge does not recombine and will have to be neutralized in the negative half cycle before negative space charge can form in the gap. More remnant space charge is therefore present near the anode surface in the case of the unpainted cages. This explains the greater change in start phase and discharge duration with increasing voltage for the unpainted cages. A small change in the discharge duration at 33 kV/cm for the unpainted cage with coarse grid dimensions indicates that the space charge recombination at the cage surface is not complete and can be reduced by minimizing the surface area of the corona cage. This reduction is however not significant when compared to the painted cage measurement.

When negative space charge reaches the painted cage, it lingers near its surface. The remnant negative space charge layer is therefore more concentrated and closer to the anode during the positive half cycle. The amplitudes and rise time constants of the onset and positive streamer discharges are therefore reduced by the change in space charge distribution caused by the collision of this charge with the painted corona cage. The corona pulse detection algorithm described in chapter 5 cannot detect the smaller onset pulses. The increase in number of detected pulses, onset streamer start phase and total discharge duration with the same increase in applied voltage will be reduced in the case of the painted cage. This occurs for both painted cage measurements in figure 6.13 at 34 kV/cm.
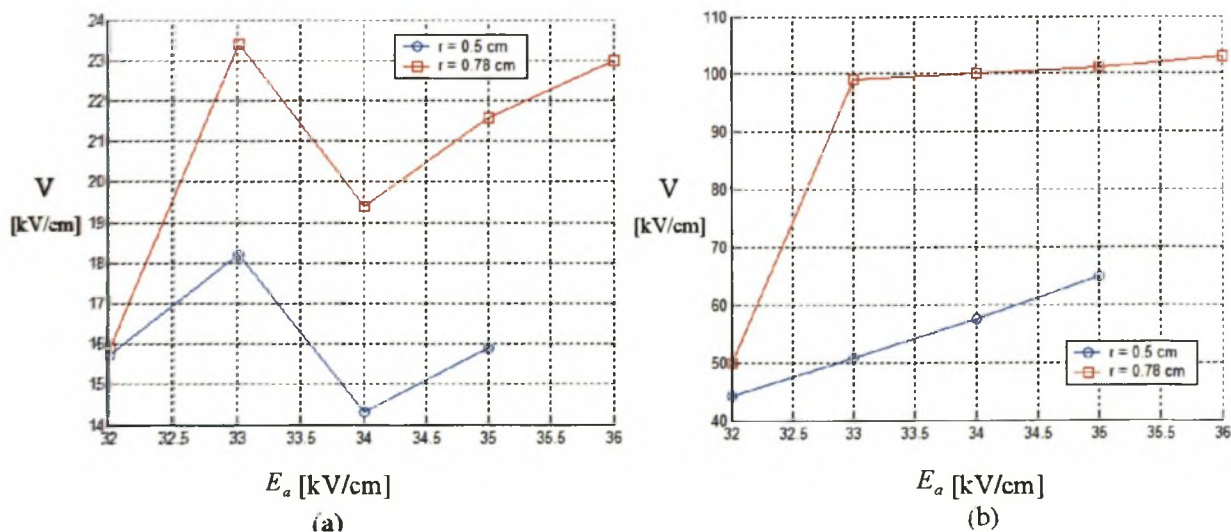
Figure 6.14: (a) The onset streamer and (b) positive streamer pulse amplitude variations for the field divergence experiment.

The reduction of onset and positive streamer pulse amplitudes at 34 kV/cm due to the collision of negative space charge with the painted cage is clearly visible in the measurements plotted in figure 6.14. The effect appears to be more significant for the onset streamers than for the positive streamers. Similarly a comparison of the rise and decay time constants extracted from the same experiment and plotted in appendix H confirm that the rise time constants are reduced and the decay time constants are increased at 34 kV/cm.

The changes in corona pulse parameters due to the collision of space charge with the painted cage are linearly related to the applied surface gradient. The effect of these collisions can therefore be accommodated by introducing a correction factor. This correction factor appears to be a linear function of applied surface gradient and is also dependent on the conductor radius and the corona mode inception gradients. The correction factors of the measurements presented in figure 6.14 can be extracted from a comparison of the rate of increase of each parameter above and below 34 kV/cm. This is the gradient at which the effect caused by space charge collisions with the painted corona cage on the discharge characteristics becomes significant.

The assumption that the change in pulse parameters is a linear function of surface gradient must next be verified. This is best done with the measurement made in the small cage conductor stranding experiment. In this experiment, a stranded ACSR Hare conductor was centred in the painted small US corona cage.
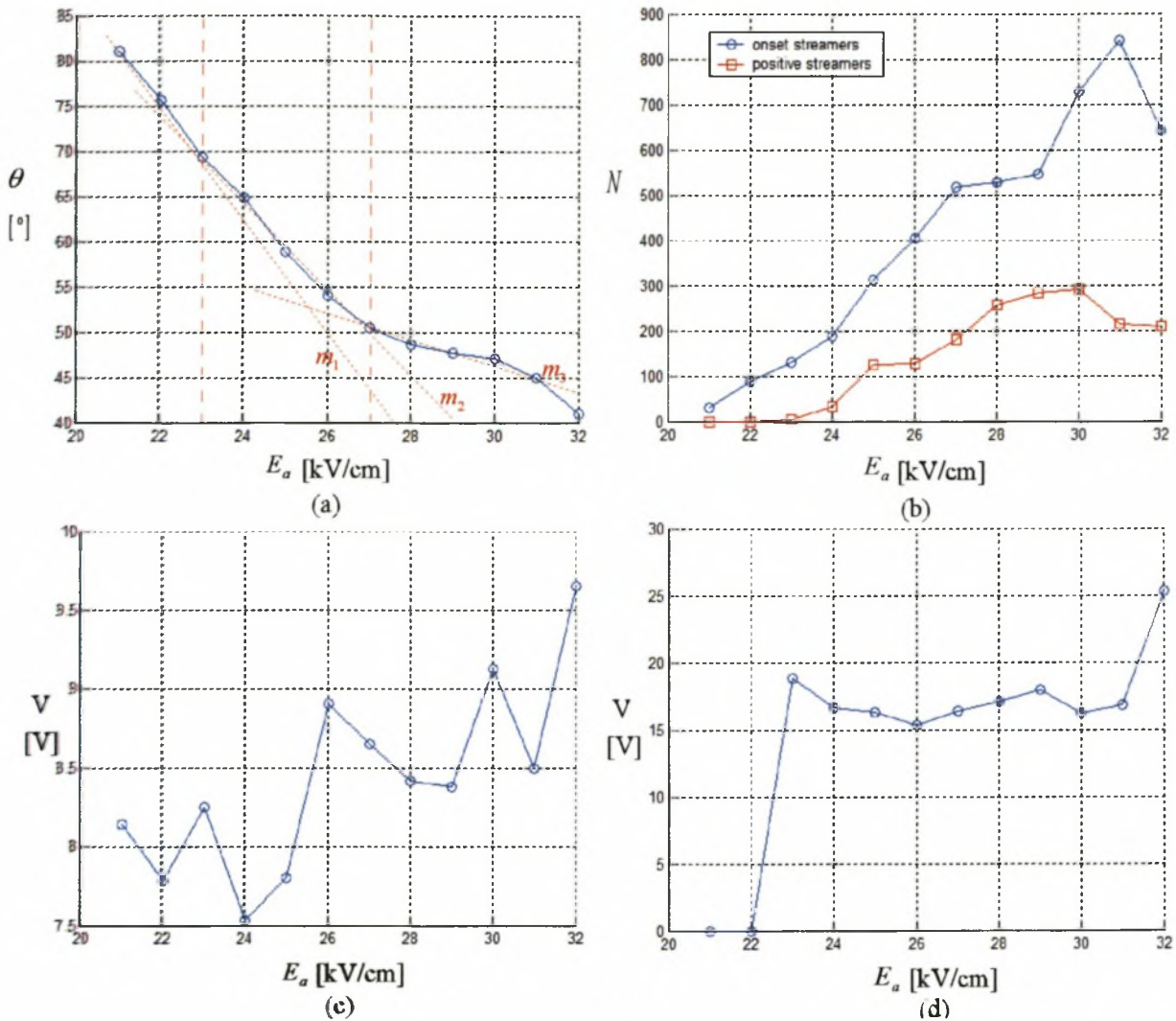
Figure 6.15: (a) The onset streamer start phase, (b) corona pulse number, (c) onset streamer pulse amplitude and (d) positive streamer pulse amplitude variation for the small cage conductor stranding experiment (all gradients are nominal values).

The variation of various selected pulse parameters of the cage conductor stranding experiment is presented in figure 6.15. From these plots as well as plots of the other pulse parameters presented in appendix H, the nominal gradient at which the painted cage begins to significantly affect the space charge position is identified as 23 kV/cm. The calculated maximum surface gradient for this applied voltage is 32 kV/cm. The effect of this change in the space charge distribution on the pulse parameters is linearly related to the change in gradient between 23 and 27 kV/cm. The maximum surface gradient at a nominal value of 27 kV/cm is 38 kV/cm. The rate of change in pulse parameters again changes at this gradient and is no longer a linear function of the applied voltage.

137

The time taken for the space charge created near the conductor surface to reach the corona cage decreases as the surface gradient is increased. A large density of space charge is therefore forced to linger near the cage surface, which is surrounded by a zero field region outside the cage and should be void of space charge. The result is a large space charge density gradient in the radial direction away from the centre conductor that increases with increased surface gradient. The space charges near the cage surface will diffuse into the zero field region in the direction of the density gradient and will not return to the centre conductor once the source voltage polarity reverses. The corona cage therefore has a maximum space charge capacity which is maintained by space charge diffusion and is dependent on the cage's radius. In the stranded conductor experiment, space charge diffusion has a significant effect on the pulse parameters if the maximum surface gradient exceeds 38 kV/cm. Once this happens, the effect of the collisions on the pulse parameters is no longer linearly related to the surface gradient increase.

6. 4.4 Conductor Placement in a Small Corona Cage

In the surface gradient distribution experiment, the smooth centre conductor was displaced from the centre of the corona cage in order to create a non-uniform surface gradient distribution on the conductor. The experimental results have not yet been used in this chapter because flash-over occurred below the negative streamer inception gradient and only marginally above the positive streamer inception gradient for a conductor displacement greater than 3 cm. To explain this, the space charge collisions at the painted cage surface must be considered.
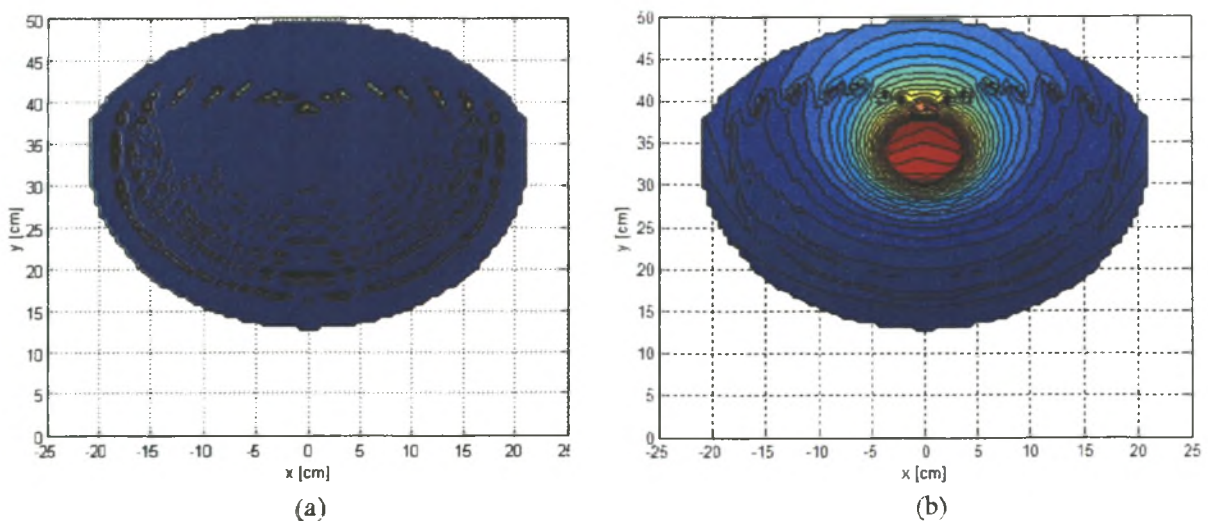
Figure 6.16: The (a) space charge and (b) electric field distributions for the small US corona cage with a smooth copper conductor displaced by 9 cm from the cage centre.

138

The simulated space charge and electric field distributions for the small US cage, with a smooth copper conductor displaced by 9 cm from the cage centre, are plotted in figure 6.15 just before the remnant positive space charge reaches the anode surface and before the inception of Trichel pulses. The space charge distribution indicates that the cage coating, which forces the positive space charge to linger at its surface, causes a non-uniform space charge distribution. This causes the electric field to become very uniform near the conductor surface in the direction of the conductor displacement inside the cage. Flash-over will occur before corona inception in a uniform field. The disturbance of the space charge distribution by the insulated corona cage, with a displaced centre conductor, causes a significant decrease in the flash-over voltage. The effect of the non-uniform space charge distribution on the pulse parameters is also not linear (c.f. appendix H). It is therefore concluded that the centre conductor cannot be displaced in a small corona cage if the space charge collides with the insulated cage surface. This is an important limitation to the small cage measurements and means that the surface gradient distribution experiment cannot be made in the small corona cage. The maximum conductor displacement in the conductor bundling experiment was only 3 cm. The extracted inception gradients should therefore not be too greatly affected by the space charge collisions with the insulated cage. A larger bundle radius could however not be used in the small corona cage.

6.5   The Predicted Wideband Excitation Functions of ACSR Conductors

The non-linearities in the relationship between the applied surface gradient and the RN generation on a conductor have been identified in section 6.3. It was found in section 6.3, that the RN generation of a conductor is the weighted sum of the contributions of each corona mode. The relationship between the RN and the applied surface gradient is therefore piecewise linear between the various corona mode inception gradients. The effect of the disturbance caused to the space charge distribution by the collision of space charge with an insulated cage is discussed in section 6.4. This effect was found to be linear with respect to the applied surface gradient provided that space charge diffusion, due to high density gradients, is not significant. The wideband excitation function of a conductor can now be extracted from the small insulated corona cage.

6.5.1 Linear Regression Analysis

The corona mode inception gradients, g_m, and the gradient at which space charge collision with the cage first affects the pulse parameters, g_c, are specific to each conductor placed in the corona cage. The extraction of the actual relationship between a pulse parameter, Y, and the applied surface gradient, g, for a specific mode requires that $g_m < g_c$ for that mode. This relationship is estimated from the limited data extracted from the experiments presented in section 6.2 with a linear first order regression model [6]:

$$Y = b_0 + b_1 g \qquad (6.9)$$

The linear relationship in equation 6.9 is estimated with a least squares approximation [6]:

$$b_1 = \frac{\sum_i \left[(g_i - \overline{g})(Y_i - \overline{Y}) \right]}{\sum_i (g_i - \overline{g})^2} \qquad (6.10)$$

$$b_0 = \overline{Y} - b_1 \overline{g} \qquad (6.11)$$

The linear effect of the insulated corona cage on the pulse parameters can also be obtained form the linear regression analysis on the data measured over the gradient range $g_d > g > g_c$, where g_d is the gradient at which space charge diffusion near the cage surface first affects the pulse parameters. The pulse parameter, Y_m, extracted from this gradient range therefore consists of the actual linear relationship defined in equation 6.9 and the linear effect of the insulated cage, Y_C:

$$Y_m = Y + Y_C = \left(b_0 + b_1 g \right) + \left(b_{0C} + b_{1C} g \right) \qquad (6.12)$$

The limited supply voltage restricted the analysis in this chapter to small gradients ranges. The

measured data is therefore too limited to extract an accurate and meaningful relationship from the regression analysis. Only the measured pulse parameters of the Hare conductor, corrected for space charge cage collisions, can be used to calculate a wideband excitation function.

6. 5.2 Variation of Hare Conductor Parameters with Applied Surface Gradient

The linear relationships between the pulse parameters and the surface gradient for the small cage Hare conductor measurement, derived from the proposed regression analysis and corrected for space charge collisions, are presented in this section.

Pulse Type	Pulse Parameter		b_0	b_1
Both Streamer Modes	Discharge Duration	-	-84.6	3.6
Onset Streamers	Pulse Number	-	-1028	50.5
	Pulse Amplitude	mean	6.85	0.055
		std	4.45	-0.0314
	Decay Time Constant	mean	146.2	6.3
		std	-15.3	4.6
	Rise Time Constant	mean	7.5	0
		std	2.1	0
Positive Streamers	Pulse Number	-	-710	31
	Pulse Amplitude	mean	-134	6.65
		std	-43	2.1
	Decay Time Constant	mean	-60.9	15.3
		std	-253	14
	Rise Time Constant	mean	4.18	-0.08
		std	0.79	-0.02

Table 6.12: The linear first order regression model parameters for the Hare conductor.

The linear first order regression model parameters for the Hare conductor are given in table 6.12. The limited dynamic range of the 8-bit sampling card adversely affected the accuracy of the onset

streamer pulse parameters extracted from the Hare conductor measurements. In particular the quantization noise of the measurement system caused a large variance of the extracted rise time constant. The accuracy of this parameter is therefore considered inadequate. It was concluded in section 6.3 that the discharge characteristics of the onset streamer mode of a stranded conductor are the same as those of a smooth conductor with the same outer diameter if the maximum surface gradient of the stranded conductor is considered. The mean and standard deviation of the rise time constant for the onset streamer pulse mode of the Hare conductor are therefore extracted from the smooth 0.78 cm aluminium conductor measurement.

6. 5.3   The Narrowband RMS Excitation Function of a Hare Conductor

The ideal pulse train for the Hare conductor is created for a complete 50 Hz cycle using the wideband excitation function parameters in table 6.12. This is then filtered in a 10 kHz bandwidth about the measurement frequency between 150 kHz to 30 MHz. The filtered pulse train is then sampled randomly using the technique described in section 5.2.4. The samples are used to calculate the probability function of the pulse train. Finally, equation 5.25 is used to calculate the narrowband RMS voltage injection element from the wideband excitation function.
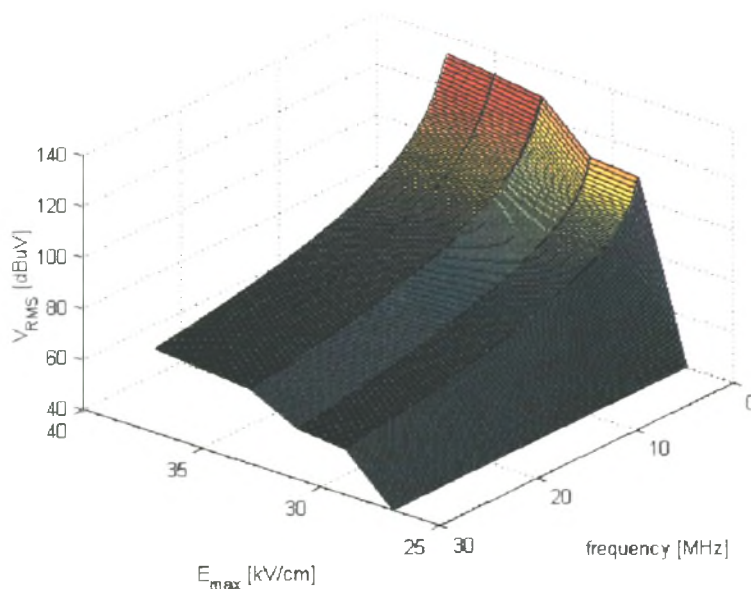
Figure 6.17: The narrowband RMS voltage injection element of a single Hare conductor extracted from small cage measurements in the frequency band 150 kHz to 30 MHz.

142
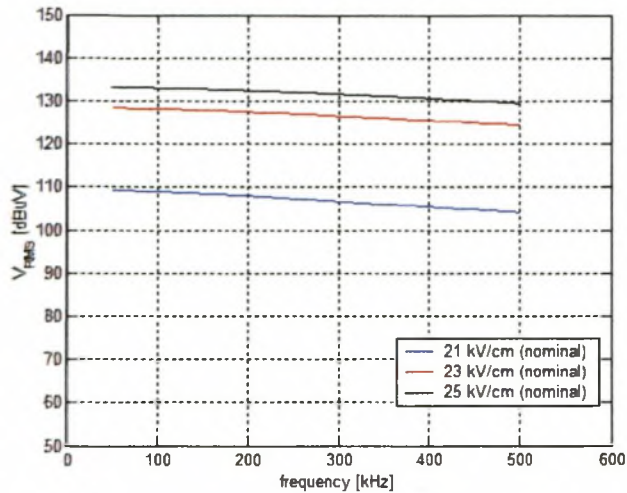
Figure 6.18: The frequency variation of the narrowband RMS voltage injection element of a single Hare conductor in the PLC frequency band at selected surface gradients.

The narrowband RMS voltage injection of the single ACSR Hare conductor is extracted from the linear regression model in table 6.12 and equation 5.25 for the small US cage is plotted for various frequency regimes in figures 6.17 and 6.18. The plots indicate a significant variation of the excitation function with frequency. This variation in the PLC band is reduced from 5.12 dB at 21 kV/cm, the onset streamer inception gradient, to 3.68 dB at 25 kV/cm.

6.5.4 The Narrowband RMS Excitation Function of a Twin Dinosaur Bundle

The maximum source voltage limitation and the choice of cage radius do not permit the measurement of a twin Dinosaur conductor bundle, such as the one used on the Acacia-Koeberg line, in the small corona cage. A wideband excitation function, such as that extracted for the Hare conductor in figure 6.17, can therefore not be extracted from the small cage measurements for such a bundle. It can however be approximated from measurements made in chapters 4 and 6 at a specific surface gradient. The wideband excitation function will be approximated for the Acacia-Koeberg line geometry in the PLC band in this section.

The excitation function of a similar twin IEC-800 bundle was measured in chapter 4. In this chapter, the corona mode inception gradients were identified from the piecewise linear curve in figure 4.4. It has already been demonstrated in this chapter, how the piecewise linear relationship between RN and surface gradient is decomposed into three linear relationships by extracting the

143

wideband excitation function, proposed in chapter 5, for the onset, positive and negative streamer modes. The surface gradients on the three phases of the Acacia-Koeberg line were found to be between 15 and 16 kV/cm. The dominant noise source in this gradient range for the twin Dinosaur conductors will be that of the positive streamer mode. Only the positive streamer excitation function need therefore be considered.

The wideband time domain measurements made on the Megawatt Park cage were used to approximate the pulse parameters of the positive streamers using the extraction method described in chapter 5. The transfer function of the Megawatt Park cage could not be extracted and has to be approximated in the frequency band 150 kHz to 10 MHz. A frequency scan in this band revealed resonances at 1 MHz and 6 MHz in the wideband measurement system. These frequency components were therefore filtered out of the measurement. The mean values for v_p, f_α and f_β were extracted at 15 kV/cm as 80 V, 325 kHz and 2.8 MHz respectively. Not enough valid pulses were extracted from the uncalibrated system to extract a meaningful standard deviation for these parameters. The standard deviation is therefore assumed to be negligible in this measurement. The extracted parameters appear to correspond to similar parameters extracted from the small cage measurements. The measurement is made in an uncalibrated system at a high altitude and no positive streamer pulse parameter correction for altitude was derived in this dissertation. The correction is therefore calculated by setting the value predicted by the wideband excitation function method equal to the EdF method prediction at 500 kHz.
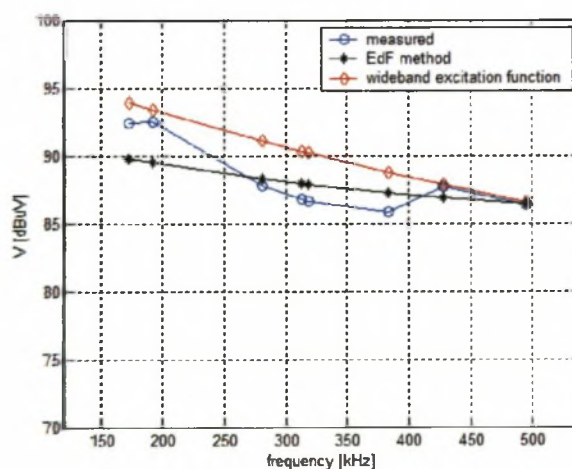
Figure 6.19: A comparison of the measured and predicted conducted RN at the Acacia sub-station showing the frequency variation of the RN in the PLC band.

The measured and predicted conducted RN at the Acacia substation is plotted in figure 6.19. The comparison suggests that the wideband excitation function method proposed in this dissertation better predicts the frequency variation of the RN in the PLC band. The variation in the measured spectrum between 280 kHz and 380 kHz is attributed to non-ideal frequency characteristics of the coupling or line matching equipment. The separation distance of the corona sources is easily calculated from the pulse number which is predicted by the wideband excitation function method proposed in this dissertation. Equation 5.32 can therefore be used to predict the RN performance of short line sections. This was not calculated for the Acacia-Koeberg line since the effect of altitude on the positive streamer pulse number could not be extracted from the small US cage due to supply voltage limitations.

The wideband excitation function method proposed in this dissertation does facilitate the prediction of a line's RN performance at frequencies other than 500 kHz. It also facilitates the calculation of the RN performance of short line sections. Existing prediction methods produce only narrowband data at 500 kHz. This data is not accurate at frequencies other than 500 kHz. The wideband excitation function should therefore be further developed so that it can predict RN levels for realistic conductor bundles under various weather conditions. This could not be done in the small corona cage design presented in this dissertation due to clean supply voltage limitations and other limitations discussed in this chapter. These limitations must be resolved before the proposed method can be extended to more realistic bundle geometries. The various limitations identified in this chapter are summarized in the next chapter. Chapter 7 is a summary of the most important conclusions drawn from the research presented in this dissertation.

6. 6 References

[1]   R.G. Urban, *Modelling Corona Noise on High Voltage Transmission Lines*, MScEng Thesis, University of Stellenbosch, 2001.

[2]   P. Sarma Maruvada, *Corona Performance of High-Voltage Transmission Lines*, Research Studies Press Ltd, 2000.

[3]   T.N. Giao, J.B. Jordan, "Modes of Corona Discharges in Air", IEEE Trans., Vol. PAS-87, 1968, pp. 1207 - 1212.

[4]   J.B. Whitehead, *High Voltage Corona in International Critical Tables*, McGraw-Hill, 1929.

[5]   IEEE Committee Report, "Transmission System Radio Influence", IEEE Trans., Vol. PAS- 84, 1965, pp. 714-722.

[6]   N.R. Draper, H. Smith, *Applied Regression Analysis*, John Wiley & Sons, 1966.

Chapter 7

Conclusions

Significant surface gradients applied to high voltage transmission line conductor bundles cause corona discharges. Conductor corona induces propagating currents in the bundle conductors and causes high noise levels across a wide frequency band. This RN interferes with broadcast radio and television reception as well as PLC teleprotection systems. The RN performance of a line is characterised by the randomly varying conducted and radiated RN levels, at calibrated frequencies and lateral distances, over a certain period of time. A good prediction of a line's RN performance is necessary to verify the reliability of the design. The RN performance is affected by many variables. The most significant variables are identified as the average maximum surface gradient, sub-conductor radius, number of sub-conductors, weather conditions, RAD, RH, wind, measurement frequency, meter characteristics and lateral distance from the line. These variables are grouped into geometrical, weather and measurement factors. Existing empirical and semi-analytical RN prediction methods primarily consider the geometrical variables. General empirical relationships are identified and used to account for the weather and measurement variables. Good RN predictions depend on an accurate account of the most significant variables for a line. Various RN measurement protocols proposed in the literature are therefore consolidated and a single comprehensive protocol is presented. A passive loop antenna must be used for the radiated RN measurements since the high RI levels will saturate an active loop antenna and restrict the lateral distances at which the RI performance can be measured.

A prediction methodology is derived by comparing the measured RN performance of selected lines to predicted data obtained from various prediction methods described in the literature. The accuracy of a prediction is evaluated with the conducted RN comparison at 500 kHz. This is because the PLC system is more easily modelled than the radiating multi-conductor line. The radiation model needed for RI predictions is evaluated by making RI measurements at the same time as the conducted RN measurements. Semi-analytical methods, which are based on the excitation function and natural mode theories, better consider the bundle geometry and therefore

predict a line's RN performance more accurately than the empirical methods do. The surface gradient, sub-conductor diameter and sub-conductor number models used in the semi-analytical methods are isolated and compared. The comparison is used to identify three prediction methods which together span a wide range of valid gradients and bundle geometries. These methods are the EdF, EPRI and IREQ methods. The proposed prediction methodology is therefore able to predict the RN performance of any practical line design. The selected semi-analytical methods predict heavy rain RN levels since these levels are more stable and reproducible. This is verified with RN measurements made in the Megawatt Park corona cage. Fair weather RN levels are then calculated from the heavy rain levels using empirical correction factors. This approach reduces the level of uncertainty of the prediction. The investigation concluded that equivalent conductor height and equivalent bundle radius approximations are valid and produce accurate results. A rigorous radiation model is required for the compact delta transmission line design. The EPRI approach is therefore used in the prediction methodology. A rigorous sub-conductor number model is required for bundles with three or more sub-conductors.

The confidence level of a RN performance prediction, made according to the suggested prediction methodology, is dependent on the variables included, the accuracy to which these variables are measured and the number of correction factors included in the prediction. The uncertainty of the prediction is minimized by using heavy rain excitation functions. The semi-analytical methods are defined at 500 kHz and are not able to predict the variation of the RN with frequency. The analytical propagation analysis correctly accounts for the frequency dependence of the line attenuation by including losses in the phase conductors and the ground. A wideband excitation function is also required. The low dynamic range of the RIV1 measurement and the limited bandwidth of the high power components do not allow for the extraction of a wideband excitation function from the Megawatt Park corona cage in its present form.

The RN of a short line section can also not be accurately calculated with the semi-analytical methods. Methods have been proposed to predict short line RN levels, as well as the relationship between RMS, QP and average RN levels. These methods, however, require that statistical properties of the measured RN current are known. The propagation analysis used in the semi-analytical methods is derived using energy concepts. RMS excitation functions should therefore

be used. The empirical relationships between the RN level and the various influencing variables are however only defined for QP levels. A new wideband excitation function which considers the statistical properties of the RN current must therefore be derived from small corona cage measurements.

The wideband excitation function proposed in this dissertation is defined by the repetition rate, peak amplitude, rise time constant and decay time constant of the double exponential current pulses induced by conductor corona discharges along the line. The repetition rate has an exponential probability distribution while the other parameters are normally distributed. Sample statistics for the pulse parameters are extracted from 7 consecutive 50 Hz periods using an optimised extraction algorithm. Corona generation in each of the 50 Hz periods is assumed to be statistically independent and confidence intervals for the pulse parameters are calculated. The frequency characteristics of the RN pulse train are then calculated from the extracted pulse parameters across the frequency band 150 kHz to 30 MHz. This wideband excitation function facilitates the calculation of the frequency variation of the RN in this band.

The variation of the wideband excitation function with surface gradient is piece-wise linear. The non-linearities occur at the various corona mode inception gradients. Three corona modes were identified as having measurable RN in the studied frequency regime. These are the onset streamer, positive streamer and negative streamer modes. If a separate excitation function is extracted for each of these modes, the individual wideband excitation functions will vary linearly with surface gradient. The number of pulses for each mode is also required for the extracted wideband excitation function. The RN performance of short line sections can therefore be predicted with the proposed wideband excitation function. Lastly, the relationship between the RMS, QP and average RN levels can be extracted from the wideband excitation function since the statistical properties of the RN pulse train are known.

The wideband excitation function is extracted from a calibrated small corona cage. Special care must be taken when designing such a cage to ensure that the electric field and space charge distributions are not affected by the cage dimensions. The cage radius must be carefully chosen so that the space charge does not reach the cage, since it will recombine, thereby affecting the

steady state space charge position inside the cage. Space charge recombination on the cage can be prevented by coating it with an insulating paint. This will still disturb the steady state position of the space charge distribution and will affect the pulse parameters extracted from the cage. The effect of space charge collisions with an insulated cage is linear with respect to changes in surface gradient, provided that space charge diffusion is not significant. The extracted parameters can be corrected for this linear change. Space charge diffusion will become significant when the surface gradient exceeds a critical gradient. The change in pulse parameters is then no longer linear. This critical gradient is dependent on the experimental setup studied and must be determined for each combination of corona cage and conductor bundle. The wideband excitation function cannot be extracted from a small cage above this critical gradient. The cage radius must also be large enough to ensure that flash-over does not occur at negative streamer inception. Conductors cannot be displaced inside a corona cage if a significant quantity of space charge accumulates at the insulated cage surface.

The choice of gradient model used in certain empirical and semi-analytical methods suggests a change in the rate at which RN increases with increased surface gradient. The surface gradient at which this rate changes is similar to the negative streamer inception gradient observed on a twin IEC-800 conductor bundle measured in the Megawatt park corona cage. The negative streamer inception gradient is dependent on the bundle geometry. The inclusion of the three different excitation functions for the three measurable corona modes in the wideband excitation function method will accurately determine the gradient at which this change in rate of increase occurs. This will ensure the validity of the method over an unlimited surface gradient range for any bundle geometry.

A passive loop antenna must be designed for the RI measurements. More lines should be measured in order to further improve the prediction methodology proposed in this dissertation and decrease the uncertainty of the RN performance predictions. In particular, a continuous QP measurement should be made on one of the studied line for a period of time greater than a year. The limited clean supply that is available at the Stellenbosch University facility must be remedied and a new corona cage must be designed so that larger ACSR conductors and conductor bundles can be measured.

Appendix A

Standard Weather Terms and Categories

A. 1   Standard Weather Terms

Standard weather terms are defined in [1]. The most important of these terms are presented in [2] and are summarized below:

- *Fair weather* - That weather condition, when precipitation intensity is zero, which results in dry conductors.

- *Foul weather* - That weather condition which causes the conductors to be wet or results in precipitation.

- *Fog* - Visible aggregate of small water drops suspended in the atmosphere near the earth

- *Rain* - Precipitation in the form of liquid water drops with diameters larger than 0.5mm. The minimum diameter of rain drops can be smaller if they are widely scattered. The rain condition is further classified according to the rainfall intensity. Rainfall intensity is the rate of rain, usually expressed as an average over some time period shorter than 1 hr in units of mm/hr.

- *Light rain* - the rainfall intensity is not more than 2.5 mm/hr.

- *Moderate rain* - the rainfall intensity is between 2.6 and 7.6 mm/hr with the maximum intensity not exceeding 0.76 mm in 6 min.

- *Heavy rain* - the rainfall intensity is greater than 7.7 mm/hr.

A. 2   Weather Categories

A set of weather categories was defined in [3] to describe all possible weather conditions according to their affect on the RN performance of a line. The categories appropriate to local conditions are included in the table presented in this appendix.

code	Description	Category
01	Rain - Heavy - Steady	Average Foul Weather + Stable Foul Weather
02	Rain - Heavy - Intermittent	
03	Rain - Medium - Steady	
04	Rain - Medium - Intermittent	
05	Rain - Light - Steady	
06	Rain - Light - Intermittent	
07	Rain - Trace - Steady	Average Foul Weather
08	Rain - Trace - Intermittent	
17	Frost - Heavy	
18	Frost - Medium	
19	Frost - Light	
20	Dew - Heavy	
21	Dew - Medium	
22	Dew - Light	
23	Fog - Heavy	
24	Fog - Medium	
25	Fog - Light	
26	Fair - Cloudy	Fair Weather
27	Haze	
32	Wet Conductor after Rain	Average Foul

References

[1] IEEE Standard No. 539-1990, *IEEE Standard Definitions of Terms Related to Corona and Field Effects of Overhead Power Lines*.

[2] P. Sarma Maruvada, *Corona Performance of High-Voltage Transmission Lines*, Research Studies Press Ltd, 2000.

[3] J.J. LaForest, M. Baretsky, Jr., D.D. MacCarthy, "Radio-Noise Levels of EHV Transmission Lines Based on Project EHV Research", IEEE Trans., Vol. PAS- 85, 1966, pp. 1213-1226.

Appendix B

A Proposed RI Measurement Protocol

- ▸ The RI performance of a line is completely characterized by a frequency spectrum, lateral profile and continuous measurement.

- ▸ The ambient weather condition must be categorized according to the standard described in appendix A and recorded. The uniformity of the weather condition along the line's length and over the duration of the measurement must be noted.

- ▸ For each of the three measurements, either L_{50} dry, L_{50} wet, L_5 wet or L_1 wet levels must be calculated from no less than 15 measurement sets for that weather condition. Each measurement set is the average of three measurements made at three calibrated test locations spaced uniformly along the line's length. For all-weather statistical distributions, the number of measurement sets used for each weather category must be proportional to the occurrence of that weather category during the time period studied.

- ▸ The L_{50} dry level correlates to average fair weather RI and must exclude the effect of mist and fog conditions. These measurements must therefore not be made early in the morning or late in the afternoon. Measurements must also not be used if precipitation occurred in the vicinity of the line four hours before or an hour after the measurement.

- ▸ The L_{50} wet level correlates to average foul weather RI. This includes all weather categories that cause the line conductors to be wet.

- ▸ The L_5 wet and L_1 wet levels correlate to average stable foul and maximum foul weather RI respectively. They are calculated under average and maximum rain rates for the line. Measurements are used to calculate these levels only if the rain conditions are uniform along the line for at least 10 km in either direction of the measurement site.

- ▸ The characteristics of the RN meter must be noted. This includes the detector type, measurement bandwidth, measurement frequency and the calibration accuracy and date.

- ▸ Measurement frequencies must be selected for the test location by considering the background noise levels. The standard CISPR measurement frequencies must be used

153

unless the background noise is less than 6 dB lower than the RI level. This is 500 kHz for the lateral profile and continuous measurements . For the frequency spectrum, the standard measurement frequencies, in MHz, are 0.15, 0.25, 0.5, 1, 1.5, 3, 6, 10, 15 and 30.

- The measurement location must be at least 10 km from any discontinuity along the line.

- The test location must be free of noise from discharge sources other than conductor corona. This is verified by checking that the QP and average detector levels differ by 20 dB or more and that QP and peak detector levels differ by less than 5 dB.

- The antenna used must be described along with its calibration factor. An electrically screened vertical loop antenna is suggested. The antenna must be kept at a height of 2 m above the ground plane. The dimensions of the loop antenna must be such that it is completely enclosed by a square with 60 cm sides. The balance of the antenna must be such that the ratio of minimum and maximum indications when rotated through 360° in a uniform field is not less than 20 dB. The orientation of maximum indication of the antenna must be noted. Plane wave conditions (i.e. $\mathbf{E} = 377\mathbf{H}$) are assumed at all lateral distances.

- The frequency spectrum and continuous measurements are made 20 m from the outer phase.

- The attachment and midspan height of the conductors must be measured and recorded.

- It must be noted if the soil at the test site is wet due to recent precipitation.

- The line voltage before and after the measurement must be recorded. The line geometry must be recorded and the surface gradient calculated to within 1% of the actual gradient.

- The presence of any air-borne pollutants must be noted. Their position with respect to the line conductors and their size must be recorded.

- Conductor age must be noted if the conductors were installed less than a year prior to the measurements.

- The temperature, pressure, altitude, RH, wind and load current must be recorded before and after the measurements.

Appendix C

Operational Transmission Line Measurements

C. 1 The Acacia-Koeberg Transmission Line

General Description	Untransposed 400 kV flat horizontal			
Geometry	Phase geometry	spacing	9	m
		attachment height	19.6	m
		measured height	11.2	m
	Bundle geometry	bundle type	2 x Dinosuar	
		bundle spacing	38	cm
		bundle orientation	0	degree
	Dinosaur	nominal diameter	3.56	cm
		stranding	54/19	
		Al. strand diameter	0.395	cm
		DC resistance	0.045	Ω/km
	Shield geometry	spacing to centre	8.3	m
		attachment height	25.2	m
		measured height	16.8	m
	Shield conductor	nominal diameter	1.65	cm
		stranding	18/7	
		Al. strand diameter	0.236	cm
		DC resistance	0.22	Ω/km
	Line length		31.3	km

Conditions	line	line voltage	405	kV
		load current	1125	A
	weather	classification	fair	
		wind	light	
	ground	resistivity	300	Ω.m
	atmospheric	pressure	759	mmHg
		RH	40	%
		temperature	22	C
		altitude	55	m
Measurement	Frequency	PLC spectrum	50 - 500	kHz
		CISPR spectrum	0.1 - 30	MHz
		lateral profile	500	kHz
	Bandwidth	peak, QP, AV	10	kHz
		RMS	3.1	kHz
	Time		10:00	am

Table C.1: Acacia-Koeberg line data.

156

C. 2 The Hydra-Droërivier Transmission Line

General Description	Untransposed 400 kV compact-delta			
Geometry	Phase geometry	spacing	7	m
		attachment height	25.31	m
			19.55	m
		measured height	18.2	m
			12.5	
	Bundle geometry	bundle type	3 x Turn	
		bundle spacing	45	cm
		bundle orientation	30	degree
	Turn conductor	nominal diameter	2.7	cm
		stranding	45/7	
		Al. strand diameter	0.338	cm
		DC resistance	0.071	Ω/km
	Shield geometry	spacing to centre	8.6	m
		attachment height	31.3	m
	Shield conductor	nominal diameter	2.65	cm
Conditions	line	line voltage	411	kV
		load current	400	A
	weather	classification	fair	
		wind	light	
	ground	resistivity	300	Ω.m
	atmospheric	pressure	760	mmHg
		RH	40	%
		temperature	24	C
		altitude	1280	m
Measurement	Frequency	PLC spectrum	50 - 500	kHz

157

		CISPR spectrum	0.1 - 30	MHz
		lateral profile	500	kHz
	Bandwidth	peak, QP	10	kHz
		RMS	3.1	kHz
	Time		10:30	am

Table C.2: Hydra-Droerivier line data.

C. 3   The Aries-Kokerboom Transmission Line

General Description	Transposed 400 kV compact-delta			
Geometry	Phase geometry	spacing	7	m
		attachment height	25.31	m
			19.55	m
		measured height	16.2	m
			10.9	
	Bundle geometry	bundle type	4 x Turn	
		bundle spacing	45	cm
		bundle orientation	45	degree
	Turn conductor	nominal diameter	2.7	cm
		stranding	45/7	
		Al. strand diameter	0.338	cm
		DC resistance	0.071	Ω/km
	Shield geometry	spacing to centre	8.6	m
		attachment height	31.3	m
	Shield conductor	nominal diameter	3.35	cm
Conditions	line	line voltage	403	kV
	weather	classification	fair	
	ground	resistivity	300	Ω.m
	atmospheric	pressure	760	mmHg
		RH	38	%
		temperature	33	C
		altitude	928	m
Measurement	Frequency	PLC spectrum	50 - 500	kHz
		CISPR spectrum	0.1 - 30	MHz

159

		lateral profile	500	kHz
	Bandwidth	peak, QP	10	kHz
		RMS	3.1	kHz

Table C.3: Aries-Kokerboom line data.
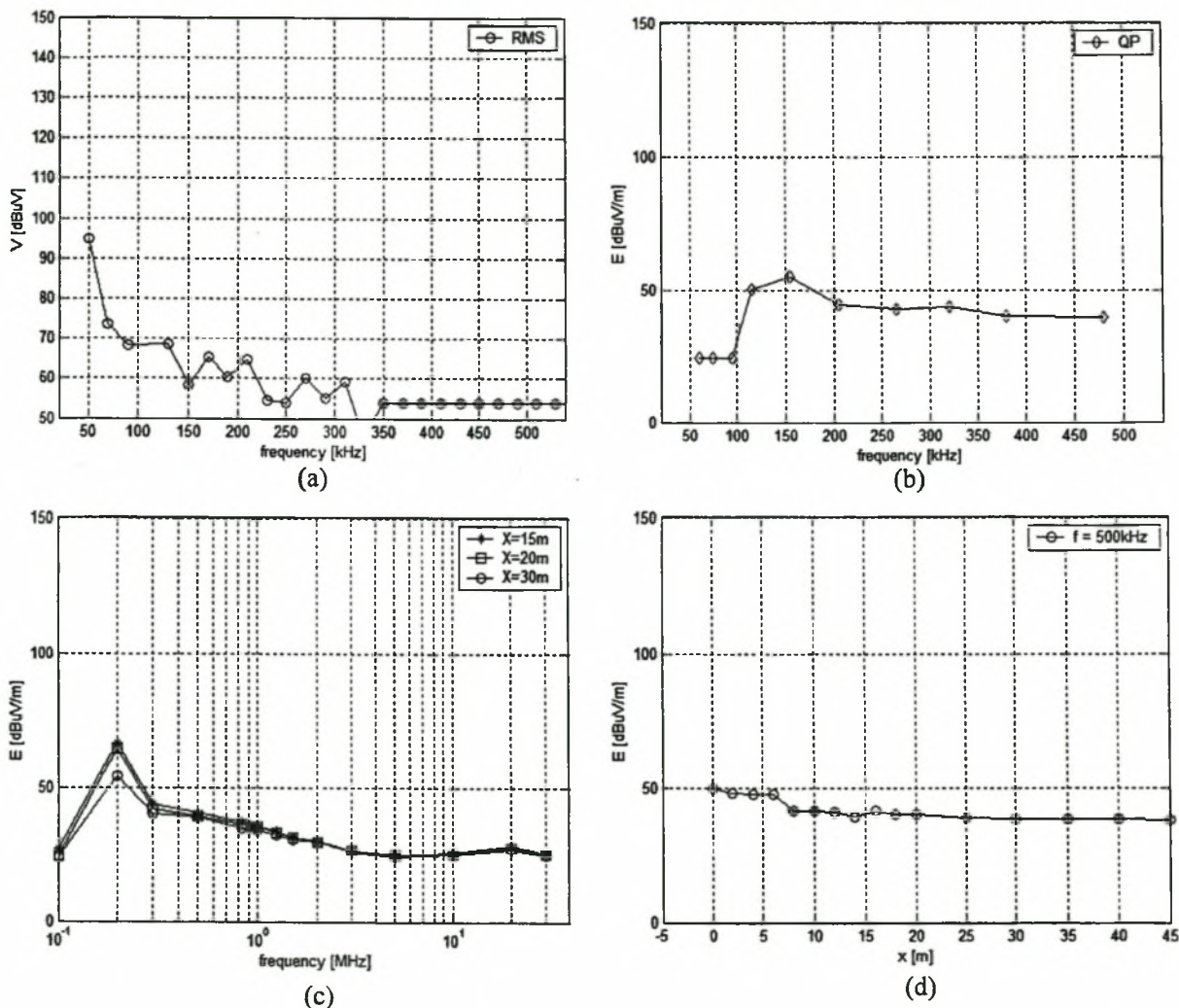
Figure C.1: The measured RN performance of the Aries-Kokerboom transmission line: (a) conducted RN levels in the PLC band; (b) RI frequency spectrum in the PLC band [x = 20 m]; (c) RI frequency spectrum at the CISPR frequencies and various lateral distances; (d) the lateral profile at 500 kHz. [BW = 10 kHz]

C. 4 The Kriel-Tutuka Transmission Line

General Description	transposed 400kV flat horizontal			
Geometry	Phase geometry	spacing	10	m
		attachment height	22.56	m
	Bundle geometry	bundle type	2 x Dinosuar	
		bundle spacing	38	cm
		bundle orientation	0	degree
	Dinosaur conductor	nominal diameter	3.56	cm
		stranding	54/7	
		Al. strand diameter	0.395	cm
		DC resistance	0.045	Ω/km
	Shield geometry	spacing to centre	8.75	m
		attachment height	28.6	m
	Shield conductor	nominal diameter	0.95	cm
	Line length		30	km
Conditions	line	line voltage	400	kV
	weather	classification	fair	
		wind	none	
	ground	resistivity	300	Ω.m
Measurement	Frequency	PLC spectrum	50 - 500	kHz
	Bandwidth	RMS	75	Hz
	Time		10:00	am

Table C.4: Kriel-Tutuka line data (twin Dinosaur section).

Appendix D

Empirical Prediction Methods

D. 1 400kV-FG Method (Germany):

The empirical equation proposed in the 400kV-FG method is [1]:

$$RI = (53.7 \pm 5) + K_g\left(g_m - 16.95\right) + 40\log_{10}\left(\frac{d}{3.93}\right) + K_n\left[10\log_{10}\left(\frac{n}{4}\right)\right] + 32\log_{10}\left(\frac{20}{D'}\right) \quad \text{(D.1)}$$

In equation D.1, $K_g = 3$ for 750 kV lines and 3.5 for lower voltage lines. Also, $K_n = 0.664$ for

single conductor bundles and 1 for bundles with more than one sub-conductor. Equation D.1 is

derived from RI level measurements made under average fair weather conditions on an ANSI

meter with a 5 kHz bandwidth and a QP detector. The reference frequency is 1 MHz and the

direct lateral distance between the phase conductor and the measurement position is 20 m. The

variables included are the average maximum surface gradient, the conductor diameter and the

lateral distance between the phase conductor and the antenna. The range of surface gradients for

which the equation is valid is 15 to 19 kV/cm. The equation is valid for measurement frequencies

between 0.5 and 1 MHz. For rain conditions, a correction factor of 17 ± 3 dB is added.

D. 2 Shiobara Method (Japan):

The empirical equation proposed in the Shiobara method is [1]:

$$RI = \left[3.7g_m + 12.2\right] + 40\log_{10}\left(\frac{d}{2.53}\right) + 20\log_{10}\left(\frac{h}{D^2}\right) - 12\left(\log_{10} f\right)^2 - 17\left(\log_{10} f\right) \quad \text{(D.2)}$$

Equation D.2 is derived from RI measurements on 500 kV lines, directly under the outer phase,

under average fair weather conditions, on an ANSI meter with a 5 kHz bandwidth and a QP

detector. The reference frequency is 1 MHz. Under heavy rain conditions, the maximum foul

weather RI level is calculated by replacing the term in square brackets with [1]:

$$
RI_g = \begin{cases} 10.5g_p - \left(\dfrac{g_p}{2}\right)^2 - 31.0 & ; g_p \leq 17 \\[4mm] 4.38g_p - \left(\dfrac{g_p}{4}\right)^2 + 19.5 & ; g_p > 17 \end{cases}
\tag{D.3}
$$

The variables included in the method are the average maximum surface gradient, the conductor diameter, conductor height, lateral distance between the phase conductor and antenna along the ground and the measurement frequency, f [MHz]. The range of surface gradients on the bottom or outer phase for which the equation is valid is 12 to 22 kV/cm. In equation D.3, g_p is the average gradient on the bottom sub-conductor of the bottom or outer phase bundle. This value is calculated from the maximum gradient as follows [1]:

$$
g_p = \frac{g_m}{1 + \dfrac{d}{S}(n-1)\sin(\pi/n)}\left(1 + \frac{d}{S}(n-1)\sin(\pi/n)\cos\gamma\right)
\tag{D.4}
$$

In equation D.4, S is the bundle separation.

D. 3 Ontario-Hydro Method (Canada):

The empirical equation proposed in the Ontario-Hydro method is [1]:

$$
RI = RI_0 + A\log_{10}\left(\frac{g_m}{18.8}\right) + 40\log_{10}\left(\frac{d}{2.54}\right) + B\log_{10}\left(\frac{30.5}{D'}\right) + 20\log_{10}\left(\frac{C+1}{C+f^2}\right)
\tag{D.5}
$$

where [1]:

$$RI_0 = \begin{cases} 34 \pm 6 & ; \text{fair} \quad \text{horizontal} \\ 37 \pm 6 & ; \text{fair} \quad \text{vertical} \\ 63 & ; \text{foul} \quad \text{horizontal} \\ 66 & ; \text{foul} \quad \text{vertical} \end{cases} \tag{D.6}$$

Also, $A = 146$ for fair weather and 120 for foul weather. $B = 40$ for horizontal lines and 32 for vertical lines. $C = 1$ for frequencies greater than 1 MHz and 0.5 for frequencies lower than 1MHz. Equation D.5 is derived from RI measurements made on 600 kV horizontal test lines under heavy rain conditions on an ANSI meter with a 5 kHz bandwidth and a QP detector. The reference frequency is 1 MHz and the direct distance between the phase conductor and measurement position is 30.5 m. The variables included are the average maximum surface gradient, the conductor diameter, the lateral distance between the phase conductor and antenna and the measurement frequency. The range of surface gradients for which the equation is valid is not specified. Stable foul weather levels can be obtained by subtracting 6 dB from equation D.5. Average foul weather levels are calculated by adding 20 dB to the average fair weather level.

D. 4 ENEL Method (Italy):

The empirical equation proposed in the ENEL method is [1]:

$$RI = 47 + 3.8(g_a - 15) + 40\log_{10}\left(\frac{d}{5}\right) + 10\log_{10} n + 30\log_{10}\left(\frac{20}{D'}\right) + \frac{A}{300} \tag{D.7}$$

where [1]:

$$g_a = \frac{g_m}{1 + \dfrac{d}{S}(n - 1)\sin(\pi/n)} \tag{D.8}$$

Equation D.7 is derived from RI measurements under average fair weather conditions on an ANSI meter with a 5 kHz bandwidth and a QP detector at 1 MHz. The direct lateral distance between the phase conductor and the antenna is 20 m. The variables included are the average surface gradient, g_a [kV/cm], conductor diameter, lateral distance between phase conductor and antenna and the measurement frequency. The range of valid surface gradients is not stated.

164

D. 5 EGU Method (Czech Republic):

The empirical equation proposed in the EGU method is [1]:

$$RI = 11 + 4.5g_m - 34 \log D' - \left[22 \log_{10} f + 15 \left(\log_{10} f \right)^2 \right] \qquad (D.9)$$

Equation D.9 is derived from RI level measurements made primarily on single-circuit horizontal lines with between 1 and 4 sub-conductors per bundle and sub-conductor diameters of between 1.92 and 3.31 cm. The measurements were made under average fair weather conditions on an ANSI meter with a 5 kHz bandwidth and a QP detector at 1 MHz. The variables included are the average maximum surface gradient, the direct lateral distance between the phase conductor and antenna and the measurement frequency. The range of surface gradients for which the equation is valid is 12 to 20 kV/cm and the frequency correction is valid up to 5 MHz.

D. 6 Westinghouse Method (USA):

The empirical equation proposed in the Westinghouse method is [1]:

$$RI = 48 + 3.5 \left(g_m - 17.5 \right) + 30 \log_{10} \left(\frac{d}{3.51} \right) + 20 \log_{10} \left(\frac{30.7h}{D^2} \right) + 10(1 - f) \qquad (D.10)$$

Equation D.10 is derived from RI measurements under average fair weather conditions on an ANSI meter with a 5 kHz bandwidth and a QP detector at 1 MHz. The distance between the phase conductor and the antenna is 30.7 m. The variables included are the average maximum surface gradient, conductor diameter, conductor height, lateral distance between the phase conductor and antenna and the measurement frequency. The range of surface gradients for which the equation is valid is not stated. The equation is valid for a lateral distance less than 60 m.

References

[1]   R.G. Olsen, S.D. Schennum, V.L. Chartier, "Comparison of Several Methods for Calculating Power Line Electromagnetic Interference Levels and Calibration with Long Term Data", IEEE Trans., Vol. PWRD-7, 1992, pp. 903-913.

Appendix E

A Comparison of RN Surface Gradient Models

Equation	model type	g	A_1	A_3	A_5	g_{range} [kV/cm]	d_{range} [cm]	g_0	weather
CIGRÉ	A	g_m	3.5	-	-	12 - 20	-	-	avg. fair
BPA	B	g_m	-	120	-	-	-	15	avg. foul
400kV-FG	A	g_m	3.5	-	-	15 - 19	-	17	avg. fair
Shiobara	A	g_p	3.7	-	-	12 - 22	-	-	avg. fair
Ontario-Hydro	B	g_m	-	120	-	-	-	18.8	avg. foul
ENEL	A	g_a	3.8	-	-	-	-	15	avg. fair
EGU	A	g_m	4.5	-	-	12 - 20	1.9 - 3.3	-	avg. fair
Westinghouse	A	g_m	3.5	-	-	-	-	17.5	avg. fair
EdF	B	g_m	-	155	-	10 - 17	3.7 - 5.2	-	heavy rain
IREQ	B	g_m	-	92	-	-	-	-	heavy rain
EPRI	C	g_m	-	-	580	-	-	-	heavy rain
LaForest [1]	A	g_m	2.5 3.5	-	-	-	-	-	avg. fair
LaCroix [2]	A	g_m	2.5	-	-	15-18	3.5	-	avg. fair
RN design guide	A	g_m	3.6	-	-	-	-	-	avg. fair

References:

[1] J.J. LaForest, M Baretsky, Jr., D.D. MacCarthy, "Radio-Noise Levels of EHV Transmission Lines Based on Project EHV Research", IEEE Trans., Vol. PAS-85, 1966, pp. 1213-1226.

[2] R.LaCroix, H. Charbonneau, "Radio Interference from the First 735-kV Line of Hydro-Québec", IEEE Trans., Vol. PAS-87, 1968, pp. 932-939.

Appendix F

A RN Prediction Methodology

▸ A selection of three semi-analytical methods is considered sufficient to predict an accurate excitation function for any possible line design as regards the applied average maximum surface gradient, sub-conductor radius and the number of sub-conductors in a bundle. Empirical correction factors for environmental and measurement factors are then added to the excitation function predictions.

▸ When selecting the most appropriate semi-analytical method for a line, the order of importance of the three geometrical parameters considered is: sub-conductor radius, surface gradient and then the number of sub-conductors.

▸ The EdF method uses a sub-conductor radius correction model which is more accurate than those of the other methods for radii greater than 4 cm. This model is only valid for conductor radii greater than 3.7 cm. The EdF method is used if the sub-conductor radius is greater than 3.7 cm.

▸ If the sub-conductor radius is smaller than 3.7 cm, either the IREQ or the EPRI method must be used. The choice of method now determined by the surface gradient and sub-conductor number models. The surface gradient model of the EPRI method is more accurate for higher surface gradients but the method does not have a rigorous sub-conductor number model. The method is also only valid if the ratio of bundle radius to sub-conductor radius is greater than 10. If the surface gradient is above 17 kV/cm, the conductor bundle has less than four sub-conductors and the ratio of bundle to sub-conductor radii is greater than 10, the EPRI method is used. If this is not the case, the IREQ method is used.

▸ The weather correction factors for the EdF and EPRI methods are calculated from table 3.3. The weather correction factors of the EPRI method are also used for the IREQ method.

▸ The altitude correction factor defined in equation 3.51 is used for a significant change in altitude above sea level. The RH correction factor defined in equation 3.53 is used for a significant change in RH from 50%.

▸ The wind speed correction factor defined in equation 3.54 is used for any detectable wind

measured in km/hr.

- ▸ Only RMS RN levels can be accurately converted to another measurement bandwidth since the repetition rate of the RN pulse train is not known for various environmental conditions. QP levels are measured and presented in a 10 kHz bandwidth.

- ▸ The rigorous EPRI radiation model is used for all line geometries to determine the RI level at a given lateral displacement from the out phase of the line.

- ▸ These are the only correction factors included in the RN predictions. An uncertainty level of 1 dB is accepted for fair weather RN predictions and 4 dB for average foul weather RN predictions due to the weather correction factors used.

Appendix G

The Calculated RN Current

The wideband excitation function voltage source is injected onto a two conductor transmission line which models a propagation mode.
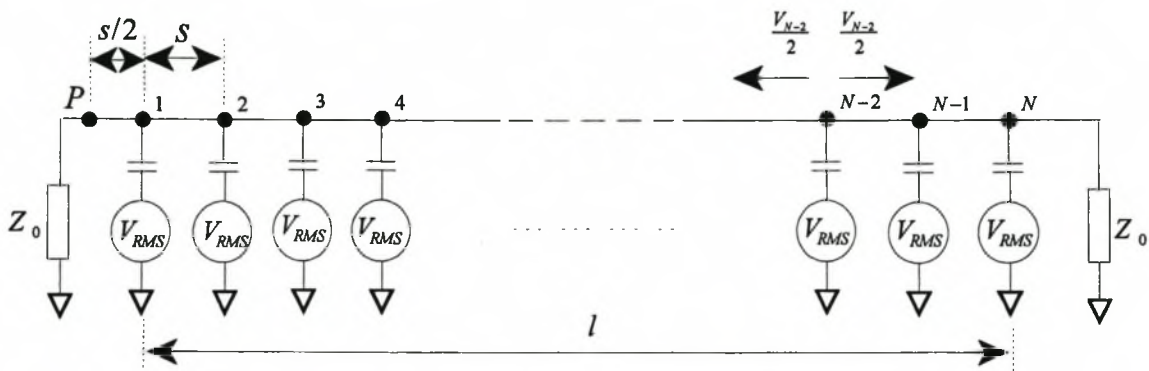
Figure G.1: Schematic diagram of a two conductor transmission line with N corona sources separated by distance s.

In figure G.1, corona discharges spaced uniformly along the finite length of the line induce equivalent sinusoidal voltages, V_s, at a specified frequency derived from the RMS excitation function for the line. Since the line is terminated in its surge impedance at both ends, the induced voltage will divide equally and the two resulting voltage waves will propagate in either direction along the line. The voltage at point P on the transmission line in figure G.1 due to the N 'th induced voltage waveform was defined in equation 3.28 as:

$$V_{PN} = \frac{V_s}{2}\left[e^{-\alpha(2N-1)(s/2)}\right] \tag{G.1}$$

The N induced voltages along the line of length l are separated by a distance:

$$s = \frac{l}{N-1} \tag{G.2}$$

169

Since the RMS excitation function has been used to derive equation G.1, the total propagating voltage at point P, due to all the attenuated voltages induced along the line equals the root mean square of the N propagating voltages defined in equation G.1:

$$V_P = \sqrt{\sum_{j=1}^{N} \left[\frac{V_s}{2} e^{-\alpha(2j-1)(s/2)} \right]^2}$$

$$= \frac{V_s}{\sqrt{2}} \left[\sqrt{\left\{ \sum_{j=1}^{N} e^{-\alpha(2j-1)s} \right\}} \right] \tag{G.3}$$

The finite summation inside the braces in equation G.3 is next considered:

$$S_n = \sum_{j=1}^{N} e^{-\alpha(2j-1)s}$$

$$= e^{-\alpha s} + e^{-3\alpha s} + \ldots + e^{-(2N-3)\alpha s} + e^{-(2N-1)\alpha s}$$

$$\Rightarrow \qquad e^{2\alpha s} S_n = e^{\alpha s} + e^{-\alpha s} + \ldots + e^{-(2N-5)\alpha s} + e^{-(2N-3)\alpha s}$$

$$\Rightarrow \qquad \left(1 - e^{2\alpha s}\right) S_n = e^{-(2N-1)\alpha s} - e^{\alpha s}$$

$$\Rightarrow \qquad S_n = -e^{\alpha s} \left[\frac{1 - e^{-2\alpha Ns}}{1 - e^{2\alpha s}} \right] \tag{G.4}$$

Substituting equations G.2 and G.4 into equation G.3 and recognizing that for $N \gg 1$, equation G.2 simplifies to $S \approx l / N$:

$$V_P \approx \frac{V_s}{\sqrt{2}} \left[\sqrt{\frac{1}{2} \left(\frac{2}{e^{\alpha l/N} - e^{-\alpha l/N}} \right) \left(1 - e^{-2\alpha l}\right)} \right]$$

$$= \frac{V_s}{2} \sqrt{\frac{1 - e^{-2\alpha l}}{\sinh(\alpha S)}} \tag{G.5}$$

The total propagating current at any point along a line of finite length can be calculated with equation G.5.

170

Appendix H

Results of Small Cage Experiments

H. 1 Quality of Supply

measurement	1	2	3
cage	US (small)	US (small)	US (small)
centre conductor	smooth Cu.	smooth Cu.	smooth Cu.
a [cm]	0.75	0.75	0.75
$\Delta V_P \mid V_{diff}$ [% | %]	1.68 | 2.39	1.53 | 2.04	0.30 | 0.58
δ	1.026	1.026	1.025
RH [%]	67	67	70
E_a / V [cm^{-1}]	0.3802	0.3802	0.3802
d_c [cm]	26.76	26.76	26.76
$(\nabla . E)_a \big|_{E=E_c}$ [kV/cm^2]	-37.3	-37.3	-37.3
$E_{c(measurable)}$ [kV/cm]	28	28	28
Flash-over Gradient [kV/cm]	34	33	32

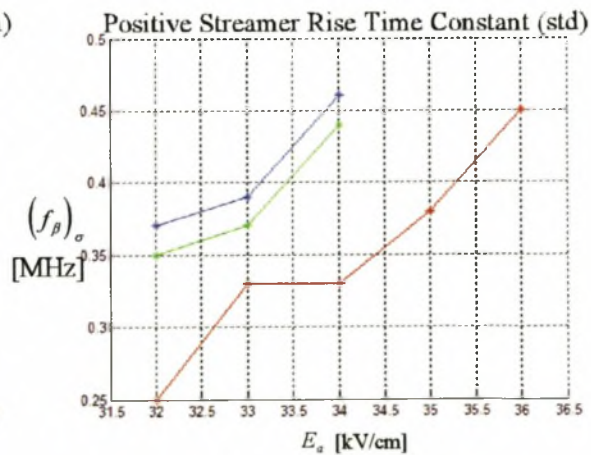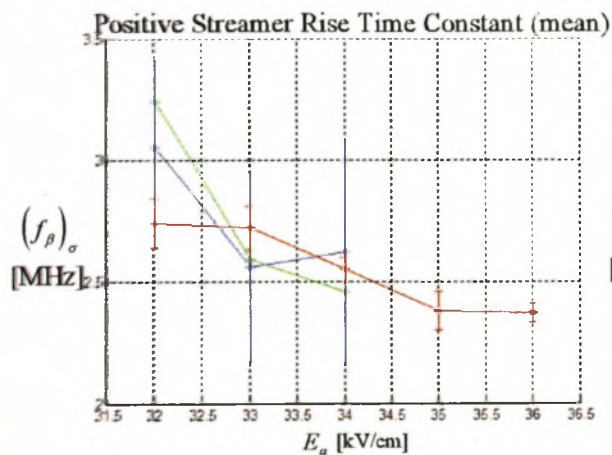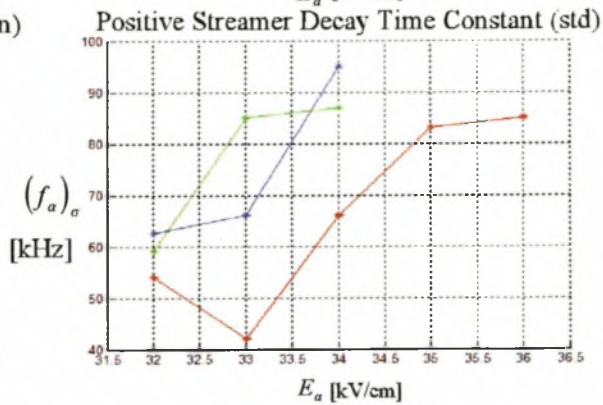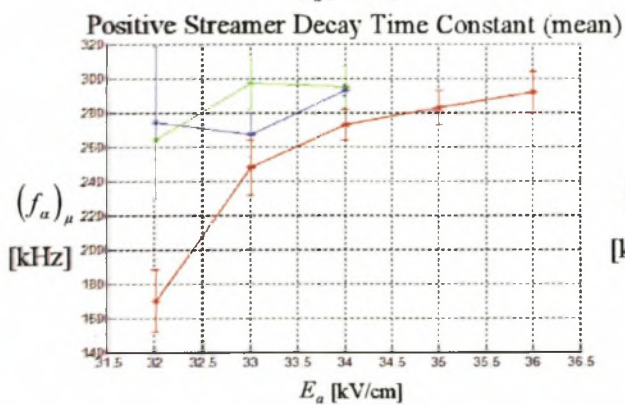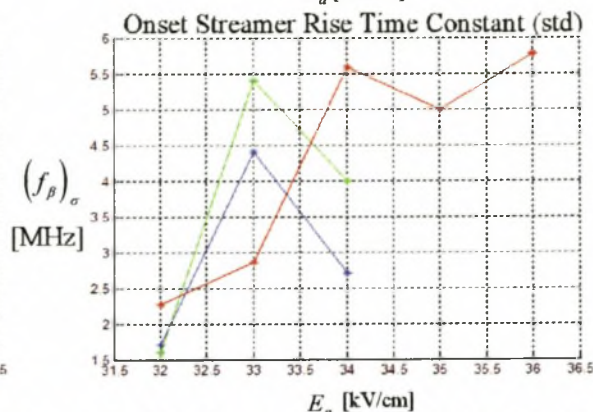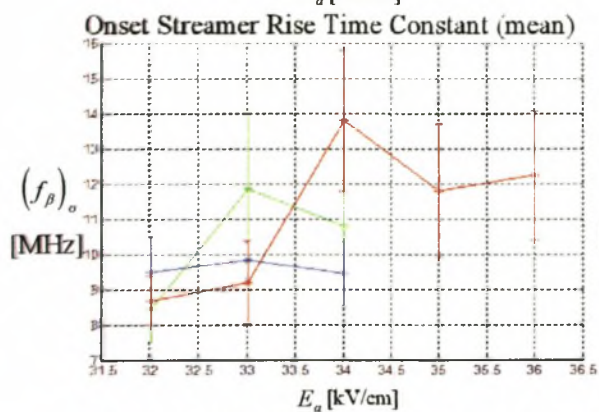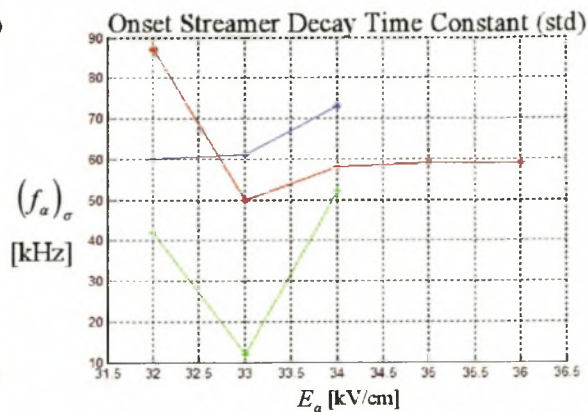**(1) Start Phase and Discharge Duration of Measurable Positive Corona Modes:**
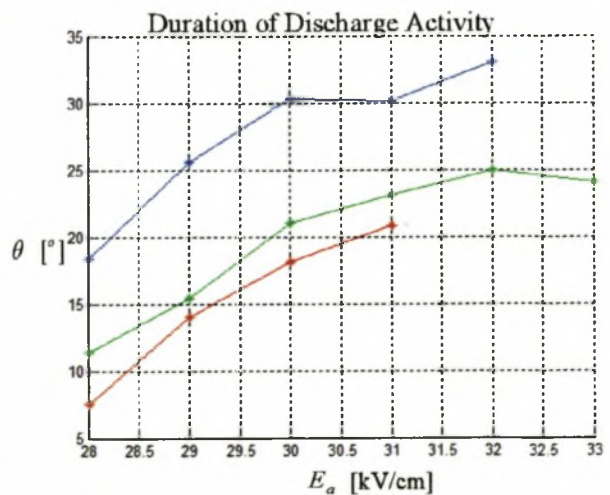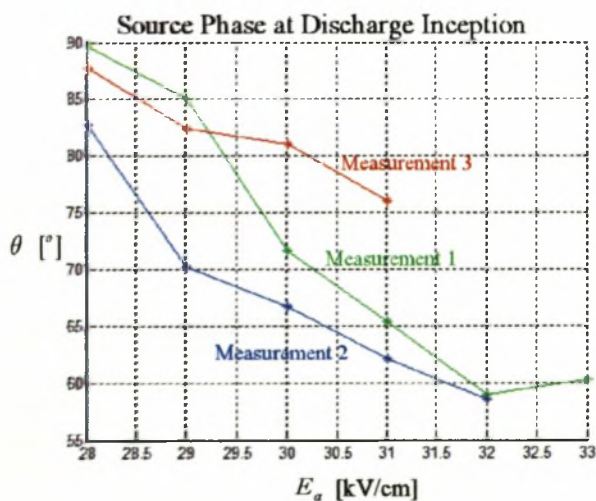
(2) Measurable Positive Corona Pulse Number and Type :

(3) Measurable Positive Corona Pulse Parameters :

Onset Streamer Decay Time Constant (mean)

Onset Streamer Decay Time Constant (std)

Onset Streamer Rise Time Constant (mean)

Onset Streamer Rise Time Constant (std)

Positive Streamer Decay Time Constant (mean)

Positive Streamer Decay Time Constant (std)

Positive Streamer Rise Time Constant (mean)

Positive Streamer Rise Time Constant (std)
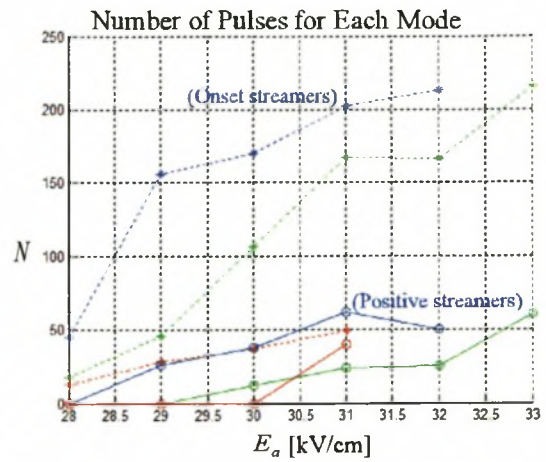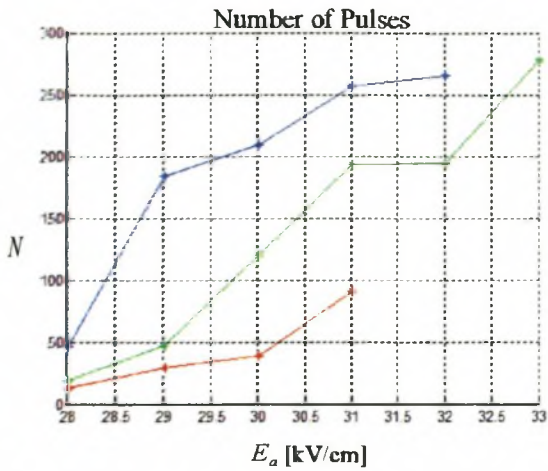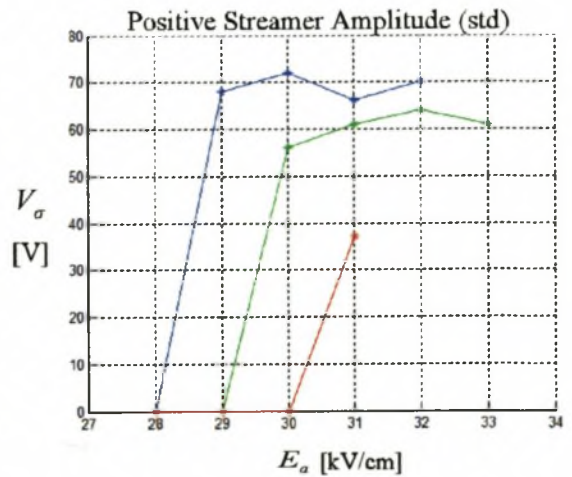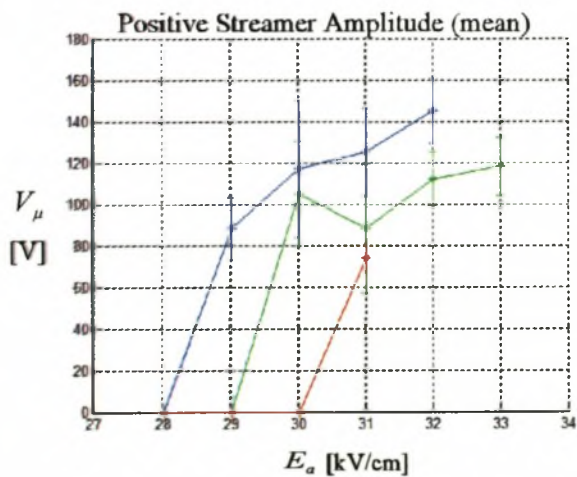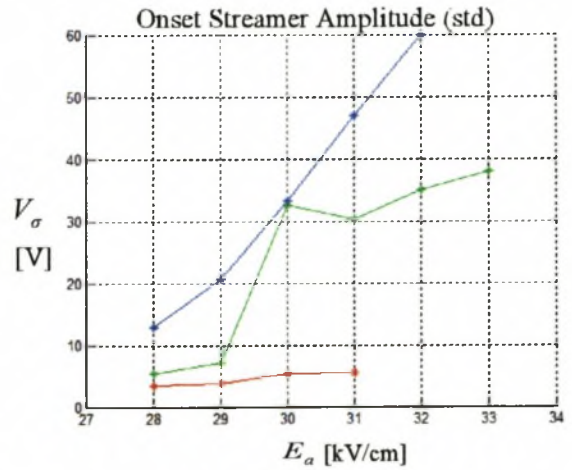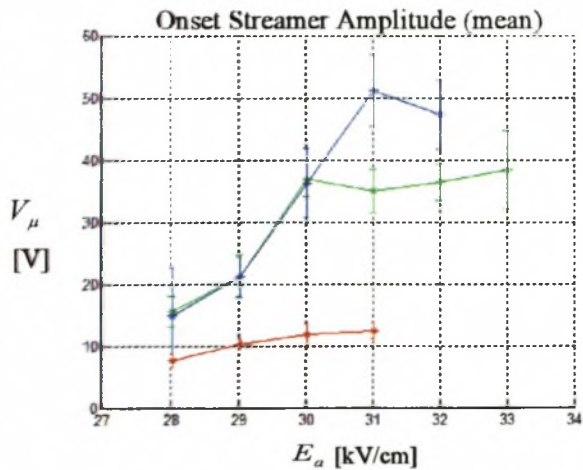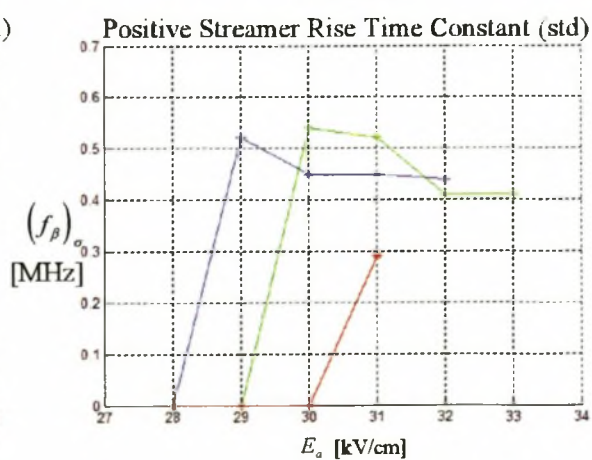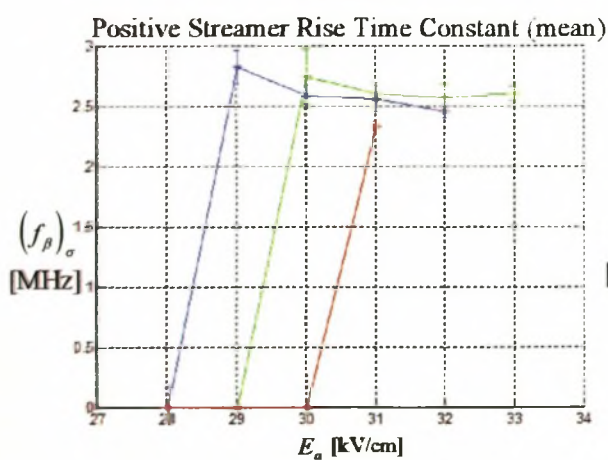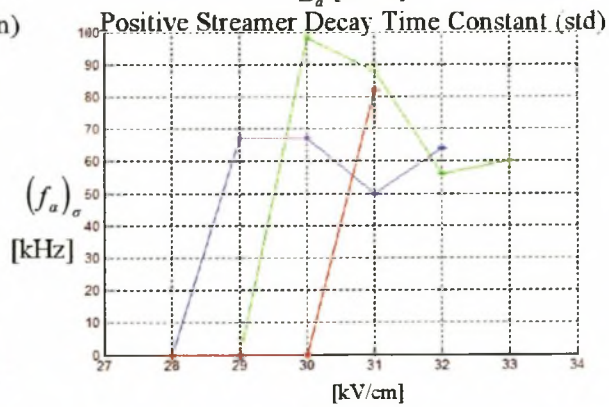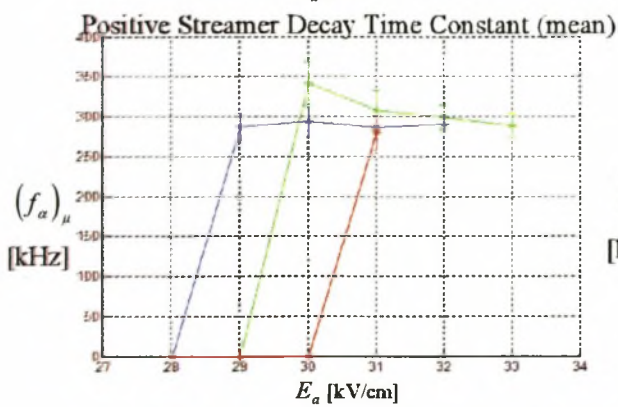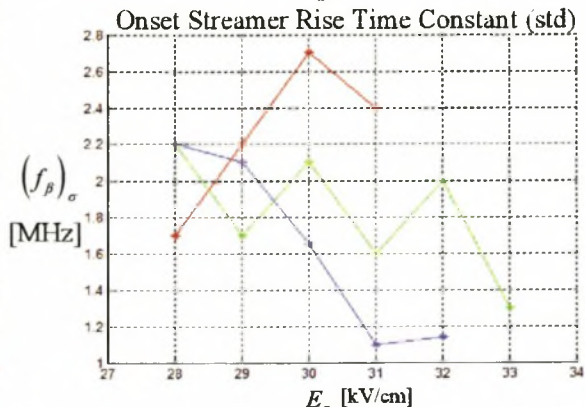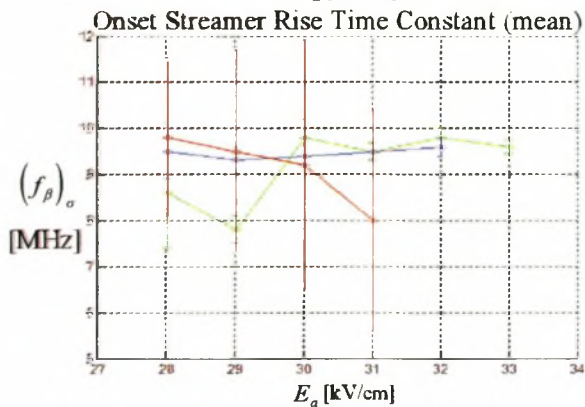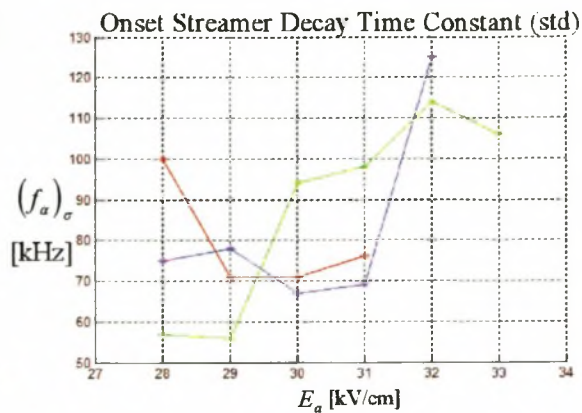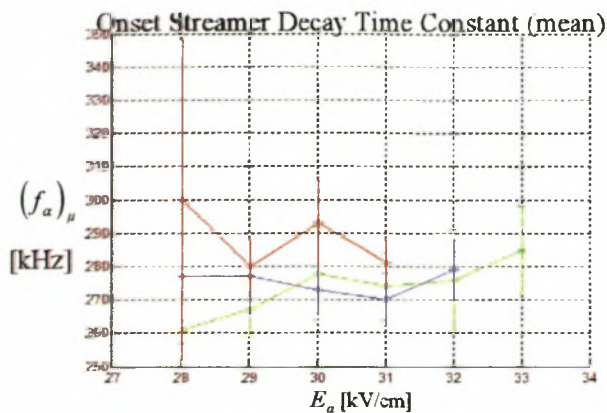
H. 2   Conductor Material

measurement	1	2
cage	US (small)	US (small)
R [cm]	250	250
centre conductor	smooth Cu.	smooth Al.
a [cm]	0.75	0.78
$\Delta V_P \| V_{diff}$ [% | %]	0.3 | 0.58	0.3 | 0.58
δ	1.025	1.033
Relative Humidity [%]	70	65
E_a / V [cm^{-1}]	0.3802	0.3698
d_c [cm]	26.76	29.21
$(\nabla . E)_a\|_{E=28kV/cm}$ [kV/cm^2]	-37.3	-35.9
C [pF]	15.8	16.1
$E_{c(measurable)}$ [kV/cm]	28	32
Flash-over Gradient [kV/cm]	32	36

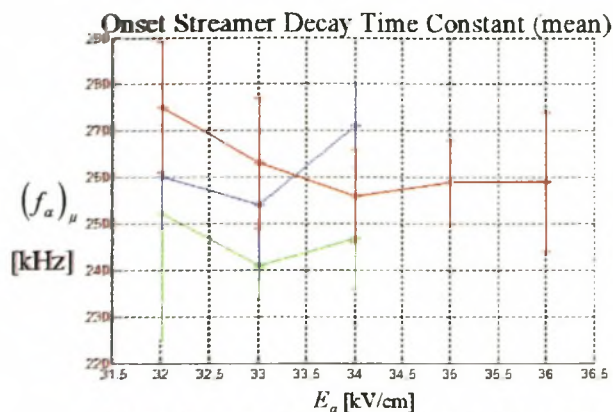### (1) Start Phase and Discharge Duration of Measurable Positive Corona Modes:
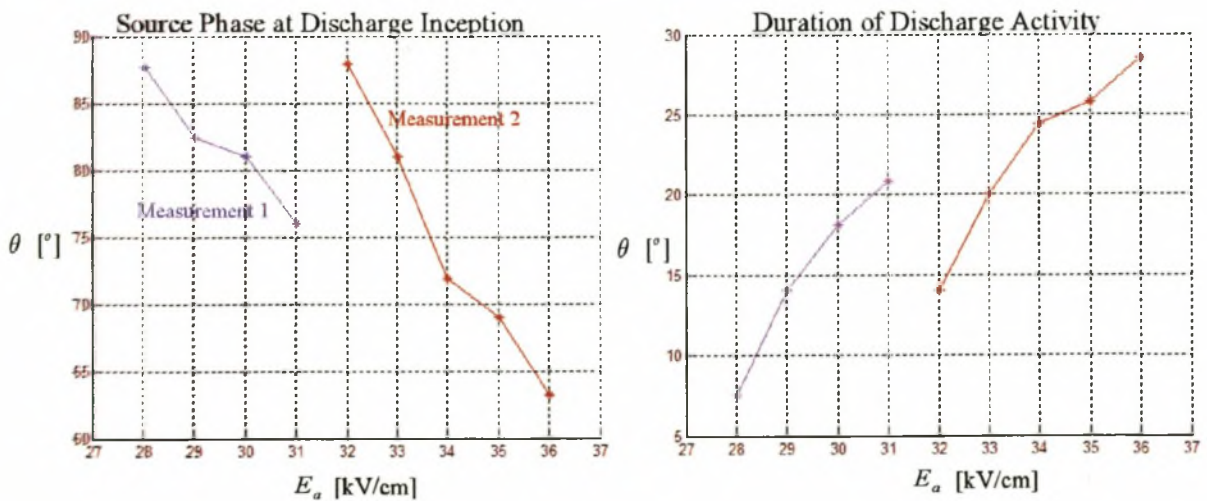
(2) Measurable Positive Corona Pulse Number and Type :

(3) Measurable Positive Corona Pulse Parameters :

Onset Streamer Decay Time Constant (mean)
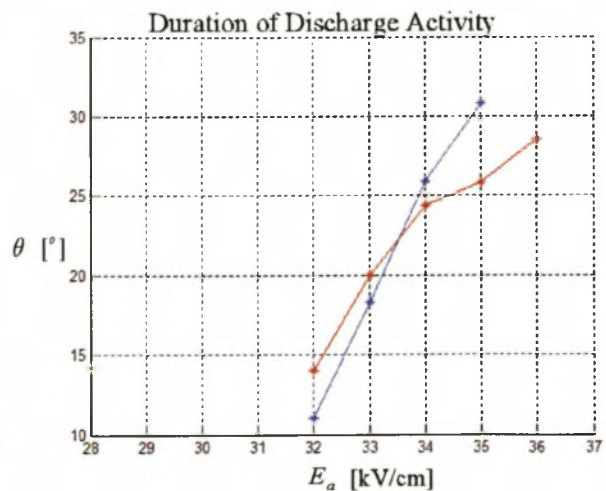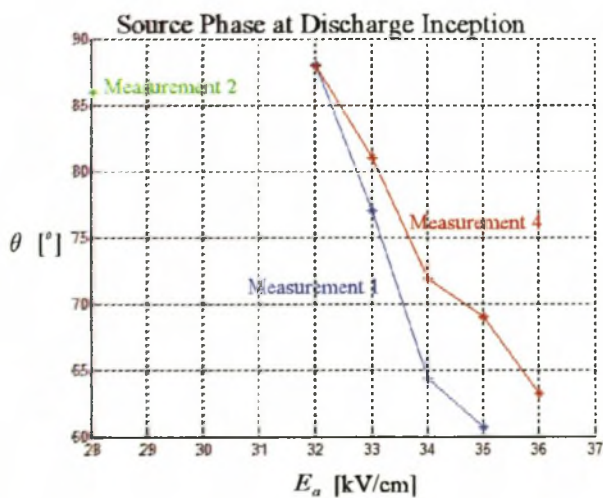
Onset Streamer Decay Time Constant (std)

Onset Streamer Rise Time Constant (mean)

Onset Streamer Rise Time Constant (std)

Positive Streamer Decay Time Constant (mean)

Positive Streamer Decay Time Constant (std)

Positive Streamer Rise Time Constant (mean)

Positive Streamer Rise Time Constant (std)

176
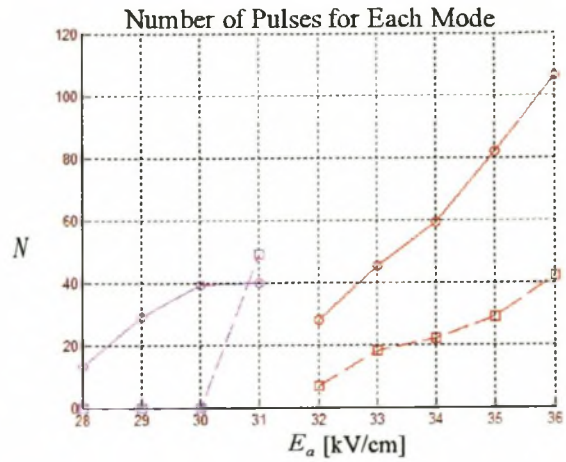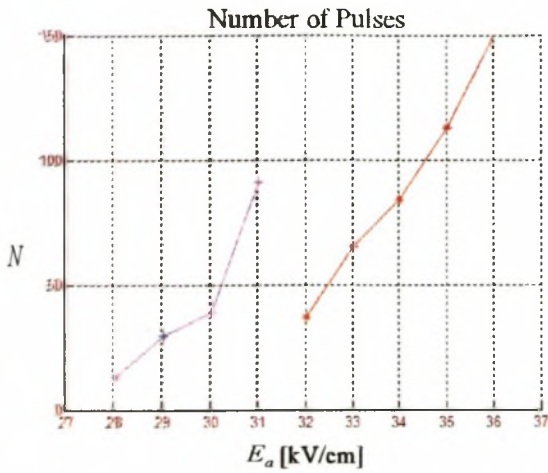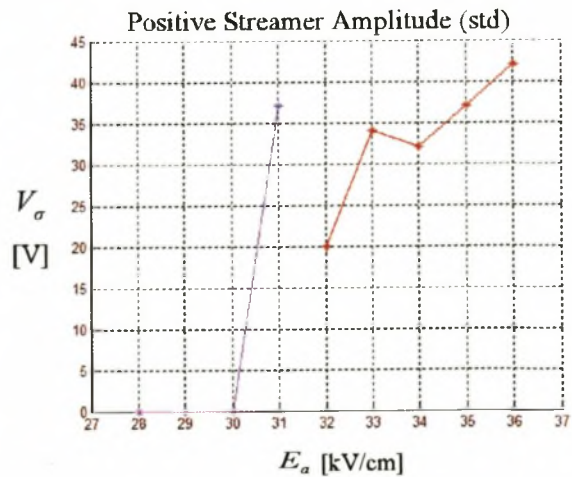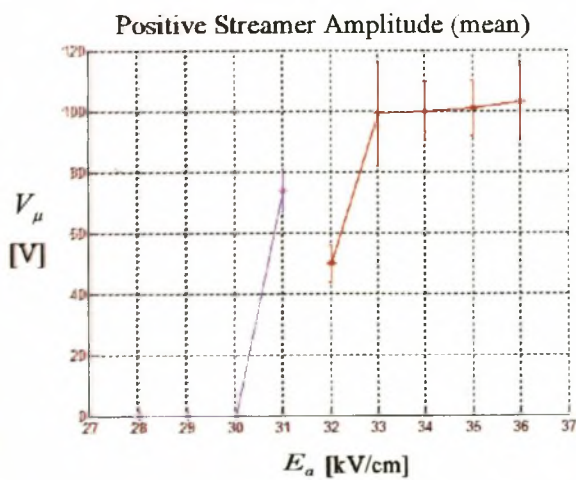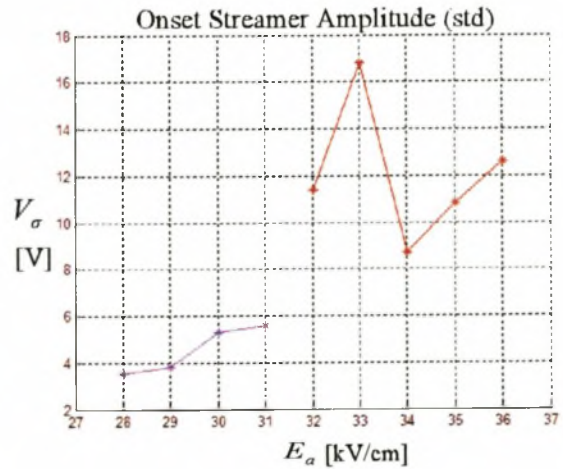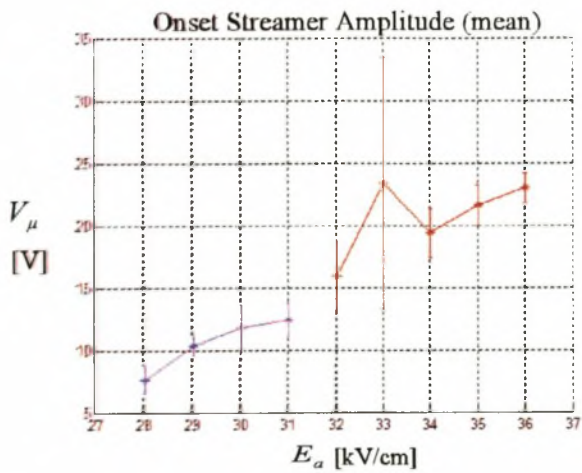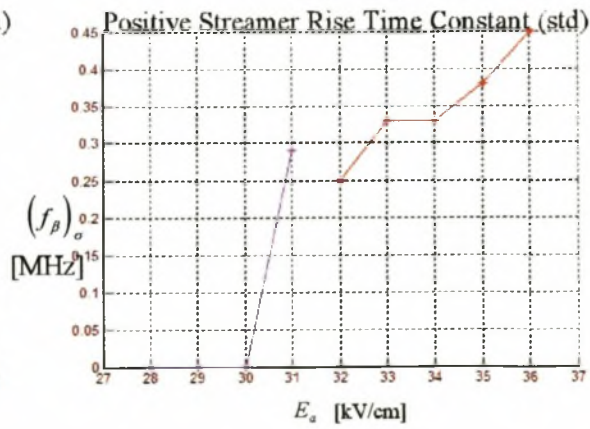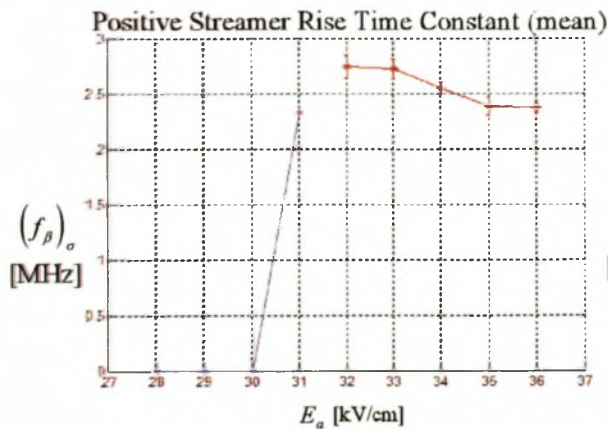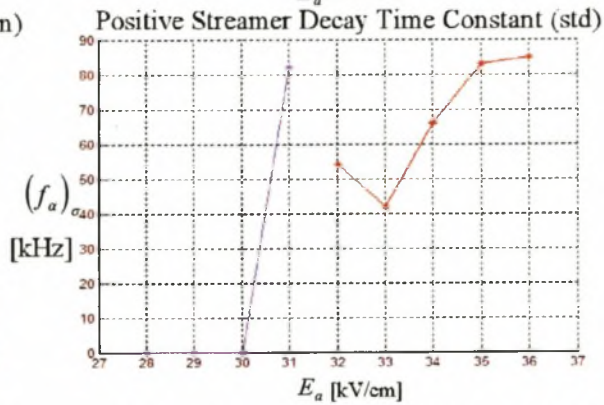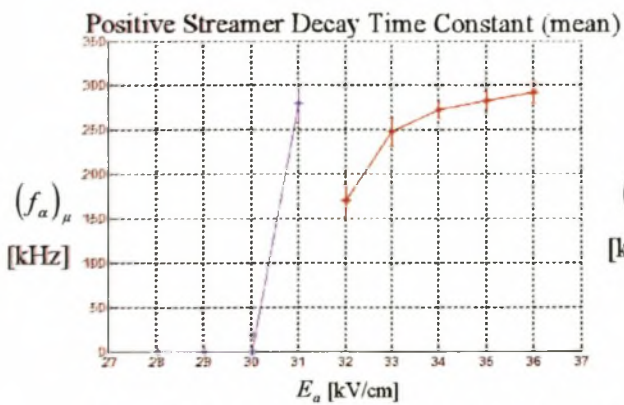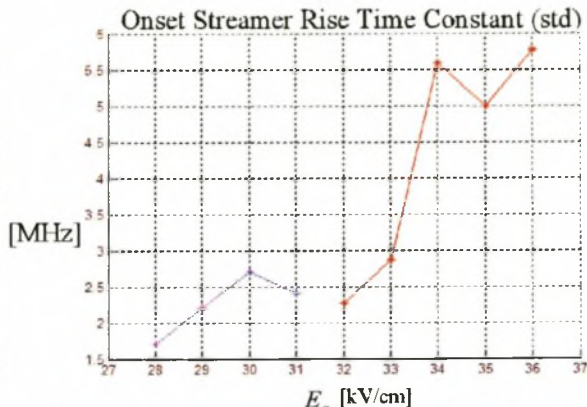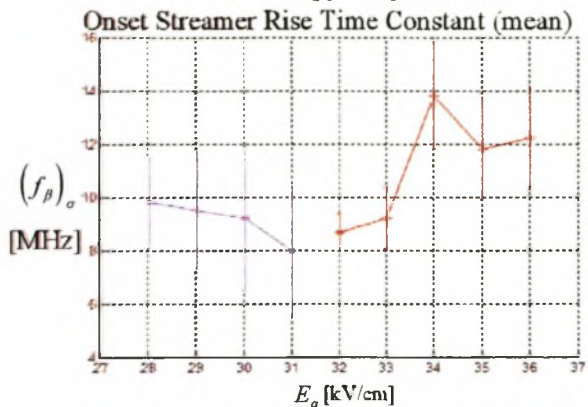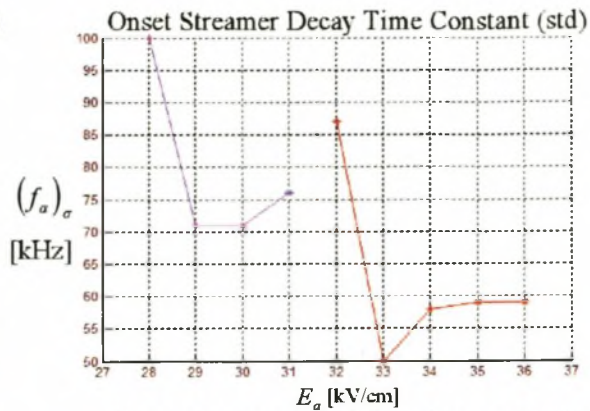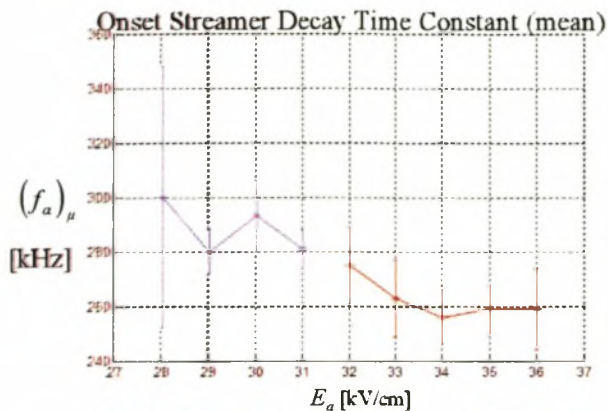
H. 3   RAD and RH

measurement	1	2	3
cage	US (small)	US (small)	US (small)
R [cm]	250	250	250
centre conductor	smooth Cu.	smooth Cu.	smooth Cu.
a [cm]	0.75	0.75	0.75
$\Delta V_P \,|\, V_{diff}$ [%	%]	0.30	0.58	0.30	0.58	0.30	0.58
δ	1.021	0.825	1.025
Relative Humidity [%]	60	72	70
E_a / V [cm^{-1}]	0.3802	0.3802	0.3802
d_c [cm]	27.2	25.6	26.8
$(\nabla . E)_a\big|_{E=28}$ [kV/cm^2]	-37.3	-37.3	-37.3
C [pF]	15.8	15.8	15.8
$E_{c(measurable)}$ [kV/cm]	29	25	28
Flash-over Gradient [kV/cm]	34	27	32

(1) Start Phase and Discharge Duration of Measurable Positive Corona Modes:
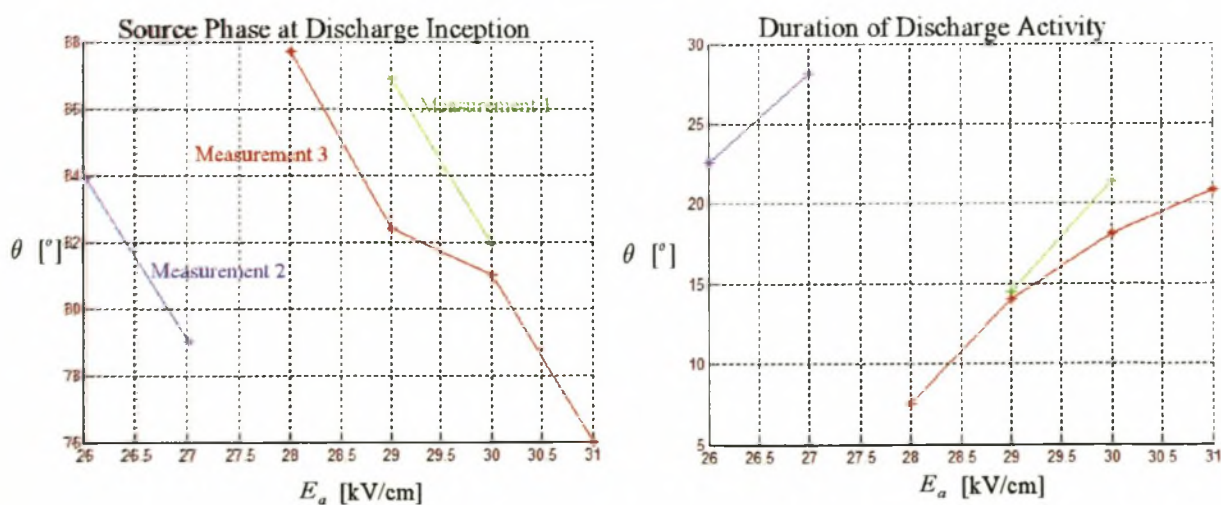
(2) Measurable Positive Corona Pulse Number and Type :
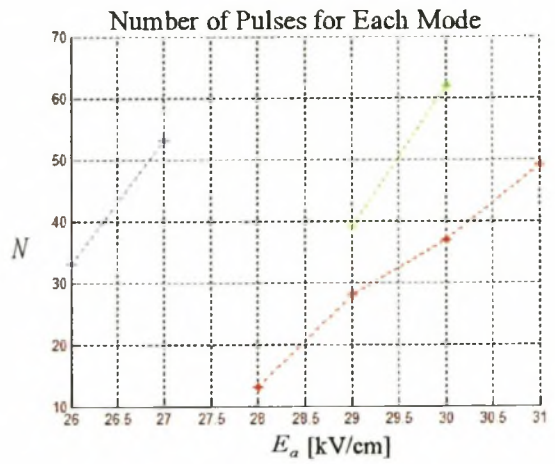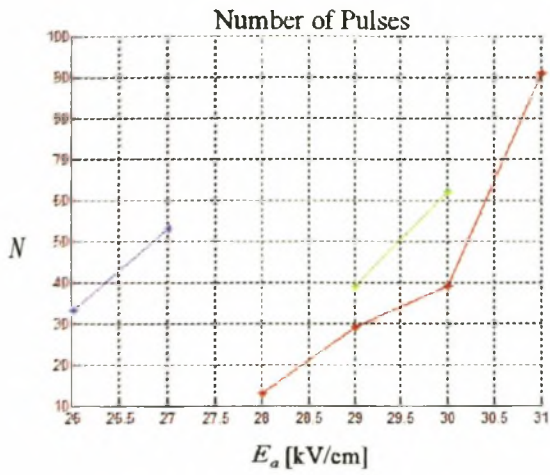

(3) Measurable Positive Corona Pulse Parameters :
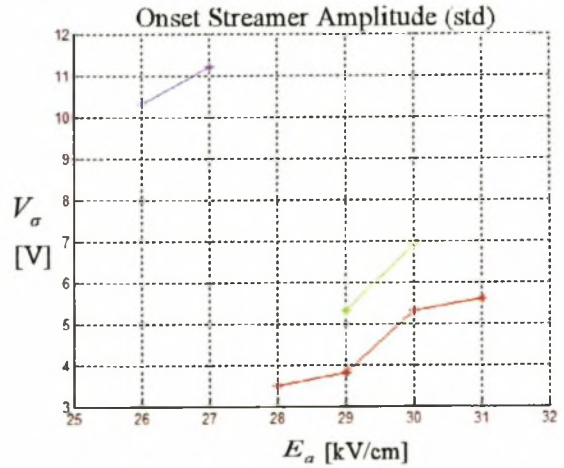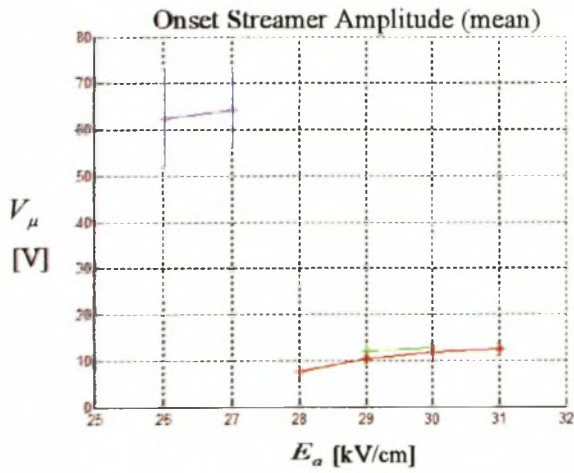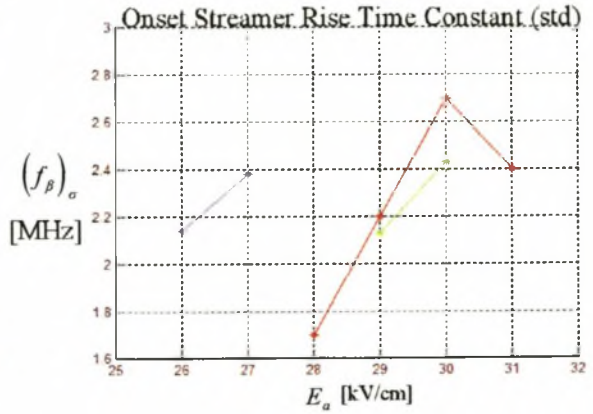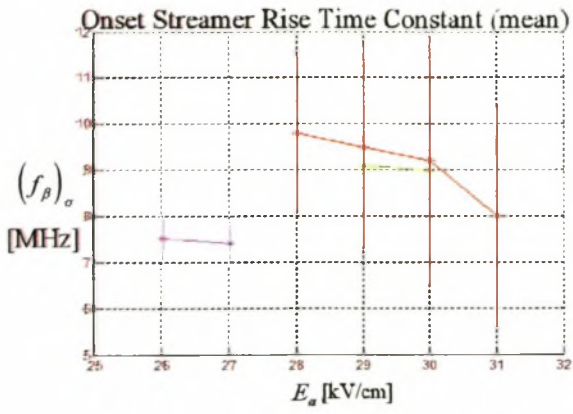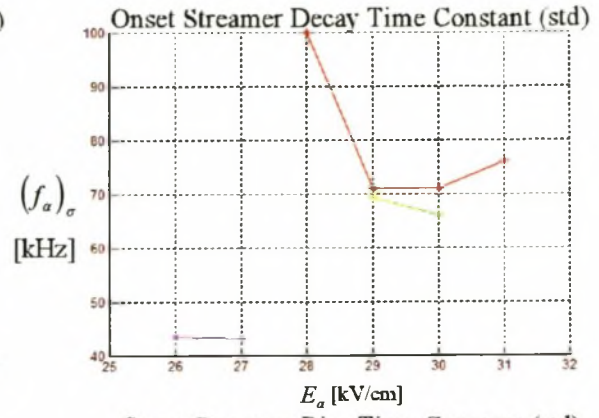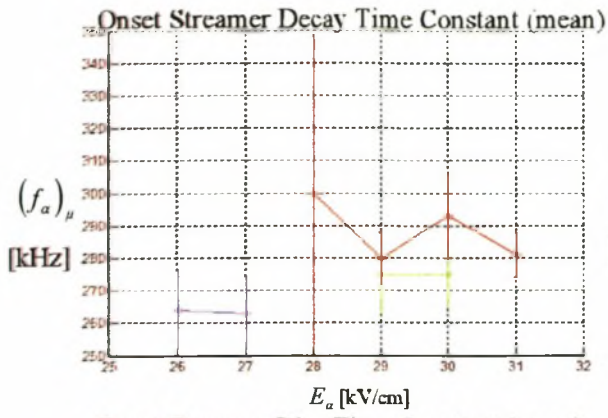
H. 4   Space Charge Distribution

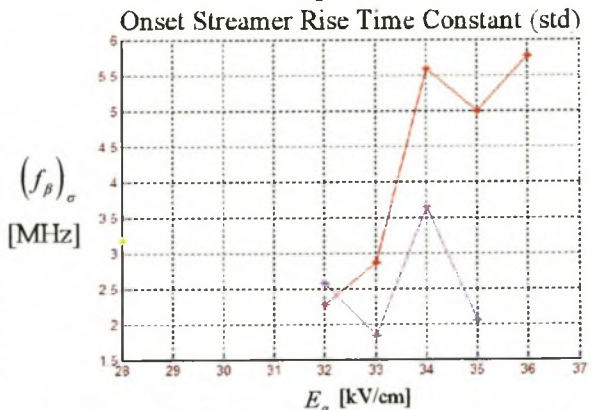| measurement	1	2	3
cage	US (small) unpainted fine mesh	US (small) unpainted coarse mesh	US (small) painted fine mesh
R [cm]	250	250	250
centre conductor	smooth Al.	smooth Al.	smooth Al.
a [cm]	0.78	0.78	0.78
$\Delta V_P \,|\, V_{diff}$ [%	%]	0.30	0.58	0.30	0.58	0.30	0.58
δ	1.035	1.035	1.033
Relative Humidity [%]	65	65	65
E_a / V [cm^{-1}]	0.3698	0.3698	0.3698
d_c [cm]	29.2	29.2	29.2
$(\nabla \cdot E)_a \big|_{E=28}$ [kV/cm^2]	-35.9	-35.9	-35.9
$E_{c(measurable)}$ [kV/cm]	32	32	32
Flash-over Gradient [kV/cm]	35	35	36

(1) Start Phase and Discharge Duration of Measurable Positive Corona Modes:

Source Phase at Discharge Inception

Duration of Discharge Activity

(2) Measurable Positive Corona Pulse Number and Type :

Number of Pulses

Number of Pulses for Each Mode

(3) Measurable Positive Corona Pulse Parameters :

Onset Streamer Amplitude (mean)

Onset Streamer Amplitude (std)

Positive Streamer Amplitude (mean)

Positive Streamer Amplitude (std)

181

Onset Streamer Decay Time Constant (mean)

Onset Streamer Decay Time Constant (std)

Onset Streamer Rise Time Constant (mean)

Onset Streamer Rise Time Constant (std)

Positive Streamer Decay Time Constant (mean)

Positive Streamer Decay Time Constant (std)

Positive Streamer Rise Time Constant (mean)

Positive Streamer Rise Time Constant (std)

H. 5   Surface Area and E-Field Divergence

measurement	1	2	3	4
cage	US (small)	US (small)	US (small)	US (small)
R [cm]	250	250	250	250
centre conductor	smooth Al.	smooth Al.	smooth Cu.	smooth Al.
a [cm]	0.5	1.25	1.1	0.78
$\Delta V_P \mid V_{diff}$ [%	%]	0.30	0.58	0.30	0.58	0.30	0.58	0.30	0.58
δ	1.031	1.031	1.031	1.033
Relative Humidity [%]	62	62	62	65
E_a / V [cm^{-1}]	0.5112	0.2670	0.2910	0.3698
d_c [cm]	23.5	34.3	30.4	29.2
$(\nabla . E)_a\big|_{E=28}$ [kV/cm^2]	-56	-22.4	-25.5	-35.9
C [pF]	14.2	18.6	17.8	16.1
$E_{c(measurable)}$ [kV/cm]	32	28	26	32
E_{fo} [kV/cm]	-	30	27	36

(1) Start Phase and Discharge Duration of Measurable Positive Corona Modes:

183

(2) Measurable Positive Corona Pulse Number and Type :

(3) Measurable Positive Corona Pulse Parameters :

184
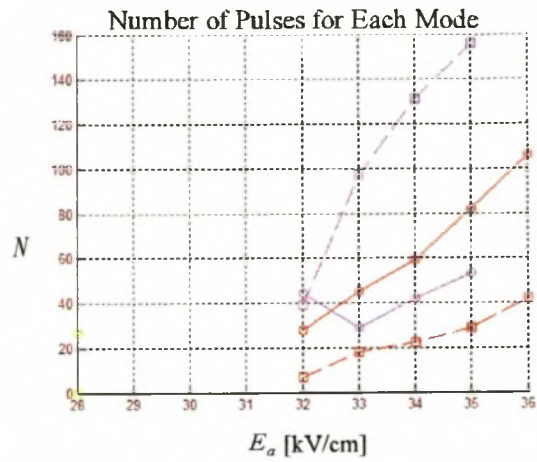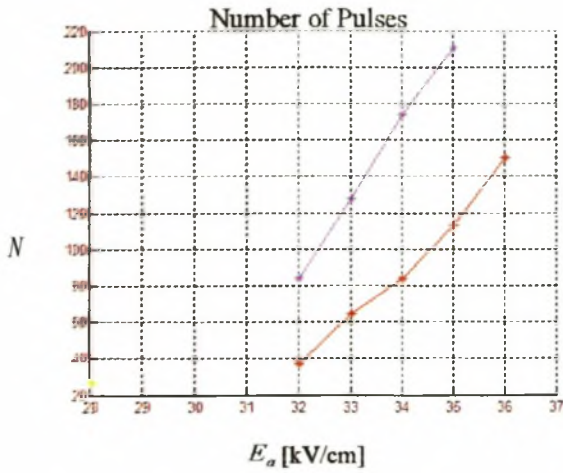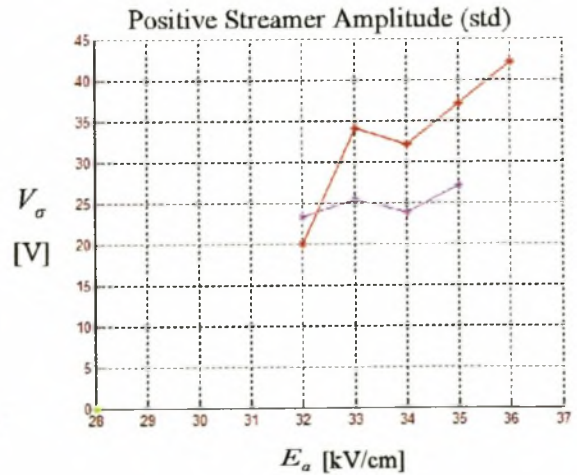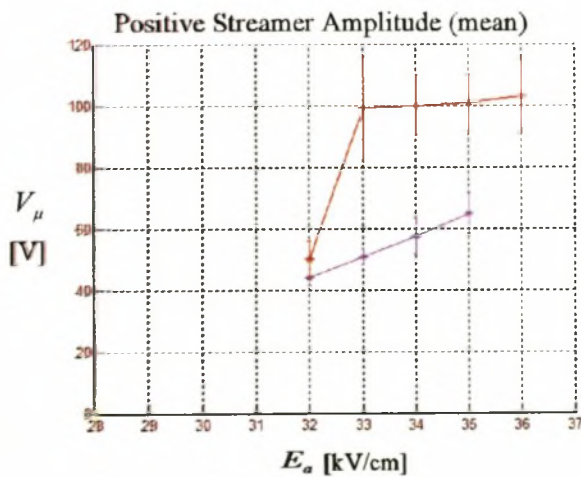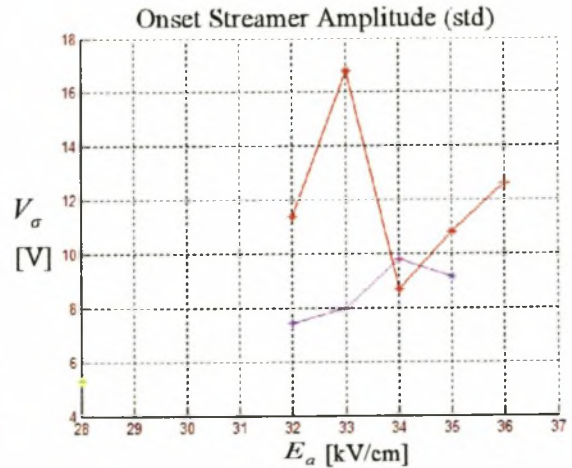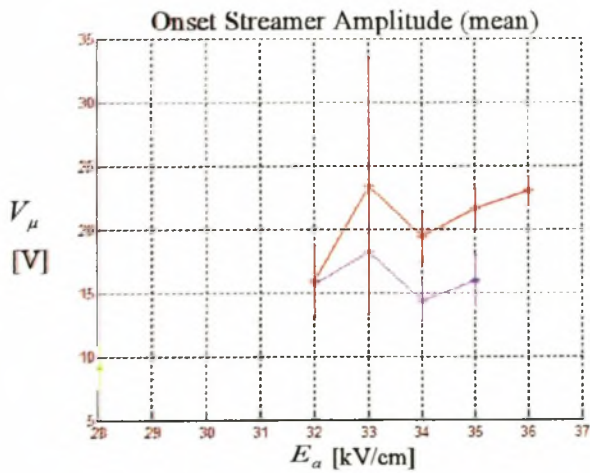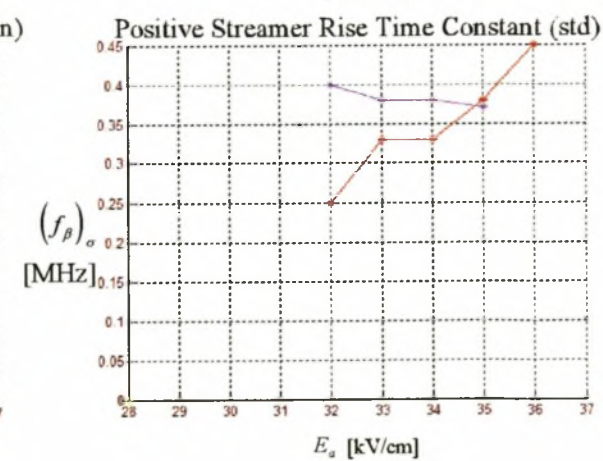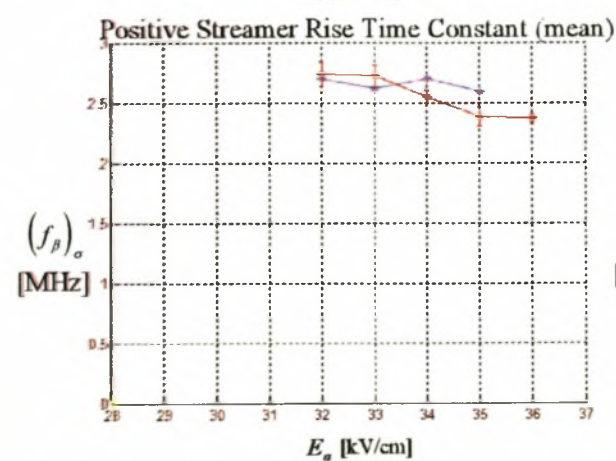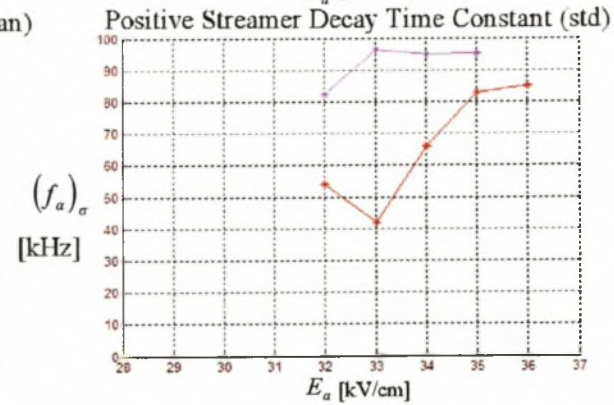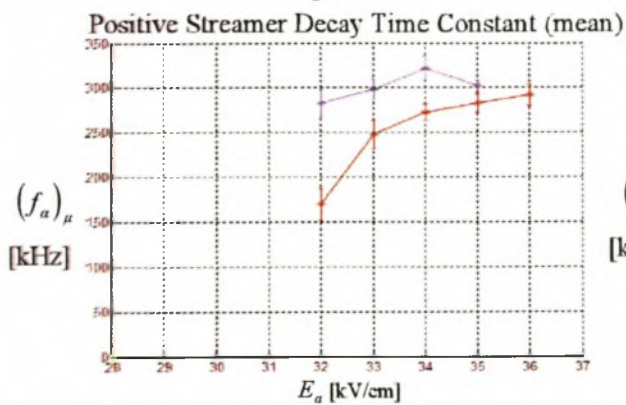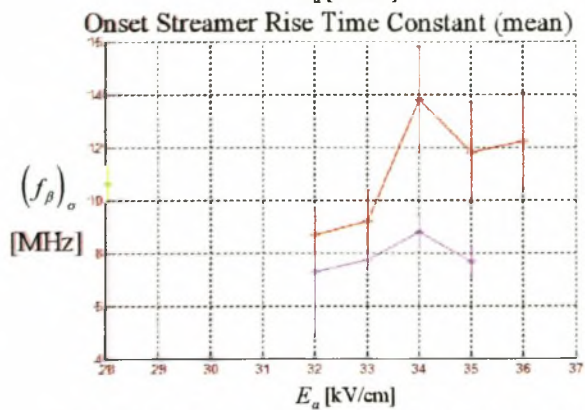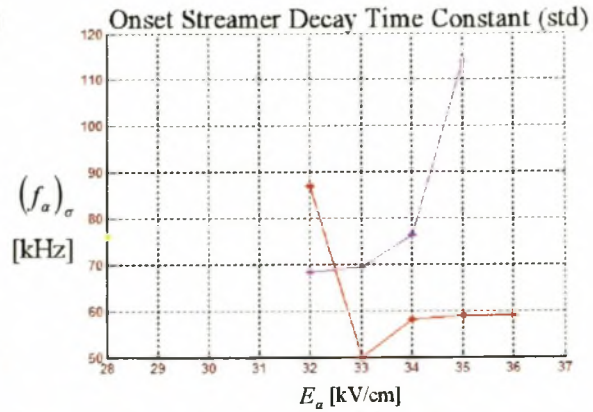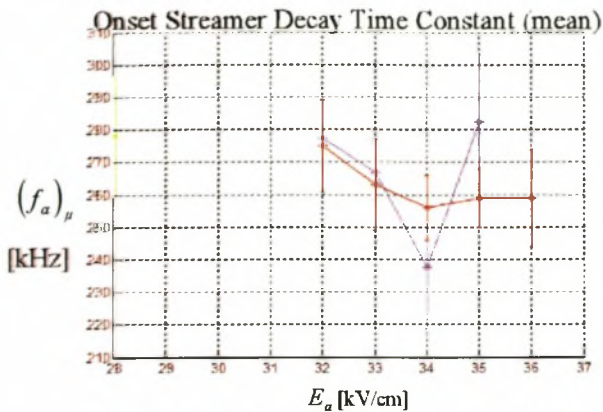
H. 6   Surface Gradient Distribution
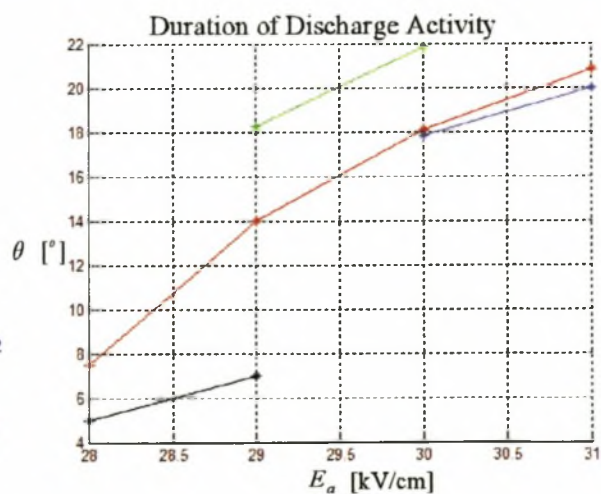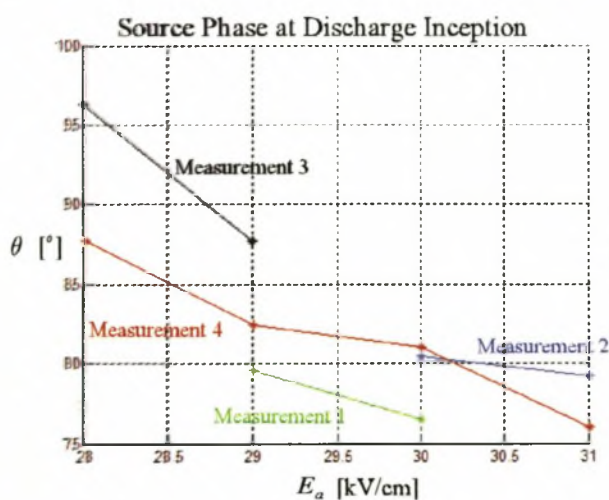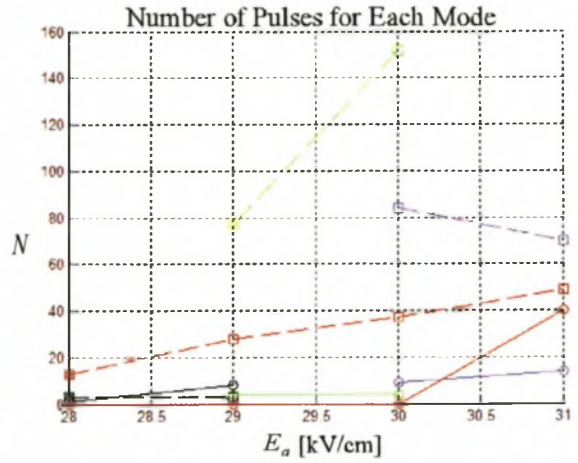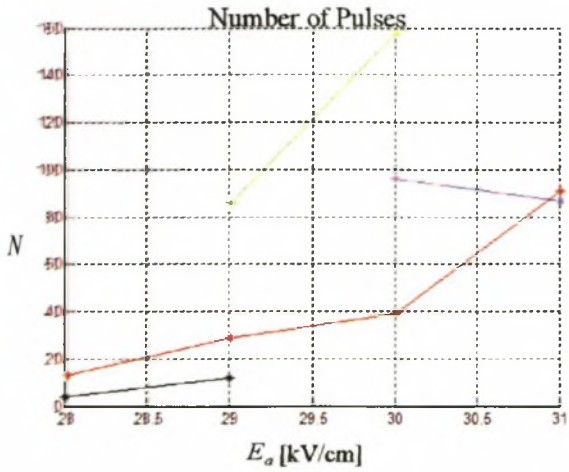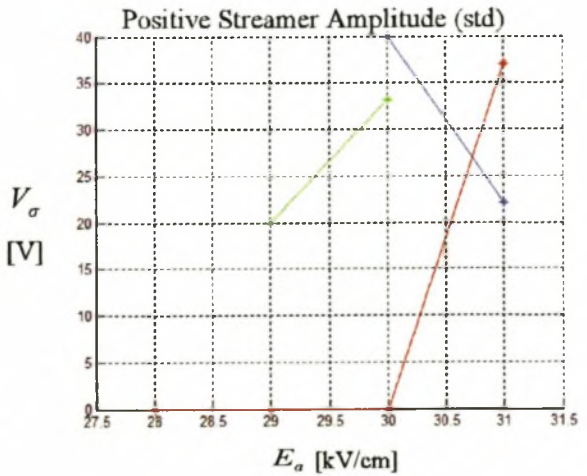
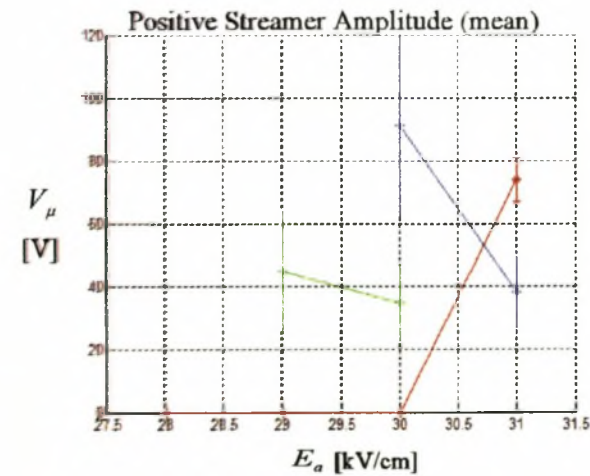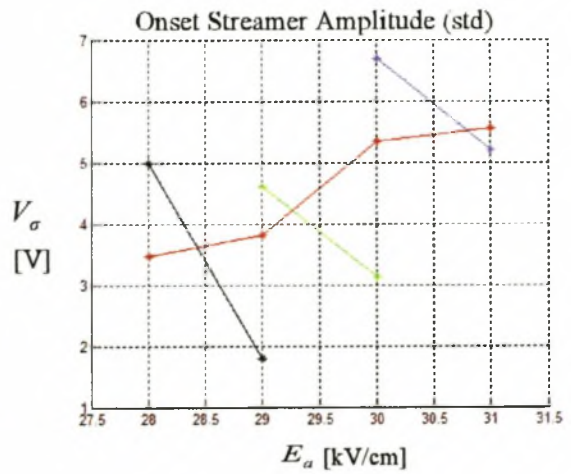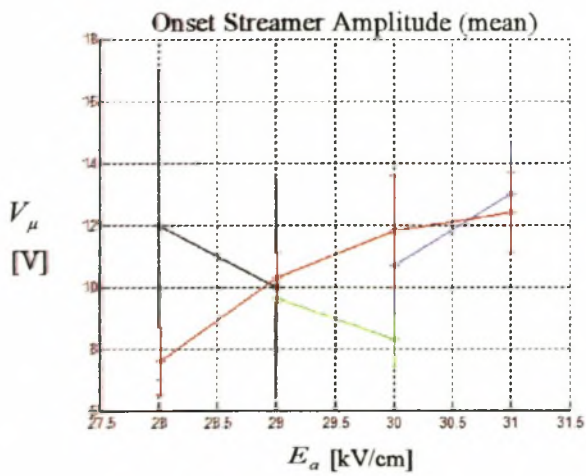| measurement	1	2	3	4
cage	US (small)	US (small)	US (small)	US (small)
R [cm]	250	250	250	250
centre conductor	smooth Cu.	smooth Cu.	smooth Cu.	smooth Cu.
a [cm]	0.75	0.75	0.75	0.75
$\Delta V_P \mid V_{diff}$ [% | %]	0.30 | 0.58	0.30 | 0.58	0.30 | 0.58	0.30 | 0.58
δ	1.025	1.025	1.025	1.025
Relative Humidity [%]	70	70	70	70
$\left(E_m\right)_a /V$ [cm^{-1}]	0.3844	0.3922	0.4056	0.3802
C [pF]	15.93	16.13	16.51	15.86
Displacement [cm]	3	6	9	0
$E_{c(measurable)}$ [kV/cm]	29	30	28	28
E_{fo} [kV/cm]	32	32	30	32

(1) Start Phase and Discharge Duration of Measurable Positive Corona Modes:

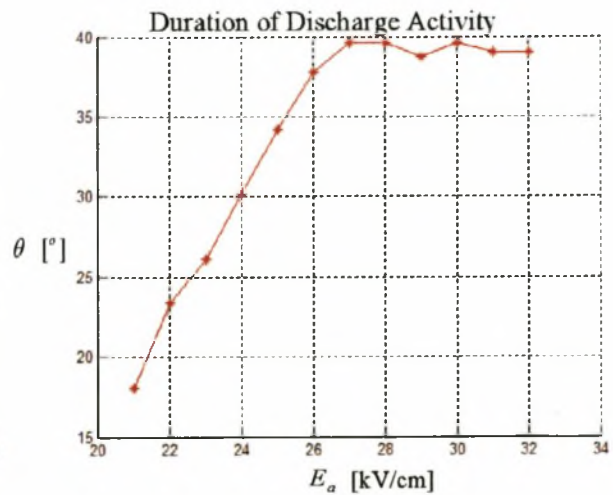**(2) Measurable Positive Corona Pulse Number and Type :**

(3) Measurable Positive Corona Pulse Parameters :

H. 7   Conductor Stranding

measurement	1
cage	US (small)
R [cm]	250
centre conductor	ACSR (hare)
a [cm]	0.71 (nominal)
$\Delta V_P \mid V_{diff}$ [% | %]	0.3 | 0.58
δ	1.02
Relative Humidity [%]	50
E_a / V [cm^{-1}]	0.3995
C [pF]	15.6
$E_{c(measurable)}$ [kV/cm]	21
Flash-over Gradient [kV/cm]	-

(1) Start Phase and Discharge Duration of Measurable Positive Corona Modes:
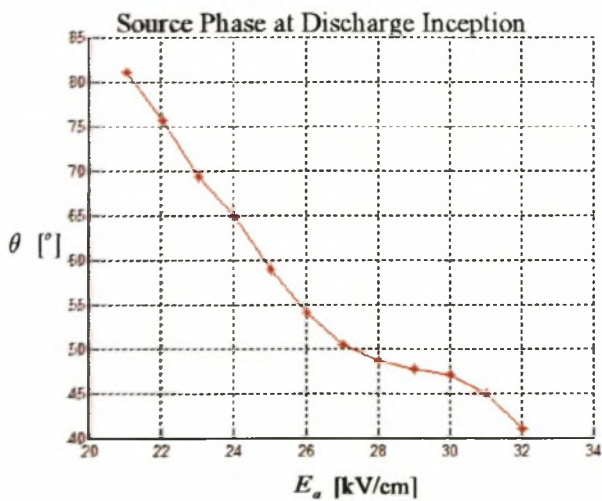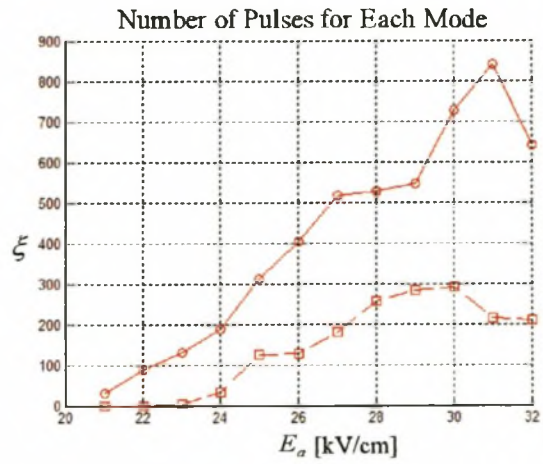
(2) Measurable Positive Corona Pulse Number and Type :

Number of Pulses

Number of Pulses for Each Mode

(3) Measurable Positive Corona Pulse Parameters :

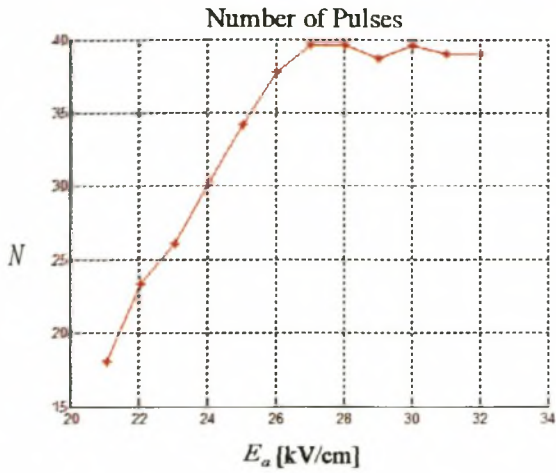Onset Streamer Amplitude (mean)

Onset Streamer Amplitude (std)

Positive Streamer Amplitude (mean)

Positive Streamer Amplitude (std)

Onset Streamer Decay Time Constant (mean)

Onset Streamer Decay Time Constant (std)

Onset Streamer Rise Time Constant (mean)

Onset Streamer Rise Time Constant (std)

Positive Streamer Decay Time Constant (mean)

Positive Streamer Decay Time Constant (std)

Positive Streamer Rise Time Constant (mean)

Positive Streamer Rise Time Constant (std)

190